Title	高官能基密度を有するポリメチレン系高分子の電解質及びバインダーとしての金属イオン二次電池への応用
Author(s)	Amarshi, Patra
Citation	
Issue Date	2024-09
Type	Thesis or Dissertation
Text version	ETD
URL	http://hdl.handle.net/10119/19399
Rights	
Description	supervisor: 松見 紀佳, 先端科学技術研究科, 博士

Doctoral Dissertation

Polymethylene Polymers with High-Density Functional Groups as Electrolyte and Binders for Metal Ion Secondary Batteries

Amarshi Patra

Supervisor: Noriyoshi Matsumi

Graduate School of Advanced Science and Technology
Japan Advanced Institute of Science and Technology

Material Science

September 2024

Abstract

Batteries are crucial in advancing efficient energy storage technology amid the global transition to renewable energies for carbon-free transportation and stationary energy storage. They are essential for decarbonizing the transport and energy sectors, while also finding applications in aerospace, medical devices, automotive, power grids, wearable electronics, and robotics. Li-ion and Na-ion batteries (LIB, SIB), with their high energy and power density, are preferred for hybrid/all-electric vehicles, power tools, and portable electronic devices, promising significant reductions in greenhouse gas emissions. Their potential extends to improving energy efficiency and quality from renewable sources in power grid applications. However, challenges loom regarding their long-term viability, cost effectiveness, availability of materials, and safety concerns such as fires, explosions, and problems that need addressing. A deeper understanding of metal-ion battery performance under adverse conditions is crucial for ensuring safer cells and their continued contribution to a sustainable energy economy.

The present doctoral work mainly focuses on synthesizing dense functional group polymers through cost-effective and non-toxic materials aiming to mitigate the abovementioned issues, divided into chapters 2,3, 4, 5, and 6 in the doctoral thesis.

In Chapter 2, LIBs are crucial for various applications, but their electrolytes' carbonate-based liquid solvents face challenges of flammability and lithium-ion movement dynamics. Poly (ethoxycarbonylmethylene) (PECM) with a high density of ester groups was explored as a polymer electrolyte to tackle these issues. PECM exhibited polar aprotic properties, enhanced cation solvation, and a glass transition temperature of 10–33 °C when combined with LiTFSI. Ionic conductivity ranged from 9.76×10^{-5} to 3.08×10^{-4} S cm^{-1} at 51 °C, with lithium-ion transference numbers between 0.80 and 0.98 and diffusion activation energies of 27.4–43.0 kJ mol^{-1}. The PECM-based cathodic half-cell displayed excellent rate capacity and long-cycle performance, retaining 80% capacity at 0.2 C for over 100 cycles. These findings highlight PECM's potential as an alternative electrolyte material for future LIB applications.

In Chapter 3, poly(fumaric acid) (PFA) as a binder in LIBs shows exceptional Li^+ diffusion kinetics. Studies, including activation energy and diffusion coefficient assessments, confirm this. The PFA binder demonstrates impressive reversible specific capacities ranging from 343 to 65 mAhg^{-1} across various current densities of graphite electrode. At a 1C rate during extended cycling, the PFA binder maintains remarkable performance, achieving a reversible specific capacity of 325 mAhg^{-1} with an impressive 79% capacity retention at 710th cycle. Additionally, under rapid 5C charging, the PFA binder reduces polarization, ensuring a specific capacity of 54 mAhg^{-1} in just 1.5 minutes. Impedance studies reveal a low-resistance solid electrolyte interphase (R_{SEI}) value, facilitating the smooth passage of Li^+ ions. Postmortem investigations confirm the PFA binder's effectiveness, forming a uniform SEI on the electrode surface, devoid of exfoliation or cracks. This highlights the binder's role in enhancing LIB performance.

In Chapter 4, SIB with PFA binder for hard carbon anodes exhibit exceptional performance. They achieve an impressive initial coulombic efficiency of 80.8% and outperform PAA and PVDF binders in terms of reversible rate capacities at various current densities, with PFA binder showing capacities ranging from 332 to 119 mAhg^{-1}. PFA binder also demonstrates excellent capacity retention, retaining 85.4% of its reversible specific capacity over 250 cycles at a higher current density of 60 mAg^{-1}, reaching a maximum capacity of 288 mAhg^{-1}. Moreover, PFA binder enhances sodium ion kinetics by modifying SEI, resulting in a lower activation energy, a higher sodium ion diffusion coefficient, and reduced resistance compared to PAA and PVDF binders.

In chapter 5, Poly(oxycarbonylmethylene 1-allyl-3-methyimidazolium) (PMAI), exhibits excellent electrochemical performance for graphite in LIB, achieving 80% capacity retention at 750 cycles with a specific capacity of 298 mAhg^{-1} at 1C compared to PVDF binder. At 5C rate, PMAI/Gr delivers a higher discharge capacity of 85 mAhg^{-1} than PVDF/Gr (47 mAh g^{-1}). Postmortem analysis reveals noticeable electrode degradation containing PVDF binder, characterized by high charge transfer resistance and thick organic species at SEI. In contrast, when PMAI serve as binders, high content of inorganic species in SEI and crack-less electrode is observed, resulting in reduced overpotential, lower activation energy and enhanced Li^+ diffusion.

In Chapter 6, PMAI binder for hard carbon in SIB is shown to be reduced during cyclic voltammetry and charge/discharge at 0.9 V vs. Na^+/Na, leading to better adhesion with electrode components and formation of functionalized SEI. The PMAI/HC`s initial coulombic efficiency is 74% and a maximum specific capacity of 254 mAhg^{-1} with a capacity retention of 96.2% was observed after 200 cycles at 60 mAg^{-1}. PMAI-containing electrodes showed better rate capability at different current densities than PVDF binder. PMAI/HC electrode exhibits an enhanced Na^+ diffusion coefficient, low R_{SEI} and R_{CT} and decreased activation energy of desolvation, which is ascribed to densely polar ionic liquid groups along the binder, enhancing the ion conductivity in electrode, influencing the Na^+ diffusion kinetics at the surface and formation of functionalized SEI due to binder reduction.

Keywords: binder for carbon anode, lithium-ion batteries, poly(ionic liquid), sodium-ion batteries, water-soluble binder

Acknowledgements

The research presented in this thesis was conducted under the supervision of Prof. Noriyoshi Matsumi at the School of Materials Sciences, Japan Advanced Institute of Science and Technology from 2021 to 2024. The focus of the studies was on synthesizing Polymethylene Polymers with High-Density Functional Groups as Electrolyte and Binders for Metal Ion Secondary Batteries.

The author extends sincere appreciation to Prof. Noriyoshi Matsumi for his invaluable guidance, insightful suggestions, and unwavering encouragement throughout the research process. Gratitude is also extended to the members of the Review committee Prof. Yuki Nagao for their time and constructive feedback on the manuscript.

Special thanks are given to Prof. Pakkirisamy Thilagar for providing the opportunity to conduct experiments at the Department of Inorganic and Physical Chemistry, Indian Institute of Science, India as well as his team for their collaboration, support, and helpful suggestions during the author's time in India.

The author also acknowledges the guidance and encouragement from Assistant Prof. Bharat Srimitra Mantripragada and other members of the laboratory at JAIST.

Heartfelt thanks go to the author's parents and love ones for their unwavering encouragement during challenging times. Finally, the author expresses gratitude to the Almighty for all blessings received.

Amarshi Patra
Graduate School of Advanced Science and Technology
Japan Advanced Institute of Science and Technology
September 2024

Table of Contents

Chapter 1

Chapter 2

Chapter 3

Chapter 4

Chapter 5

Chapter 6

Chapter 7

Chapter 1

Introduction

Abstract

This chapter provides a robust examination of battery evolution, particularly focusing on lithium-ion batteries and sodium ion batteries. It delves deeply into the diverse materials utilized across electrolyte, binders, anode, and cathode segments. Furthermore, it highlights the benefits associated with integrating ionic liquids in binders and explores the potential of high-density functional group polymer compounds as effective ion transportation and battery performances. Moreover, it introduces the concept of crafting organic-inorganic hybrids through the manipulation of precursor materials. Essentially, this chapter serves as the cornerstone for the research methodology employed throughout the doctoral investigation.

Introduction to Batteries:

General background:

The advancement of technology has heavily relied on fossil fuels, but their limited supply and environmental impact, including pollution and increasing carbon footprints, necessitate a shift towards alternative energy sources. This has prompted global efforts to develop renewable resources like solar, geothermal, and wind power. Concurrently, material innovations are underway to align current technologies with future needs, leading to emergence of electric vehicles. Li-ion batteries, tailored to meet consumer demands for efficiency, safety, and environmental sustainability, play a pivotal role in this evolution. From the implementation of lead-acid and Ni-based batteries in vehicles to LIB in electronic devices, energy sources in daily life vary widely. Environmental awareness drives ongoing improvement and scrutiny of technologies, particularly LIB and emerging alternatives like Li-metal batteries. Research efforts, especially in hybrid vehicles, are accelerating, promising advancements in battery technology and the broader battery market.

A battery is composed of electrochemical cells, which function as transducers, converting between electrochemical and chemical energy and vice versa. These batteries are interconnected depending on the required output voltage. Each cell comprises a cathode (positive electrode), an anode (negative electrode), and an electrolyte for Li-ion transport. The electrolyte serves a dual purpose: It functions as a barrier between the electrodes while enabling ion conduction between them. Additionally, external connections between electrodes establish a pathway for electron movement, completing the electrochemical circuit. While batteries are conceptually straightforward, their evolution has not been as straightforward as in other electronics sectors. Due to the numerous variables involved, battery research and development represent a significant challenge.

Historical perspective:

Indeed, battery technology has made remarkable advancements compared to its historical predecessors. Throughout the last century, primary batteries (MnO2-based) and secondary types utilizing Lead acid, Nickel, or Zinc-based systems were predominantly used. However, the efficiency and performance of Ni or Zn-metal batteries and Pb-acid batteries eventually reached a plateau. This prompted the emergence of new technologies like lithium-ion batteries, which have gained traction due to evolving industrial needs and the pursuit of technological superiority. The drive towards a technologically advanced future, while also considering the responsible use of Earth's resources, motivates ongoing energy research endeavors. Although renewable energy sources have successfully harnessed, the need for portable energy solutions for domestic applications highlights the importance of further advancements in existing technologies. Since 1990, lithium-ion batteries have undergone significant advancements, particularly in power and safety, and have catalyzed the development of related technologies through extensive research efforts in this field[1,2].

The progression of battery technology over time can be organized in a chronological manner as shown in Figure 1.

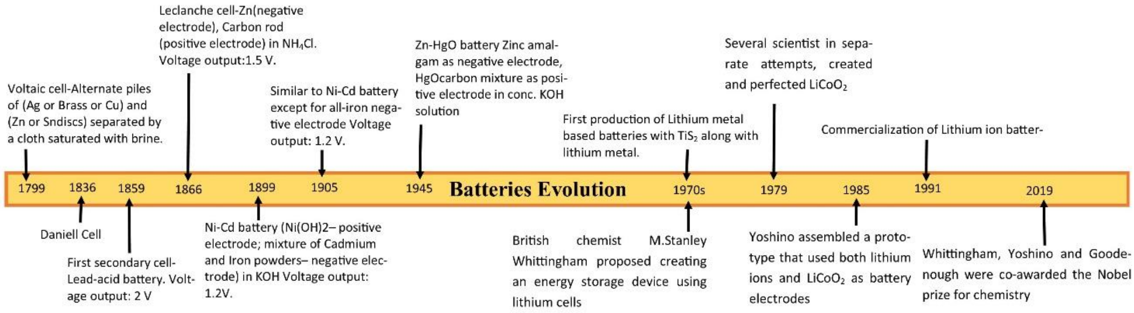

Figure 1: Timeline of evolution in batteries breakthroughs.

Battery:

At its essence, a battery serves two primary functions: delivering energy output over a set period and storing energy. Primary batteries handle energy output, while secondary batteries go a step further by storing energy post-charging. These functions are regulated by charge-discharge mechanisms involving internal battery components. Energy conversion involves a complex process of electron and ion transfer across electrode/electrolyte interface. Interfacial characteristics are determined by respective phases, with time-dependent changes impacting battery shelf-life. The voltage of cell is influenced through the electric double layer formed between the electrode and electrolyte at these interfaces. Secondary battery technology relies on the interaction of materials in electrodes and electrolytes, emphasizing the importance of understanding their chemistry for battery performance[3].

LIB have appeared as prominent energy sources due to their superiority over conventional secondary sources. Tarascon and Armand's influential Nature article in 2001 offered a historical and developmental overview of lithium-ion batteries, analyzing contributions related to the anode, cathode, and electrolytes. Notable advancements were comprehensively outlined, with recognition of areas warranting further investigation. Figure 2, illustrates the battery technology landscape at the time, highlighting lithium-ion batteries' superior energy density compared to conventional sources. It offers a comparative analysis of the technical features of LIB in relation to other battery types[4,5].

Figure 2: Profiles of maximum volumetric and gravimetric energy densities for different

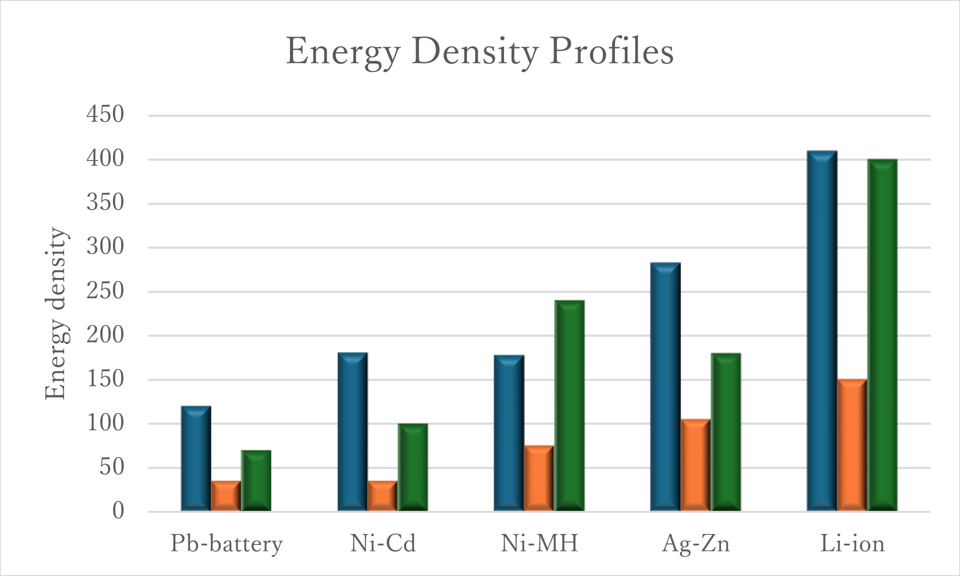

batteries.

In a recent publication in Nature, the authors revisited the topic of lithium-ion batteries, delving into their ongoing evolution and futuristic potentials. They extensively discussed advancements in battery architecture and design, current technologies and future prospects. With energy demands rising and fossil fuel resources depleting while environmental concerns persist, there is a clear imperative for continual technological innovation in energy sources[6].

Lithium-ion batteries have gained popularity due to their superior energy density and eco-friendliness compared to traditional options like lead-acid or Ni-Cd batteries. They offer advantages such as both gravimetric and volumetric energy density, a substantial optimum operating voltage, stability during operation, low self-discharge rates and rapid recharging capabilities. Despite their established reputation for portability, efficiency, and adaptability, challenges persist regarding reliability, lifespan, safety (particularly thermal stability), and affordability[7].

In response, the scientific community is actively pursuing improvements in the architecture and design of lithium-ion batteries' key components, aiming to address these challenges and further enhance their performance and viability.

The growing demand for energy has spurred the emergence of various alternative technologies alongside LIB. Recent years have seen intensive research efforts directing to the development of promising technologies aimed at complementing existing ones. Examples include lithium-metal batteries[8], aluminum batteries[9], magnesium batteries[10], and sodium batteries[11,12], all of which boast impressive energy density profiles and pose stiff competition to established LIBs. However, due to their early stage of development, these alternative technologies require time to establish solid viability, capacity, durability, safety, and commercial reproducibility.

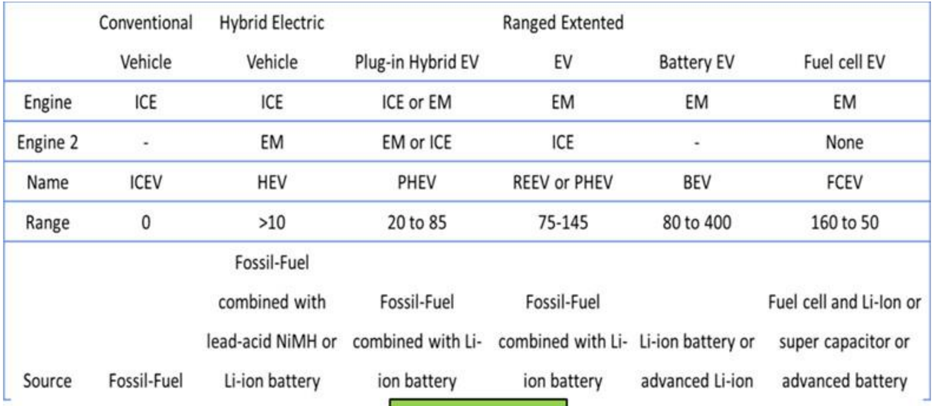

	Conventional Vehicle	Hybrid Electric Vehicle	Plug-in Hybrid EV	Ranged Extented EV	Battery EV	Fuel cell EV
Engine	ICE	ICE	ICE or EM	EM	EM	EM
Engine 2	-	EM	EM or ICE	ICE	-	None
Name	ICEV	HEV	PHEV	REEV or PHEV	BEV	FCEV
Range	0	>10	20 to 85	75-145	80 to 400	160 to 50
Source	Fossil-Fuel	Fossil-Fuel combined with lead-acid NiMH or Li-ion battery	Fossil-Fuel combined with Li-ion battery	Fossil-Fuel combined with Li-ion battery	Li-ion battery or advanced Li-ion	Fuel cell and Li-Ion or super capacitor or advanced battery

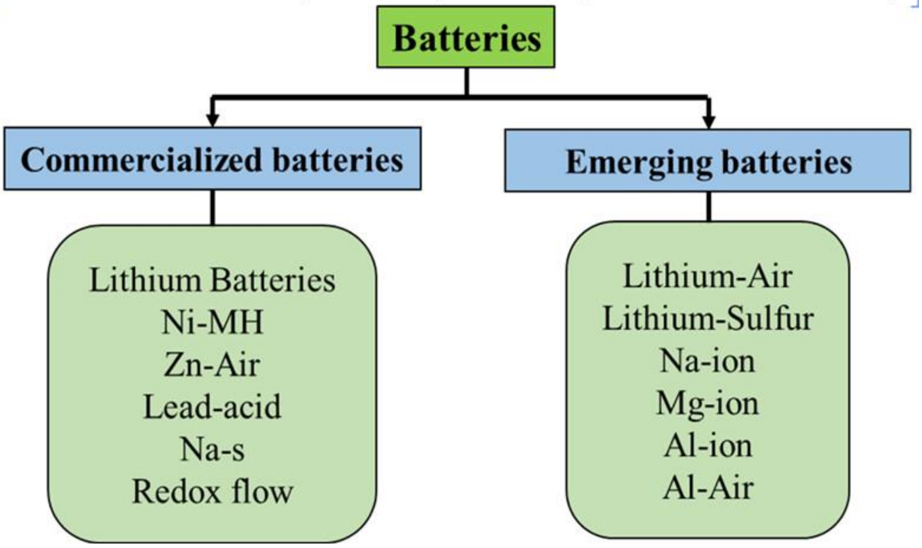

Figure 3: Battery categories[13].

In contrast, enhancing the established technology of LIBs is relatively straightforward. Currently, LIBs are the most widely adopted form of portable energy source, with ongoing developmental evolution. Figure 3 illustrates the most capable successors to the Li-ion technology, including magnesium-based systems, which are seen as a significant advancement. While Li-metal technology holds future potential, it is still in its early developmental stages. In practical terms, while Mg and Li-metal batteries hold significant theoretical promise, their successful implementation has not yet been achieved.

Lithium-ion batteries:

The feasibility of commercializing LIBs emerged with the discovery of intercalation materials, recognized as promising electrode substances. Initially, Exxon employed lithium metal anodes, but this strategy carried safety concerns due to lithium's reactivity with electrolyte moisture. In the late 1970s, Armand et al. introduced a solid-state polymer electrolyte created by combining a coordinating polymer with a lithium salt, marking a significant advancement in energy research[14].

The interaction between Li-ions and negatively charged oxygen atoms along PEO chains promoted the dissociation of lithium salts and facilitated ion movement within the electrolyte structure. Gel polymer electrolytes were developed to enhance the ionic conductivity of PEO-based electrolytes by incorporating a liquid electrolyte to make the polymer more flexible, which significantly advanced battery technology. Different forms of these gel polymer electrolytes are now widely used in electronic devices.

The viability of lithium batteries rested on substituting hazardous lithium metal anodes with dependable alternatives. Insertion electrodes emerged as a successful solution for manufacturers, enabling the development of battery systems featuring two distinct electrodes: an anode capable of accepting lithium ions and a cathode capable of releasing them[15,16].

Charging a lithium-ion battery entails applying an electric potential to propel Li-ions from the cathode through the electrolyte layer to anode, where they intercalate into the material. Discharging reverses this process, with Li-ions dislodging from anode and returning to cathode. This movement results in an elevation of output voltage, monitored by an external circuit. These systems operate akin to concentration cells, with lithium ions shuttling between alternate electrodes, giving rise to the concept of the "lithium rocking chair battery" as shown in Figure 4[17].

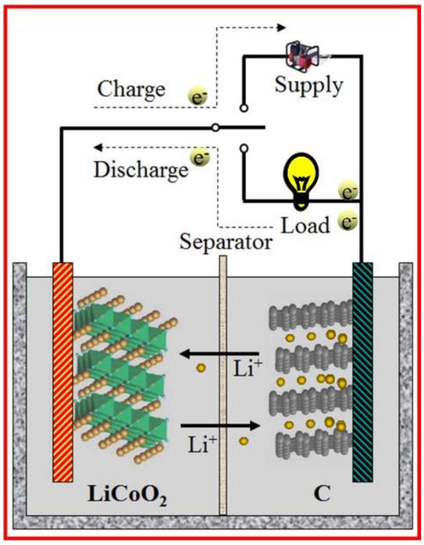

Figure 4: An illustrative diagram demonstrating the fundamental elements and operating principle of a lithium-ion cell[17].

The conventional intercalation-deintercalation sequence in a LIB can be illustrated as follows:

- Charge: Lithium ions migrate from the cathode and electrolyte towards the anode, where they intercalate into the anodic material.
- Discharge: Lithium ions de-intercalate from the anode, reverting to the cathode, accompanied by a rise in output voltage.

Although the idea for rocking chair batteries first surfaced in the 1980s, the Japanese firm Sony Corporation's innovative efforts were ultimately responsible for the system's widespread acceptance. Sony saw the potential of utilizing lithium cobalt oxide as the source cathode and graphite as the sink anode, a combination that was incredibly successful in the commercial sector. The groundbreaking research by Peled on the development of a passivating layer known as the Solid Electrolyte Interphase (SEI) between the electrode and electrolyte had an impact on the selection of graphite as the anode material[18].

This chapter's latter sections will go into greater detail about lithium-ion batteries, first going over the materials that make them up and then going into great detail about the electrolytic materials that have been used in lithium-ion batteries up to this point. Although this survey of the literature addresses a number of topics related to LIB, the major emphasis is still on electrolyte and the reasoning for the creation of new electrolyte materials.

Anode/Negative electrode:

The ideal anode, or negative electrode, for batteries should ideally possess a low potential vs Li/Li$^+$ and demonstrate efficient lithiation/delithiation processes. Lithium itself meets these criteria perfectly. However, safety concerns arose from early Li-based batteries, notably those produced by Exxon, which suffered accidents due to short circuits caused by lithium dendrites. Consequently, there was a shift towards exploring materials with intercalation properties to address these safety issues.

Among the various materials investigated, carbonaceous materials gained popularity, especially after Sony Corporation's successful commercial use of carbonaceous material in its batteries as an anode. While this material addressed the issue of dendritic growth, there was a compromise on capacity. It is reported that carbon-based materials exhibit barely 1/10th of the theoretical capacity of a lithium anode[19,20].

The anodic active materials utilized in developing LIBs can be broadly classified as shown in Figure 5.

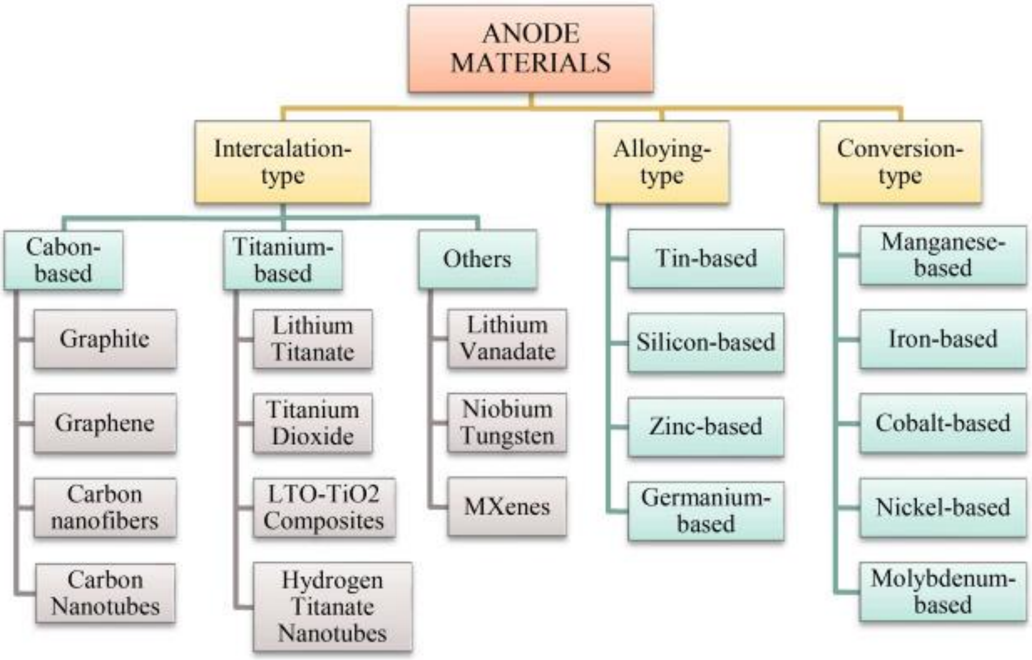

Figure 5: Synopsis of studied anode materials: classifications and divisions examined[20].

Graphite-based materials:

Armand and Touzain first documented the use of graphite as an anode material for specific applications[21]. This discovery spurred extensive research efforts aimed at understanding the mechanisms of lithiation/delithiation within graphite structures. Lithium ions are intercalated into the graphite host matrix as guest species, a process that is largely reversible and occurs in a topotactic manner[22]. Initially, lithium intercalation forms Li_xC_6 with $0 < x < 1$, transitioning to LiC_6 at maximum intercalation, as illustrated in Figure 6[23]. Peled and Aurbach's research extensively investigates the formation of the Solid Electrolyte Interphase (SEI) layer, which acts as a protective film on the anode, ensuring both the safety and efficient movement of lithium ions[24].

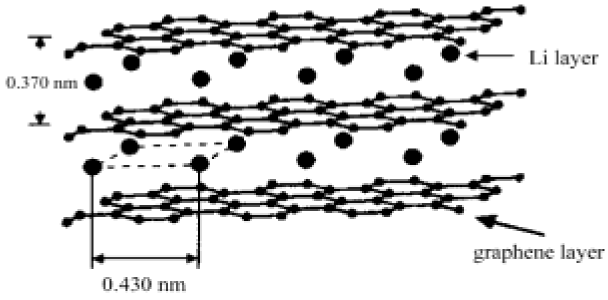

Figure 6: Lithium intercalation into Graphite[22].

Group-IV alloys-based anodes:

Various Li-metal alloys find applications as anode active materials in LIBs, including Si, Sn, Ge and even Pb[25].

For Si alloys, the practical limit reaches up to 3579 $mAhg^{-1}$ in pure form, during full lithiation to $Li_{15}Si_4$. However, their performance is hindered by significant volume expansion and contraction during charge-discharge cycles, particularly at higher charging rates. This can lead to mechanical disintegration and electrode failure. To address this issue, researchers have turned to nanostructured materials, which alleviate stress on surfaces and provide expansion in void space[26–30].

Ge, despite being more expensive than Si, remains a viable option due to its excellent conductivity and ability to facilitate the diffusion of lithium ions. During the intercalation process, lithium ions are incorporated into a crystalline intermediate state, eventually forming $Li_{15}Ge_4$, with an amorphous, porous phase observed upon delithiation. While optimization of Ge sheet thickness remains a challenge, studies indicate excellent capacity retention profiles and high current tolerance without surface cracking. Recent research suggests that coating Si nanotubes with germanium enhances rate capabilities[31–33].

The theoretical capacity limit of tin (Sn)-based anodes is capped at 990 mAh/g, similar to silicon (Si) in terms of volumetric capacity. However, in the fully lithiated state, such as Li_2Sn_5, the material becomes brittle, which hinders reaching the theoretical capacity. Commercially popular approaches include the use of Sn nanoparticles, Sn-O_2 composites, and Sn-Co-C alloy-based anodes.[34].

Pb-based anodes face limitations due to the toxicity of lead compounds, despite their high volumetric capacity and abundance. Research in this area has not yet achieved the theoretical capacity of Pb-based anodes[35].

Cathodes:

High-quality cathode materials for LIBs must meet numerous key characteristics to ensure optimal performance and safety[36]:

- Low Lithium Chemical Potential: Cathodes should have a lower lithium chemical potential compared to the anode, influencing the cell's voltage capacity.
- Abundant and Accessible Sites: They should provide abundant and easily accessible sites within the electrode matrix for the insertion and extraction of lithium ions.
- Reversible Lithiation/Delithiation: Cathode materials should enable reversible lithiation/delithiation processes using minimum change to their crystal structure to enhance durability.
- Balanced Conductivity: There should be a proper consideration between electronic and Li-ion conductivity to mitigate polarization losses in process of cycling. This balance is influenced by factors such as crystal structure, geometry, and the availability of intercalation sites.
- Aligned Redox Energy: The cathode's redox energy should align well with the electrolyte and anode, ensuring smooth charge and discharge processes.
- Economic Viability and Stability: Cathodes should be economically viable, chemically and thermally stable, and environmentally friendly.

Layered Metal Oxides: Materials like $LiMO_2$ (where M = V, Cr, Co, Ni) propose high theoretical capacities nevertheless may experience practical limitations because of structural degradation. $LiCoO_2$ is widely used despite its limitations, and research focuses on improving materials' performance and reducing toxicity[37].

Spinel Oxide Cathodes: Spinel materials like $LiMn_2O_4$ offer cost-effectiveness and durability but face challenges related to structural changes during cycling. Remedial procedures and doping with other metals aim to improve cyclability[38].

Polyanion-Based Materials: These materials, such as $LiFePO_4$ and Li_2MSiO_4, offer enhanced stability and safety. While $LiFePO_4$ has shown promising performance, Li_2MSiO_4 faces challenges in achieving its theoretical capacity due to poor cycle life and slow reaction kinetics. Doping with other metals shows potential for improvement[39].

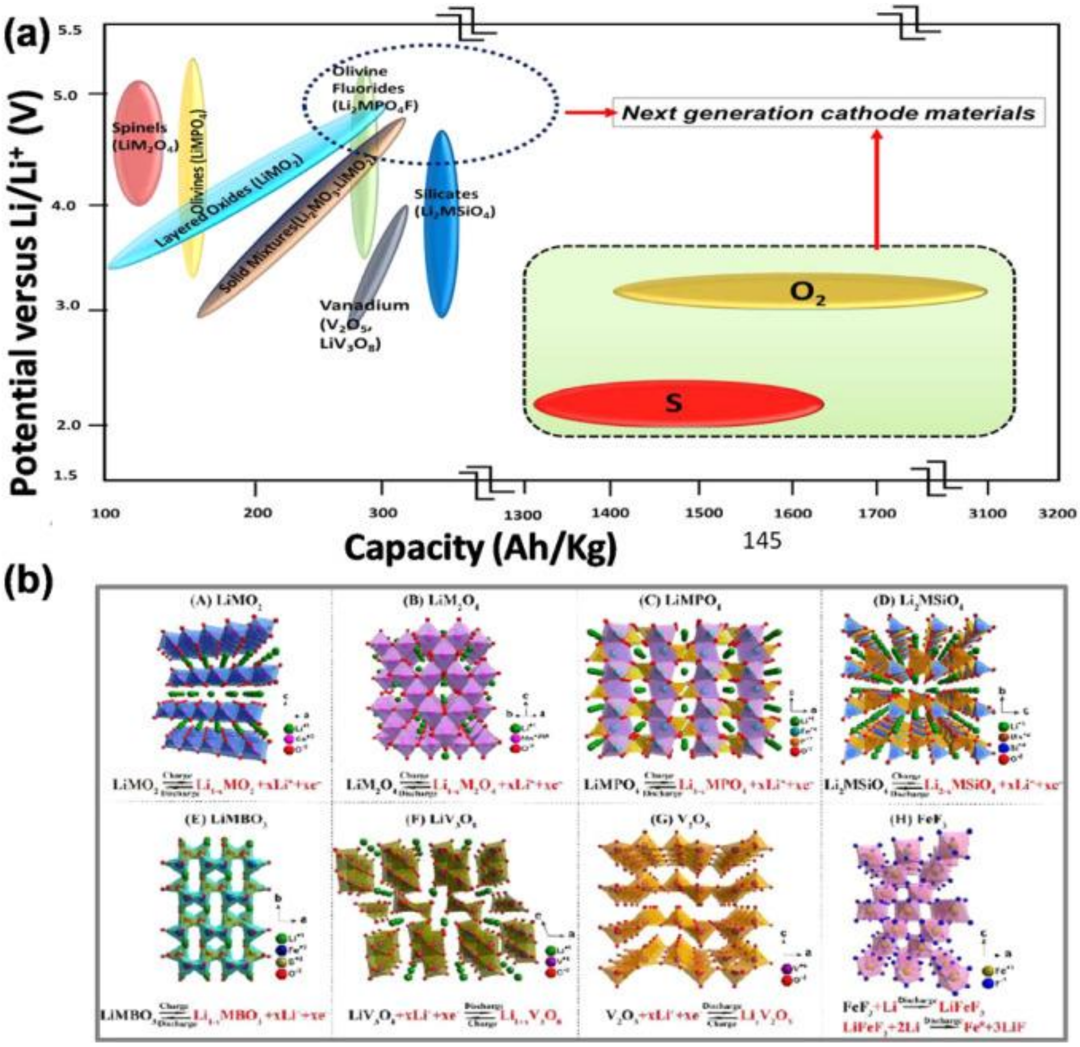

Figure 7: a) Characteristics and electrochemical behaviours of cathode materials utilized in contemporary lithium-ion battery (LIB) technologies[40]. (b) Structural configurations

and electrochemical responses of different cathode materials[41], encompassing Layered $LiMO_2$, spinel LiM_2O_4, olivine $LiMPO_4$, Li_2MSiO_4, $LiMBO_3$, LiV_3O_8, V_2O_5, and FeF_3.

In summary, ongoing research focuses on developing cathode materials that balance performance, cost-effectiveness, and sustainability, aiming to advance lithium-ion battery technology for various applications (Figure 7).

Electrolytes:

The performance of batteries is significantly influenced by electrolytes, as they serve as the pathway for lithium-ion conduction between the anode and cathode. Maintaining stability and consistent lithium-ion conduction over repeated cycling is crucial for the long-term viability of the cell. Since the 1970s, when PEO-based electrolytes were discovered, there has been ongoing development of novel electrolyte systems to meet evolving requirements. However, due to the continuous evolution of electrolytes, providing a comprehensive classification for them is a challenging task. While there is no formal classification method for electrolytes, a simplified evolution of electrolytes is presented in Figure 8.

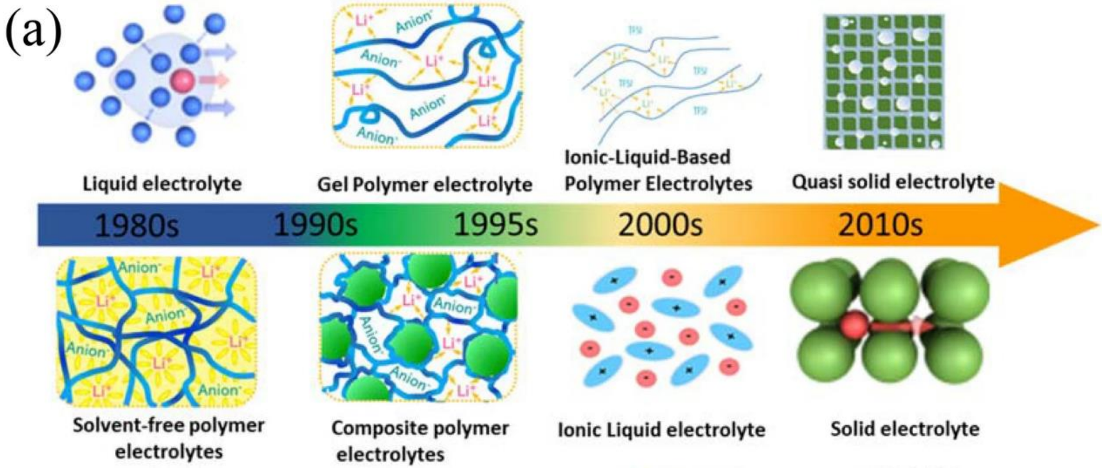

Figure 8: Evolution of electrolytes for LIB[42,43].

Liquid non-aqueous electrolytes:

In typical electrolyte solutions, a combination of solvent and salt is used, with the salt usually being a lithium salt. Solvent choice in LIBs hinges on several structural considerations, including polarizability,, as well as kinetic or thermodynamic factors like the Taft's parameters or Donor number[44]. Careful consideration of these material parameters has led to the identification of commonly used solvents suitable for lithium-ion batteries are Ethylene Carbonate (EC), Ethyl Methyl Carbonate (EMC), Diethyl Carbonate (DEC), Dimethyl Carbonate (DMC), Propylene Carbonate (PC), Ionic Liquids and Mixtures of Carbonates and Esters.

Regarding the salts that make up the other component of liquid electrolyte systems, some fundamental characteristics are outlined here:

- High ionic conductivity
- Better solubility in several solvents
- Thermal stability and electrochemical stability
- Stability concerning interactions with anode and cathode materials.
- Concerns such as economic viability and low toxicity

Several lithium salts are utilized, including $LiPF_6$, $LiBF_4$, $LiN(CF_3SO_2)_3$, $LiClO_4$, $LiAsF_6$, and $LiCF_3SO_3$. Among these, $LiPF_6$ is prevalent due to its better conductivity upon mixing in alkyl carbonates, reaching up to ~10 mS cm^{-1} at room temperature, and its oxidative stability close to 5 V. It's also soluble in many commonly used solvent systems. However, $LiPF_6$ exhibits thermal instability and hygroscopic properties, decomposing into LiF and PF_5, which further hydrolyzes to corrosive gases in the presence of even trace amounts of moisture[45].

While LiTFSI shows good ratings overall, it is considerably expensive. herefore, $LiPF_6$ is extensively used in the commercial market due to its balanced properties across various factors. Other salts like LiBOB (lithium bis(oxalato)borate) and its derivatives have also been investigated in research for their beneficial characteristics in forming SEI. A summary of several chosen lithium salts and the ionic conductivities of their corresponding electrolytes within the temperature range of 25 to 30 ^{O}C. are depicted in Figure 9.

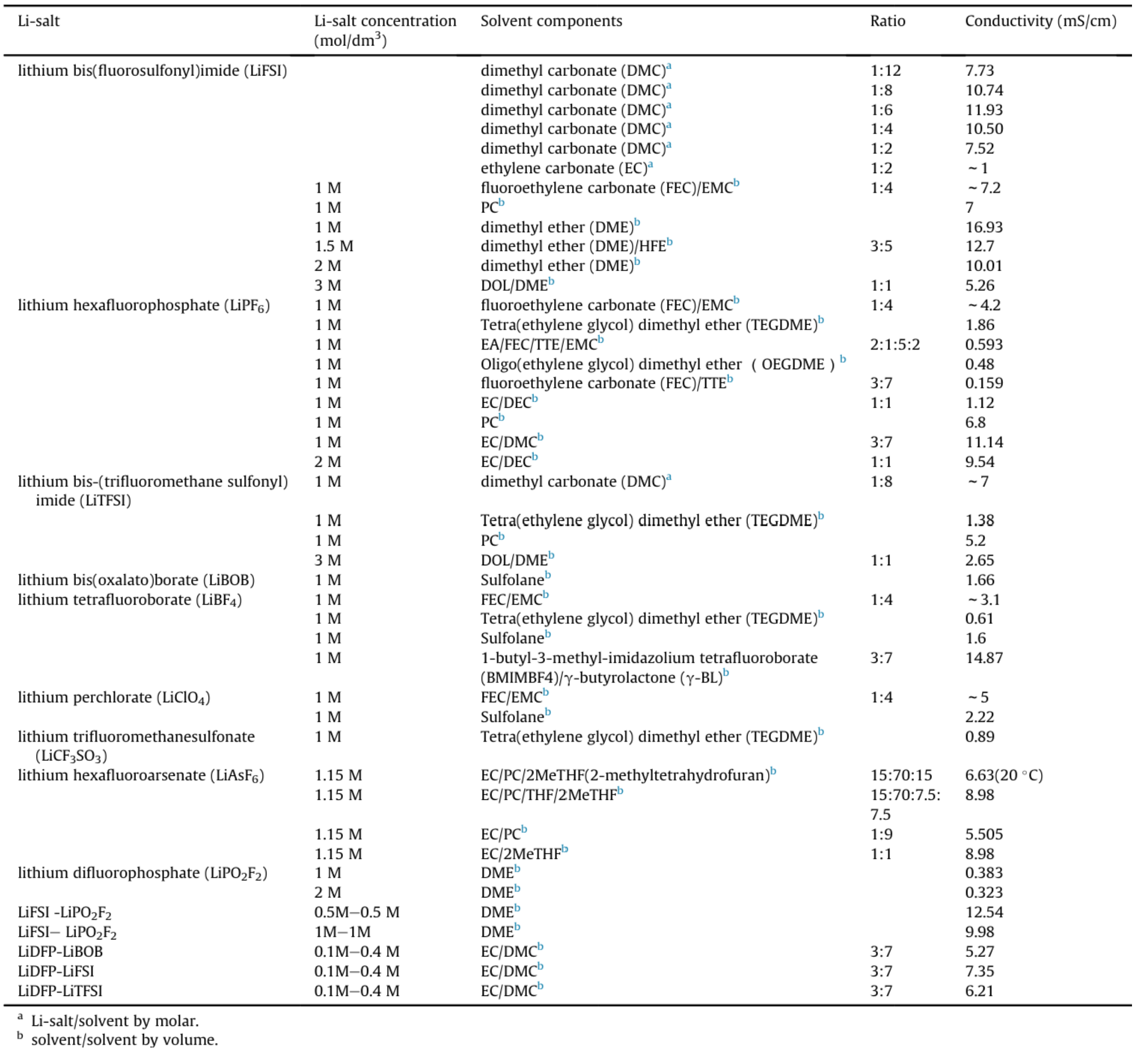

Li-salt	Li-salt concentration (mol/dm^3)	Solvent components	Ratio	Conductivity (mS/cm)
lithium bis(fluorosulfonyl)imide (LiFSI)		dimethyl carbonate (DMC)[a]	1:12	7.73
		dimethyl carbonate (DMC)[a]	1:8	10.74
		dimethyl carbonate (DMC)[a]	1:6	11.93
		dimethyl carbonate (DMC)[a]	1:4	10.50
		dimethyl carbonate (DMC)[a]	1:2	7.52
		ethylene carbonate (EC)[a]	1:2	~ 1
	1 M	fluoroethylene carbonate (FEC)/EMC[b]	1:4	~ 7.2
	1 M	PC[b]		7
	1 M	dimethyl ether (DME)[b]		16.93
	1.5 M	dimethyl ether (DME)/HFE[b]	3:5	12.7
	2 M	dimethyl ether (DME)[b]		10.01
	3 M	DOL/DME[b]	1:1	5.26
lithium hexafluorophosphate ($LiPF_6$)	1 M	fluoroethylene carbonate (FEC)/EMC[b]	1:4	~ 4.2
	1 M	Tetra(ethylene glycol) dimethyl ether (TEGDME)[b]		1.86
	1 M	EA/FEC/TTE/EMC[b]	2:1:5:2	0.593
	1 M	Oligo(ethylene glycol) dimethyl ether （OEGDME）[b]		0.48
	1 M	fluoroethylene carbonate (FEC)/TTE[b]	3:7	0.159
	1 M	EC/DEC[b]	1:1	1.12
	1 M	PC[b]		6.8
	1 M	EC/DMC[b]	3:7	11.14
	2 M	EC/DEC[b]	1:1	9.54
lithium bis-(trifluoromethane sulfonyl) imide (LiTFSI)	1 M	dimethyl carbonate (DMC)[a]	1:8	~ 7
	1 M	Tetra(ethylene glycol) dimethyl ether (TEGDME)[b]		1.38
	1 M	PC[b]		5.2
	3 M	DOL/DME[b]	1:1	2.65
lithium bis(oxalato)borate (LiBOB)	1 M	Sulfolane[b]		1.66
lithium tetrafluoroborate ($LiBF_4$)	1 M	FEC/EMC[b]	1:4	~ 3.1
	1 M	Tetra(ethylene glycol) dimethyl ether (TEGDME)[b]		0.61
	1 M	Sulfolane[b]		1.6
	1 M	1-butyl-3-methyl-imidazolium tetrafluoroborate (BMIMBF4)/γ-butyrolactone (γ-BL)[b]	3:7	14.87
lithium perchlorate ($LiClO_4$)	1 M	FEC/EMC[b]	1:4	~ 5
	1 M	Sulfolane[b]		2.22
lithium trifluoromethanesulfonate ($LiCF_3SO_3$)	1 M	Tetra(ethylene glycol) dimethyl ether (TEGDME)[b]		0.89
lithium hexafluoroarsenate ($LiAsF_6$)	1.15 M	EC/PC/2MeTHF(2-methyltetrahydrofuran)[b]	15:70:15	6.63(20 °C)
	1.15 M	EC/PC/THF/2MeTHF[b]	15:70:7.5: 7.5	8.98
	1.15 M	EC/PC[b]	1:9	5.505
	1.15 M	EC/2MeTHF[b]	1:1	8.98
lithium difluorophosphate ($LiPO_2F_2$)	1 M	DME[b]		0.383
	2 M	DME[b]		0.323
LiFSI -$LiPO_2F_2$	0.5M–0.5 M	DME[b]		12.54
LiFSI– $LiPO_2F_2$	1M–1M	DME[b]		9.98
LiDFP-LiBOB	0.1M–0.4 M	EC/DMC[b]	3:7	5.27
LiDFP-LiFSI	0.1M–0.4 M	EC/DMC[b]	3:7	7.35
LiDFP-LiTFSI	0.1M–0.4 M	EC/DMC[b]	3:7	6.21

[a] Li-salt/solvent by molar.
[b] solvent/solvent by volume.

Figure 9: Summary of several chosen lithium salts in corresponding and the ionic conductivities[45].

Polymer electrolyte:

Polymer electrolytes represent a diverse family of materials crucial for lithium-ion batteries, with various compositions and properties. They share similarities with gel polymer electrolytes and early reported in 1993, still in early developmental stages. While a comprehensive discussion of their classification is beyond scope here, the focus is primarily on solvent-free polymer-based systems for LIBs. Although often used alongside ceramic electrolytes in solid-state systems, for classification purposes, polymer electrolytes are addressed separately[46].

These electrolytes are favored for their ease of preparation and distinctive physicochemical properties. They encompass compounds like polyesters, polyethers, polythioethers and polyimines. he interaction between metal salts and polymer matrices are influenced by factors such as the cation-coordinating atom interactions, salt lattice energy parameters, and electrostatic interactions within the ion matrix[46–48].

The solvation sphere around the cation is crucial and is determined by the Hard Soft Acid Base (HSAB) concept, proposed by Pearson. According to this concept, interactions between hard acids and hard bases depend on ionic interactions, while those between soft acids and soft bases involve covalent interactions. In low-molecular-weight solvents, the surrounding molecules number affects ion pairs cation dissociation, while in higher polymeric systems, characteristics of the repeating units play a significant role.

Polyethylene oxide or polypropylene oxide chains are commonly used as polymer matrix. The interaction parameters with cations in polyethers generally follow the order $(CH_2O)n$ $–<< –(CH_2CH_2O)n – >> –(CH_2CH_2CH_2O)n –$, especially with hard cations like Li^+, Na^+, Mg^{2+}, and Ca^{2+}.

Ion association/dissociation constants in a polymeric matrices are crucial, as ion association is often undesirable for conductivity. Factors such as ion-pair formation, aggregation at high salt concentrations, and steric effects of the polymer structure can hinder ionic conductivity. Anion stability also contributes significantly to conductivity; for example, large anions with delocalized negative charges are preferred because of their minimum solvation energy compared to common halides[49].

In conclusion, an ideal polymeric matrix in this category should have minimum crystallinity and an anion with delocalized negative charges.. Some typical examples of anions include ClO_4^-, $CF_3SO_3^-$, $(CF_3SO_2)_2N^-$, BF_4^-, BPh_4^-, AsF_6^-, and SCN^-.

Gel electrolytes represent a significant advancement in electrolyte technology, offering substantially higher ionic conductivities compared to their dry counterparts. Two primary methods are commonly employed in this category[50]:

- Incorporating a soluble polymer to immobilize the liquid solvent.
- Filling liquid electrolyte in the porous matrix, such as microporous polyethylene.

Due to entanglements within the matrix leading to solidification, these electrolytes exhibit liquid-like behavior at elevated temperatures and rubber-like behavior at lower temperatures. Consequently, their Vogel-Fulcher-Tammann (VFT) dependence varies significantly with temperature. Using solid-state gel polymer electrolytes (GPEs) to enhance the safety and durability of lithium metal batteries (LMBs) by protecting the lithium anode, shielding cathodes, and improving thermal stability as shown in Figure 10.

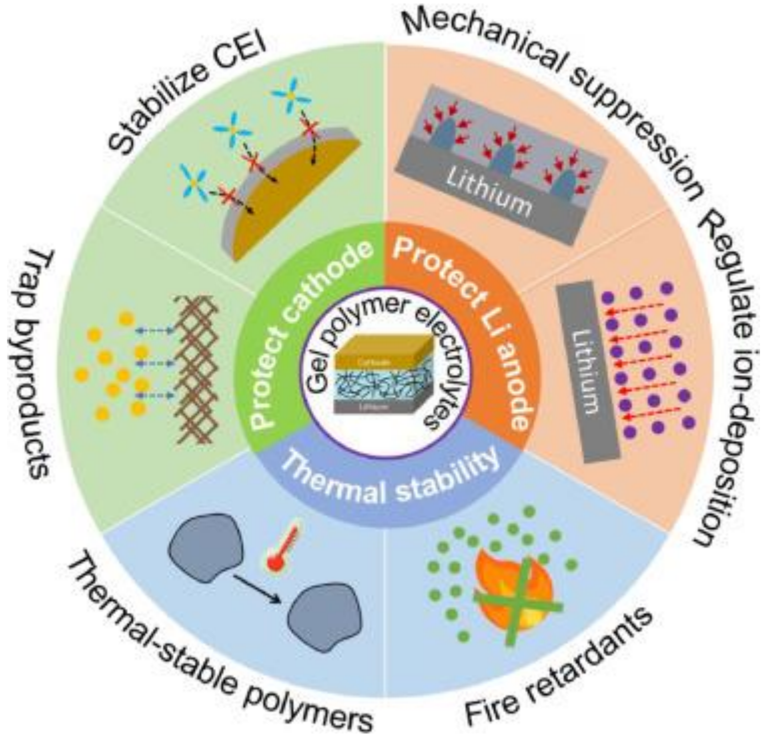

Figure 10: Strategies for better gel polymer electrolyte[51].

PVdF-based gel polymer electrolytes, including PVdF-HFP copolymers, meet the criteria for a polymer matrix in gel electrolytes. These polymers boast high electrochemical stability and incombustibility owing to electron-withdrawing substituents in their chains. However, they tend to react with lithium anodes, forming LiF, which limits their compatibility with graphite anodes. Porosity in polymeric membranes, often achieved through phase inversion or electrospinning, is crucial. Microporous polymer electrolytes, enhanced with ceramic porous additives like TiO_2 and SiO_2, exhibit improved conductivity profiles[52–57].

PMMA-based electrolytes, typically prepared via solution-casting, suffer from poor conductivity in the existence of different polymers or ionic liquids. However, reports indicate improved conductivity with PEG-based copolymers or PVC-based polymers[58,59].

Polymer electrolyte based on PAN, containing Li salts and many plasticizers, demonstrate high electrochemical stability and transference numbers, along with inherent thermal resistance. Nevertheless, they generally do not offer high ionic conductivity profiles, although additives like $LiClO_4$ and succinonitrile (SN) have been reported to enhance conductivity[60–64].

Poly(vinyl chloride) (PVC) electrolytes are widely available commercially and are resistant to ignition, owing to the lone pair on the chlorine atom that facilitates easy salt dissociation. However, similar to PAN-based systems, PVC electrolytes generally demonstrate low ionic conductivity, unless modified as in PEMA-based systems. Nevertheless, Li-ion batteries utilizing PVC electrolytes may experience capacity reduction due to the formation of an anodic passivating layer of LiCl[65].

Polymeric binders in LIBs:

Lithium-ion batteries (LIBs) have dominated the consumer electronics market due to their impressive attributes like high-energy density, efficiency, lightweight design, and portability. Both academic and industrial efforts persist in elevating LIB performance to meet the growing demand for large-scale energy storage in sectors such as electric vehicles, military applications, and aerospace technology. Despite advancements in electrode materials with respectable capacity and rate capabilities, the performance of LIBs is still restricted by conventional binder systems[66–68].

These systems typically employ a conductive additive to ensure electrode conductivity, while non-conductive polymers bind active materials and other additives together. However, the mixture of conductive phases lacks cohesive force and is unevenly distributed, resulting in bottlenecks and inadequate contacts that hinder battery efficiency. Ideally, each active particle should be precisely shaped, sized, dispersed, and linked to the current collector and electrolyte through low-resistance pathways for both electrons and ions[69,70].

Hence, the development of innovative binder systems that facilitate electron and ion transport, provide mechanical adhesion and flexibility, enhance surface compatibility, and optimize active particle dispersion is vital for the progression of next-generation high-energy, high-power LIBs.

Traditional binders present significant hurdles for future ultrahigh-capacity electrodes, particularly those subjected to substantial volume changes during electrochemical processes. These materials often endure heightened stress levels compared to graphite, leading to electrode fracturing and delamination. In response, recent investigations have delved into polymers rich in carboxylic groups, such as carboxymethyl cellulose (CMC), poly(acrylic acid) (PAA), and alginate, as novel binding agents. These polymers alter active particle surfaces through chemical bonding, fostering the formation of a stable solid electrolyte interface (SEI) layer, and providing a high elastic modulus to accommodate volume fluctuations, thereby notably bolstering the stability of high-capacity electrodes (Figure 11).[71–73]

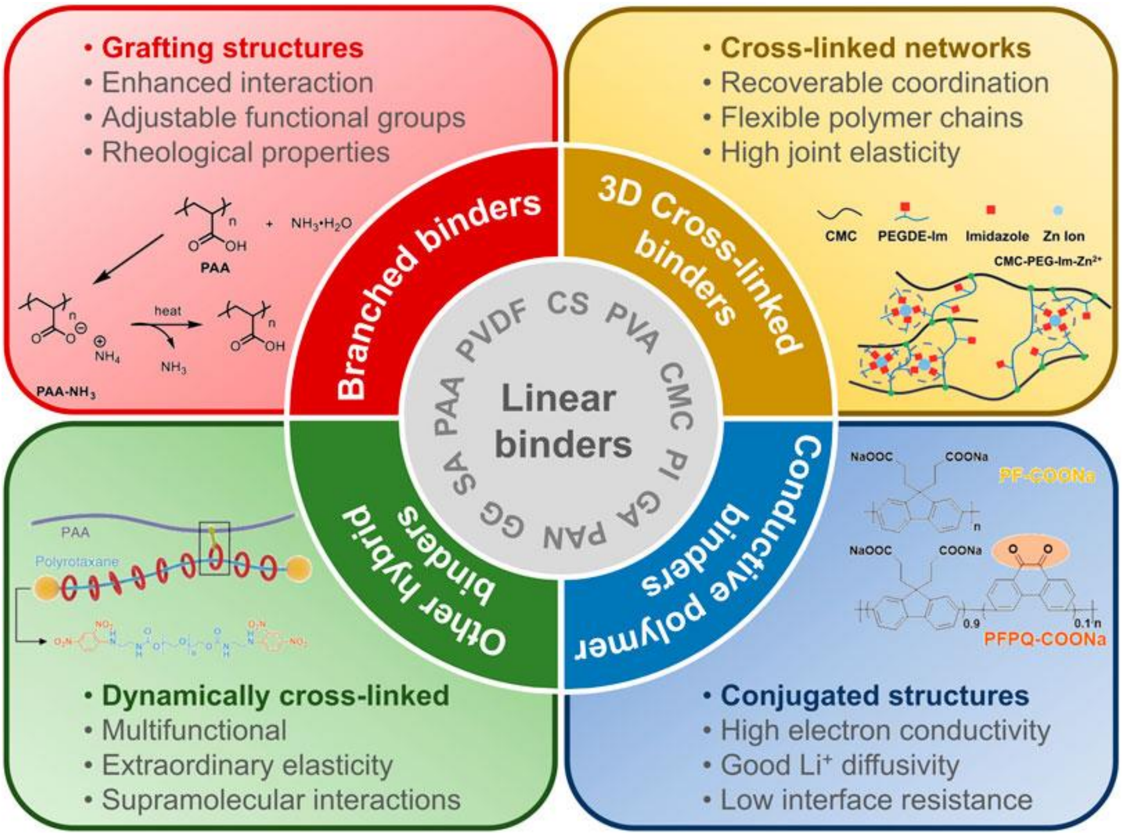

Figure 11: Various binders for LIB and its characteristics[74].

Within dual-component binder systems, carbon additives remain pivotal, albeit at the expense of lower energy density. Consequently, there has been a recent shift towards single-component multifunctional binder systems rooted in conductive polymers. These systems amalgamate the benefits of organic conductors and conventional polymers, serving as both conductive supplements and adhesive elements. Diverse strategies have been devised to tailor their properties and introduce innovative functionalities. Molecular alterations have been employed to introduce varied functional groups onto conductive polymer frameworks, enabling adjustments in electronic structures, mechanical adhesion, and electrolyte absorption. Furthermore, multifunctional binders have been derived from conductive polymers by manipulating their meso- and nanostructures. For instance, 3D nanostructured conductive polymer gels synthesized via dopant molecule cross-linking methods have emerged as promising functional binders for battery electrodes. These gels establish connections between active particles, furnish hierarchical pores for electrolyte diffusion and ion transport, and create uniform coatings on each particle to prevent aggregation and accommodate volume fluctuations in active particles[75–79]. Binder surrounding the active material in an electrode is shown in Figure 12.

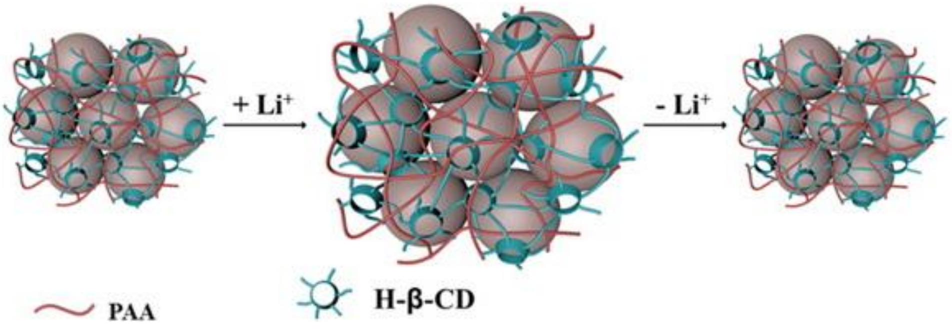

Figure 12: Binder impact during charge discharge of LIB.

Furthermore, through molecular design or the synthesis of hybrid materials, supplementary functionalities such as self-healing properties, mechanical flexibility and stretchability, and environmental responsiveness can be incorporated into future-generation binder systems to further enhance battery performance.

Sodium-ion batteries:

The widespread use of fossil fuels as an energy resource has led to concerns regarding resource depletion, environmental pollution, and geopolitical instability. Consequently, there has been a rapid adoption of alternating renewable energy sources. To effectively integrate renewable energy sources into the electrical grid or large-scale energy storage systems are crucial for managing peak demand.

Including numerous energy storage technologies, secondary ion batteries are highly favorable due to their flexibility, efficiency, and ease of maintenance. LIBs, popularized since Sony's commercialization in the early 1990s, are widely employed in portable devices and increasingly favored for EVs, including hybrid and plug-in hybrid models.

However, the primary ingredient in LIBs, lithium, is unevenly distributed globally, leading to concerns about supply stability and rising prices. The high demand for lithium driven by EVs and other large-scale uses could strain reserves, potentially posing challenges and increasing costs[80–84]. An overview of various components of SIB is shown in Figure 13.

In 2008, global lithium consumption was approximately 20,000 tons, suggesting that existing mineable resources may sustain used for around 60 years at a 5% annual growth rate. This underscores the urgency of finding alternatives or optimizing usage to mitigate potential supply constraints and price volatility in the future.

Figure 13: Illustration of SIB components and battery system[85].

Sodium, abundant and economically advantageous compared to lithium, presents a strong case for Sodium-ion Batteries (SIBs) as substitutes for Lithium-ion Batteries (LIBs). Despite initial exploration alongside LIB development in the 1970s-80s, SIBs were largely disregarded due to the rapid commercial success of LIBs and challenges in material handling. In the 1980s, some US and Japanese companies pursued SIBs using Na-Pb alloy composites and P2 Na_xCoO_2 cathodes in full cell configurations. Despite demonstrating impressive cycling > 300 cycles, their lower average discharge output voltages compared to LIBs hindered widespread adoption.

While SIBs and LIBs share similar battery components and storage mechanisms, differences arise due to sodium's larger size and higher standard electrode potential. Despite lower energy density than LIBs, the mass of cyclable lithium/sodium is a minimum fraction of overall component mass, suggesting minimal energy density consequences in principle. Additionally, aluminum serves as a affordable replacement to copper as an anode current collector for SIBs due to its alloy reaction with lithium[86–93].

Overall, SIBs offer significant potential for large-scale applications due to the abundance and economic viability of sodium resources, providing a sustainable alternative to lithium-based technologies.

A wide range of cathode materials have been studied for SIBs, encompassing transition metal oxides featuring layered structures, transition metal sulfides and transition metal fluorides, Prussian blue analogues, oxyanionic compounds and polymers. Despite progress in cathode development, identifying an appropriate anode material that balances sodium voltage storage, structural stability, better reversible capacity and continues to pose a significant challenge for advancing SIB technology. (Figure 14).

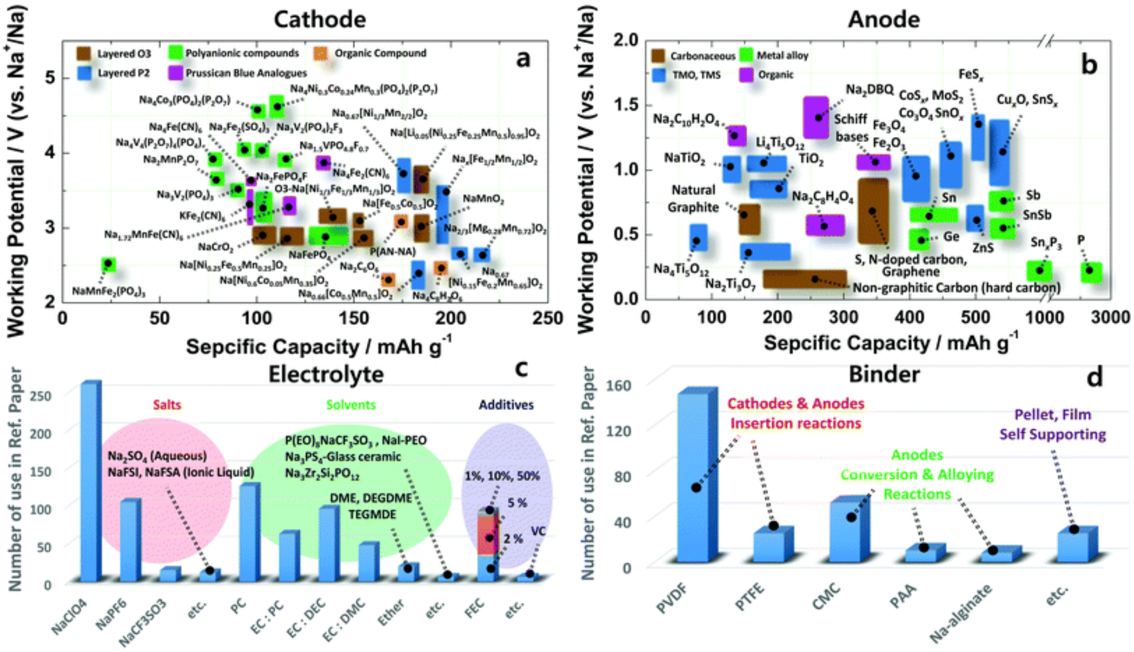

Figure 14: Recent progress in the research of SIB for cathode, anode, electrolyte and binder[85].

Graphite, commonly used as an anode material in Lithium-ion Batteries (LIBs), exhibits a moderate capacity for lithium storage but does not efficiently intercalate sodium ions.

Non-graphitic anodes, primarily composed of different carbonaceous materials such as carbon black and pitch-based carbon fibers, enable the insertion of sodium ions. Among these, hard carbons synthesized at high temperatures from carbon-based precursors are considered the preferred "first-generation" anodes for SIBs (Figure 14).

Due to issues such as high reactivity, dendrite formation and unstable passivation layer, sodium-ion batteries are not typically fabricated with metallic Na anodes. The reactivity of metallic sodium with organic electrolyte solvents and dendrite formation during sodium metal deposition pose significant challenges, emphasizing the importance of using a Na-ion system where Na ions are traded between cathodes and anodes system in a 'rocking-chair' fashion[94–98].

The development of a new electrolyte type is crucial for SIBs due to practicality and safety concerns associated with organic liquid electrolytes. Although widely used electrolyte compositions for SIBs typically include salts such as $NaClO_4$ or $NaPF_6$ dissolved in carbonate ester solvents, wherein metallic Na anodes face continuous corrosion in these organic electrolytes. This corrosion process results in the formation of unstable SEI. Aqueous electrolytes have emerged as promising alternatives, offering the potential for higher energy density with appropriate electrode material selection. However, transitioning to an aqueous electrolyte system introduces complexities such as eliminating residual oxygen from the electrolyte, maintaining electrode stability, inhibiting H_3O^+ co-intercalation into electrodes, and managing the consumption of oxygen and hydrogen produced during overcharging or discharging in closed aqueous-based battery system. These challenges are crucial considerations for realistic application of aqueous-based battery systems[99–102].

Poly(substituted methylene):

Vinyl polymerization stands as a cornerstone in polymer synthesis, enabling the creation of diverse carbon–carbon (C–C) main chain polymers via radical, cationic, anionic, or coordination mechanisms. Technological advancements, including living and stereoselective polymerizations, have facilitated precise control over polymer structure in terms of molecular weight and tacticity. Polyethylene, polypropylene, polystyrene, and poly(methyl methacrylate) exemplify vinyl polymers that have significantly impacted modern society as versatile synthetic materials.

Despite these achievements, vinyl polymerization faces notable limitations. Copolymerization of non-polar olefins like ethylene with polar monomers such as alkyl acrylates poses challenges due to differences in reactivity. While recent discoveries, like certain palladium complexes, offer partial solutions, the efficient synthesis of such copolymers remains a long-standing goal. Consequently, there is ongoing interest in alternative synthetic methods for C–C main chain polymers that diverge from traditional vinyl polymerization[103–107].

One promising approach involves constructing main chains from individual carbon units, enabling the synthesis of a variety of novel C–C main chain polymers, including those unattainable through vinyl polymerization. This method, termed "poly(substituted methylene) synthesis (PSMS)," offers structural flexibility, allowing for different distribution patterns of substituents along the main chain compared to vinyl polymerization, where substituents occur at every other carbon atom. By identifying monomers with suitable reactivity and substituent compatibility, PSMS offers a promising avenue for expanding the scope of polymer synthesis[108–111]. Figure 15 shows the vinyl and 1,2 disubstituted ethylene polymerization.

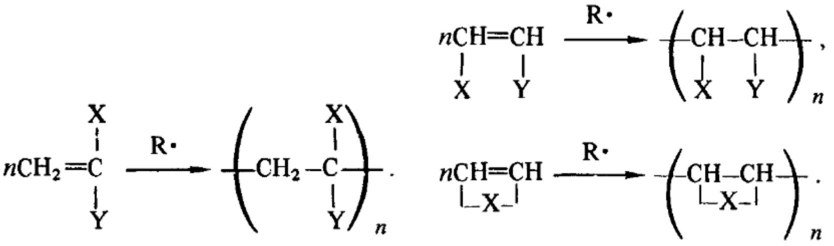

Figure 15: Synthetic scheme of vinyl polymerization and 1,2 disubstituted ethylenes.

Several monosubstituted ethylenes (where X = H and Y = R) and 1,1-disubstituted ethylenes (where both X and Y = R) undergo homopolymerization when exposed to a radical initiator. This process yields high molecular weight polymers composed of a polyethylene structure with a recurring unit containing a methylene group.

Extensive studies have been conducted to examine the relationship between monomer structure and polymerization reactivity, considering factors such as polar, resonance, and steric effects of substituents, as well as the relationship between polymer structure and physical properties. The presence of a methylene group in these polymers contributes to their flexibility and processability, leading to the industrial production of numerous plastic materials.

In contrast, it is widely acknowledged that cis or trans and cyclic 1,2-disubstituted ethylenes typically do not undergo homopolymerization due to the increased steric hindrance caused by the substituents. However, there are exceptions to this rule, which will be discussed later. If these ethylenes do undergo homopolymerization, they yield polymers with a substituted polymethylene structure.

Polymers derived from ethylenes with substituents that are independent from each other, as well as those with a cyclized substituent, are likely to exhibit distinct properties compared to polyethylenes. This expectation arises from the reduced flexibility of the former, which is more pronounced than that of the latter.

Objective and scope of the thesis:

Commercial batteries commonly utilize carbonate based liquid electrolyte, graphite and hard carbon based anodes, yet they face challenges such as capacity fade and flammability concerns. The SEI plays a pivotal part in battery functioning, longevity, and safety. Tailoring the SEI's structure and composition is crucial for enhancing electric vehicle (EV) driving range and extending battery life for portable electronics.

Exploration of alternative electrolyte materials like electrolyte and enhancing the specific capacity and cycle life of graphite and hard carbon is paramount needed in secondary ion batteries. Poly(substituted methylene) represents a versatile material class with combined properties of mechanical strength, chemical stability, electrochemical stability, high ionic conductivity and cost-effectiveness. They serve as effective interfacing agents at the electrode-electrolyte interface, improving interfacial properties such as resistance and ion permeability, directly impacting battery performance.

The thesis aims to develop various poly(substituted methylene)-based polymers for electrolyte and binders for LIB and SIB to enhance ionic conductivity, transference number , rate capability, long cycling and interfacial properties crucial for battery performance. Chapter 2 explores the potential of Poly(ethoxycarbonylmethylene) (PECM) as a polymer electrolyte for LIBs. PECM, when combined with LiTFSI, exhibits polar aprotic properties and a glass transition temperature of 10–33 °C. It demonstrates ionic conductivity ranging from 9.76×10^{-5} to 3.08×10^{-4} S cm^{-1} at 51 °C, with favorable lithium-ion transference numbers and diffusion activation energies. The PECM-based cathodic half-cell displays excellent rate capacity and long-cycle performance, retaining 80% capacity at 0.2 C for over 100 cycles, showcasing its potential for future LIB applications.

In Chapter 3, poly(fumaric acid) (PFA) emerges as a promising binder material for LIBs, exhibiting exceptional Li^+ diffusion kinetics. PFA demonstrates impressive reversible specific capacities across various current densities, with remarkable performance retention even under rapid charging conditions. Impedance studies reveal low-resistance solid electrolyte interphase (SEI) values, indicating smooth Li^+ ion passage. Postmortem investigations confirm PFA's effectiveness in forming a uniform SEI, highlighting its role in enhancing LIB performance.

Chapter 4 explores the use of PFA binder in sodium-ion batteries (SIBs) with hard carbon anodes. PFA binder enhances sodium ion kinetics by modifying the SEI, resulting in improved capacity retention and lower resistance compared to other binders like PAA and PVDF. PFA exhibits exceptional reversible rate capacities and capacity retention over 250 cycles, showcasing its potential for SIB applications.

In Chapter 5, Poly(oxycarbonylmethylene 1-allyl-3-methyimidazolium) (PMAI) emerges as an effective binder for graphite in LIBs, outperforming PVDF binder in terms of capacity retention and discharge capacity. Postmortem analysis reveals reduced electrode degradation and enhanced Li^+ diffusion with PMAI binder, attributed to its ability to form a functionalized SEI.

Finally, Chapter 6 demonstrates the effectiveness of PMAI binder for hard carbon in SIBs, showing improved adhesion with electrode components and formation of a functionalized SEI. PMAI-containing electrodes exhibit enhanced rate capability and reduced activation energy of desolvation, indicating improved ion conductance and diffusion kinetics, making it a promising binder material for SIBs.

Overall, the chapters collectively highlight the potential of these polymer binders in enhancing the performance and durability of both LIBs and SIBs through improved electrolyte properties, SEI modification, and enhanced ion kinetics.

Chapter 2

Charge–Discharge Behavior of Lithium-Ion Batteries Using a Polymer Electrolyte Bearing High-Density Functional Groups

Abstract

Lithium-ion batteries (LIBs) have become crucial for various applications, but carbonate-based liquid solvents, commonly used in their electrolytes, suffer from the flammability and exchange dynamic of lithium-ion movement in electrolytes. To address these issues, poly(ethoxycarbonylmethylene) (PECM) with a dense distribution of functional ester groups was evaluated as a polymer electrolyte in LIBs. The polymer was shown to be polar aprotic with an $E_T(30)$ value of 43.85 kcalmol^{-1} and to offer improved solvation of cations. Polymer electrolytes (PEs) in combination with LiTFSI showed a glass transition temperature in the range of 10−33 °C. PEs demonstrated good ionic conductivity within the range of 9.76×10^{-5}–3.08×10^{-4} Scm^{-1} at 51 °C, lithium-ion transference number between 0.80 and 0.98, and activation energy of diffusion within 27.4−43.0 kJmol^{-1}. The PECM-based cathodic half-cell exhibited good rate capacity at varied current densities, and long-cycle performance showed 80% capacity retention at 0.2C for more than 100 cycles. The effect of polarity on the conductivity and transference number and interfacial compatibility with the cathode show promise as an alternative electrolyte material for future lithium-ion battery applications.

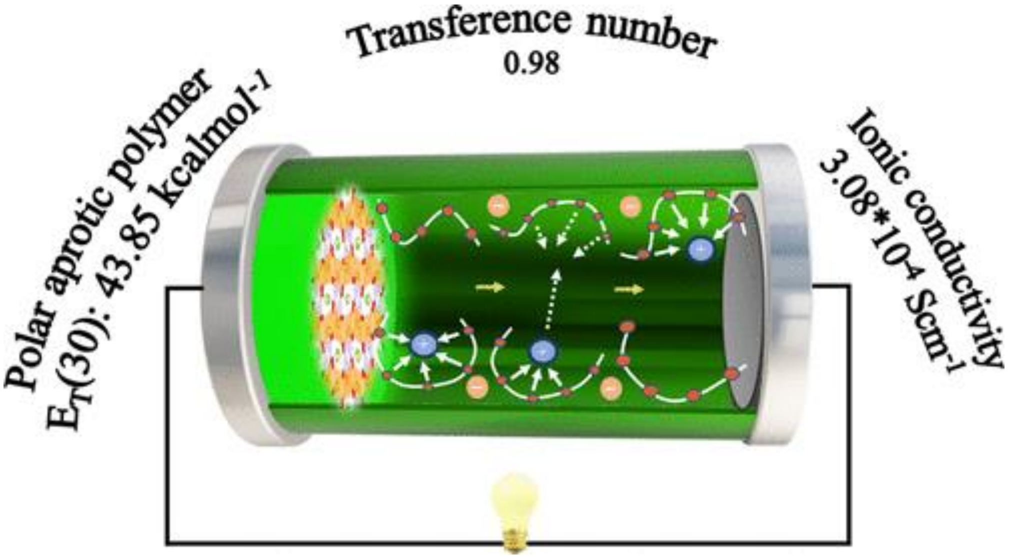

Introduction:

Lithium-ion batteries (LIBs) have revolutionized the energy storage landscape and are a preferred power source for various applications, ranging from portable electronics to electric vehicles. The constant drive and growth in battery research and development aim to enhance their performance, energy density, and safety[112,113]. Among the critical components of lithium-ion batteries, electrolytes play a pivotal role in facilitating ion transport between the electrodes, thereby influencing battery efficiency and stability.

Aprotic polar solvents have garnered significant attention in improving electrolytes due to their high dielectric constant and better lithium salt solubility[114]. Carbonate-based solvents (ethylene carbonate (EC), propylene carbonate (PC), dimethoxyethane (DME) etc.) have been widely studied and utilized due to their advantageous solvating properties, enabling effective interaction with cationic species while limiting the solvation of anionic species. This selectivity promotes lithium transport and enhances ionic conductivity. Moreover, carbonate-based solvents exhibit desirable characteristics such as high boiling points and low vapor pressures, contributing to their wider electrochemical stability within the battery system[115].

However, despite their benefits, carbonate-based solvents possess certain limitations. One notable drawback is their susceptibility to fire, making them potentially hazardous in high-energy-density battery applications. Additionally, the dramatic effect of solvation structure and exchange dynamic of electrolytes on ion movement within the system can impede ion transport and ultimately compromise battery performance[116–118].

To address the issue of dynamic molecular movement and flammability, a lot of work on organic polymer electrolytes was initiated in the 1970s[119]. A polymer electrolyte (PE) is an ionically conducting composite material composed of a polymer matrix of desired molecular weight (solvent) and dissolved salts which act as solutes[120]. The several advantages of PE are solvent-free, lightweight, thin film forming, better ionic conductivity and wide electrochemical windows. PE also enhance safety by preventing electrolyte leakage, dendrite formation, formation of harmful gas and non-combustible products[121]. Some of the host polymers commonly used in PE are poly(vinyl chloride)[122], poly(acrylic acid), poly(ethylene oxide)[123], poly(acrylonitrile)[124], poly(vinylidene fluoride)[125,126], poly(methyl methacrylate)[127] etc. All of these polymers fall under the poly(substituted ethylene) category, and their ionic conductivity has not surpassed the value of 10^{-5} S cm^{-1} at 51 ^{0}C. Liu et al. reviewed different polymer backbones (polyether, polycarbonate, polyacetal) containing polar groups facilitating lithium salt dissociation, dissolution, and ionic conduction. They emphasized that increasing the degree of branching and/or number of the functional group helps dissolve lithium salts, thereby improving ionic conductivity and promoting lithium-ion transport[128]. Carbonyl group interactions are weaker, allowing significant enhancement of lithium transport compared with PEO[129,130]. Polyester has improved thermal stability and a low tendency for depolymerization in the presence of highly nucleophilic anions of lithium salts. But linear polyester-like polycaprolactone features crystallinity which hinders ionic conductivity at room temperature and limits their practical applicability even after modification to suppress the crystallinity[131,132]. Rosenbach et al. reported using different side chain polyester (poly(substituted ethylene) category) to suppress crystallinity. Still, the ionic conductivity is 10^{-5} S cm^{-1} at 51 ^{0}C, and their lithium transference number was below 0.6[133].

Considering the drawbacks and benefits from the years of analysis and design, we have been motivated to present a high-density functional polymer characterized by a dense distribution of functional groups along the polymer backbone that can emerge as a potential solution, offering a unique set of advantages that can address these limitations. A promising approach lies in attaching an ester polar aprotic functional group to a novel category poly(substituted methylene)[134] chain by incorporating a high concentration of functional ester groups along each main chain carbon. Otsu et. al. reported synthesizing a series of substituted polymethylenes using dialkyl fumarates in the presence of a radical initiator. Such polymethylenes are expected to show properties different from that of polyethylenes, due to the decrease of flexibility of the former more than that of the latter. It was observed that a bulky substituent homopolymerizes easier and gives a high molecular weight polymer, inspite of the increased steric effect of the substituents[135–137]. These polymers have distinctive qualities, including their ability to strongly dissolve salts and exhibit weak interaction with Li^+ ions ester groups. These features boost the dissolution of cationic species while reducing anion coordination, resulting in enhanced ionic conductivity, efficient ion transport and improved battery performance. The blending capability of organic polymers with inorganic salts mitigates interface-related issues and enhances the dynamic movement of the lithium-ion. Furthermore, incorporating inert and nonflammable functional groups within the polymer structure significantly mitigates the safety concerns associated with traditional electrolytes. It holds immense promise as an alternative electrolyte material for lithium-ion batteries, potentially enhancing safety, stability, and overall battery performance.

A dense ester group in the polymer for electrolyte was found in poly(alkyoxycarbonylmethylene) based polymethylene polymer. Wherein the presence of consecutive ester groups at the polymer backbone is present, which might help in forming better ion channels and enhance the cations movement in the PE. The presence of ethoxy in the side chains helps form better molecular weight polymer than methoxy and the monomer is affordable. Therefore, this work presents the utilization of poly(ethoxycarbonylmethylene) (PECM), containing ethoxycarbonyl ester group in the main chain's carbon. In a step-up process, biomolecule fumaric acid can be used as a precursor for synthesizing diethyl fumarate through esterification using ethanol, with which PECM was synthesized. A study and discussion on ionic conductivity, lithium transference, thermal parameters (T_g and DTA), electrochemical stability and successful cathodic half-cell fabrication were executed. By studying their polarity, solvating properties, ion transport characteristics and safety aspects, we intend to shed light on the ability of high-density functional group aprotic polar polymers as promising alternatives for future LIB applications.

Materials and methods:

Synthesis of Poly (ethoxycarbonylmethylene):

Poly (ethoxycarbonylmethylene) (PECM) was prepared in vacuum-sealed tubes using the bulk polymerization. Diethyl fumarate (Sigma-Aldrich, 98%) was added to Schlaker reaction tube (Sigma-Aldrich) containing 2,2'-azoisobutyronitrile (AIBN, Sigma-Aldrich, >98%), then the freeze-thaw cycle was executed followed by stirring at 70 ^{0}C for 24 hr. AIBN was purified by recrystallization method using methanol before being used for polymerization. After 24 hr., the resulting content was reprecipitated in excess hexane, then the hexane was removed, and the polymer was dried under a vacuum overnight. The yield and density of the polymer were determined to be 82% and 1.89 g/ml respectively.

Polymer electrolyte preparation:

The different weight ratios such as 1:0.5, 1:1, 1:2 and 1:5 of polymer PECM and lithium bis(trifluoromethanesulfonyl)imide (LiTFSI, Sigma-Aldrich, 99.99%) respectively were taken in respective glass vials and dissolved in THF. The above procedure was conducted under an argon glove box atmosphere. Then the solvent was removed, and the mixture was dried under a high vacuum for 24 hr. LiTFSI was only used because when other lithium salts such as $LiClO_4$ and $LiPF_6$ were used, non-homogenous mixture was formed due to non-compatibility with such salts. The PEs were used as such without any solvent addition for all the electrochemical studies.

Characterisation of PECM:

Nuclear magnetic resonance (NMR) spectra were obtained with Bruker Advance II-400 MHz spectrometer. Deuterated solvents (ETOD and $CDCl_3$) were used as an internal standard. Fourier transformation infrared absorption (FT-IR) spectra were recorded with PerkinElmer 100 FTIR spectrometer. The spectra obtained were averaged with 50 scans with 2 cm^{-1} resolution. The molecular weight of PECM was determined using MALDI-TOF-MS spectra. Thermogravimetric analysis was performed using Hitachi STA7200 at a heating rate of 10 ^{O}C/min under an N_2 flow rate of 200ml/min. Differential scanning calorimetry studies were carried out using Shimadzu DSC-60plus instrument. For polymer polarity determination, a film of Reichardt`s dye (RD) doped polymer was prepared using the following procedure. RD and PECM were dissolved using THF and made a coating inside of quartz cell by pouring out excess of the mixture and then vacuum dried. Absorption reading was obtained using Jasco V-770 Spectrophotometer. The $E_T(30)$ and E_T^N formula for the determination of solvent polarity are as follows:

$$E_T(30)\ (\text{kcal mol}^{-1}) = hc\nu_{max} N_A = (2.8591 \times 10^{-3})\ \nu_{max}\ (\text{cm}^{-1}) = \frac{28591}{\lambda_{max}(\text{nm})} \quad \text{.....eq. 1}$$

$$E_T^N = \frac{E_T(solvent) - E_T(TMS)}{E_T(water) - E_T(TMS)} = \frac{E_T(solvent) - 30.7}{32.4} \text{.....eq. 2}$$

Where ν_{max} is the frequency and λ_{max} is the wavelength of maximum of the longest absorption band that is due to π-π^* transition and intramolecular charge transfer.

Electrochemical characterization:

Ionic conductivities of the different weight ratios were determined by electrochemical impedance spectroscopy in the frequency range of 1 MHz and 10 mHz with a sinusoidal amplitude of 10 mV using Solartron 1260. The temperature-dependent impedance was analyzed between the temperature range of 30 ^{0}C and 60 ^{0}C, and the ionic conductivity was calculated as follows:

$\sigma = \frac{l}{RA}$….. eq. 3

Where σ is ionic conductivity, l is thickness of the electrolyte, R is resistance of the electrolyte.

Lithium-ion transference number was determined using electrochemical impedance and chronoamperometry (CA) in a coin cell setup (Li|PECM|Li) at room temperature. The impedance were recorded in the frequency range of 1 MHz and 10 mHz, followed by applying DC potential of 0.030 V for measuring CA until steady state current was observed. The transference number is calculated referring to Bruce and Vincent method and using the following formula[138]:

$t_{Li^+} = \frac{I_{ss}(\Delta V - I_0 R_0)}{I_0(\Delta V - I_{ss} R_{ss})}$…..eq. 4

Where ΔV is the potential applied and I_{ss} and I_0 are the initial and steady-state current, respectively from the CA profile, while R_0 and R_{ss} are interfacial resistance before and after CA measurement.

A linear sweep voltammetry was studied for electrochemical stabilities at room temperature. An asymmetric CR2025 coin cell was fabricated with two electrodes set up (St|PECM|Li), and the measurement was determined from 0 to 6V vs. Li/Li^+ at a potential rate of 0.1 mV s^{-1}. The potential is swept in oxidation (OCP to 6 V) and reduction (OCP to 0 V) direction using different coin cells.

Cathodic half-cell preparation:

Commercial $LiNiCoAlO_2$ (LiNCAO, 1.5 mAh/cm^2, Piotrek, Lot.No. PT-EdC3A15m-19x24-1) electrode was used for all the cathodic half-cell studies. Half cells were fabricated as CR2025 coin cells using electrolyte PECM:LiTFSI(1:1) in an argon-filled glove box. The weight ratio 1:1 of polymer PECM and LiTFSI was taken in glass vials and dissolved in THF. After which the solvent was partly removed and the viscous solution was poured on the cathode electrode disc and lithium metal slowly. Then, carefully dried under vacuum for 24 hr. to remove all THF traces. This process helps the PE to penetrate maximum pores of the cathode and improves their interfacial contact. An amount of ~100 mg of PE was used for all the cell fabrications. To prevent short circuit of the coin cell during fabrication, four concentric rings of polypropylene separator (thickness: 100µm) of almost the same diameter as cathode disc were used between the lithium and cathode electrode. Cyclic voltammograms were carried out in a Biologic VSP workstation at 0.1 mV s^{-1}. Electrofield ABE 1024 battery cycler was used at room temperature between 2.8-4.2 V for the cathodic half-cell for charge-discharge measurement of the assembled battery cells. Rate capability measurements were performed at room temperature under C-rates of 0.1, 0.25, 0.5, 0.75, 1, 2and 0.1 in the following order. At the same time, the long cycling was performed for the cathodic half-cell at 0.2C, 0.5C and 1C. DEIS study was performed after long cycling charge-discharge in the frequency range of 1.0 MHz to 0.1 Hz with AC amplitude of 10 mV at potential range of 2.8 -4.2 V.

Post-mortem Studies:

The chemical composition formed/deposited on the cathode surface was identified using X-ray photoelectron spectroscopy (XPS) from Fisons instruments S-probe TM 2803. The surface morphology of the cycled cathode was observed by FESEM using Hitachi S-4500 instrument at 1.0 kV voltage.

Results and discussion:

Characterization of PECM:

The incorporation of ethoxycarbonyl ester sidechain in every carbon of backbone of the polymer poly(substituted methylene) is to ensure obtaining high functional group concentration polymer. Polymer PECM was synthesized using radical bulk polymerization at 70 ^{O}C with AIBN as initiator with a ca. 80-90% conversion (Figure 1).

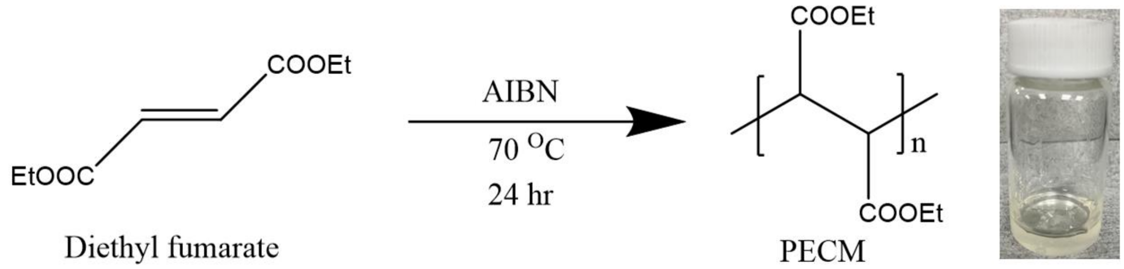

Figure 1. Schematic illustration of the synthesis of PECM. Inset: dried PECM polymer in a vial.

^{1}H NMR, ^{13}C NMR and FT-IR confirmed PECM formation. ^{1}H NMR of diethyl fumarate is shown in Figure 2(a) for peak comparison with ^{1}H NMR of PECM. Figures 2(b) and 2(c) show peaks at 3.3 ppm (^{1}H NMR) and 45.8 ppm (^{13}C NMR), respectively, assigned to poly(substituted methylene) backbone. Besides, the ethyl peak was observed at 4.27 ppm and 1.33 ppm in ^{1}H NMR. Compared to ethyl peak in ^{1}H NMR of diethyl fumarate the peak in PECM is shifted slightly to higher ppm after polymerization (Table 1). While the ethylene hydrogen peak of diethyl fumarate shifted from 6.79 to 3.32 ppm in PECM. Ethylene hydrogen of diethyl fumarate is singlet due to no coupling with adjacent hydrogen because it is opposite, while the methylene hydrogen in PECM is quintet due to β-hydrogen coupling from the polymer chain. The peak value, peak splitting and J value of diethyl fumarate and PECM hydrogen are tabulated in Table 11. Wherein ^{13}C NMR shows an ethyl peak at 61.6 ppm and 14.1 ppm, and carbonyl peak at 170 ppm. The peak at 170 ppm from the ^{13}C NMR shows identical NMR spectra with the reported NMR spectra by Eiji Ihara et al[139], thereby indicating the polymer to be syndiotactic in a stereospecific manner. The C-H stretching vibration peak of alkane at 2900 cm^{-1} was observed in the FT-IR spectra as shown in Figure 2(d). The ester absorption bands were observed at 1730 cm^{-1} and 1150 cm^{-1}. The absence of C-H signal at 3100 cm^{-1} which belongs to alkene confirms that the monomer was polymerized completely.

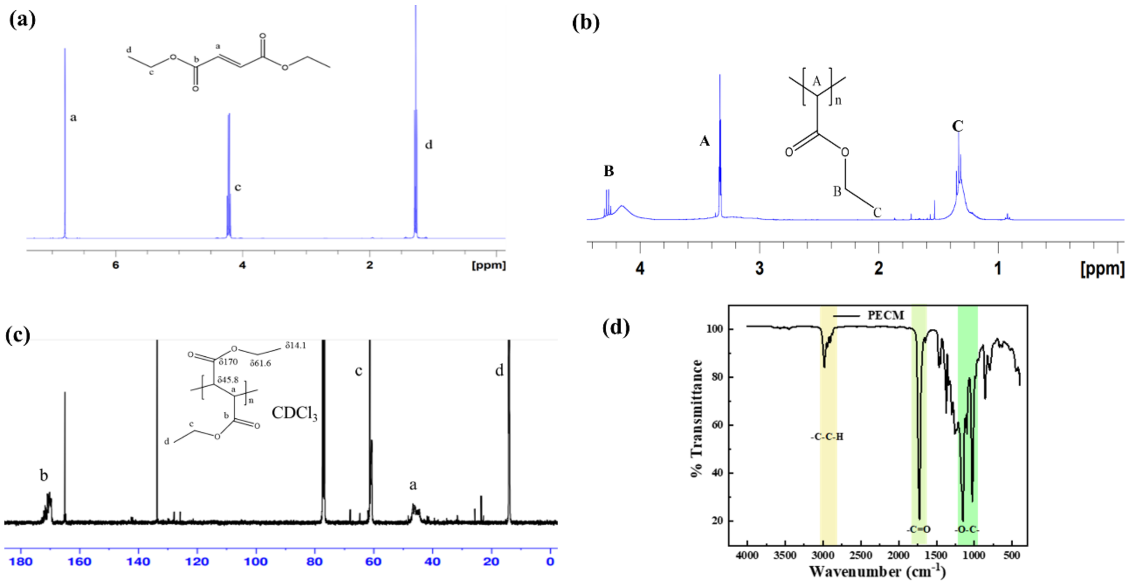

Figure 2: (a) ^{1}H NMR of diethyl fumarate. (b) ^{1}H NMR spectrum (EtOD). (c) ^{13}C NMR spectrum ($CDCl_3$). (d) FT-IR spectrum of PECM.

Diethyl fumarate	^{1}H NMR		
	Peak (ppm)	Peak splitting	J value (Hz)
a	6.79	singlet	
c	4.21	quartet	6.8
d	1.27	triplet	7.2

PECM	^{1}H NMR			^{13}C NMR
	Peak (ppm)	Peak splitting	J value (Hz)	Peak (ppm)
i	3.32	quintet	1.6	45.8
ii				170
iii	4.27	quartet	7.2	61.6
iv	1.33	triplet	7.2	14.1

Table 1: ^{1}H NMR peak values, peak splitting and J values of diethyl fumarate; and ^{13}C NMR peak values of PECM.

As for PECM, the average number molecular weight was determined to be around 4400 m/z. MALDI-TOF-MS spectra showed peak at intervals of m/z = 172 ($CHCO_2Et \times 2$) (Figure 3(b)). Characterization of polymer polarity in the field of polymer electrolytes has not been investigated before and the effect of polarity on the electrochemical performance of PE had been unknown to the best of our knowledge. In our work the polarity of the polymer PECM was determined using solvatochromic dye (Reichardt's dye) it is a chemical agent that produces optical properties modification when immobilized with analyte chemical composition. Reichardt's dye where common name is pyridinium-N-phenoxide betaine dye shows solvatochromic effect, which is a hypsochromic shift of long wavelength absorption band by 357 nm from a non-polar solvent (diphenyl ether, λ_{max}=810 nm) to high polar solvent (water, λ=453 nm). E_T (30) and E_T^N scale were used to find the solvent polarity using the classification made by Reichardt in 1994. E_T (30) values are molar electronic transition energies of dissolved solvatochromoic dye, measured in kcal/mol at room temperature and normal pressure. While E_T^N is a normalized dimensionless value ranging from 0.0 for tetramethylsilane, the most nonpolar solvent, to 1.0 for water, the most polar solvent. E_T values are divided into three different groups: (a) hydrogen bond donor (HBD)/protic solvents [E_T(30): 47-63 kcal mol^{-1}; E_T^N: 0.5-1.0], (b) dipolar non-hydrogen bond donor/aprotic solvents (non-HBD) [E_T(30): 40-47 kcal mol^{-1}; E_T^N: 0.3-0.5], and (c) apolar non-hydrogen donor donor solvents [E_T(30): 30—40 kcal mol^{-1}; E_T^N: 0.0—0.3]. The E_T(30) and E_T^N values of

PECM are determined to be 43.85 kcal mol^{-1} and 0.40 respectively (Figure 3(a)). Hence the empirical parameter of polymer polarity $E_T(30)$ and normalized E_T^N obtained from the absorption band of negatively solvatochromic Reichard`s dye are in the range of DMF ($E_T(30)$: 43.2 kcal mol^{-1}; E_T^N: 0.38) and DMSO ($E_T(30)$: 45.1 kcal mol^{-1}; E_T^N: 0.44) which confirms the polymer to be polar aprotic (non-HBD)[140,141]. The high polarity of PECM, despite its ester side chain, is due to the strong dipole moment of the ester groups and their repetitive presence along the polymer backbone, which creates a highly polar environment similar to DMF and DMSO.

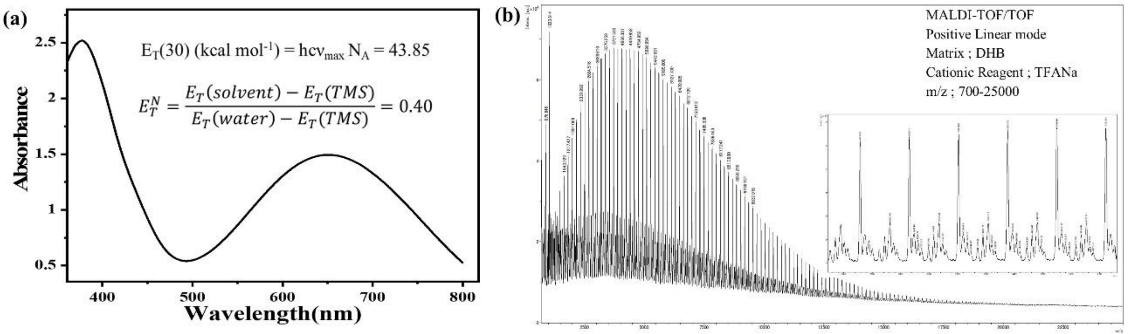

Figure 3: (a) UV-visible absorption spectrum of Reichardt's dye-doped PECM polymer. (b) MALDI-TOF spectra of PECM.

Thermal Performance and FT-IR studies of PEs:

PECM was considered for use as a polymer host for PE for the reason of its excellent compatibility with lithium salt and affordable synthesis. The different weight ratio of PECM and LiTFSI were obtained for further studies of PE and are abbreviated as PECM:LiTFSI(1:0.5), PECM:LiTFSI(1:1), PECM:LiTFSI(1:2), PECM:LiTFSI(1:5). PEs samples are shown in Figure4.

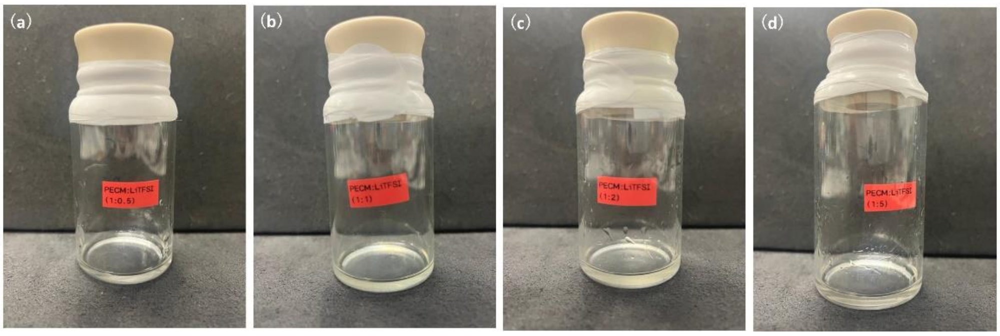

Figure 4: Polymer electrolytes sample of different concentration (a) PECM:LiTFSI(1:0.5), (b) PECM:LiTFSI(1:1), (c) PECM:LiTFSI(1:2) and (d) PECM:LiTFSI(1:1).

TGA, DSC and flame tests were conducted on the electrolytes to evaluate thermal stability and affirm the composition of all the PEs. Thermal stability and affirming the PEs component were evaluated through TGA. The values of 10 wt.% loss temperature (T_{d10}) of the four PEs were above 200 ^{O}C, as shown in Figure 5. In other words, the PEs showed thermostability until 200 ^{O}C, which is much safer than commercial liquid electrolytes that catch fire due to leakage of solvent electrolytes at high temperatures and meet the practical applicability of LIBs[142]. PECM showed two degradation temperatures, initial and maximum degradation temperatures at ~200 ^{O}C and ~380 ^{O}C respectively which was reported by Otsu et al[137]. Besides, another step at T> 400 ^{O}C is associated with the thermal degradation of LiTFSI[143].

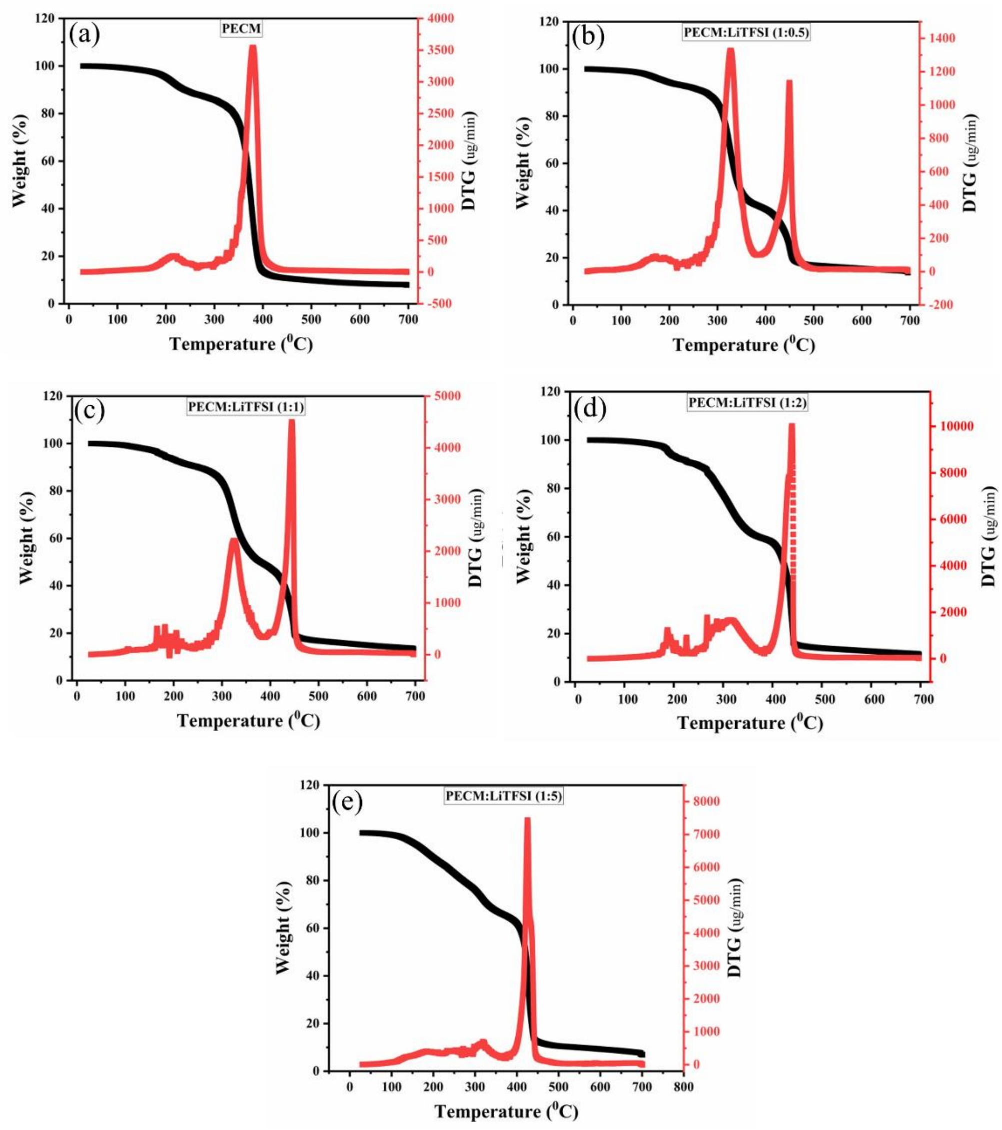

Figure 5: TGA profile of PECM and different polymer electrolytes.

The weight % of the starting point of LiTFSI degradation is shown to be increasing as the concentration of LiTFSI salt in polymer electrolytes increases. This indicates the polymer electrolyte components and compositions. The influence of the structure on thermal properties becomes noticeable and can be used to tune the electrochemical behavior for examination in battery applications.

DSC was used to investigate the phase behavior of PEs and is summarized in Table 2. The DSC curves of PEs with different concentrations of LiTFSI composition are shown in Figure 6, and it can be seen that PECM:LiTFSI (1:1) has a lower glass transition temperature (T_g). T_g significantly impacts ionic conductivity because a decrease in T_g value enhances the smooth migration of ions. Therefore, improvement in ionic conductivity is expected[144]. However, the T_g value trend is not systematic with salt concentration due to the presence of two polymer electrolyte domains showing two different trends. The coordination of the Li^+ with ester group is weak and the effect of soft anion $TFSI^-$ makes the polymer electrolyte soft which leads to a decrease in T_g value in salt in polymer domain. However, the polymer in salt domain wherein an increase in T_g is observed, owing to the presence of more crystalline LiTFSI and the effect of soft anion on the polymer is less due to the low amount of polymer in PE.

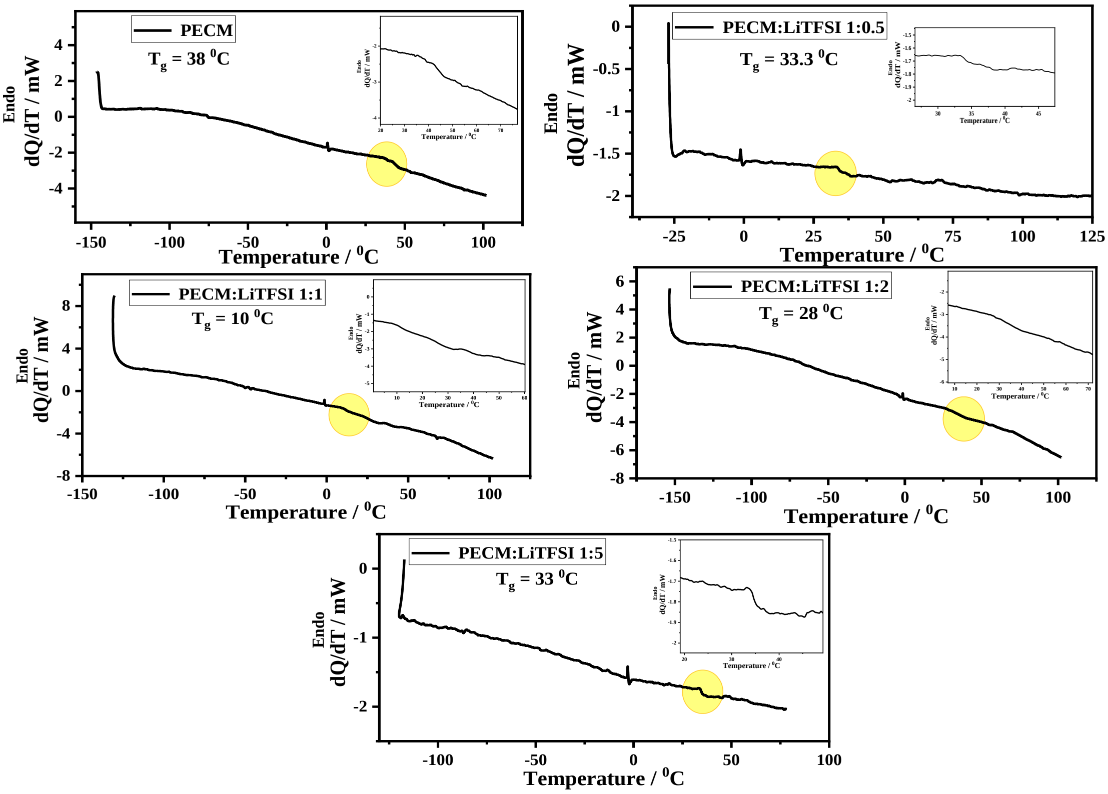

Figure 6: DSC profile showing T_g of PECM and different polymer electrolytes.

Flame tests of the PE were performed by subjecting a small amount of the electrolyte to a direct flame for a specific time frame (1 min). PECM:LiTFSI(1:1) exhibited non-flammability (Figure 7). The PE did not support a flame when the flame source was removed and only melted due to the flame's heat.

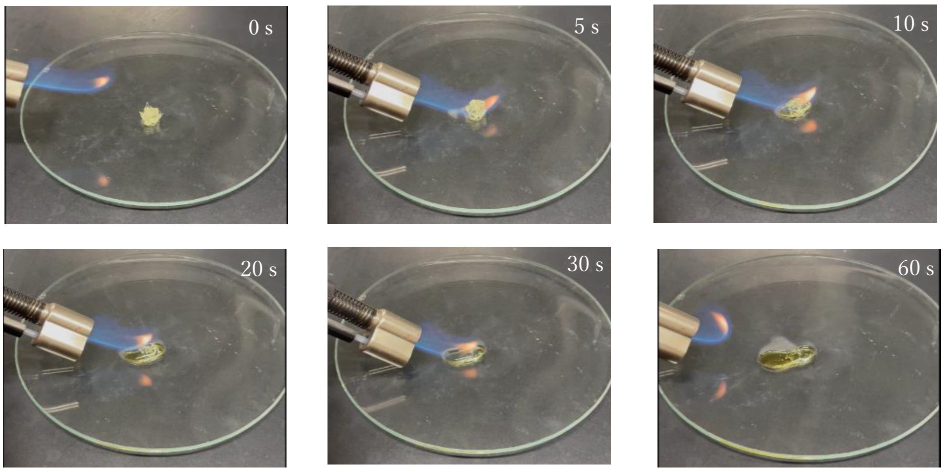

Figure 7: Flame test PECM:LiTFSI(1:1) for 1 minute.

We performed FT-IR spectroscopic studies to understand the coordination mechanism of Li^+ with the polymer. Figure 8 shows the FT-IR spectra of the distribution of lithium coordinated and free carbonyl units and ether units in the wavenumber region of 1800-1650 cm^{-1} and 1250-1000 cm^{-1} respectively. The region covers the stretching vibration of the C=O (Figure 8(a)) and C-O (Figure 8(b)) of the ester group. The pristine PECM showed a sharp peak at 1730 cm^{-1} in analogy to literature reports on polycaprolactones, polycarbonates and polyacrylates-based electrolytes[145]. Upon increased salt concentration, three significant changes are observed in the carbonyl peaks, overlapping additional peaks, increasing in intensity and shift in the peak attributed to the carbonyl group coordinating with lithium-ion. The FT-IR studies also observed splitting and shifting of the ether peak (Figure 8(b)). Figure 8 shows the IR spectra of PEs with molar ratios coordinating ester groups of the polymer to Li^+ are 67:1, 33:1, 17:1, 6:1. The spectra of PECM:LiTFSI(1:5) show high intensity of $C=O\ldots Li^+$ peak indicating maximum coordination of polymer with LiTFSI at 6:1 molar ratio. The peak shift is mainly due to the direct coordination and electrostatic influence of electrophilic cations (Li^+) on the carbonyl group surrounded in a sphere shape. The influence of the coordination of Li+ with the carbonyl group has restricted the amplitude of vibration, causing a redshift of the carbonyl double bond.

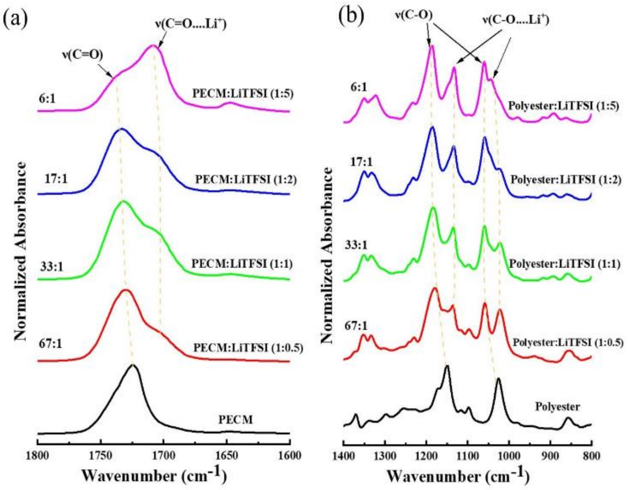

Figure 8: (a)) FT-IR spectra of PEs and pristine PECM showing carbonyl oxygen (~1725 cm^{-1}). (b) FT-IR spectra of PEs and pristine PECM showing ether (~1100 cm^{-1}). Note: Molar ratio of ester groups to lithium are mentioned on right side.

Comparative studies of ionic conductivity, transference number and linear sweep voltammetry of PEs:

A comparison study was conducted to screen for better PE ratio containing optimum salt concentration and determine the effect of glass transition temperature on ionic conductivity and transference number. Since there are reports on high ionic conductivities of two regimes, first is that of polymer in salt domain (>50 wt.% salt) and the other in salt in the polymer (>50 wt.% salt), the two regimes were screened to check their ionic conductivities influenced by salt concentration. Comparative studies of different salt concentrations with ionic conductivity at 51 ^{O}C, transference number, T_g and activation number are displayed in Table 2. Arrhenius plots of the PEs of the PEIS measurement at different temperatures are displayed in Figure 9(a). The R-squared value for the linear fitting of the Arrhenius plots was in the range of 0.92-0.99 indicating the fitting to be good. The activation energies for the diffusion of Li^+ ions in the PEs are shown in Figure 9(b). We observed maximum ionic conductivity with PECM:LiTFSI(1:1) values of $3.08*10^{-4}$ S cm^{-1} at 51 ^{O}C which was higher than other solvent-free polymer complexes reported by Dias et. al.[146] .

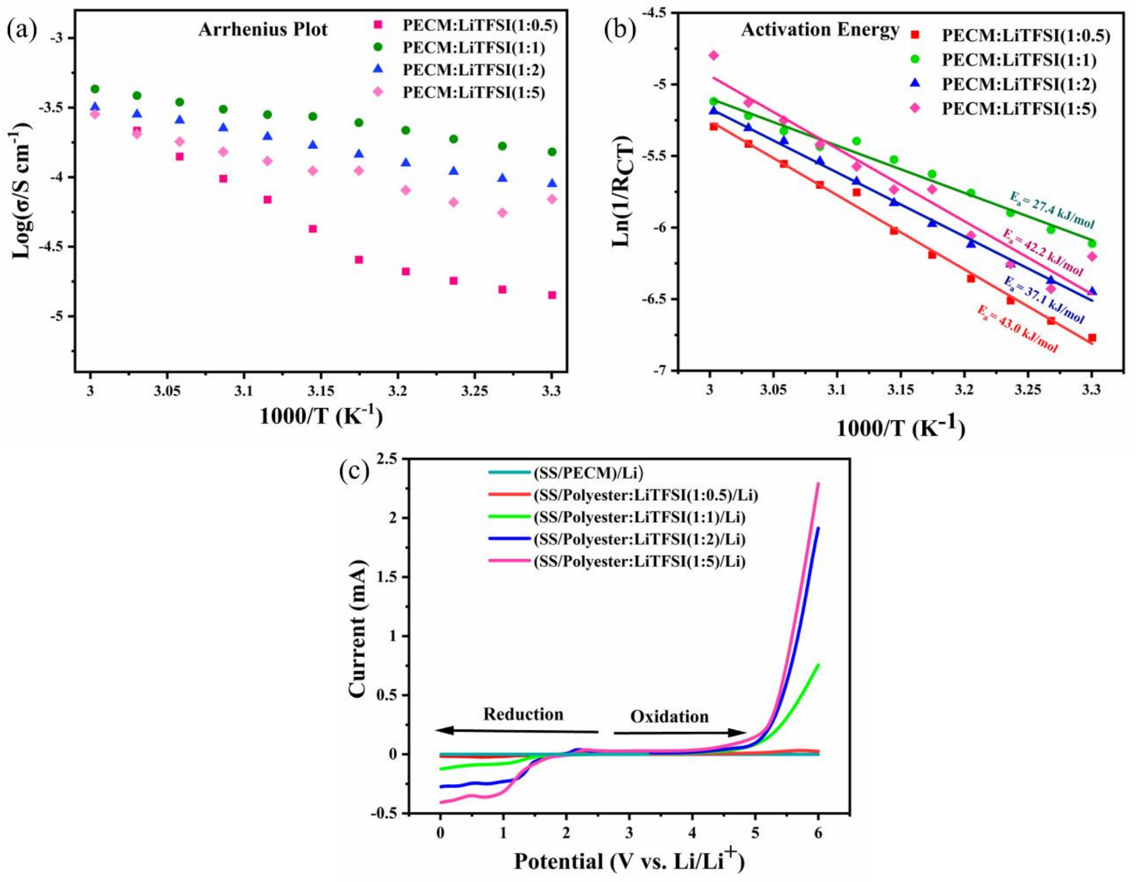

Figure 9: (a) Ionic conductivity measurements under different electrolyte concentrations at 30-60 ^{O}C temperature range, (b) Comparison of E_a values of PEs, (c) Linear sweep voltammograms of various electrolytes indicates electrolyte stability in the range of 1.5 to 4.5 V.

Sample	**Ionic conductivity at 51 ^{O}C (Scm^{-1})**	**t_{Li}^{+}**	**E_a (kJmol^{-1})**	**T_g (^{O}C)**
PECM:LiTFSI (1:0.5)	$9.76*10^{-5}$	0.80	43.0	33
PECM:LiTFSI (1:1)	$3.08*10^{-4}$	0.98	27.4	10
PECM:LiTFSI (1:2)	$2.25*10^{-4}$	0.95	37.1	28
PECM:LiTFSI (1:5)	$1.55*10^{-4}$	0.88	61.5	33

Table 2: Comparison of various electrolyte concentrations.

The ionic conductivity increases at higher temperatures due to increased vibrational mode chains segmental motion and mobile carriers causing voids formation and free volume that promotes better charge conduction and conductivity enhancement [147]. The T_g values are in accordance with the ionic conductivity and better ionic conductivity is at the trade-off between charge carrier concentration and segmental mobility of the polymer governed by T_g. We observed a decline in ionic conductivity at 51 ^{O}C from PECM:LiTFSI(1:2). This concluded that for better ionic conductivity of the polymer electrolyte, low T_g and optimum concentration of Li^+ are not only crucial, but the presence of balanced and sufficient amounts of both lithium influenced carbonyl groups and unoccupied carbonyl groups are needed. According to Ebadi et al. polymers with side chains prevent interchain coordination and Li^+ ion hopping between interaction sites. This limitation results in reduced Li^+ diffusion and consequently, lower conductivity[148]. In contrast our work on sidechain functional group polymer observed an increase in ionic conductivity and transport number, possibly due to the high density of polar aprotic functional group polymer at the side chain. Hence the polarity of the polymer plays a crucial role in the Li^+ diffusion and weak coordination with the interaction sites.

In these electrolytes, commonly referred to as salt-in-polymer electrolytes, ionic motion is linked to the local segmental motion. This system is known as a coupled system, where the conduction relaxation time is dependent on the relaxation time of the polymer matrix's segmental motion. To achieve fast ion transport in such systems, molecular design focuses on creating polyethers with low Tg and hyperbranched structures. This design influences the rapid molecular motion of the ion-coordinating side chains to enhance ionic transport. Still, the ionic conductivity of such modulation is lower than conventional aprotic electrolyte solutions. Hence, high ionic conductivity at ambient temperature may be achieved without coupling to the segmental motion of the polymers, allowing the conduction relaxation time to be decoupled from and much faster than the structural relaxation time. To understand the issue of coupling between ion transport and relaxation based on polymer electrolytes. Angell formalized the use of decoupling index, defined by

$$\log(R_\tau) \approx 14.3 + \log \sigma(T_g) \ldots\ldots eq(5)$$

The decoupling index (R_τ) defined as the ratio of the conductivity relaxation time (τ_σ) to the structural relaxation time (τ_s) uses the ionic conductivity value at Tg ($\sigma(T_g)$). The $\log(R_\tau)$ value of PECM:LiTFSI electrolytes are in the range of 9.49-10.45. Such high value of Rτ indicates that the ionic motion of Li^+ is poorly influenced by the immobile part of the polymer, suggesting significant decoupling of conductivity from the polymer chains segmental motion[149,150].

A linear sweep voltammogram was conducted to evaluate the electrochemical stability window of the PEs and PECM. Figure 9(c) shows no degradation of PEs between 1.5 to 4.5 V vs. Li^+/Li, although the current intensity of oxidation peaks increases with increased concentration. This demonstrates that the PEs are stable at high voltage and can be applied to lithium-based cathodic half cells. Overall, the oxidation peak of the PEs indicates that the instability after 4.5 V is mainly due to the electrochemical oxidation of LiTFSI as the PECM didn't show major oxidation peak after 4.5 V[151]. The reduction peak at ~1 V is shown to be increasing with concentration of LiTFSI indicating that the polymer reduces/degrades in the influence of Li-salt at lower potential.

PEs were subjected to further electrochemical characterization because of their optimal conductivity. The lithium-ion transference number of the polymer electrolytes was determined by the method developed by Evans and Vincent at fixed temperature using impedance analysis and DC polarization (chronoamperometry) (Figure 10). The transference number values are in the same line as the ionic conductivity, which has a trade-off at a salt concentration of more than 50 wt.%. PECM:LiTFSI(1:1) was observed to be of a higher transference number of 0.98 than common polymer electrolytes (<0.5) (Table 2). The higher lithium transport value is attributed to the weak Li^+-polymer interactions, which facilitate lithium-ion movement along the polymer chain. Additionally, the rigid backbone of the polymer reduces the dependency on segmental motion, commonly observed in PEO-based polymer electrolytes, and acts as a rigid matrix similar to inorganic solid electrolytes which have t_{Li+} close to 1. The consecutive ester groups on the polymer backbone help form ion channels and increase the Li^+ transport due to the presence of adjacent polar groups. The anion movement is hindered due to large size and repulsion from all sides by the polar ester groups, making the anion static. Therefore, the PEs lower the polarisation and concentration gradient in electrolyte and in turn, improves lithium-ion diffusion in the electrolyte and cyclability of cells[152,153].

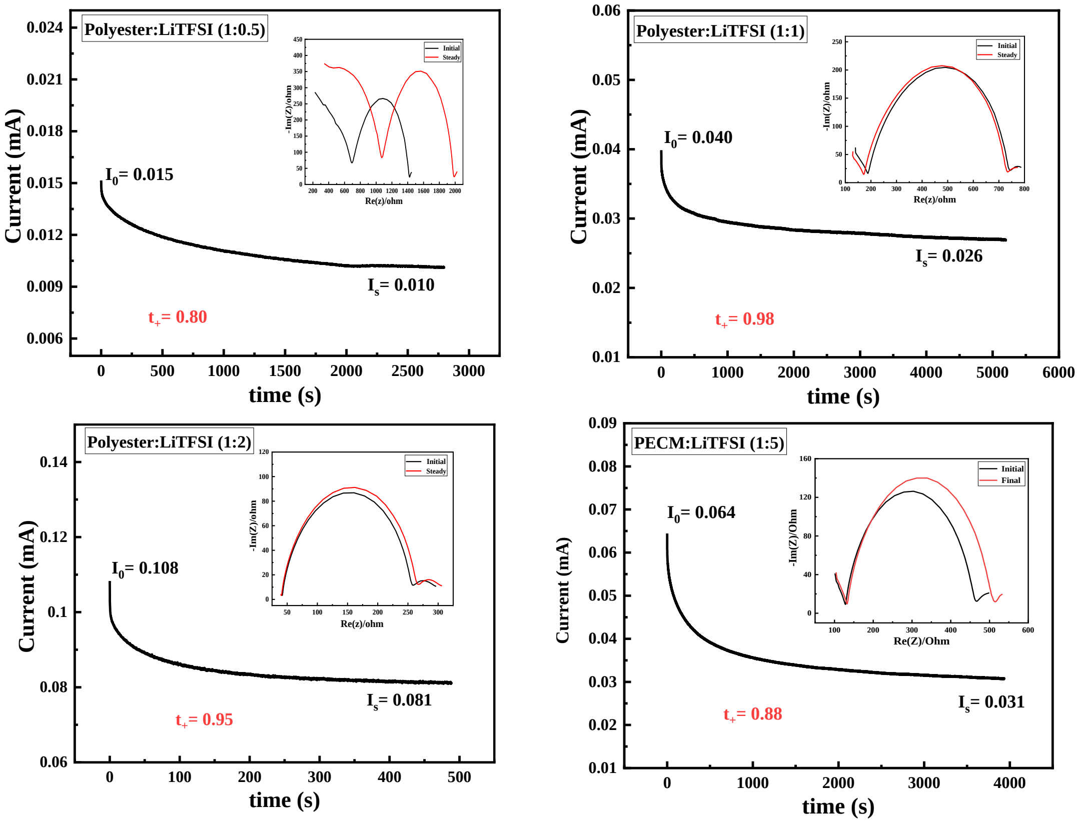

Figure 10: Chronoamperometry of different polymer electrolytes at potential step of 30 mV. The inset shows the ac impedance spectra of before and after polarization at 25 ^{0}C.

Lithium plating/stripping experiments was conducted with the polymer electrolyte and showed high ionic conductivity (PECM:LiTFSI(1:1)) to evaluate interfacial impedance and Li$^+$ transport across polymer electrolyte and lithium metal interface. Galvanostatic cycling of symmetric coin cell Li/PECM:LiTFSI(1:1)/Li at a current density of 0.2 mA cm^{-2} and charging-discharging for 2 hr. was performed (Figure 11). The symmetric cell showed a stable voltage of 70 mV for 130 hr., which confirmed that the electrolyte/lithium interphase is stable in the coin cell. The result indicates that longer cycling performance of LIBs is possible with polymer electrolytes without dendrite formations[133]. Hence A polar aprotic polymer with better lithium-ion solvation properties can mitigate dendrite by providing a favorable environment for lithium platting and striping.

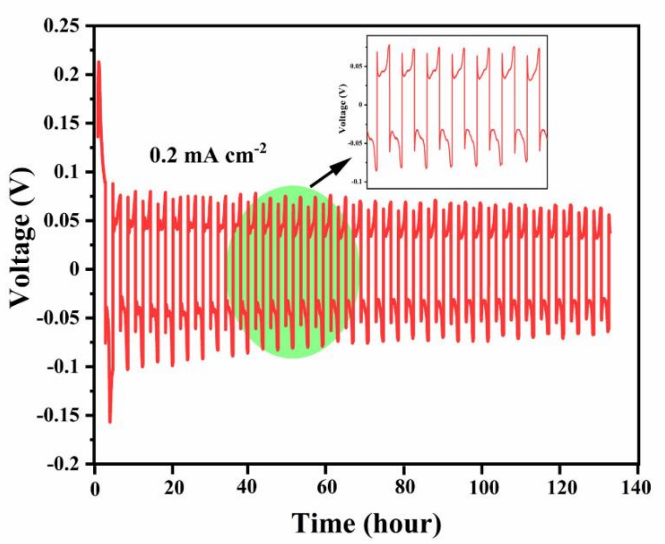

Figure 11: Lithium plating and stripping test using galvanostatic cycling of Li/PECM:LiTFSI (1:1)/LiNCAO at a current density of 0.2 mA cm^{-2} at 25 ºC.

Electrochemical performance of cathodic half-cell:

To evaluate the potential application of PEs in commercial application of lithium-ion batteries, cathodic half-cell was fabricated. Among the PEs studied, PECM:LiTFSI(1:1) showed better ionic conductivity and transference number. LNCAO material was chosen as a cathode to evaluate cathodic half-cell due to its thermal stability, operating voltage 2.8-4.2 V vs Li/Li^{+}, environmental friendliness, low cost and better cycling capability. Cyclic voltammogram of Li/PECM:LiTFSI(1:1)/LiNCAO coin cell was studied at a scan rate 0.1 mV s^{-1} as shown in Figure 12(a). From the CV curve, the first cycle displays a higher abnormal current peak and an overpotential from the second to fourth cycles. Various authors reported that such initial overpotential in rich Ni containing cathode electrodes is due to electrode exposure to moisture, which was recognized to deposition of surface impurites. Some common impurities are hydroxides formed via. NCA surface reaction with humidity and carbonates via. CO_2 reaction with formed surface hydroxides. These impurities form an insulating and resistive layer on the cathode surface leading to overpotential. The absence of overpotential in subsequent cycles indicates that the impurities get decomposed in the first cycle[154–157]. Cell galvanostatic charge-discharge rate capability was studied at varied C-rates/current densities (1C=190 mA g^{-1}) as shown in Figure 12(b). High reversible discharge capacities of the Li/PECM:LiTFSI(1:1)/LiNCAO were 178 mAh g^{-1} (1.42 mAh cm^{-2}) at 0.1C, 164 mAh g^{-1} (1.31 mAh cm^{-2}) at 0.2C, 149 mAh g^{-1} (1.19 mAh cm^{-2}) at 0.5C, 134 mAh g^{-1} (1.07

mAh cm^{-2}) at 0.75C, 117 mAh g^{-1} (0.93 mAh cm^{-2}) at 1C, 65 mAh g^{-1} (0.52 mAh cm^{-2}) at 2 C. Furthermore, the cell showed a reversible discharge capacity of 174 mAh g^{-1} (1.39 mAh cm^{-2}) at 0.1C after cycles at 2C, similar to the initial stable capacity, indicating the cell delivered better rate performance.

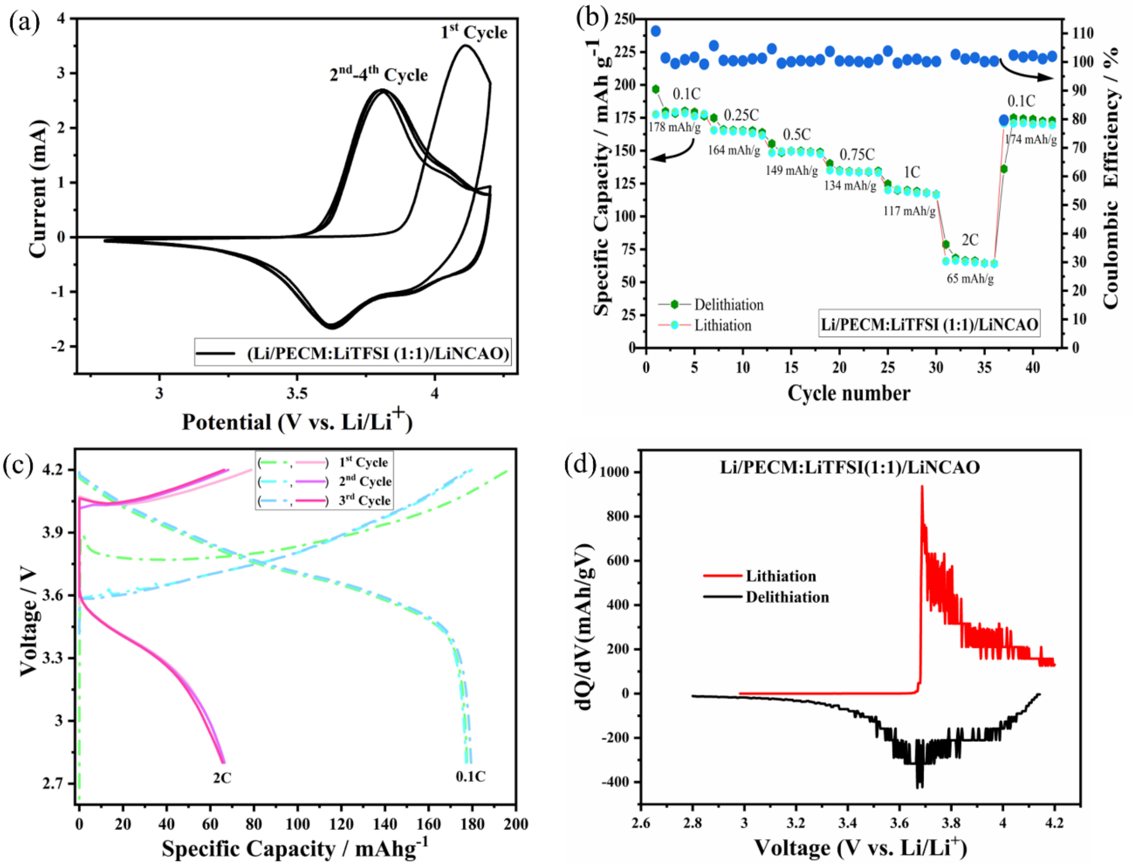

Figure 12: (a) Cyclic voltammograms of cathodic half-cell at 0.1 mV/s, (b) Charge Discharge studies of cathodic half-cell at different current density, (c) Potential vs. Specific capacity curve of cathodic half-cell at 0.1C and 2C, (d) dQ/dV curves of lithiation and delitiation at 25 °C.

During the charge-discharge of the cell, a continuous voltage change at a wide potential range is observed as shown in Figure 12(c). Such slanted charge-discharge profiles are due to the diffusion of ions within electrolytes, electrodes, and interface of the two electrodes over a wide voltage range rather than at a particular voltage. The ohmic loss was seen in the initial voltage drops during lithiation which was further confirmed by the differential capacity profiles (Figure 12(d)). In differential capacity profiles, the sudden peak increase during lithiation at 3.6 V is due to intercalation of lithium in the cathode. The ohmic loss observed during the initial voltage might be due to volume change. Also, the gap created during the process of charge-discharge is not being filled immediately by PE. Such ohmic loss does not take place during delithiation due to no gap present between the interfacial of polymer electrolyte and cathode. The cell polaraization calculated from the maximum peak of lithiation and delithiation is 18 mV which is lower. Long cycling galvanostatic charge-discharge showed better discharge capacities of 167 mAh g^{-1} (1.33 mAh cm^{-2}) at a low C-rate (0.2C). Despite the capacity fading due to slow irreversible consumption of Li at the cathode, the obtained capacity retention is close to 80% after 100 cycles. This proves that the PE can afford an excellent cycle performance even at 25 ºC (Figure 13(a)). While at C rates of 0.5C and 1C the capacities were 149 mAh g^{-1} (1.19 mAh cm^{-2}) and 143 mAh g^{-1} (1.14 mAh cm^{-2}) respectively (Figure 13 (b) and 13(c)). Despite the current rate being doubled the capacity values are almost similar indicating the electrolytes' fast charging capability and the influencing the lithiation-delithiation at high C-rate. The good long cycling charge-discharge can be attributed to free ion transport between the electrodes and better compatibility between electrode and electrolyte. The ionic conductivity of PECM:LiTFSI(1:1) at 25 ºC is determined to be 6.95*10^{-5} Scm^{-1}.

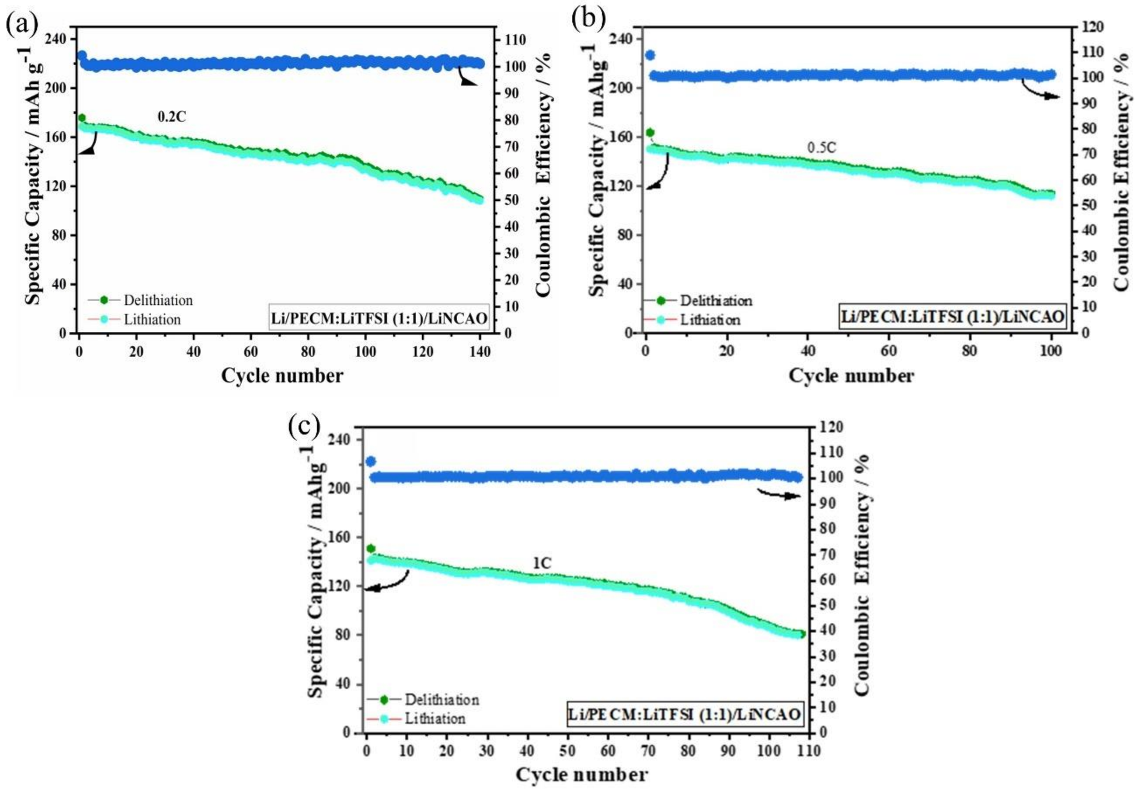

Figure 13: Long cycling charge discharge of Li/ PECM:LiTFSI(1:1)/LNCAO at (a) 0.2C (b) 0.5C and (c) 1C (25 ºC).

Dynamic electrochemical impedance spectroscopy (DEIS) was performed to evaluate the changes after long cycling galvanostatic charging and discharging. The circuit $R_{IR}L(QR_{CEI})(QR_{CT})(QR_{PD})(QR_{CD}W)$ was used to analyze the interfaces and overall cell impedance. The abbreviations of the circuit are "R" in this circuit which stands for internal resistance (IR), charge transfer resistance (CT), CEI resistance (CEI), pre-diffusion process (PD), and complex diffusion (CD). The term pre-diffusion represents the fast migration of Li^+ at the interface between the electrode and the electrolyte in low impedance phase. Complex diffusion refers to slower diffusion of Li^+ within the bulk electrode materials during the intercalation and deintercalation of ions. The "Q" is constant phase element, "L" stands for inductance and "W" is Warburg diffusion coefficient. The data was segregated according to specific frequency ranges such as 1,000,000–100,000 Hz for internal resistance; 100,000–10,000 Hz for charge transfer resistance; 10,000–1,000 Hz for CEI resistance; 3.0–0.3 Hz for prediffusion resistance and 0.3–0.01 Hz for complex diffusion resistance.

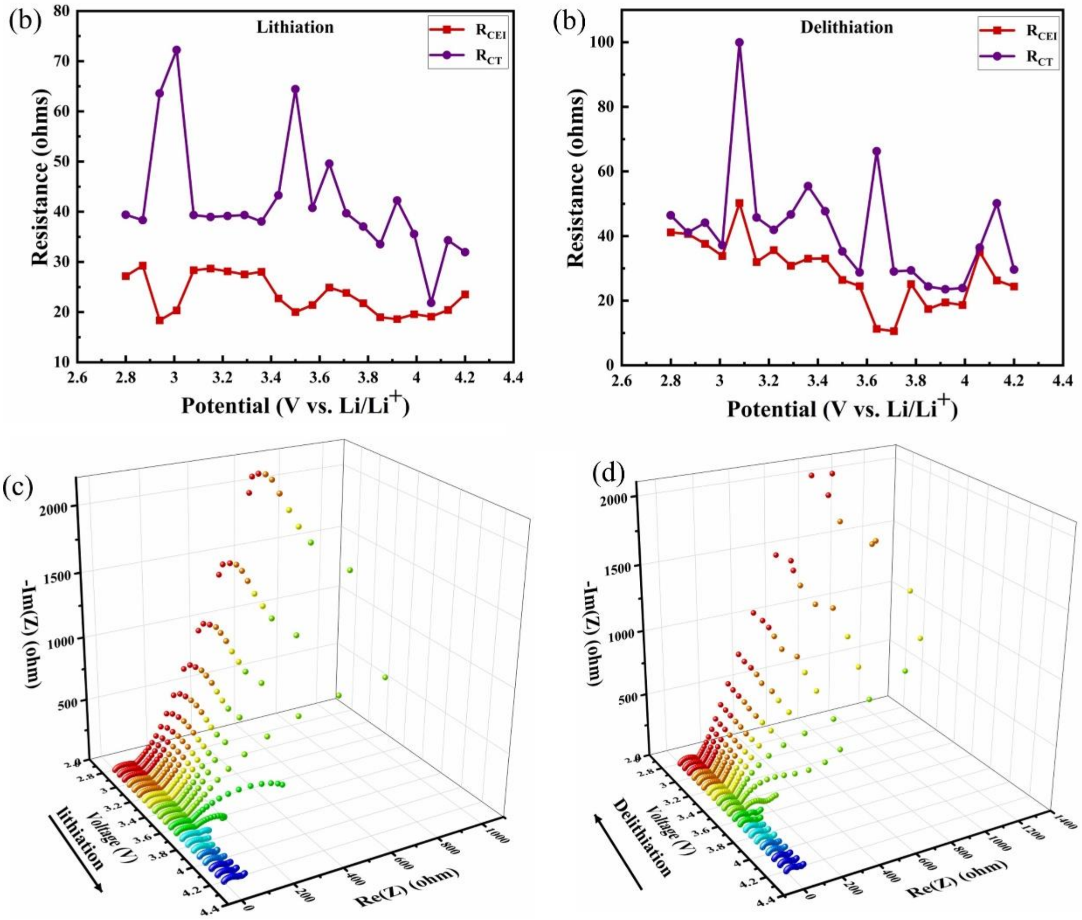

Figure 14: R_{CEI} and R_{CT} vs. Potential plot of (a) lithiation and (b) delithiation using PECM:LiTFSI(1:1). DEIS Nyquist profile in the (c) lithiation and (d) delithiation of cathodic half-cell after long cycling respectively.

The CEI resistance at different potential was shown to be lower than charge transfer resistance due to the less decomposition of electrolytes on the surface of the cathode (Figure 14(a) and 14(b)). Impedance graphs were obtained at different potentials along the charging and discharging potential range, which reflects various interfacial processes during the cycling (Figure 14(c) and 14(d)). A surge in R_{CT} leading to a dip in R_{CEI} at two different potentials (2.9 V and 3.5 V) during lithiation can be attributed to voltage-dependent charge transfer and voltage-dependent CEI behavior. The surge in R_{CT} indicates that rate of charge transfer reactions is slow at specific potentials possibly due to the limitation in availability of active sites on the electrode for electrochemical reactions. While at potentials, CEI may be more stable and less reactive resulting in low R_{CEI}. In contrast, some potentials the CEI become less stable and changes, leading to an increase in R_{CEI}. These changes in CEI can influence the overall R_{CT}. The R_{CT} and R_{CEI} traits are inherent to dynamic nature of LIB chemistry and operation. A surge in both R_{CEI} and R_{CT} at 3.1 V during delithiation might be due to formation of thicker CEI which can hinder ion transport, leading to higher R_{CT}. Higher R_{CT} also suggests that rate of deintercalation is slow at that particular potential due to kinetic limitation or change in electrochemical activity of cathode. At specific states of charge cathode electrolytes electrochemical environment may be different leading to variations in R_{CEI} and R_{CT}. Further, to probe Lithium-ion diffusion coefficient, Warburg plots (Z real vs. $\omega^{-1/2}$) have used from low frequency of the DEIS Nyquist plots. The diffusion coefficient during lithiation and delithiation was calculated through the following equation[158]:

$$D_{Li^+} = \frac{R^2T^2}{A^2n^4F^4C^2\sigma^2} \quad \text{...eq(6)}$$

Where D - diffusion coefficient, R - universal gas constant, T is temperature, A - surface area of electrode, n - no. of electrons taken per Li^+, F - Faraday's constant, C - Li^+ electrolyte concentration and σ - the slope fitting of $\omega^{-1/2}$ vs. Z_{real}. The Li^+ ion diffusion coefficient increases from ~10^{-15} to -10^{-11} cm^2 s^{-1} in the lithiation/delithiation potential range of 3.6-4.2 V (Figure 15). The high value of diffusion coefficient supports stability and reversibility of charge-discharge during long cycling and enduring enhanced Li^+ ions storage ability.

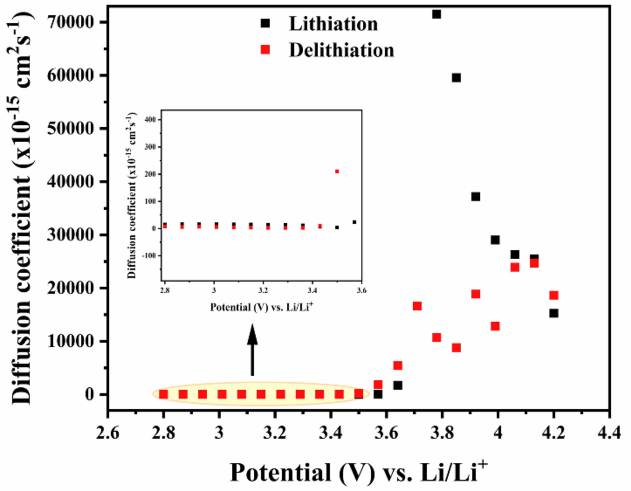

Figure 15: Li^+ diffusion coefficient during lithiation and delithiation potentials deduced from DEIS profiles.

Post-mortem studies of the surface composition and morphology of the cathode after long cell cycling were characterized using ex-situ XPS and SEM techniques. The XPS analysis of the cathode surface after 100 cycles suggests the presence of an inorganic layer consisting of lithium carbonate-based compounds in the CEI, as observed from O 1s and C 1s which were due to sacrificial polymer electrolyte decomposition at the cathode surface (Figure 16). The top surface also reveals the presence of LiF from the F 1s spectra which suggests rich inorganic (LiF) and organic fluoride (CF_3) distribution at surface of CEI[159,160].

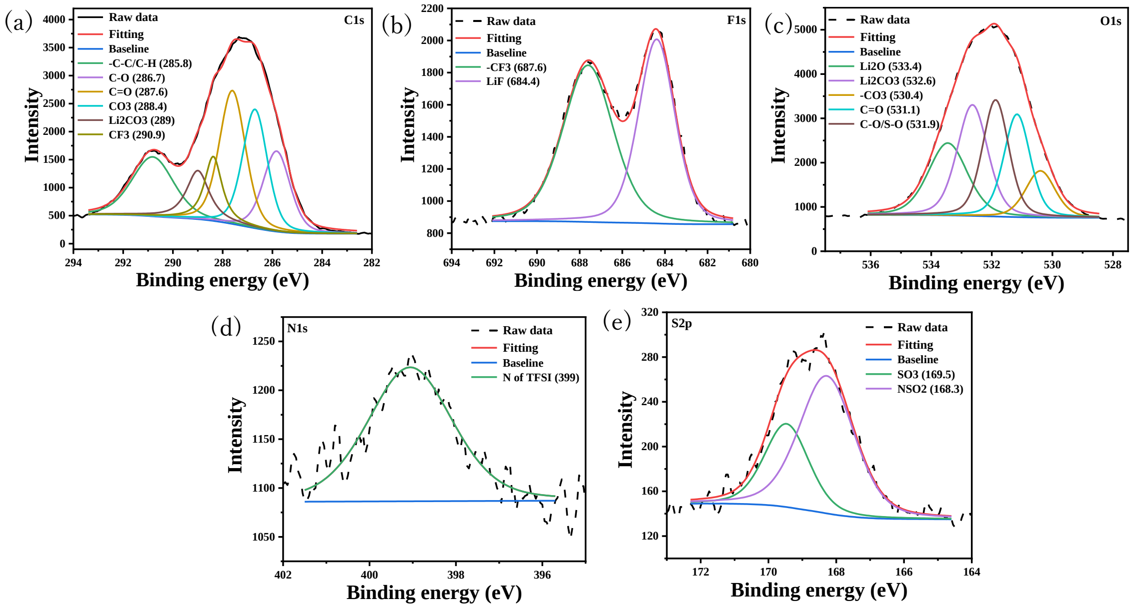

Figure 16: Postmortem XPS spectra of (a) C1s, (b) O1s, (c) F1s, (d) N1s and (e) S2p of cathode surface after long cycling studies.

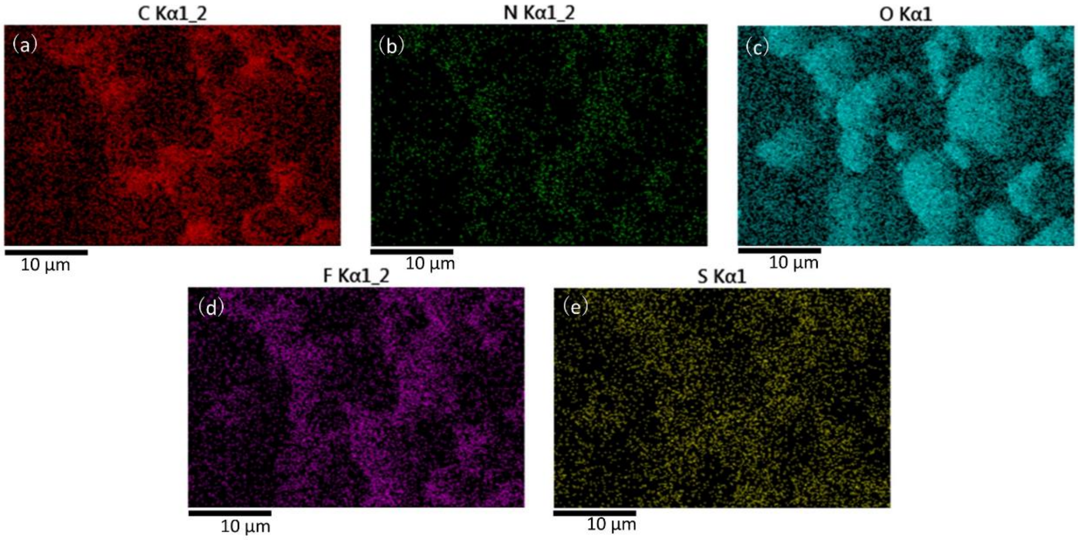

Figure 17: Postmortem EDS map of (a) carbon, (b) nitrogen, (c) oxygen, (d) fluorine and (e) sulphur of cathode surface after long cycling studies.

Map Sum Spectrum				
Element	**Line Type**	**Weight %**	**Weight % Sigma**	**Atomic %**
C	K series	30.84	0.49	37.64
N	K series	2.63	0.97	2.75
O	K series	59.56	0.77	54.57
F	K series	5.90	0.62	4.55
S	K series	1.07	0.06	0.49
Total		100.00		100.00

Table 3: Atomic percentage of different elements obtained from the EDS mapping.

TFSI anion of the lithium salt was shown to be present on the surface of cathode which was confirmed from the C 1s and F 1s spectra due to presence of CF_3 and from N 1s and S 2p spectra (Figure 16). The uniform distribution of the different elements on the surface of the cycled electrode was validated by EDS elemental mapping (Figure 17) which also supports the XPS data. The atomic percentages of different elements present are mentioned in Table 3. The effect of the CEI and long cycling on the morphology of cathode surface was studied using SEM. Figure 18(c) and 18(d) shows uniform particle distribution of cycled cathode material. Cross-sectional and surface-view SEM image of the cycled cell was observed to understand the effect of long cycling on cathode material. The comparision with the pristine LiNCAO electrode SEM images is shown in Figure

18(a) and 18(b). Small cracks are being observed on the spherical particles which might be due to continuous charge and discharge at high current rate. These cracks lead to irreversible consumption of Li-ion and capacity fading as observed in long cycling. Noting that complete eradication of the cracking using electrolyte is not possible, the aim of the work was to find a better electrolyte with high conductivity, transference number and compatibility with cathode for LIB[161]. No dendrite formation was observed at the cross-sectional studies.

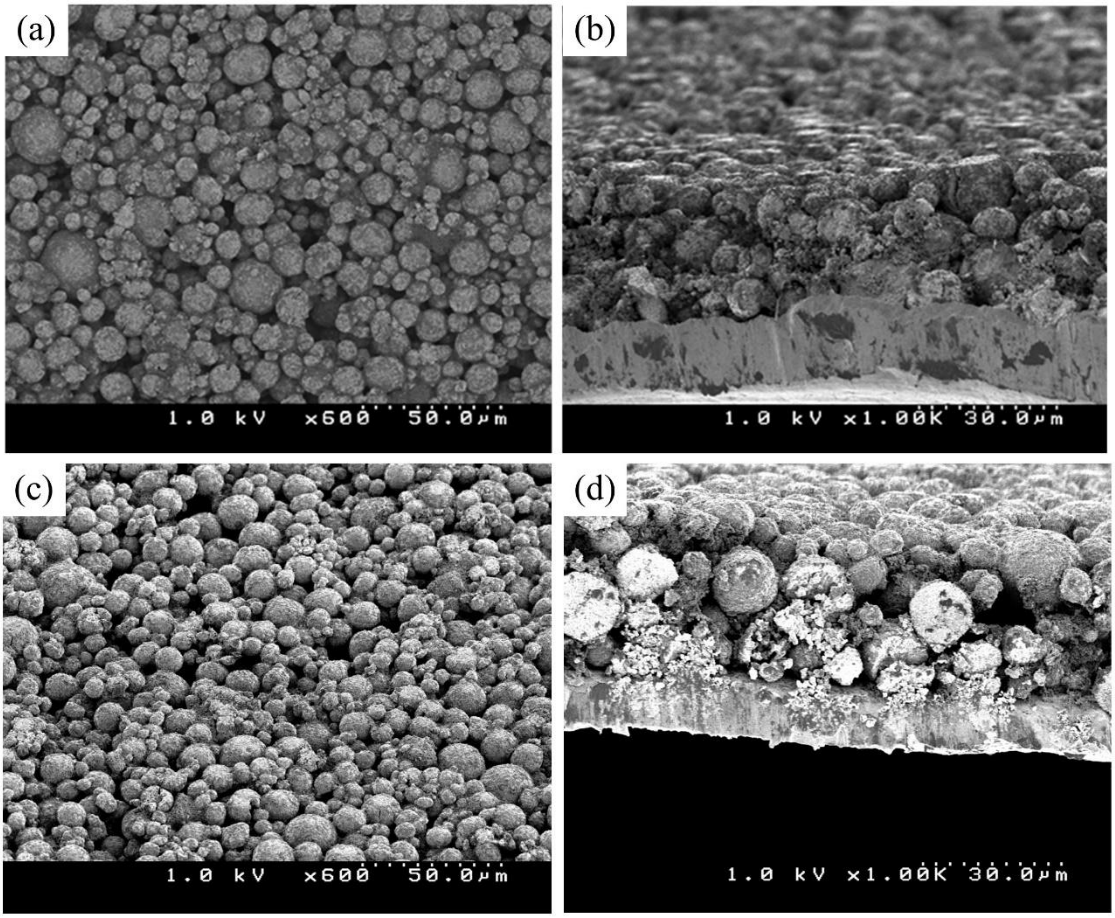

Figure 18: The SEM images of the cathode electrode after charge discharge cycling (a) Cross-sectional view of the electrode, (b) top surface view of the electrode.

Conclusion:

We investigated battery performance of high-density functional group polymer of the poly(substituted methylene) with ethoxy carbonyl ester group on each carbon of the polymer chain known as poly(ethoxycarbonylmethylene) (PECM). Three main evident traits are as follows: (i) an approach towards using high-density functional group polymer as polymer electrolyte (ii) introducing the effect of polymer polarity in performance of electrolyte (iii) high ionic conductivity and transference number without any additives. The polar aprotic polymer with abundant ethoxy carbonyl ester group exhibited ionic conductivity $3.08*10^{-4}$ S cm^{-1} at 51 ^{O}C and demonstrated higher transference number of 0.98 for PECM:LiTFSI (1:1). The polar aprotic side chain groups help in the formation of weak interaction and solvation sphere around lithium-ion from LiTFSI, thereby allowing the free movement of lithium and hindering the bulky anion. The Li/LiNCAO cathodic half-cell with PECM exhibits a better cycle life of 167 mAh g^{-1} (1.33 mAh cm^{-2}) capacity with capacity retention of 80% at 0.2C for 100 cycle. It also performed better long cycling performance at low and high current density. A polar aprotic polymer in LIBs electrolyte enhances solvation of lithium-ion, contributes to formation of stable SEI, reduces the risk of dendrite formation, offers thermal stability and broadens the electrochemical stability window. It is noteworthy that the research work will contribute significant in affordable and environmentally friendly polymer electrolyte. The approach towards finding a new category of PE will help in potential development of commercial lithium-ion battery based on organic polymer electrolyte.

Chapter 3

Robust Electrochemical Performance of LIB using Polymethylene-based High-Density Carboxylic Acid Binder in Graphite Anode

Abstract

A durable electrochemical performance in lithium-ion batteries is increasingly important in future applications. Various strategies were used to develop functional binders for long cycles, high loading, and fast charging. However, despite constant efforts, the strategies mentioned above remain critically challenging and must be addressed. Herein, we utilised a non-toxic, water-soluble and bio-derived polymethylene-based binder containing a high concentration of carboxylic acid functional groups as side chains, demonstrating improved lithium-ion transport and minimising electrolyte decomposition. Polymethylene's less flexible rod-like polymer architecture succeeds in exhibiting long cycling at 1C with a specific capacity of 336 mAh g^{-1} and capacity retention of 81% for 700 cycles. It also performed better fast charging behavior at 5C with a specific capacity of 54 mAh g^{-1} and showed better rate and long cycling stability with high loading of graphite up to 3.4 mg cm^{-2}. Hence, a poly(fumaric acid) binder enhances the LIB's electrochemical performance and mechanical strength.

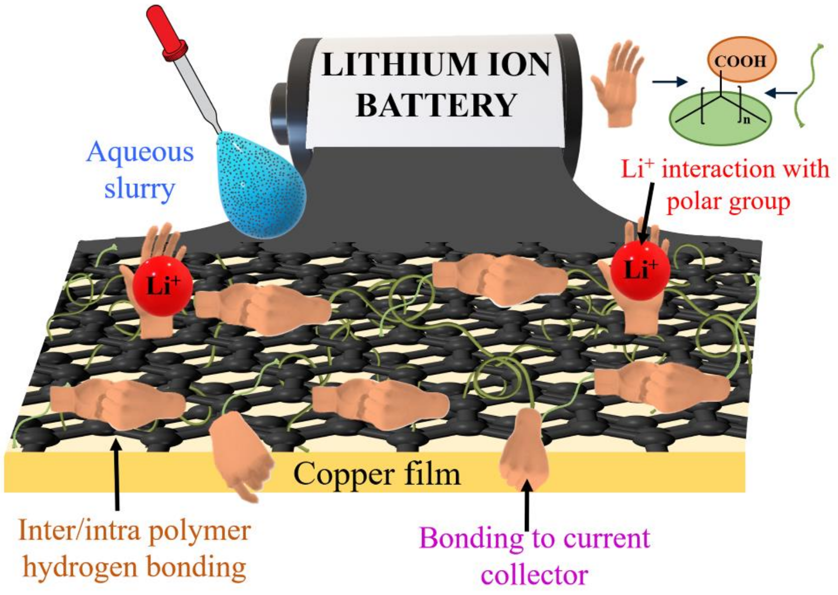

Introduction:

Carbon-based graphite anode has revolutionized energy storage and is widely used in various lithium-ion battery (LIBs) applications. LIBs offer several advantages including high energy density, long cycle life and low self-discharge, leading to their ever-increasing market demand[162,163]. The continuous pursuit of enhancing LIB performance, energy density and safety has prompted researchers to explore various aspects of battery components[112,113,164,165].

The performance and reliability of LIBs depend mainly on the electrochemical properties and integrity of the electrode (both anode and cathode) materials. Electrochemical performance primarily depends on the solid electrolyte interphase (SEI). SEI is a passivation layer that forms due to in-situ electrolyte degradation on the negative electrode. Stable and uniform SEI helps reversible charge-discharge, enabling long cycling. A thin SEI has low resistance due to which it facilitates Li^+ transport into the electrode and increases the lithium diffusion kinetics[166]. SEI stability is improved by additives, polymer coating and binders[167–169]. Dense functional polymer binders might alter electrode surface chemistry and act as local electrolyte components at the SEI, providing better interaction between the polymer and its surroundings[170,171]. Regarding integrity, binder plays an integral part in maintaining the stability of the electrodes by binding the active material (graphite) and conductive carbon together and holding them to the current collector through multiple interactions such as hydrogen bonding, Vander Waals forces, mechanical interlocking, etc., which is predominantly related to the functional groups and backbone structure of polymer binders[172]. According to the solvent used for dissolving the binder, the suspension containing graphite, conductive additive and binder is classified into aqueous-based and nonaqueous-based slurry.

Traditionally, poly(vinylidene fluoride) (PVDF) is a commercial binder for LIBs, but its interaction with electrode components through van der Waals force results in weak adhesion and lowers the long cycling stability[173]. Besides it requires toxic, flammable, and environmentally unfriendly solvent N-methyl-1-2-pyrrolidine (NMP) for processing[174]. As a result, there has been a growing interest in exploring binders to replace PVDF and address the environmental aspect.

Thus, aqueous binders have attracted much attention for their environmental friendliness and fabrication cost. Some water-soluble functional binders are chitosan, poly(acrylic acid) (PAA), sodium alginate and sodium carboxyl methylcellulose-based binders[175–177]. Among the above polymers, PAA has a higher functional group concentration. A few important characteristics of PAA are (i) strong self-associated polymer[178]; (ii)Better rheological properties due to increasing adhesion strength; (iii) enhancement in the ionic conductivity [179]; (iv) capability to undergo electrostatic interaction with cation, thereby enhancing the desolvation of Li^+ and increases reversible lithium intercalation[180,181]. However, the graphite/PAA electrode observed a thick SEI layer due to inhomogeneous binder distribution in the electrode matrix due to PAA's inability to modify the surface chemistry[170,182]. In addition, the electrochemical performance and adhesive strength decrease significantly at high mass loading of the electrode[177].

Considering the drawbacks of PVDF and the benefits of carboxylic acid group of PAA, this study proposes a polymethylene-based polymer binder with high-density carboxylic acid functional groups at the side chain. The presence of dense and well-distributed functional groups has shown a high affinity towards graphite and increases the capacity retention of LIBs[183]. Poly(fumaric acid) is one of the polymethylene group molecules, a less flexible rod-like polymer and is also known as poly(hydroxycarbonylmethylene). As brittle or stiff binders (Na-CMC) have shown enhanced long cyclability and retention capacity compared to flexible polymer binder (PVDF-HFP)[184]. Such polymethylenes are expected to exhibit superior properties that differ from polyethylenes such as PAA and PVDF due to their stiffness in structure[137]. Otsu et al. and Kitano et al. synthesised poly(fumaric acid) from poly(di-t-butyl fumarate) and poly(di-trimethylsilyl fumarate), respectively, which are expensive and hazardous[136,185]. To the best of our knowledge, there have been no such articles based on high-density functional groups of polymethylene-based binders for LIBs. Herein, a novel synthesis route using precursor di-ethyl fumarate, which can be obtained from biomolecule fumaric acid, was used to obtain poly(fumaric acid) (PFA) through economical and unhazardous chemicals. Fumaric acid is an intermediate product of the citric acid cycle, which is a cellular process generating energy in mitochondria. It can also can be produced or isolated from plants (genus *Fumaria*) and filamentous fungi (*Rhizopus* spp.) [186–188]. Fumaric acid esters have been used for oral treatment of psoriasis, indicating that the starting molecule is non-toxic[189]. PFA contains -COOH functional group on every backbone carbon compared to PAA and PVDF in which functional groups are present in alternate carbon of the backbone. Water-soluble PFA polymer offers the potential to form thin and stable SEI by preventing electrode cracking during cycling and providing better adhesion to electrode components due to high-concentration of functional groups. As a result, they would enhance the overall electrochemical performance of LIBs.

By delving into the electrochemical properties, adhesion of electrode material, and overall impact on cell performance, we seek to shed light on using high-density functional group polymer as a binder to improve the functionality and performance of graphite anodes in LIBs.

Experimental:

Materials:

Diethyl fumarate (98%), Hydrochloric acid (12N), 2,2'-Azobis(isobutyronitrile) (AIBN), poly(vinylidene difluoride) (PVDF) binder (MW: 540,000), polyacrylic acid, 1.0 M $LiPF_6$ (50/50) ethylene carbonate/diethyl carbonate (EC/DEC) electrolyte and battery grade graphite were purchased from Sigma-Aldrich. The potassium hydroxide, ethanol (99.5), N-methyl pyrrolidone (NMP) were purchased from Wako. Super P conductive (99+% (metal basis)) was ordered from Alfa Aesar. Dialysis tubing was obtained from Fisherbrand regenerated cellulose dialysis tubing.

Preparation of poly(fumaric acid):

Diethyl fumarate (2 gm, 11.6 mmol) was polymerized using freeze-thaw vacuum-sealed bulk polymerization method at 70 °C in the presence of radical initiator AIBN (38 mg, 0.23 mmol) for 24 hr. The content obtained after 24 hr. was poured into an excess of hexane (50 ml) and stirred, followed by removing hexane and vacuum drying the polymer overnight. The polymer was hydrolyzed using excess KOH in a solvent mixture of ethanol: water (2:1) under reflux for 24 hr. Then the mixture was concentrated and acidified with 1 N HCl. The resulting solution was treated for dialysis using a cellulose acetate tube. The pure poly(fumaric acid) polymer was obtained after evaporation of the aqueous polymer obtained after dialysis. The PFA polymer was obtained in good yields (1.1 gm, 82%).

Characterization of poly(fumaric acid):

^1H NMR and ^{13}C NMR spectra were recorded in D_2O solvent using Bruker Advance II-400 MHz spectrometer. PerkinElmer 100 FTIR spectrometer was used for obtaining

Fourier transform infrared absorption spectra. TGA of PFA was conducted using a Hitachi STA7200 thermal analysis system at 10 ºC min^{-1} heating rate and N_2 flow rate of 200 ml min^{-1}.

Electrode fabrication:

An anode slurry was prepared by mixing 80 wt.% graphite, 10 wt.% super P conductive carbon and 10 wt.% PFA in water and ball milled for 1 hour. Using a doctor blade of 100 µm, the obtained slurry was coated onto a copper foil (20 µm thickness) and dried under vacuum at 80 ºC for 12 h. Subsequently, the dried electrode was compressed using a hot rolling machine and cut into circular discs of 13 mm diameter. The coin cells of CR2025 were fabricated within an argon-filled glove box under O_2 and H_2O levels below 0.5 ppm. A lithium disc was used as the counter electrode, a polypropylene Celgard 2500 as the separator and 70 µl of commercial 1.0 M $LiPF_6$ in EC:DEC as electrolyte. To compare the battery performance, 10 wt.% of PAA in water and 10 wt.% of PVDF in NMP were used as binders and followed the above procedure for fabrication of anodic half-cells. The graphite areal loading and areal capacity are in the range of 0.85-1.37 mg cm^{-2} and 0.318-0.510 mAh cm^{-2}, respectively. The porosity and thickness of the electrodes are kept almost constant for all the studies. The PFA-based anodic half-cell is named PFA/Gr, while the PAA-based anodic half-cell is PAA/Gr and the PVDF-based anodic half-cell is PVDF/Gr.

Electrochemical test:

Cyclic voltammetry (CV) studies were carried out in the potential range of 0.01-2.1 V and were subjected to varied scan rates of 0.1, 0.2, 0.4, 0.6, 0.8 mV s^{-1} using Bio-Logic Science Instruments for determining lithium-ion diffusion coefficient of the anode. The electrochemical impedance spectroscopy (EIS) was performed before and after CV in the frequency range of 1.0 MHz to 0.1 Hz at an AC amplitude of 10 mV. Dynamic electrochemical impedance spectroscopy (DEIS) measurement was done after 700 cycles of charge and discharge at different voltage perturbations in the frequency range of 1.0 MHz to 0.1 Hz at an AC amplitude of 10 mV. Galvanostatic cycling measurements were carried out using Electrofield ABE 1024 between 0.01-2.1 V in constant-current mode. The activation energy of the cycled anodic half-cells was calculated using the EIS method using cycled anodic half-cells after the output circuit potential was brought to 0.2 V at which lithium intercalates in graphite vs. Li^+/Li. The potential was maintained, and EIS was measured at different temperature ranges.

Physical characterization of electrode:

The rheology of the slurries and electrodes was determined using viscosity and peel tests respectively. The viscosity measurement was carried out using Toki Sangyo Viscometer TV-35. The peel test was conducted using Instron 3342 for a 40 mm long electrode. The adhesive tape was attached to the roll-pressed coated electrode and was peeled at 90^{o} angle at a constant displacement rate of 1 mm min^{-1}.

Postmortem studies of the long-cycled electrodes were undertaken using XPS and SEM. The morphology of the graphite anode was analyzed using Field Emission SEM (FESEM, Hitachi S-4500) images at an accelerating voltage of 1.0 kV. Chemical composition analysis on the surface of the cycled anode was identified using X-ray photoelectron spectroscopy (XPS, Fisons instruments S-probe TM 2803).

Results and discussions:

Characterization of PFA:

Poly(fumaric acid), a high-density carboxylic acid functional group polymer was synthesized to enhance the performance of LIBs as a high-efficiency binder compared to PVDF and PAA. The PFA was synthesized using radical-initiated bulk polymerization, followed by ester hydrolysis and dialysis as depicted in Figure 1(a). The polymer formation can be initially confirmed by checking the dissolved PFA's pH in water. The polymer failed to form if bulk polymerization was carried out in the presence of air.

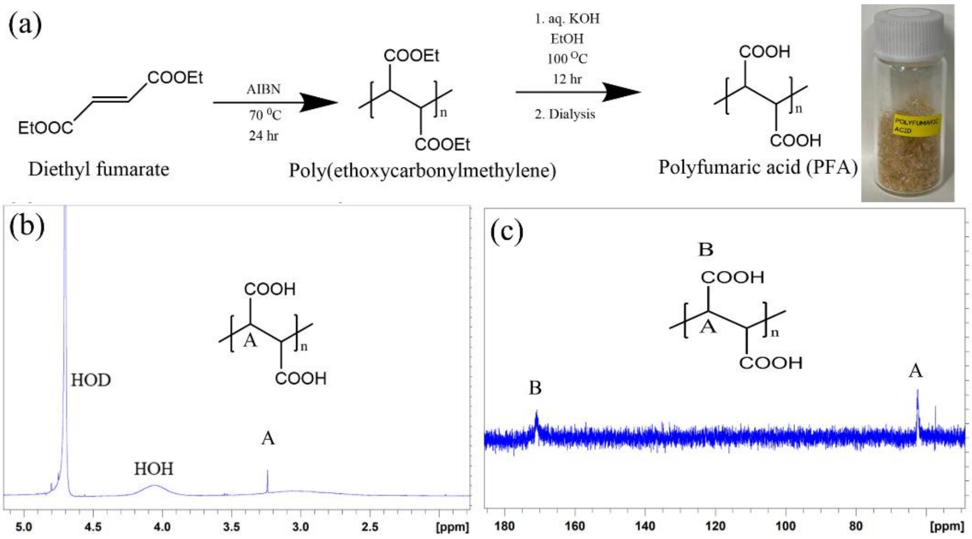

Figure 1: (a) Schematic illustration of the synthesis of PFA, (b) ^{1}H NMR spectrum (D_2O), (C) ^{13}C NMR spectrum (D_2O).

The ^{1}H and ^{13}C NMR spectra of PFA are demonstrated in Figure 1(b) and 1(c) respectively. The peak at 3.25 ppm in the ^{1}H NMR corresponds to C-H group of the main chain[185]. The characteristic peaks at 170.8 ppm and 62.4 ppm from ^{13}C NMR correspond to the carboxylic acid's carbonyl and C-H carbon respectively. The FT-IR spectrum of PFA is depicted in Figure 2(a). The board peak at 3500 cm^{-1} was observed due to O-H stretching of carboxylic acid which was absent in the poly(ethoxycarbonylmethylene) polymer. The characteristic absorption peaks at 2977 cm^{-1} correspond to -CH- stretching of the methylene backbone. The carbonyl and ether peaks were absorbed in 1715 and 1090 cm^{-1}, respectively. The molecular weight was determined to be 3000 m/z by MALDI-TOF (Figure 2(b)). The measured pH of the PFA was determined to be 4.57 (Figure 2(c)). These results suggest that the current approach towards the synthesis is suitable for obtaining PFA.

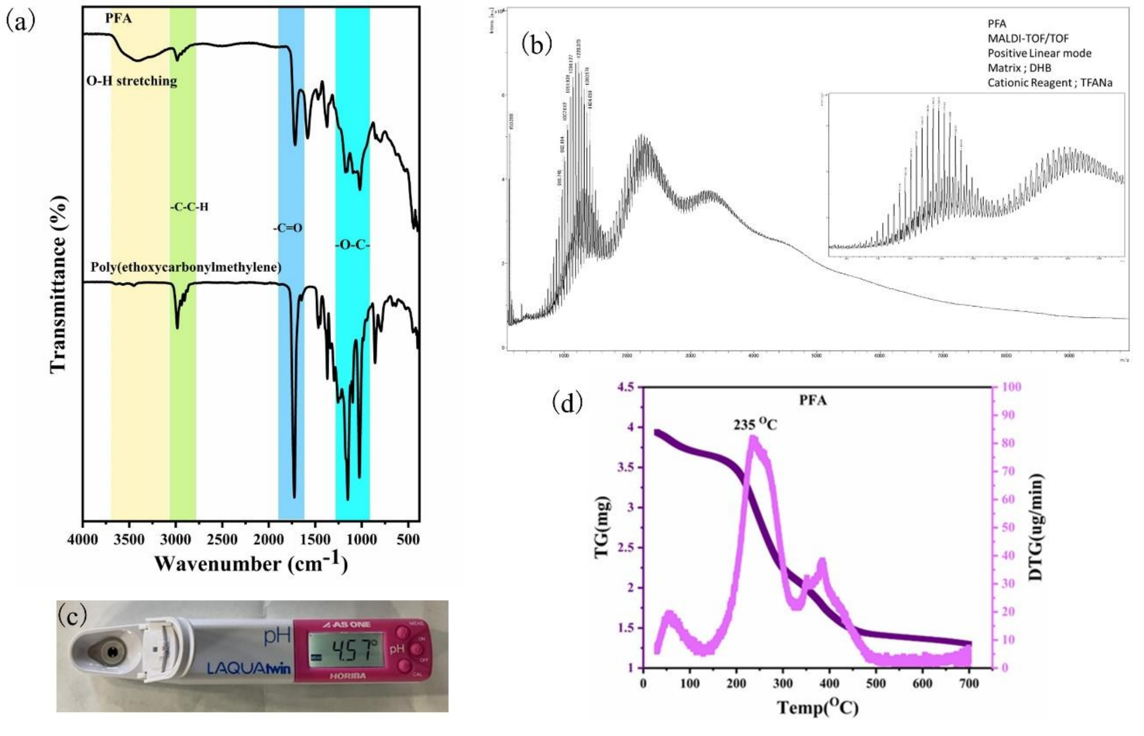

Figure 2: (a) FT-IR spectra of PFA and poly(ethoxycarbonylmethylene). (b) MALDI-TOF of PFA. (c) pH measurement of PFA using pH meter.

The thermal stability of the PFA was investigated through thermogravimetric analysis (TGA). TG and DTG profiles of PFA are demonstrated in Figure 2(d). The initial weight reduction of around 100 °C was assigned to the vaporization of adsorbed moisture by the hydrophilic acidic groups. PFA exhibited thermal stability up to ~235 °C. With the increase in temperature, a steep slope of degradation was observed, which could likely indicate dehydration due to the formation of anhydrous linkages from the intra and inter-bond formation and subsequent evolution of CO_2[185]. Hence PFA can be used as a binder for high-temperature LIBs due to its good thermal stability.

Binders effect on rheology:

The interfacial adhesion of anode materials containing different binders was investigated by observing the amount of material removed from the electrode and measuring the average peel force. The average peel force of the electrode film using PFA (10.94 N) as binder is higher than that of PAA (9.96 N) and PVDF (9.22 N) binder, indicating PFA`s enhanced adhesion ability (Figure 3(a)). This can be ascribed to the Vander Waals force resulting from the high-density functional groups in PFA that effectively holds the electrode components and the current collector together. The physical properties of the PFA binder can accommodate the volume expansion during lithiation without disintegrating the electrode component during delithiation[190]. Inset in Figure 3 (a) shows the optical images of the adhesive tape of the electrodes containing different binders after the peel test. It was clearly seen that PFA adhesive tape contains less active material than PAA and PVDF adhesive tape.

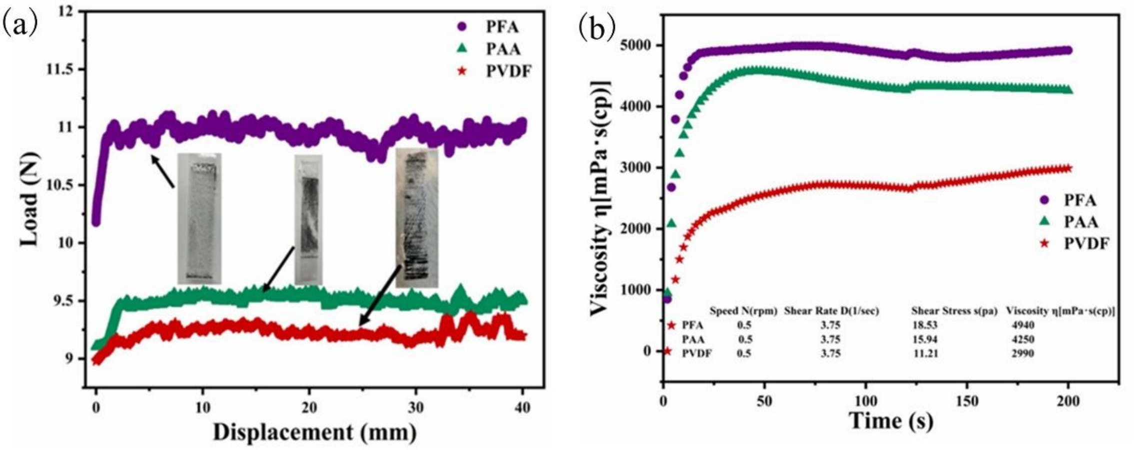

	Speed N(rpm)	Shear Rate D(1/sec)	Shear Stress s(pa)	Viscosity η[mPa·s(cp)]
PFA	0.5	3.75	18.53	4940
PAA	0.5	3.75	15.94	4250
PVDF	0.5	3.75	11.21	2990

Figure 3: (a) Peel curves of graphite electrodes with different binders; Inset: photographs of the tape after the peel test. (b) Viscosity profile of graphite slurry with different binders.

In rheology, slurry viscosity provides insights into achieving the optimal dispersion state of electrode materials, which is essential for enhancing the bond formation within binder and with the electrode components. The stabilized viscosity varies with changes in mixing sequence due to the solvent’s diffusion into the solid particle's internal pores and is also affected by the mixing method[191]. Slurry rheology is also important for subsequent production and commercialization, as the homogenous binder solution must be optimized to obtain uniform electrode material distribution[192]. At a shear rate of 3.75 s^{-1}, the viscosity of slurry containing PFA binder was 4.9 Pa.s, which is higher than PAA with 4.2 Pa.s and PVDF with 2.9 Pa.s (Figure 3(b)). Higher viscosity slurry is reported to facilitate the production of uniform electrode coating[193]. The suspension properties can impact adhesion strength which is a key factor in achieving high cyclability of the battery.

Electrochemical performance:

The electrochemical stability of the binders in the graphite electrodes was assessed by cyclic voltammogram. The CV curves of the graphite electrodes containing different binders at a scanning rate of 0.1, 0.2, 0.4, 0.6 and 0.8 mV s^{-1} were illustrated in Figure 4. All the samples identified a reduction peak at 0.7 V associated with the electrolyte's decomposition, leading to a SEI. Cyclic voltammograms demonstrate the decrease in overpotential difference in delithiation peak between 0.1 mV s^{-1} and 1.0 mV s^{-1} in the PFA/Gr (0.117 V) compared to PAA/Gr (0.129 V) and PVDF/Gr (0.132 V). The presence of more carboxylic acid in the PFA binder induces facile penetration of lithium ions through the SEI layer and participation in the diffusion kinetics of Li^+, which keeps the anode surface away from lithium plating[194]. The high overpotential in PAA/Gr and PVDF/Gr suggest that the capacity attainment is impeded. The peak shift towards the right with scan rates is attributed to the interfacial kinetics of Li^+ during the deintercalation process. An increase in scan rate in higher current density at electrode surface, thereby enhancing interfacial reaction and leading to increase in peak current with rise in scan rate. This induces higher polarization and shifts in peak, even with small changes in scan rate, as observed in reported papers[195].

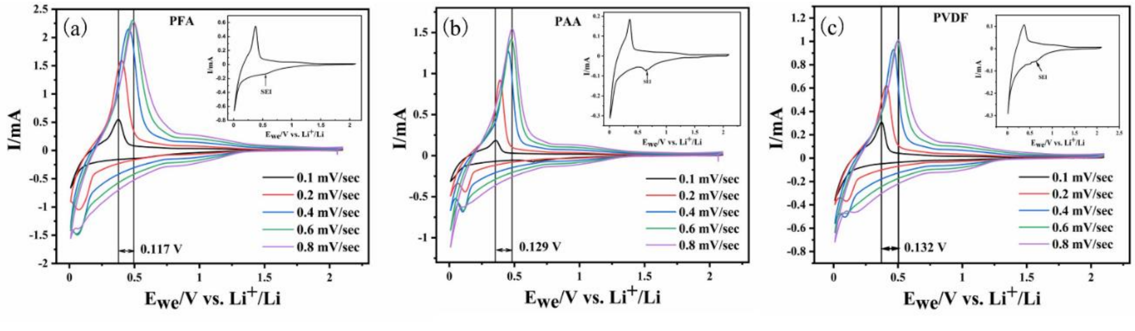

Figure 4: Characterizations of CV curves for graphite electrodes with different binders at scan rates from 0.1 to 0.8 mV s^{-1} (a) PFA/Gr, (b) PAA/Gr, (C) PVDF/Gr.

To further investigate and understand the diffusion kinetics of lithium-ion, the lithium-ion diffusion coefficient was determined using the Randles-Sevick equation[196], wherein the slope values were obtained from the plot of different scan rates vs. peak current (Figure 5(a)).

$I_p = 2.69\times10^5 n^{3/2} A D_{Li} C_{Li} V^{1/2}$ ……eq(1)

Where Ip denotes peak current in amperes, n is the number of electrons involved in the reaction, A represents the area of the electrode in cm^2, D denotes diffusion coefficient of the lithium-ion in $cm^2\ s^{-1}$, C represents the molar concentration in mol cm^{-3} and V denotes scan rate in V s^{-1}. The lithium-ion diffusion coefficient was observed to be highest for PFA/Gr with 3.57×10^{-8} $cm^2\ s^{-1}$, whereas PAA/Gr and PVDF/Gr exhibited values of 2.11×10^{-8} $cm^2\ s^{-1}$ and 6.59×10^{-9} $cm^2\ s^{-1}$ respectively. Therefore, PFA promotes lithium diffusion owing to a dense functional group that undergoes weak interaction with Li^+ ions and conducts ions in the electrode domain[197].

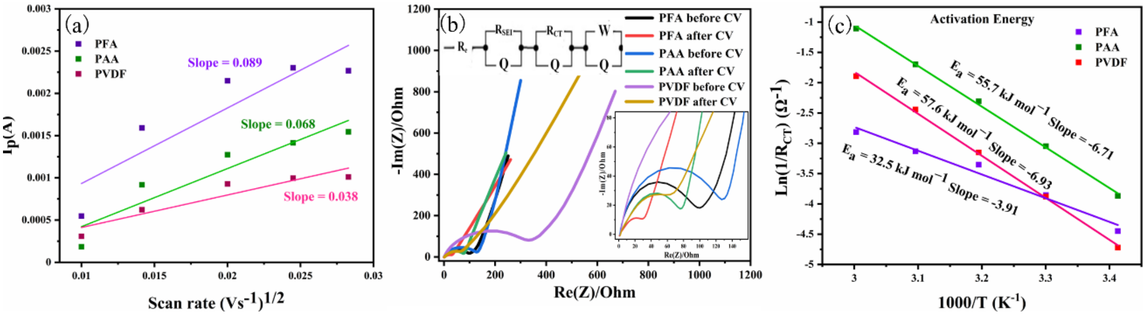

Figure 5: (a) Relationship of CV peak current to scan rate of anodic half-cells. (b) Nyquist plots obtained before and after CV of different binders. (c) Temperature dependence of lithium-ion transfer through electrode/electrolyte interface.

The electrode's interfacial resistance consists of SEI resistance and charge transfer resistance[198]. Figure 5(b) illustrates the Nyquist plots of anodic half-cells containing three binders. The semicircle observed from the Nyquist plots is from the overlap of two semicircles contributing from interfacial layer resistance (SEI resistance, R_{SEI}) at high frequency region and charge transfer resistance (R_{CT}) at medium frequency region. The straight line at the low-frequency range corresponds to diffusion-controlled Warburg impedance (W). It is observed from the plot that the semicircle diameter decreases after CV in all three cells, indicating a decrease in interfacial resistance and charge transfer resistance due to the formation of SEI film on the electrode surface. The Nyquist plots after CV were simulated using the software Zsimpwin with an equivalent circuit

(R_e(QR_{SEI})(QR_{CT})(QW), inset of Figure 4(b)) to obtain ohmic resistance (R_e), R_{SEI} and R_{CT}. The R_{SEI} and R_{CT} values of PFA/Gr are 2.57Ω and 26.19 Ω respectively, which are much lower than those of PAA/Gr (R_{SEI} = 6.06 Ω and R_{CT} = 71.71 Ω) and PVDF/Gr (R_{SEI} = 3.92 Ω and R_{CT} = 60.24 Ω). This suggests that less flexible, high-density carboxylic acid-based PFA binder facilitates the formation of thin SEI and decreases the impedance to Li^+ charge transfer. In addition, the impact of R_{CT} value, influenced by the binder, can negatively affect cycle life, as it is related to the concentration of Li^+ ions on the surface of the electrode, forming the SEI layer. Hence, PFA binder, which lowers R_{CT} value and plays a role in reducing lithium-ion concentration on the electrode surface, thereby suppressing lithium lithium plating[199].

To further understand the influence of dense carboxylic acid of PFA in Li^+ desolvation on the electrode surface, activation energy was evaluated from R_{CT} at different temperature ranges. The Arrhenius-type behavior was observed in the plot of conductivity as a function of reciprocal temperature and demonstrated a decrease in charge transfer resistance with increased temperature (Figure 5(c)).

$$\mathrm{Ln}(\sigma) = \ln(\mathrm{A}) - \frac{E_a}{R}\left(\frac{1}{T}\right) \quad \ldots\ldots \text{ eq(2)}$$

Where σ or $1/R_{CT}$, R, E_a, A and T denote charge transfer conductivity, gas constant (8.314 J K^{-1} mol^{-1}), activation energy, pre-exponential entropic factor and temperature respectively. The activation energy values of PFA/Gr, PAA/Gr and PVDF/Gr are 32.5, 55.7 and 57.6 kJ mol^{-1} respectively as calculated from the slopes of the Arrhenius plots (Figure 5(c)). The lower value of activation energy by PFA/Gr is attributed to the formation of smooth pathway for Li^+ transport within the electrode system with the help of a dense polar carboxylic group involved in the desolvation of Li^+ and the creation of binder-electrolyte affinity, which is crucial for the wettability of electrode by the liquid electrolyte[200]. In contrast, the PAA/Gr and PVDF/Gr exhibited high ionic charge transfer resistance. This is attributed to the reduced impact of the less dense polar functional groups in PAA and the poor influence on Li^+ from the fluorine of PVDF.

Given the promising results, the influence of binders on the galvanostatic charge-discharge cycle was evaluated to provide insight into practical applicability in LIB. Figure 6 compares the lithiation/delithiation voltage profiles of anodic half-cells with different binders (PFA/Gr, PAA/Gr and PVDF/Gr). The peak at 0.7 V observed in all the anodic half-cells containing different binders during the first lithiation at 0.1C corresponds to SEI formation resulting from the electrolyte reduction. The initial coulombic efficiency is determined to be 75% for PFA/Gr, 66% for PAA/Gr and 71 % for PVDF/Gr. The first lithiation capacity is higher than the subsequent lithiation capacity due to electron consumption by the electrolyte, leading to decomposition and trapping of solvated cations in the SEI. The initial lithiation-specific capacity for PVDF/Gr (465 mAh g^{-1}) is higher than PFA/Gr (424 mAh g^{-1}) and PAA/Gr (404 mAh g^{-1}), possibly resulting in thick SEI as indicated by impedance and activation energy studies. Wherein PFA/Gr showed higher capacity than PAA/Gr, this might be attributed to high concentration of carboxylic acid groups in PFA. The protons of carboxylic acid in PFA may be ion-exchanged by Li$^+$ in the electrolyte media, or the carboxylate group directly would have interact with solvated lithium ion[180].

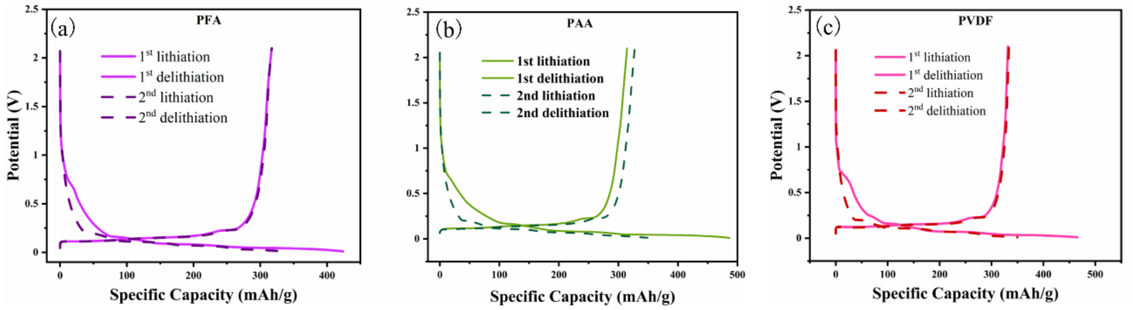

Figure 6: Lithiation-delithiation profiles of (a) PFA/Gr, (b) PAA/Gr and (c) PVDF/Gr.

The SEI formation and lithiation/delithiation on graphite were further confirmed by the differential capacity plots of the first lithiation and delithiation cycle. The dQ/dV plots (Figure 7) show a broad cathodic peak at ~0.7 V in all the different binders-based anodic half-cells. This peak is attributed to surface film formation on the electrode. Below 0.2 V, a sharp cathodic current peak is ascribed to lithium-ion intercalation into the graphene layer, consistent with the capacity voltage profile plateau in Figure 6. In the first delithiation cycle, no additional oxidation peak except lithium-ion deintercalation was observed.

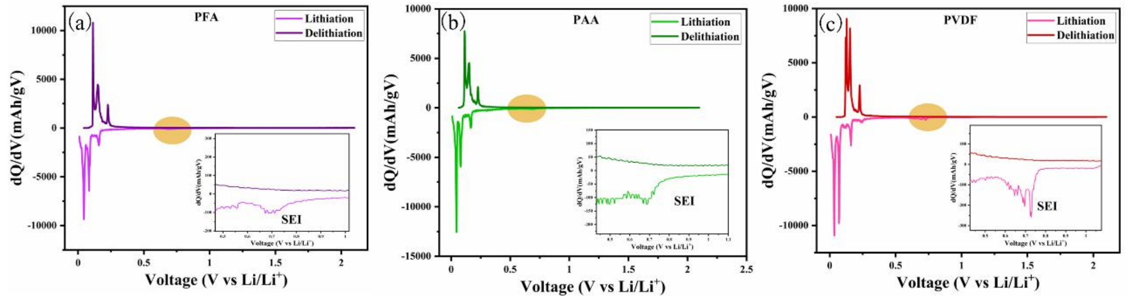

Figure 7: dQ/dV plot of (a) PFA/Gr, (b) PAA/Gr and (c) PVDF/Gr.

Rate capability studies were performed on anodic half cells at different current densities, as shown in Figure 8. The PFA/Gr demonstrated an average discharge specific capacity of 335, 301, 240, 175, 136, 70 mAh g^{-1} at 0.1C, 0.25C, 0.5C, 0.75C, 1C and 2C respectively. Comparative analysis on the influence of binder at varied C-rates indicates that PFA/Gr demostrated greater lithiation/delithiation charge transfer kinetics at higher current densities than PAA/Gr and PVDF/Gr. The average discharge-specific capacity values for PFA/Gr, PAA/Gr and PVDF/Gr in rate studies are summarized in Table 1.

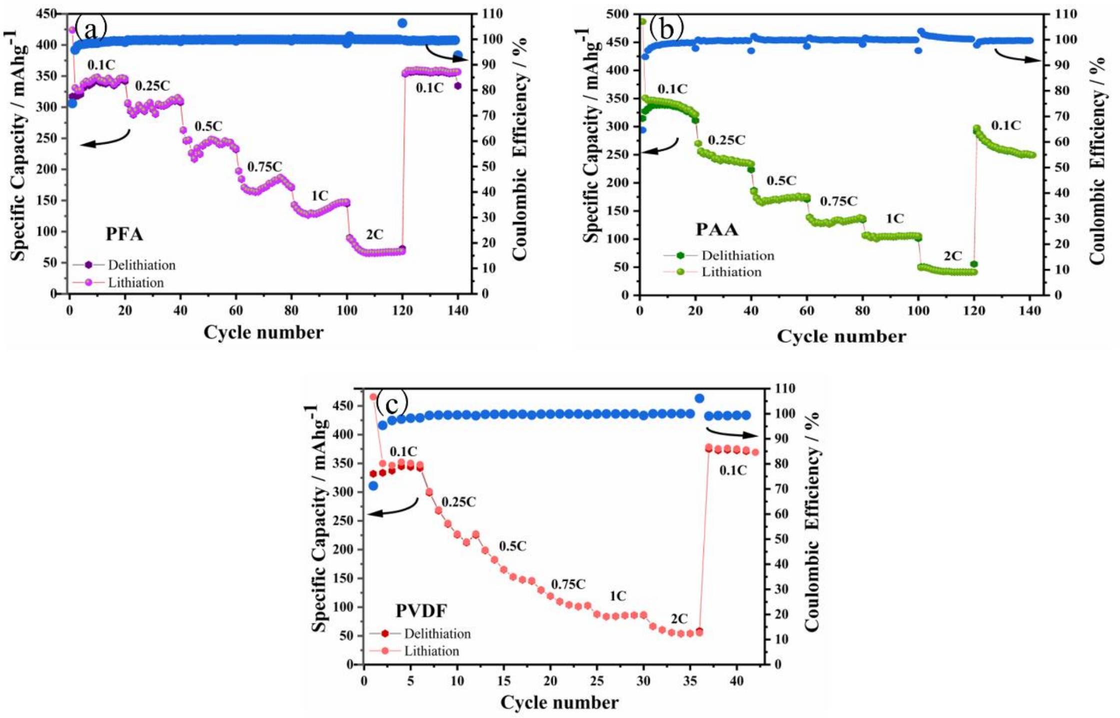

Figure 8: Galvanostatic charge-discharge of (a) PFA/Gr, (b) PAA/Gr and (c) PVDF/Gr at varied current densities.

Table 1: Comparison of average discharge specific capacity at different current densities of the PFA/Gr, PAA/Gr and PVDF/Gr.

Binder/Gr	0.1C	0.25C	0.5C	0.75C	1C	2C
PFA/Gr	335 mAhg^{-1}	301 mAhg^{-1}	240 mAhg^{-1}	175 mAhg^{-1}	136 mAhg^{-1}	70 mAhg^{-1}
PAA/Gr	331 mAhg^{-1}	242 mAhg^{-1}	172 mAhg^{-1}	132 mAhg^{-1}	104 mAhg^{-1}	44 mAhg^{-1}
PVDF/Gr	338 mAhg^{-1}	246 mAhg^{-1}	165 mAhg^{-1}	111 mAhg^{-1}	85 mAhg^{-1}	58 mAhg^{-1}

The investigation into long-term cycle durability investigated for the electrodes with different binders is summarized in Figures 9(a) and 9(b). At a 1C current density, PFA/Gr, PAA/Gr, and PVDF/Gr achieved the highest reversible specific capacity of 325, 251, and

254 mAh g^{-1}, respectively (Figure 9(a)). The high specific capacity attainment of the PFA/Gr suggests that the high concentration of carboxylic acid functional group in the PFA plays a role in providing high ionic conductivity and stronger adhesive force between the active material and the substrate. Such mitigation of volume change during lithiation/delithiation enhances the capacity retention of PFA/Gr with 79% at 710th cycle (calculated with respect to the maximum capacity), compared to 60.4% for PAA/Gr and 72% for PVDF/Gr. The initial decline in specific capacity and subsequent recovery are ascribed to the activation process occurring in graphite, a phenomenon observed in previous works on graphite[201–203]. Interestingly, PFA/Gr attained the maximum capacity in 122 cycles comparable to that of PVDF/Gr, which reached after 140 cycles. In addition, the capacity continuously increases due to further increase in accessible active sites for Li intercalation. This enhancement is attributed to improved Li$^+$ transport to a maximum number of graphite edges, supported by the continuous functional groups in the polymer chain of the PFA binder within the electrode domain, acting as efficient ion channels.

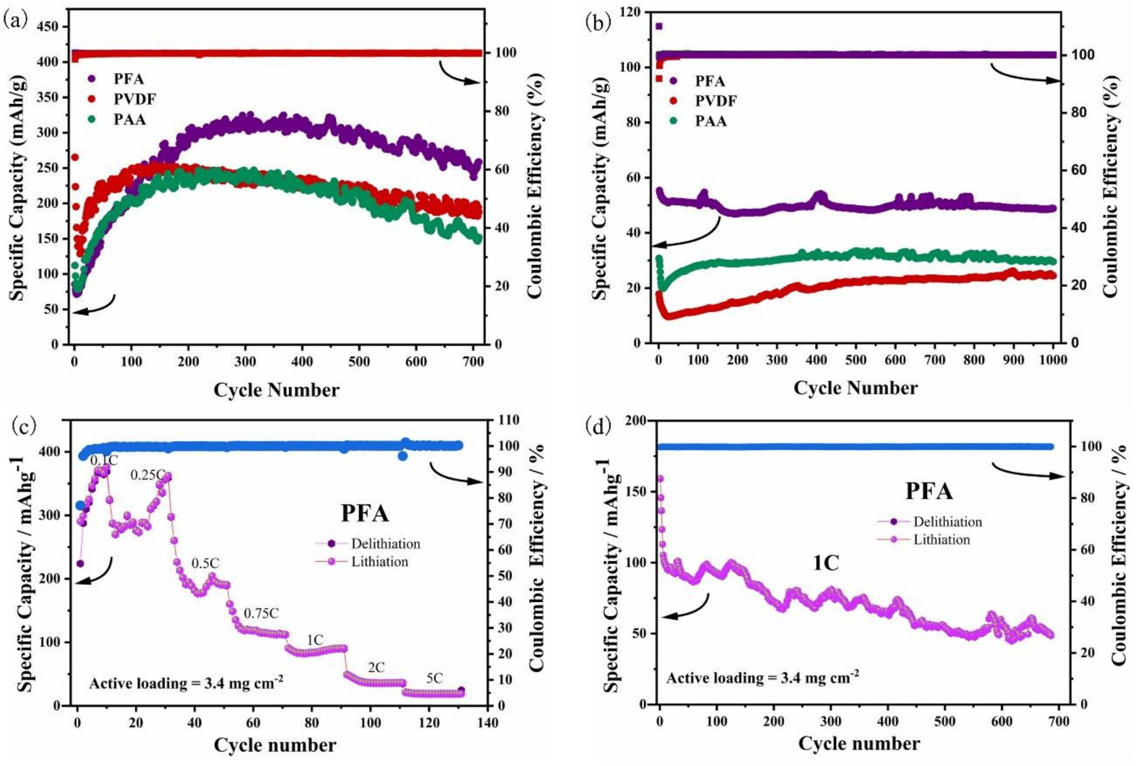

Figure 9: Charge-discharge performance of PFA/Gr, PAA/Gr and PVDF/Gr at (a) 1C, (b) 5C. Galvanostatic charge-discharge of high active mass loading PFA/Gr for (c) rate studies at varied current densities and (d) long cycling at 1C.

Considering the outcomes observed from the electrochemical studies, fast charging and discharging at a 5C rate were studied (Figure 9(b)). The PFA/Gr delivered a maximum reversible specific capacity of 54 mAh g^{-1} for 1000 cycles, outperforming PAA/Gr with 33 mAh g^{-1} and PVDF/Gr with 24 mAh g^{-1}. Thinner SEI and low R_{CT} of PFA/Gr facilitate high Li^+ diffusion and reduce lithiation/delithiation overpotential, increasing the reaction sites and enhancing the fast-charging capability. Even though carboxylic acid groups are present in PAA, the poor electrochemical performance of PAA/Gr can be ascribed to two main factors: (1) The carboxylic acid groups on alternate carbons in PAA do not efficiently act as ion channels for Li^+ transport within the electrode domain, leading to a capacity similar to PVDF/Gr. (2) The strong electrostatic forces and hydrogen bonding in PAA cause powder agglomeration, reducing contact between graphite and conductive carbon, resulting in poor electronic conduction and capacity retention[204]. This effect is not observed in PFA/Gr due to PFA's non-flexible backbone, exhibiting different physical properties than polyethylene-type polymers[136,137]. Fabricating high energy density electrodes is closely tied with the high packing efficiency of graphite sheets, which depends on particle stability and suspension properties[205]. A high loading of 3.4 mg cm^{-2} active mass containing electrode using PFA binder was fabricated for testing its suitability in commercial application. The anodic half-cell was subjected to rate studies at varied current densities and long cycling charge-discharge at 1C current density as shown in Figure 9 (c) and 9 (d) respectively. A good rate capability was shown due to its low activation energy and better SEI formation which nullified the trade-off with high loading, while long cycling displayed good cyclability without any cell failure.

To determine real-time interfacial phenomenon during the lithiation and delithiation process, dynamic electrochemical impedance spectroscopy (DEIS) was studied after cycling the anodic half-cell at 1C. This technique measured impedance at a potential range of 0.01-2.1 V and frequency range of 0.01 Hz-1.0 MHz. All the DEIS profiles of anodic half-cells with different binders are portrayed in Figure 10. The impedance values were obtained by fitting impedance data to an equivalent circuit. The circuit $R_{int}L(XR_{CT})(XR_{SEI})(QW)$ was used wherein R_{int} is internal resistance, R_{CT} is charge transfer resistance, R_{SEI} is SEI resistance, W is Warburg diffusion coefficient and X equals Q (constant phase element) or C (capacitance). The lithiation and delithiation plots of R_{SEI} against potentials as shown in Figure 11, reveal a lower impedance of SEI in the case of PFA/Gr compared to PAA/Gr and PVDF/Gr in the potential range of 0.01-0.8 V at which maximum lithiation/delithiation takes place.

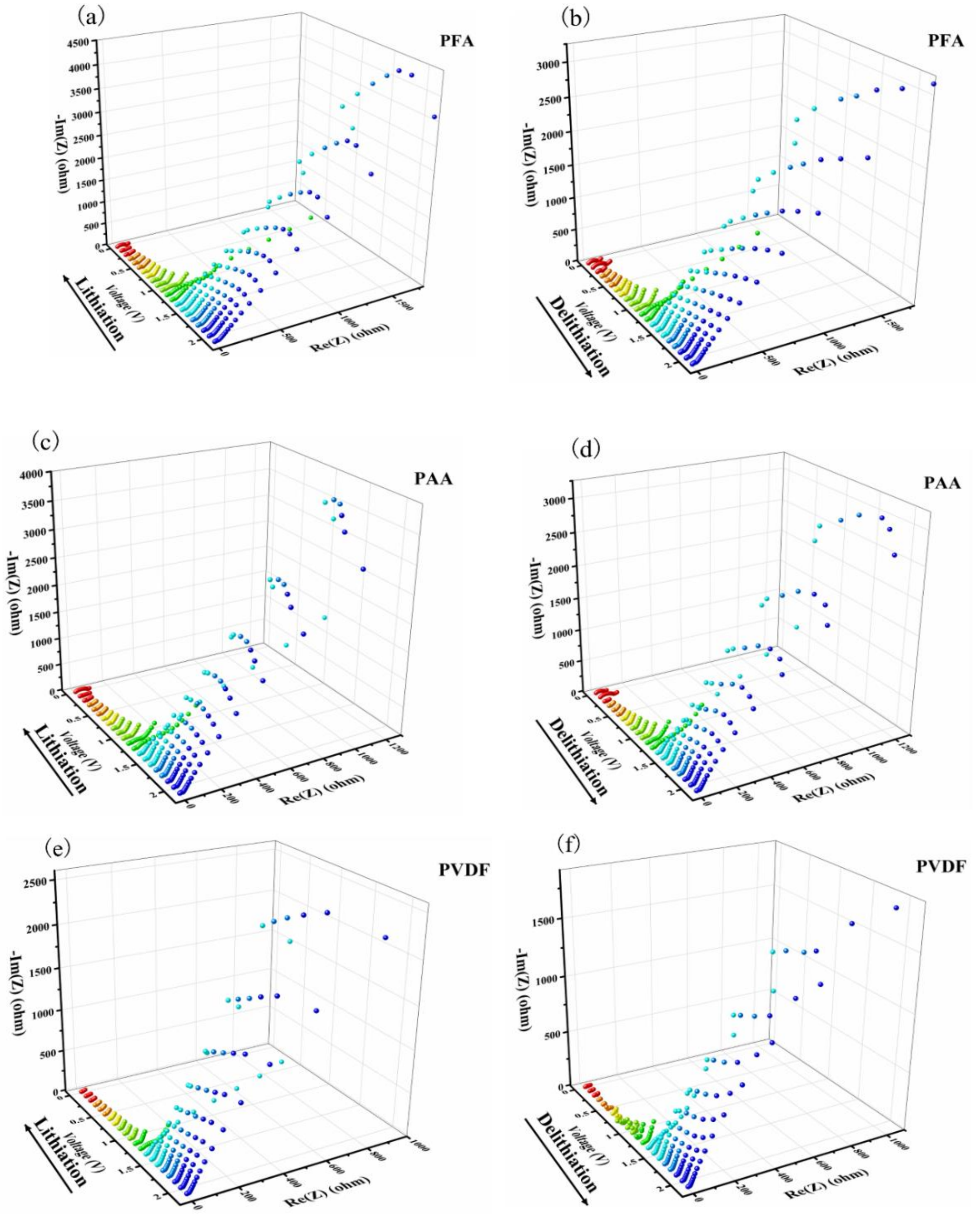

Figure 10: DEIS profiles of PFA/Gr, PAA/Gr and PVDF/Gr during (a), (c), (e) charging and (b), (d), (f) discharging.

This confirms the formation of thin and efficient lithium-ion conducting SEI, which was also justified by lower activation energy at lithiation and better reversible capacity and performance by the PFA/Gr. We see fluctuation in the R_{SEI} value between 0.8-2.1 V at which no intercalation/deintercalation occurs, which might be due to interface dynamics at varied voltage. Despite PVDF/Gr interfacial resistance being only slightly higher than PFA/Gr in the lithiation/delithiation potential range, its galvanostatic charge-discharge performance is poorer compared to PFA/Gr. This trend can be justified by considering that R_{SEI} is not the only factor influencing the specific capacity of an electrode. Other factors, such as binder's facilitation in Li^+ transfer within electrode and activation energy for Li^+ desolvation, need to be considered, as these are lower in the case of PVDF/Gr.

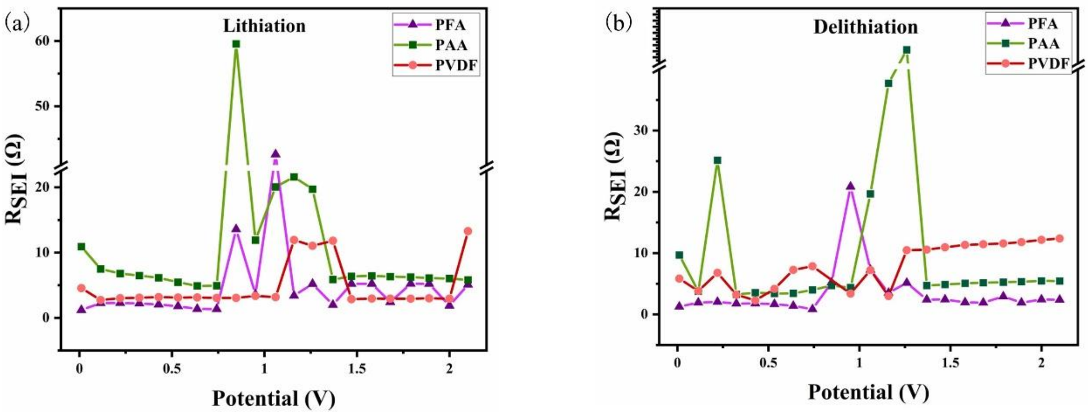

Figure 11: R_{SEI} vs. potential of anodic half-cell consisting of different binders (a) lithiation, (b) delithiation.

Post-mortem studies such as XPS and SEM were conducted to understand the SEI composition formed while cycling and the impact on electrode morphology after cycling respectively. To obtain an insight into the surface chemistry of the cycled electrodes due to the decomposition of electrolytes and formation of SEI, XPS analysis was performed. The F1s spectra confirm the presence of Li_xPF_y and LiF in the PFA and PAA binder-based electrodes which were derived from the $LiPF_6$ salt (Figure 12 (a_1) and (a_2)). While F 1s spectrum of the PVDF binder-based electrode showed the presence of Li_xPF_y and C-F (Figure 12 (a_3)). The C-F peak was from the PVDF exposed due to cracks on the surface of the electrode. It is also hard to dissolve even at high temperatures, porous to only lithium-ion and resists further electrolyte attacks[166,206]. In the C1s spectra, species such as C-C/C-H, C-O, C=O and Li_2CO_3 were observed on all the different binder-based electrodes, which is attributed typically to the decomposition of organic solvent (Figure 12 (b)). Compared to PFA and PAA binder-based electrodes, the PVDF binder-based electrode shows higher peak intensity for all the organic species (e.g., C-O, C=O and Li_2CO_3)[207]. Moreover, the LiC peak observed in C 1s of PVDF electrode is from the presence of Li intercalated compound on the surface of graphite electrode[208]. In the O1s spectrum (Figure 12 (c)), the peak located at ~531.8 eV is assigned to Li_2CO_3 which is present in all the different binder-based electrodes. PVDF binder-based electrode exhibits a high fraction of Li_2CO_3 possibly due to severe electrolyte decomposition. It is reasonable to conclude that high-density functional carboxylic acid group-based binder induces enhanced electrode stability and suppresses electrolyte decomposition compared to PVDF binder during repeated volume expansion and contraction.

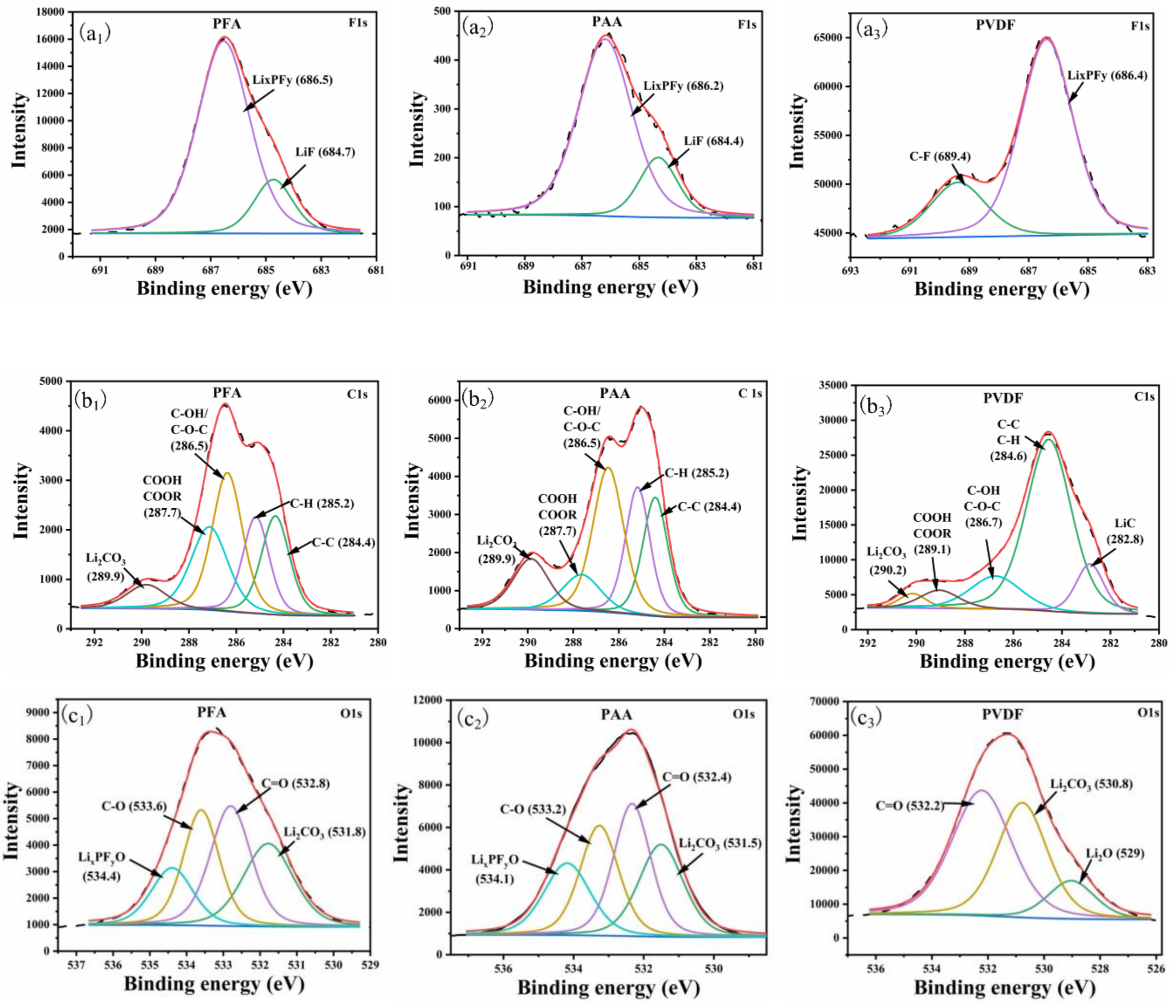

Figure 12: Characterization of the SEI compositions on cycled graphite electrodes by XPS. (a) F 1s, (b) C 1s and (c) O 1s are XPS profiles of the cycled PFA/Gr, PAA/Gr, and PVDF/Gr electrodes.

The surface morphology of the pristine and cycled electrodes with PFA, PAA and PVDF binder were investigated using scanning electron microscopy. All the electrodes containing different binders are observed to have good integrity of electrode components in pristine electrodes with porous morphology (Figure 13(a_1), (b_1), (c_1)). The cycled PFA binder-based electrode surface shown in Figure 13 (a_2), (a_3) did not show a significant difference compared to the pristine electrode. The smooth surface and absence of cracks on the PFA binder-based electrode indicates the formation of uniform and stable SEI layer without further slow continuous electrolyte reduction. The SEM images of PAA (Figure 13 (b_2), (b_3)) and PVDF (Figure 13 (c_2), (c_3)) binder-based electrodes indicate multiple cracks compared with the pristine electrodes. The cracks might be formed due to weak interaction and holding capacity of the binder with the graphite and conductive carbon leading to failure in preventing volumetric changes in the graphite during lithiation/delithiation. This led to slow electrolyte decomposition and the formation of thick SEI, which was also justified by R_{SEI} and XPS. The presence of cracks in PVDF has exposed the intercalated lithium on the graphite surface, as observed by the presence of LiC peak in XPS spectra. Cross-sectional studies of the cycled electrodes were obtained as shown in Figure 13 (a_4), (b_4), and (c_4). PAA and PVDF binder-based electrodes exhibit poor integrity within the electrode material and with the current collector. The PFA binder-based electrode has maintained the electrode intact without any change in morphology, possibly due to the dense functional groups and the less flexible backbone of binder helping to form hydrogen bonding and strong interaction with the copper current collector. Thus, PFA exhibited excellent binding performance during the extended cycling.

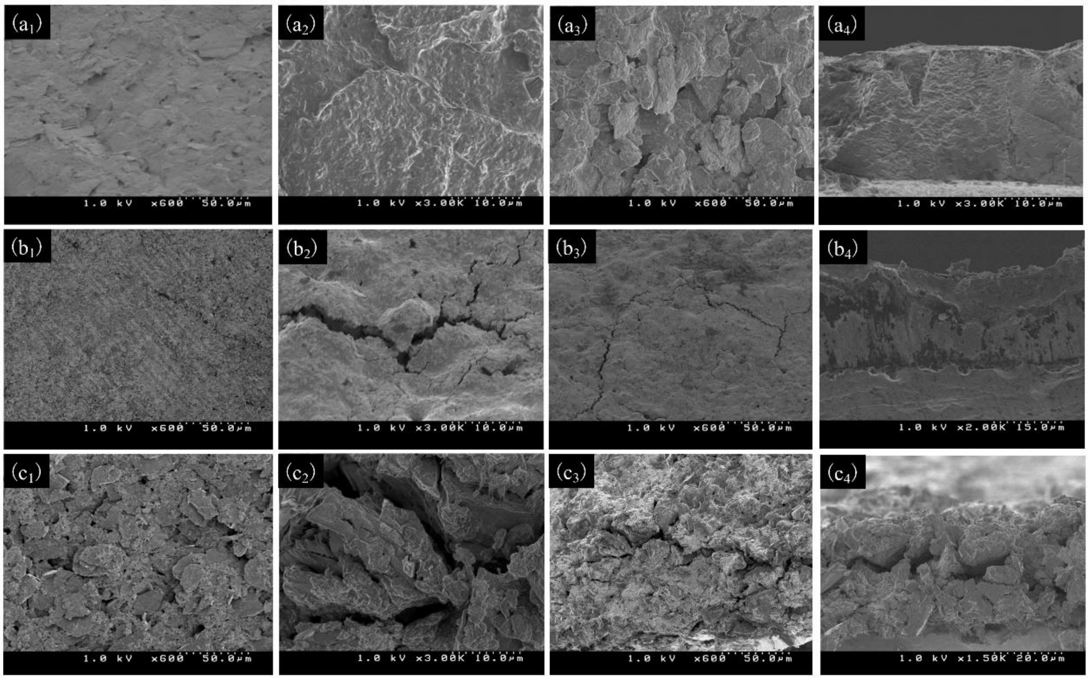

Figure 13: Morphological characterization of graphite electrodes with different binders of pristine and after cycling. Top-view SEM images of (a_1) PFA/Gr, (b_1) PAA/Gr, and (c_1) PVDF/Gr pristine electrodes. Top-view SEM images of (a_2) (a_3) PFA/Gr, (b_2) (b_3) PAA/Gr, and (c_2) (c_3) PVDF/Gr electrodes after long cycling at 1C. Cross-sectional SEM images of (a_4) PFA/Gr, (b_4) PAA/Gr, and (c_4) PVDF/Gr electrodes after long cycling at 1C.

PFA, as a binder, significantly enhances cell performance by promoting Li^+ transport across electrode domain and interfacial layer due to its dense and continuous polar carboxylic acid functional groups along the polymer chain. Its non-flexible backbone prevents powder agglomeration, promoting strong bonds with the current collector and electrode material for improved capacity retention. The polar carboxylic acid groups also influence SEI formation by facilitating inorganic species deposition, preventing continuous electrolyte degradation and crack formation. Table 2 presents comparative studies of the electrochemical performance of PFA/Gr with various water-soluble binders containing -OH and -COOH functional groups for graphite anodes.

Table 2: Electrochemical performance comparison of PFA/Gr and other binders reported for graphite anode.

Binders	Discharge capacity (mAh g^{-1})	Current density	Reference
PFA/Gr	325 54	1C 5C	this work
CMC-Na	~200	1C	[209]
Na-Alginate	~110	1C	[209]
Gelatin	~190	1C	[209]
Li-PAA	102	1C	[163]
PAA/Gr	~250	1C	[210], this work
Acryl S020	~166	1C	[211]
AMAC	~210	0.5 mA/cm	[212]
PAA/CMC/SBR	~150	0.5C	[213]
Guar gum	124	1C	[214]
PVDF	~250	1C	[215], this work

Conclusion:

In this study, a novel route for synthesis was executed for obtaining poly(fumaric acid) that attempts to address the cost and use of hazardous chemicals while maintaining the functionality of the polymer. The utilization of poly(fumaric acid) provides enhanced rheology, such as high viscosity and high peel strength that is beneficial towards better lamination of graphite anodes, adversely impacting electrochemical performances. Polymethylene-based polymer's decreased flexibility and its higher concentration of carboxylic acid than polyethylene-based polymers have been shown to offer better lithium-ion diffusion kinetics from studies such as impedance spectroscopy (R_{CT}), activation energy and diffusion coefficient. PFA-based anodic half-cells achieved better rate capability at varied current densities. Moreover, at 1C long cycling galvanostatic charge-discharge, a reversible specific capacity of 336 mAh g^{-1} was achieved with remarkable capacity retention of 81% for more than 700 cycles. PFA/Gr exhibited enhanced fast charging performances at 5C with reduced polarization and stabilized coulombic efficiency, leading to attaining a specific capacity of 54 mAh g^{-1} with a charging time of 1.5 mins. Furthermore, DEIS studies have shown a low R_{SEI} value in the lithiation and delithiation voltage region which helps Li^+ easily pass into the electrode. Postmortem studies confirm the formation of thin SEI on the electrode surface of PFA/Gr from the XPS and SEM without any exfoliation and cracks. Concomitantly, our work on high-density functional group polymer binder has shown to be environmentally friendly. It exhibits better long cycling, fast charging and high-loading charging/discharging electrochemical performance in lithium-ion batteries. Hence further work on polymethylene-based high-density functional group polymer binders will open the door for better rechargeable high-energy battery applications.

Chapter 4

Water soluble densely functionalized poly(hydroxycarbonylmethylene) binder for higher performance of hard carbon anode-based sodium-ion batteries

Abstract

A promising anode material in developing sodium-ion batteries (SIBs) has been hard carbon(HC). Due to diminish ion diffusion kinetics, low initial coulombic efficiency (ICE) and continuous electrolyte decomposition, HC based SIBs led to sluggish rate capability and specific capacity. Herein, we utilised a dense functional groups polymer containing carboxylic acid at side chains as a binder that demonstrates ion transport, defect passivation and better mechanical stability. The consecutive polar functional groups provide ion transfer channels and enhanced adhesion to electrode components. Poly(hydroxycarbonylmethylene) (PFA) binder for HC electrode achieved the highest ICE of 80.8 % and specific capacity of 288 mAh g^{-1} and 254 mAh g^{-1} at 30 mA g^{-1} and 60 mA g^{-1} respectively which are superior to HC electrode containing PAA and PVDF binders. Anodic half-cells containing PFA binder showed high capacity retention of 85.4 % (250 cycles) and 91.6 % (200 cycles) at current densities of 60 mA g^{-1} and 30 mA g^{-1} respectively. In addition, the presence of dense polar groups boosted the diffusion kinetics and lowered the Na^+ activation energy. XPS and SEM studies have further verified that dense functional groups influence the formation of thin, stable and inorganic-rich SEI and crack-free electrodes. Therefore, dense functional group polymers will help in the early adoption of SIBs in the market.

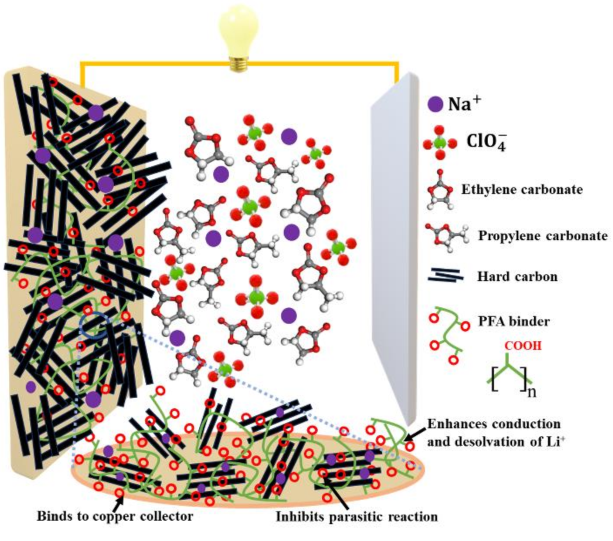

Introduction:

The growing demand for energy storage systems has led to the search for low-cost and abundant resources-based rechargeable batteries[173]. SIBs have become a promising alternative to lithium-ion batteries[162], potassium ion batteries[216] and zinc ion batteries[217] due to unlimited sodium resources in seawater and salt deposits[13,216] and safe shipping at 0 V when Al is used as current collector on anode[218]. Moreover, the chemistry of lithium and sodium is similar; sodium is the lightest and smallest alkali metal after lithium[219]. The key components of SIBs explored in the last decade are positive electrodes (transition metal oxides[220,221], Prussian blue analogues[222,223]), negative electrodes (hard carbon[224] (HC), TiO_2 polymorphs[225], Na-Sn alloy system[226]) and electrolytes, to deliver long cycles and stable and thin solid electrolyte interface (SEI). A promising anode for practical application has been hard carbon, however, it suffers from commercialisation due to low ICE and poor rate capability in traditional organic electrolytes[227]. It was observed that defect-rich hard carbon leads to the formation of uneven, thick and poor mechanical strength SEI due to increased electrolyte consumption, which lowers cycling stability and reaction kinetics[228–233]. Much research was focused on electrolytes[234], defects optimization and introducing oxygen functional groups in HC[235], artificial SEI[236,237], presodiation[238], HC/MoS_2/NC nanocomposite[239] etc., to obtain a stable, uniform, and thin SEI. However, such methods are complicated and challenging for large-scale applications. Therefore, a need for a solution that is easy, low-cost and can be considered for practical application in SIBs.

The influence factors of the electrochemical performance of HC depend on electrolyte composition and concentration, active materials properties, choice of binders, electrode morphology, operating conditions, cycling rate, electrolyte additives, electrolyte solvent choice, interface stability and passivation layer composition[226,240–242]. Concerning binders, they play an essential role in the mechanical integrity of anode material's adhesion, impedance, cycling stability and SEI formation[164,165,194]. At the same time, functional binders participate between the metal ion-solvated structures and interfaces, which affects the decomposition of ester electrolytes and induces SEI formation compositions[243,244]. The factor affecting the dynamic performance of SIBs is the desolvation kinetics, wherein, reducing the energy barrier of sodium ions from the solvated sphere will help form stable SEI and initiate faster Na^+ transport[245,246]. However, a few papers on functional binders have been reported for HC in SIBs. Komaba et al. reported that sodium carboxymethyl cellulose (CMC) demonstrated superior binding, reversibility and cycling ability compared to poly(vinylidene fluoride) (PVDF) binder. Surface analysis revealed a different surface and passivation chemistry due to the presence of carboxylate polyanion in the CMC binder which improves the sodiation reversibility. Whereas, Monofluoroethylene carbonate as an electrolyte additive is essential for PVDF electrodes to improve cyclability[247]. Li et al. demonstrated a trifunctional SA/PEO binder exhibiting a better rate capability and cycling stability with higher ICE than traditional PVDF binder. The structural design of SA/PEO binder leads to the formation of uniform SEI film which inhibits slow continuous electrolyte decomposition. The ionic SA/PEO enhances the diffusion kinetics of Na^+ by reducing impedance and facilitating ion transport[248]. Naylor et al. reported a sustainable biopolymer LgSA binder for HC in SIBs[249]. They fabricated full cells with prussian white cathode, which showed better cycling stability for 40 cycles with 122 $mAhg^{-1}$ specific capacity at 60 mA g^{-1} in 1M $NaPF_6$ EC:DEC electrolyte. This might be due to the functional group (sodium sulfonate) present in lignin polymer which helps form stable and uniform SEI and affects the diffusion kinetics of Na^+. Shen et al. reported using a composite binder consisting of chondroitin sulfate A and polyethylene oxide for HC in SIB. The anodic half-cell exhibits 84% ICE and long cyclability with 94% retention capacity for 150 cycles at 50 mA g^{-1}. The $-SO_3$- and -CO-NH- functional groups of the chondroitin sulfate A are involved in the fast transportation of Na^+, reducing electrolyte decomposition and helping in formation of inorganic-rich SEI[250]. Trivedi et al. reported use of inorganic binders such as $(NaPO_3)_3$, $(NaPO_3)_6$ and $(NaPO_3)_n$ in HC electrode showed better capacity than organic binders due to enhanced electronic and ionic conductivity[242]. These binder studies have indicated that not only do functional groups form good coordination with hard carbon, but also reduce electrolyte consumption, and build better SEI than PVDF[251]. However, there are no studies on countering the poor rate capability and specific capacity owing to the slow Na^+ diffusion kinetics and facilitating Na^+ transmission by providing ion channels. Therefore, there is an urgent need for a dense functional group binder to improve the electrochemical rate capability performances by influencing the surface chemistry of SEI and enhancing the Na^+ transport in the electrode domain.

Herein, we propose using polymethylene-based polymer poly(hydroxycarbonylmethylene), also known as poly(fumaric acid) (PFA), as a dense carboxylic acid functional group polymer binder. PFA is synthesised through a novel synthetic route using precursor diethyl fumarate that uses cost-effective and non-hazardous chemicals[189]. Diethyl fumarate can be obtained from biomolecule fumaric acid, a product of the citric acid cycle in mitochondria and isolated from plants and fungi[186–188]. In contrast, PVDF synthesis involves using costly fluorinate precursors, which affects the environment. PAA and styrene-butadiene rubber require acrylic acid and styrene-butadiene monomer from petrochemical sources, impacting sustainability, environment and cost-effectiveness[252–254]. Polymethylene-based polymers are less flexible at their polymer backbone and expected to show different properties than polyethylene polymers[136,137]. PFA as a binder can passivate the hard carbon’s surface defects through hydrogen bonding between the binder's dense carboxylic acid polar functional group and the oxygen functional group present on the surface defects of HC. Thereby preventing the defects from being exposed to electrolytes due to more functional groups covering the defects and reducing the ability of the defects to decompose the electrolyte and form thick SEI[250]. Moreover, cross-linkable and intermolecular hydrogen bonding hybrid binder has shown stable electrode-electrolyte interphase, increased ionic conductivity, prevented electrolyte decomposition, mitigated transition metal dissolution and enhanced rate capability[255]. The polar carboxylic functional group could interact with the Na^+ and reduce the activation energy of sodium ions from the solvation sphere[256,257]. PFA binder offers water solubility and non-toxicity compared to PVDF binder which requires N-methyl-2-pyrrolidone, a hazardous and expensive organic solvent[258]. At the same time, the carboxylic acid group provides better adhesion with the electrode material through hydrogen bonding, ion-dipole and chemical bonds which is absent in PVDF as it contains an inactive C-F functional group[259]. Introducing functional groups at every carbon of the polymer chain can provide a directional Na^+ transmission path and thereby counter the sluggish diffusion kinetics of Na^+ due to its large ionic radius and atomic mass[260]. Furthermore, the dense carboxylic acid groups will reduce the agglomeration effect due to electrostatic repulsion, which makes the binder wet and uniformly covers the hard carbon particle's surface[248,261]. PFA’s binder performance was evaluated using cyclic voltammetry, Impedance and galvanostatic charge-discharge against PAA and PVDF. In addition, the impact of binders on rheology and surface chemistry of electrodes was investigated. Our findings offer a new perspective on choosing a binder that sheds light on the charge-discharge mechanism and interfacial Na^+ transport.

Experimental:

Preparation of PFA polymer:

The PFA was prepared from ester hydrolysis of poly(ethoxycarbonylmethylene). poly(ethoxycarbonylmethylene) was derived from radical bulk polymerisation of diethyl fumarate (Sigma-Aldrich, 98%) in a vacuum Schlaker reaction tube using 2,2'-azoisobutyronitrile (AIBN, Sigma-Aldrich, >98%) as radical initiator at 70 °C for 24 hr. It was further purified by washing with excess hexane and dried overnight under vacuum. Poly(ethoxycarbonylmethylene) was base hydrolysed using an excess of KOH (Wako) in an EtOH:H_2O (2:1) solvent mixture under reflux[262]. After hydrolysing, the mixture was acidified using 1N HCl (Sigma-Aldrich, 12N) and dialysed using a cellulose acetate tube (Fisherbrand). Water was evaporated from aqueous polymer after dialysis to obtain PFA. The yield of PFA was 82% with respect to diethyl fumarate.

Electrode preparations:

Hard carbon (Kuranode Type 2 (5 µm), Kuraray), Super P carbon (Alfa Aesar, 99+%) and PFA were mixed in water at a weight ratio of 80:10:10 to obtain a homogenous slurry. The slurry was cast onto copper foil and dried overnight. The coated copper was calendared and punched into 13 mm-diameter discs. CR-2025 coin cells were assembled using the obtained HC electrode as anode, sodium metal disc as the counter electrode, glass fibre from Whatman as separator and 1M $NaClO_4$ in EC:PC (1:1, by vol.) as an electrolyte in an argon-filled glove box with O_2 and H_2O levels < 0.5 ppm. Before electrochemical measurements, the coin cells were kept at rest to allow them to reach open circuit voltage for 24 hr. Various weight percentages (wt%) of PFA binders (3, 5 and 15 wt%) along with corresponding HC amounts, keeping wt% of super P carbon at 10%, were fabricated. In addition, PAA (polyacrylic acid, Sigma-Aldrich) and PVDF (Sigma-Aldrich, MW: 540,000) binders were used for HC electrode using the above procedure and CR2025 coin cells were fabricated for comparative studies.

Characterization:

PFA was characterized using ^1H NMR, and ^{13}C NMR using Bruker Advance II-400 MHz spectrometer in D_2O solvent. FT-IR was performed using PerkinElmer 100 FT-IR spectrometer. Thermogravimetric analysis (TGA) was recorded using instrument Hitachi STA7200 at 10 °C min^{-1} heating rate under 200 ml min^{-1} N_2 flow rate. The rheology of the HC-coated electrode was tested using a peel test (Instron 3342). Galvanostatic charge-discharge was tested using Electrofield ABE 1024 in the 0.01-2.5 V Vs. Na/Na$^+$ voltage range. Cyclic voltammetry (CV) measurements were performed on Bio-Logic Science Instruments with scan rates of 0.1, 0.2, 0.4, 0.6, 0.8 and 1 mVs^{-1}. The electrochemical impedance spectroscopy (EIS) measurements were tested in the frequency range from 1.0 MHz to 0.1 Hz with an AC amplitude of 10 mV. Using the EIS method, the cycled electrodes were further used for dynamic electrochemical impedance spectroscopy (DEIS) measurement and activation energy evaluation at different voltage perturbations and temperatures respectively. Postmortem studies were carried out for the surface morphology structure and elemental composition distribution of prolong cycled HC using a scanning electron microscope (SEM, Hitachi S-4500) and X-ray photoelectron spectroscopy (XPS, Fisons instruments S-probe TM 2803) respectively.

Results and discussion:

A highly dense functional group polymer binder, PFA was utilised based on the desired physicochemical properties such as better adhesion, self-healing ability, rate capability and ionic conductivity in SIBs. The reaction method for synthesising PFA utilising radical bulk polymerisation and base-catalyzed ester hydrolysis is depicted in Figure 1(a).

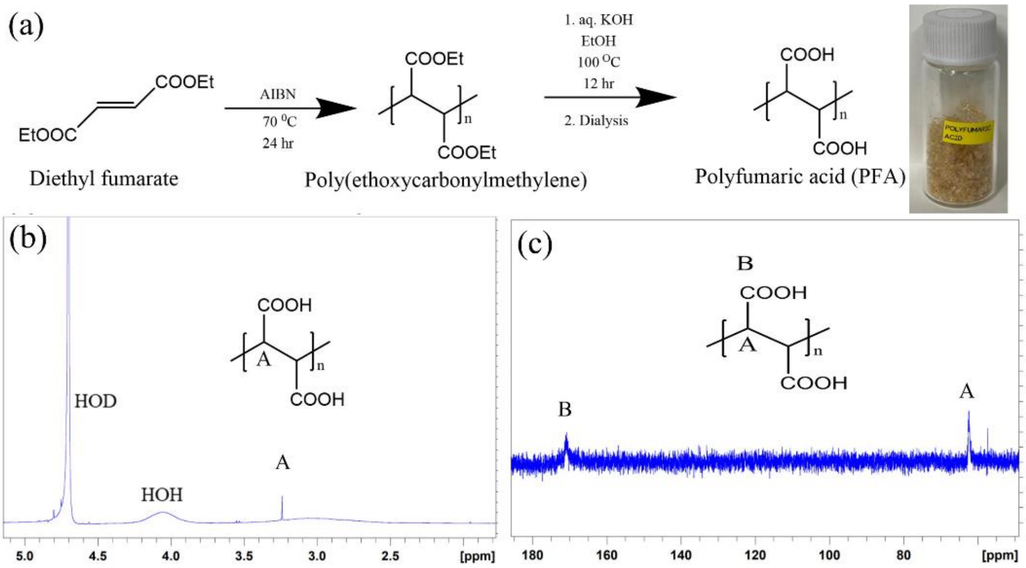

Figure 1: (a) Schematic representation of the syntheses of poly(fumaric acid). (b) ^{1}H NMR spectrum (D_2O), (C) ^{13}C NMR spectrum (D_2O).

To examine the purity of the PFA obtained, NMR and IR analyses were executed. Figure 1 (b) shows that the peak at 3.25 ppm of ^{1}H NMR spectra corresponds to the polymer chain's methylene proton and is consistent with the reported literature. In ^{13}C NMR spectra (Figure 1 (c)), the peaks at 170.8 ppm and 62.4 ppm were assigned to the carbonyl of carboxylic acid and methylene carbon respectively. Further, PFA was confirmed by FT-IR spectra, as observed in Figure 2(a). The strong board peak at 3500 cm^{-1} is attributed to the O-H stretching vibration of carboxylic acid. The 1715 and 1090 cm^{-1} peaks are assigned to carboxylic acid's carbonyl and ether peaks. The MALDI-TOF data reveal the molecular weight of the PFA polymer to be 3000 m/z (Figure 2(b)). The pH of the polymer is determined to be pH 4.5 as shown in Figure 2(c). The thermal stability analysis of PFA was evaluated using TGA. Figure 2(d) shows the TG and DTG profiles of PFA. The initial weight loss at ~100 ^{O}C corresponds to vaporization of moisture absorbed by the hydrophilic carboxylic group. PFA is shown to be stable up to ~235 ^{O}C, after which a steep degradation slope is observed, making it suitable as a binder for high-temperature SIB. These observations reveal that the PFA polymer was formed through the new synthetic route undertaken.

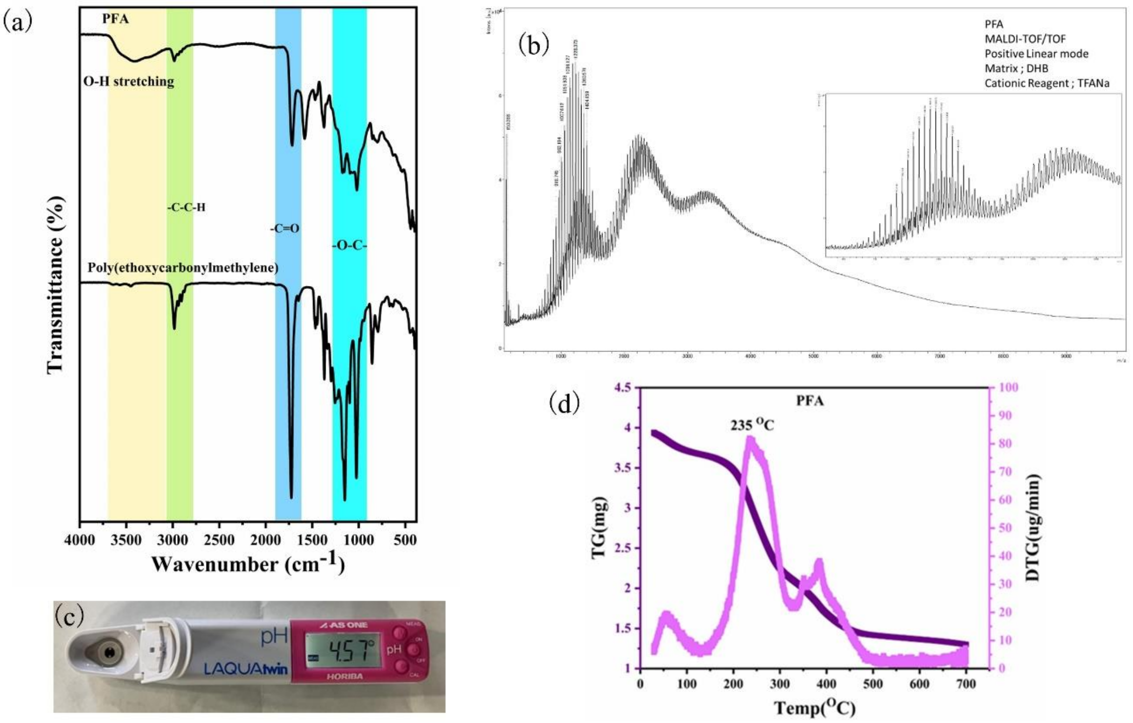

Figure 2: (a) FT-IR spectra of PFA and poly(ethoxycarbonylmethylene). (b) MALDI-TOF of PFA. (c) pH measurement of PFA using pH meter.

The peeling test was performed to test the binder effect on adhesion between electrode components and the current collector. For a better cycle life of SIBs, a stronger adhesion force of electrode material to copper is needed. The peeling force vs. displacement curves are shown in Figure 3. The peeling force of the PFA binder-containing HC electrode was 12.5 N, which was higher than PAA (11.5 N) and PVDF (9.8 N) electrodes due to the dense amount of -COOH groups present in PFA. PAA and PVDF have low carboxylic groups and no polar group for binding to copper respectively which lead to poor adhesion capability. The tape in the inset exposes the amount of HC peeled from the peel tests, indicating a better binding of PFA to copper and exposes a severe amount of HC sticking onto the tape containing PAA and PVDF binder.

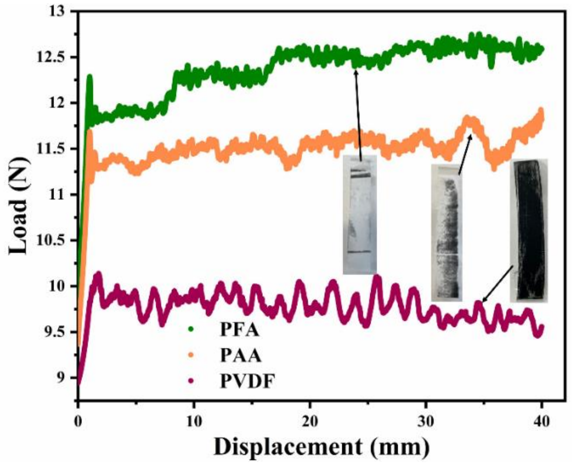

Figure 3: Force vs. displacement profiles of peel test for coated electrode with varied binders.

To determine the influence of binders on electrochemical performances, CV and galvanostatic charge-discharge studies were conducted. HC-based anodic half cells using PFA, PAA and PVDF binders are named PFA/HC, PAA/HC and PVDF/HC, respectively. $NaClO_4$ in EC-PC (1:1) is used as an electrolyte for our studies because of its better cycle performance among various electrolyte solutions for HC reported by Ponrouch et al.[241], as also confirmed by the studies of Komaba et al.[226,263]. In addition, PC doesn't co-intercalate with Na^+ due to unique structure of HC containing defects, nanovoids and random graphene layer orientation, which restrains graphene layer exfoliation[264]. All the CV curves of anodic half cells reveal that the board cathodic peak observed between 0.3 V and 1.0 V in the first cycle is ascribed to the decomposition of electrolyte and SEI formation (Figure 4 (a), (b), (c)). The second and third curves reveal no large additional irreversible electrolyte consumption, and an SEI film is only in the first cycle. The two main redox peaks at ~0.01 and ~0.3 V correspond to intercalation and deintercalation of

Na$^+$ in HC. Considering the batteries' overpotential due to internal and interfacial resistances is also necessary. The CV profiles at different potential rates showed overpotentials of 0.200 V, 0.221 V and 0.237 V for PFA/HC, PAA/HC and PVDF/HC respectively. Suggesting PFA/HC has less over potential than PAA/HC and PVDF/HC due to the presence of dense polar groups on the surface and in the electrode domain which is helpful for facile sodium ion transport. In addition, it prevents continuous side reactions between the electrolyte and active material[194,265].

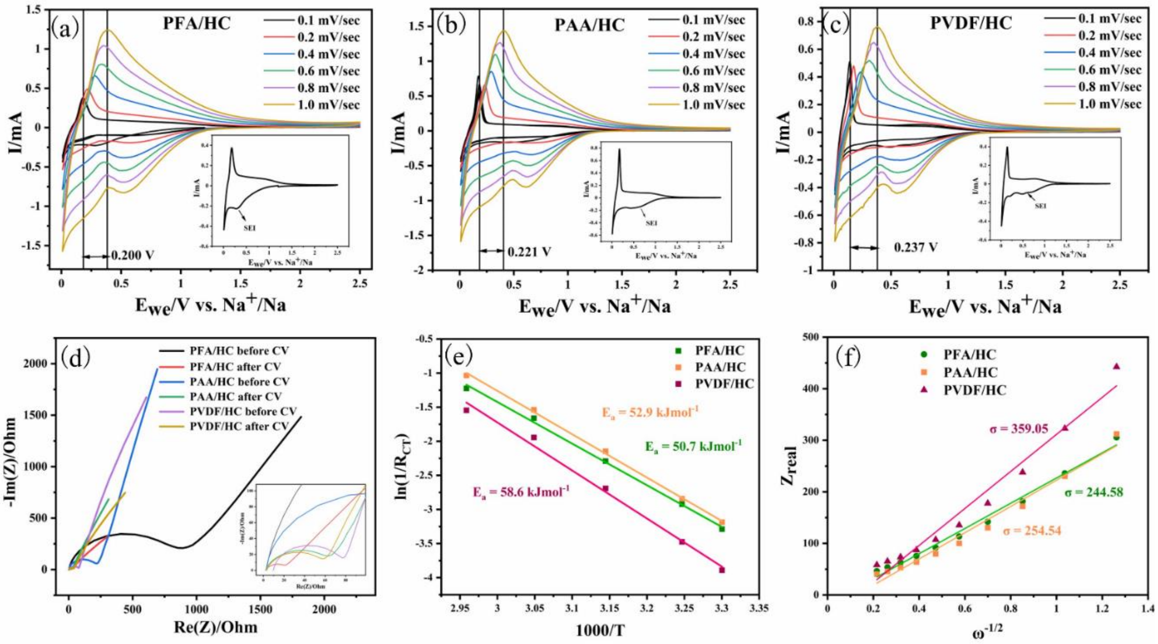

Figure 4: Cyclic voltammograms (CV) curves of (a) PFA/HC, (b) PAA/HC and (c) PVDF/HC. Inset CV at 0.1 mV/sec. (d) EIS profiles before and after CV of PFA/HC, PAA/HC and PVDF/HC. (e) Arrhenius plots at various temperatures. (f) Warburg plots are deduced from the low-frequency portion of Figure 3(d).

Furthermore, to investigate Na$^+$ storage kinetics in HC anode and SEI layer formation during cycling, electrochemical impedance spectroscopy (EIS) was performed. The Nyquist plots of before and after CV are depicted in Figure 4 (d). The charge transfer from the electrolyte into the active material through SEI is in the mid-frequency range (~1 kHz-10 mHz), represented by a semicircular arch in the impedance spectrum154. The smaller semicircle diameter corresponds to low charge transfer resistance (R_{CT}). All the anodic half-cells showed lower charge transfer resistance after the CV impedance than the before CV cycle impedance. The SEI formed shows the lowest R_{SEI} (18.1 Ω) and R_{CT} (673.4 Ω) in PFA/HC compared to PAA/HC (R_{SEI}=22.3 Ω, R_{CT}=4051 Ω) and PVDF/HC (R_{SEI}= 31.6 Ω, R_{CT}=412.2 Ω) by circuit fitting of EIS using RL(QR)(QR)W after CV cycles. This implies that the dense carboxylic acid might influence the formation of a thin SEI layer on the surface of the HC electrode consisting of PFA binder and will enhance the sodium-ion transport process across the electrode-electrolyte interface. To understand the effect of binder on Na^+ desolvation and ion crossing in the SEI, activation energy was calculated from the following equation.

$$\mathrm{Ln}(\sigma) = \ln(\mathrm{A}) - \frac{E_a}{R}\left(\frac{1}{T}\right) \ldots eq(1)$$

Where σ corresponds to conductivity or R_{CT}^{-1}, A denotes pre-exponential entropic factor, R is gas constant (8.314 $JK^{-1}mol^{-1}$), E_a denotes activation energy and T is temperature. According to Arrhenius's law, the activation energies of the anodic half-cells were calculated from the R_{CT} obtained from circuit fitting of the EIS measured at different temperatures using R(QR)(QR)W (Figure 4 (e), Figure 5). The activation energy of PFA/HC is 50.7 $kJmol^{-1}$, which is lower than PAA/HC (52.9 $kJmol^{-1}$) and PVDF/HC (58.6 $kJmo^{-1}$).

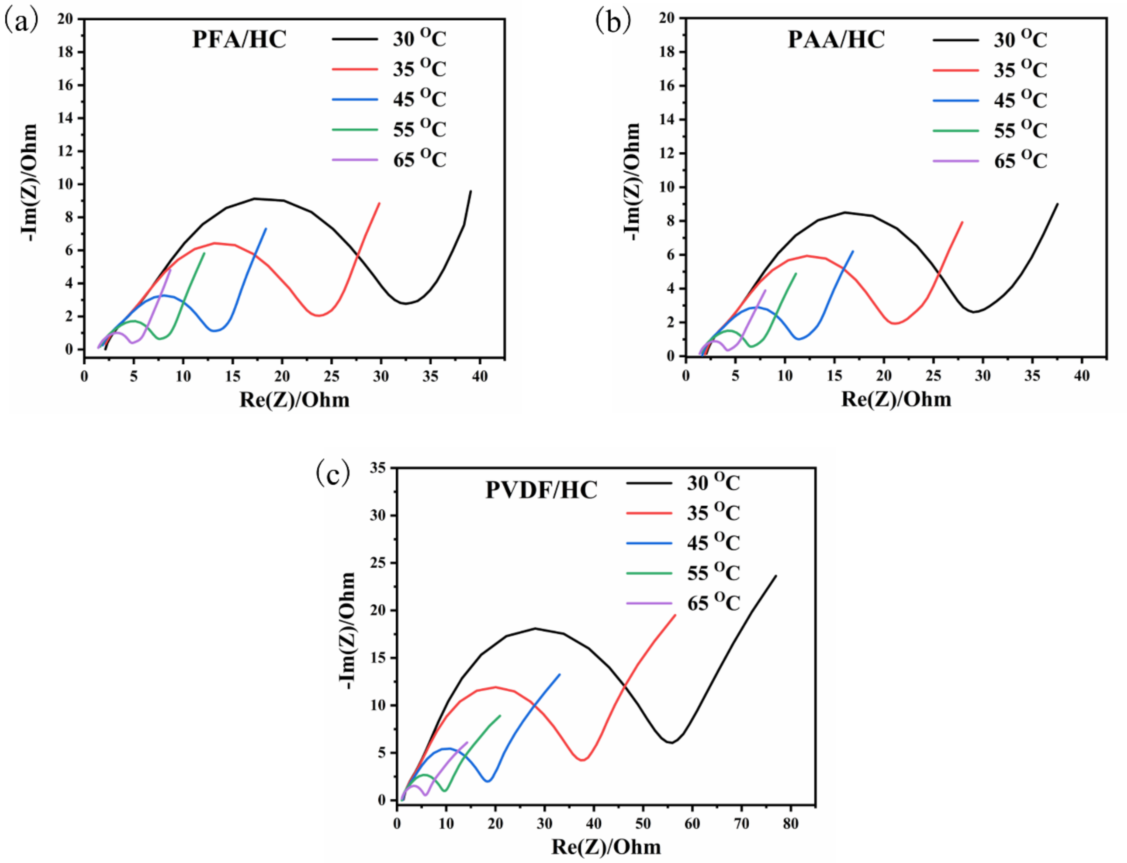

Figure 5: EIS measurement of anodic half-cells (a) PFA/HC, (b) PAA/HC and (c) PVDF/HC at different temperatures.

Further, sodium-ion diffusion coefficient was calculated by analysing the EIS after CV at low frequency through the following equation:

$$D_{Na^+} = \frac{R^2T^2}{2A^2n^4F^4C^2\sigma^2} \quad \ldots\text{eq(2)}$$

Where D is the diffusion coefficient, R is universal gas constant, T is temperature, A is surface area of electrode, n is no. of electrons taken per Na^+, F is Faraday's constant, C is Na^+ electrolyte concentration and σ is the slope fitting of $\omega^{-1/2}$ vs. Z_{real}. The Na^+ ion diffusion coefficient for PFA/HC is estimated to be 1.90E-13 cm^2s^{-1} compared to 1.75E-13 cm^2s^{-1} for PAA/HC and 8.80E-14 cm^2s^{-1} for PVDF/HC (Figure 4(f)). The dense polar carboxylic acid functional groups in the PFA polymer offer reversible weak bonding with Na^+ during sodiation/desodiation in the HC electrodes and act as self-healing component by hydrogen bonding during volume change. Thereby, the continuous carboxylic acid group facilitates the Na^+ transport within the polymer domain by surface hopping mechanism, resulting in a high diffusion coefficient and lower activation energy at the surface of the electrode[267,268]. The R_{SEI}, R_{CT}, E_a and D_{Na+} values reveal the formation of thin SEI due to the influence of the dense carboxylic acid group present on the surface of the HC electrodes.

The galvanostatic charge-discharge curves of the first two cycles at 10 mAg^{-1} are depicted in Figure 6 (a) (b) (c). The first sodiation capacities are 441.9 $mAhg^{-1}$, 404.7 $mAhg^{-1}$ and 273.1 $mAhg^{-1}$ with the ICEs of 80.8%, 75.7% and 76.3% for PFA/HC, PAA/HC and PVDF/HC respectively. The low ICE in the PAA/HC and PVDF/HC indicates a large SEI amount was accumulated in the first cycle. As expected, two sodium storage regions are observed in the sloping region（>0.1 V）and plateau region（<0.1 V）. In some recent articles, the sloping region is ascribed to Na intercalation into a misaligned graphene layer, whereas the plateau region corresponds to the insertion of Na into HC-closed pores[269]. The slope region exhibits a lack of reversibility during the initial cycle, indicating it possesses a high surface area which develops SEI, resulting in low ICE. This SEI film formation mainly impacts the specific capacity of slope region. Moreover, it contains large defects and oxygen-related functional groups which could entrap sodium. PFA/HC exhibits highest plateau capacity with better reversibility. Both slope and plateau capacity are considered for calculating coulombic efficiency. The impact of irreversible capacity on ICE at high voltage was mitigated by the improved plateau capacity of PFA/HC.

A low discharge voltage and longer plateau region are important for high output voltage, high ICE and high energy density batteries. However, capacity from the slope region limits energy density[230]. To further understand the impact of the plateau region on the ICE, the percentage and capacity of the plateau region in the initial sodiation cycle were determined to be 52.4% and 214.7 mAhg^{-1} for PFA/HC, 48.4% and 196 mAhg^{-1} for PAA/HC and 46.4% and 126.8 mAhg^{-1} for PVDF/HC. The values indicate that the high percentage of plateau region resulting from sodiation in the PFA/HC helps in increasing the ICE and minimising the impact of SEI from the slope region[231]. In addition, the high capacity in the plateau region obtained by PFA/HC is due to Na$^+$ transport to all the edges of the graphene layers and helping in the intercalation of ions. An electrolyte reduction peak was observed in CV between 0.7 and 0.01 V in the first cycle. A similar irreversible capacity peak occurs in the first sodiation in all the anodic half-cells containing different binders[270].

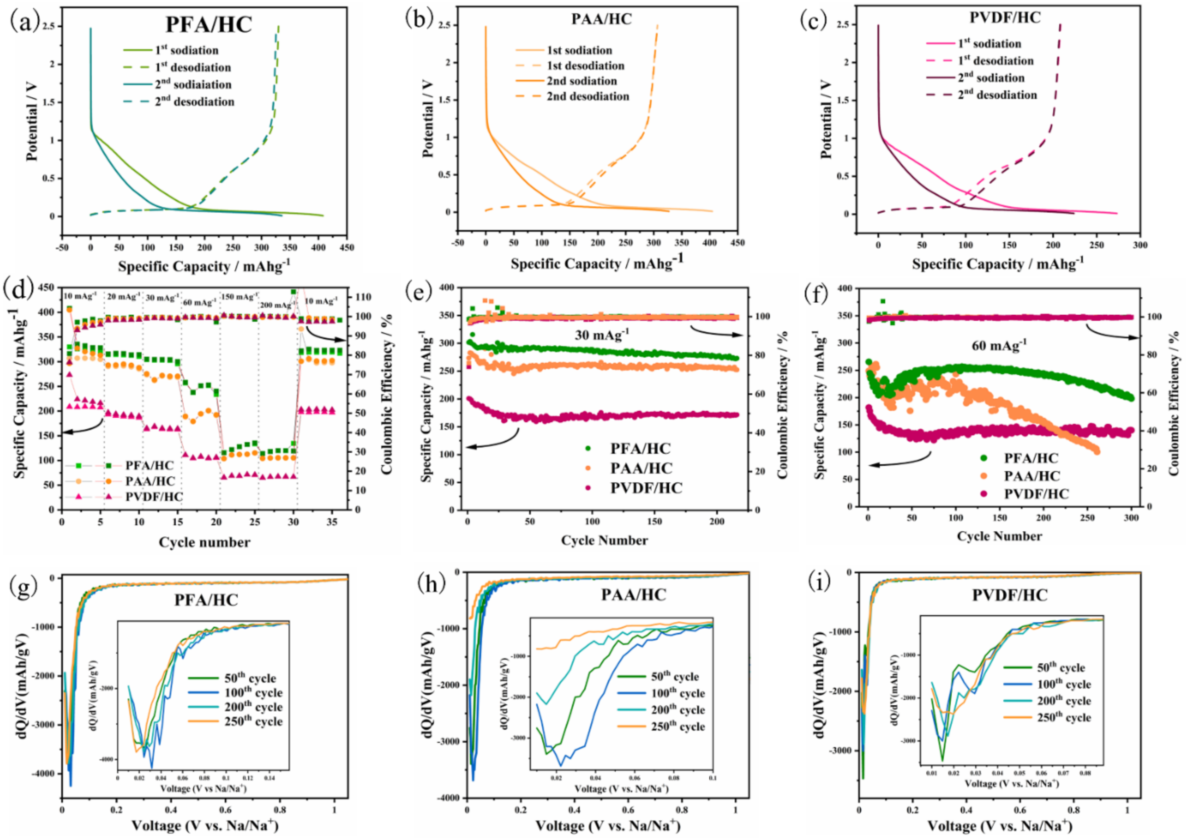

Figure 6: Galvanostatic charge-discharge profiles at 10 mAg^{-1} of (a) PFA/HC, (b) PAA/HC and (c) PVDF/HC. (d) Rate performances at different current densities of the varied anodic half cells. Long cycle at current densities (e) 30 mAg^{-1} and (f) 60 mAg^{-1}. dQ/dV curves at different cycles of the (g) PFA/HC, (h) PAA/HC and (i) PVDF/HC.

To compare the electrochemical properties and structural stability of HC containing different binders, rate capabilities and long cycling tests were further conducted. The rate capability of the HC electrodes was evaluated at different current densities from 10 to 200 mAg^{-1} (Figure 6(d)). The discharge capacity of PFA/HC reaches 332 $mAhg^{-1}$ at a current density of 10 mAg^{-1}, which decreases to 313, 303, 251, and 132 $mAhg^{-1}$ at 20, 30, 60, 150 mAg^{-1} respectively. When the current density is 20 times the initial current density, a capacity of 119 $mAhg^{-1}$ is achieved. For comparison, the PAA/HC and PVDF/HC showed poorer rate performance (Table 1). At a current density of 10 mAg^{-1}, the rate capacity of PAA/HC and PVDF/HC are 316 and 208 $mAhg^{-1}$ respectively, which decline to 105 and 67 $mAhg^{-1}$ respectively at the current density of 200 mAg^{-1} (Table 1) (Figure 6(d)).

Current density	**PFA/HC**	**PAA/HC**	**PVDF/HC**
10 mA/g	332	316	208
20 mA/g	313	289	189
30 mA/g	303	268	163
60 mA/g	251	200	107
150 mA/g	132	111	68
200 mA/g	119	105	67

Table 1: Specific capacity values at different current densities of PFA/HC, PAA/HC and PVDF/HC.

The exceptional rate performances of PFA/HC are mainly due to the dense polar carboxylic acid accelerating the ion transport rate. PFA binder has reflected a better result for ICE and rate capability that was challenging in HC due to significant effect of dense carboxylic acid in formation of crosslinking via hydrogen bonding, influencing thin SEI formation and enhancing the ion transmission. To evaluate the service lifespan of the HC electrode, Figure 6 (e) and Figure 6 (f) display the long cycling capacities at current densities of 30 mAg^{-1} and 60 mAg^{-1} respectively. PFA/HC achieved stable higher reversible specific capacities of 288 $mAhg^{-1}$ and 254 $mAhg^{-1}$ at 30 mAg^{-1} and 60 mAg^{-1}

respectively than PAA/HC (260 mAhg^{-1} at 30 mAg^{-1} and 224 mAhg^{-1} at 60 mAg^{-1}) and PVDF/HC (171 mAhg^{-1} at 30 mAg^{-1} and 145 mAhg^{-1} at 60 mAg^{-1}). After 250 cycles the capacity retentions of PFA/HC, PAA/HC and PVDF/HC at 60 mAg^{-1} are 85.4%, 46.1% and 74% respectively. Whereas at 30 mAg^{-1} the capacity retention of PFA/HC, PAA/HC and PVDF/HC after 200 cycles are 91.6%, 90.3% and 85.1% respectively. The differential capacity profiles of different cycles for the anodic half-cells sodiation clearly indicate the loss of active material from the HC electrode in the PAA/HC (Figure 6 (h)) and PVDF/HC (Figure 6 (i)) as the peak height decreases at approximately constant voltage. Whereas the PFA/HC (Figure 6 (g)) dQ/dV peaks remains almost constant which attributes to no loss of electrical contact in the electrode. The dense hydrogen bonding within the electrode system holds the electrode materials together and enhances the stability of HC electrode during cycling[271,272].

To evaluate the influence of binder loading on specific capacity and stability, charge-discharge cycles were carried with 3, 5 and 15 wt% of PFA, as shown in Figure 7 (a). Interestingly, increasing the binder loading to 15 wt% results in higher specific capacity, showing a capacity of 267 mAhg^{-1}, higher than 10 wt% of PFA. Whereas, decreasing binder content to 5 and 3 wt% led to a decrease in capacity of 249 mAhg^{-1} and 231 mAhg^{-1}, respectively, compared to 10 wt% PFA. This signifies that increasing binder amount led to obtaining higher specific capacity, as increasing binder content does facilitate Na^{+} transport to additional activation sites, whereas decreasing binder content lowers the ion transport to several active sites. All wt% of PFA showed higher capacity than 10 wt% PVDF and 10 wt% PAA binders. However, a decrease in stability is observed in 3 wt% after 25 cycles due to insufficient binder content to hold the electrode material together. The compatibility of a binder with various types of electrolytes is important to understand binder's adaptability to various SIB chemistries. Figure 7 (b) shows the charge-discharge performance of 10 wt% PFA binder in various electrolytes such as 1M $NaClO_4$ in EC:DMC, 1M NaTFSI in EC:PC, 1M NaTFSI in EC:DMC, 1M NaTFSI in EC:DEC and 1M $NaClO_4$ in EC:DEC. 1M NaTFSI in EC:PC, 1M NaTFSI in EC:DEC and 1M $NaClO_4$ in EC: DEC showed better capacity and stability than electrolytes containing EC:DMC solvent. In both Komaba et al.'s study and ours, the EC:DMC solvent system results in a reduced capacity due to severe decomposition of DMC, leading to the formation of Na alkoxide and Na alkyl on HC[263]. The result suggests that PFA-containing electrodes showed better performance and compatibility with EC:PC and EC:DEC solvents containing $NaClO_4$ and NaTFSI salts than EC:DMC solvent system. These results of galvanostatic charge-discharge show that the dense functional group inhibit the loss of irreversible capacity and maintains high-capacity retention during long cycling. The PFA binder helps Na^+ to percolate into every graphitic domain of the HC and increases the specific capacity through ion conduction by the consecutive presence of carboxylic acid in the polymer backbone. Moreover, PFA keeps intact the electronic conductivity during long cycling and facilitates Na^+ transport which proved to be an effective approach for low temperature performance[273]. Therefore, using the PFA binder led to better rate capability, electrochemical stability and specific capacity.

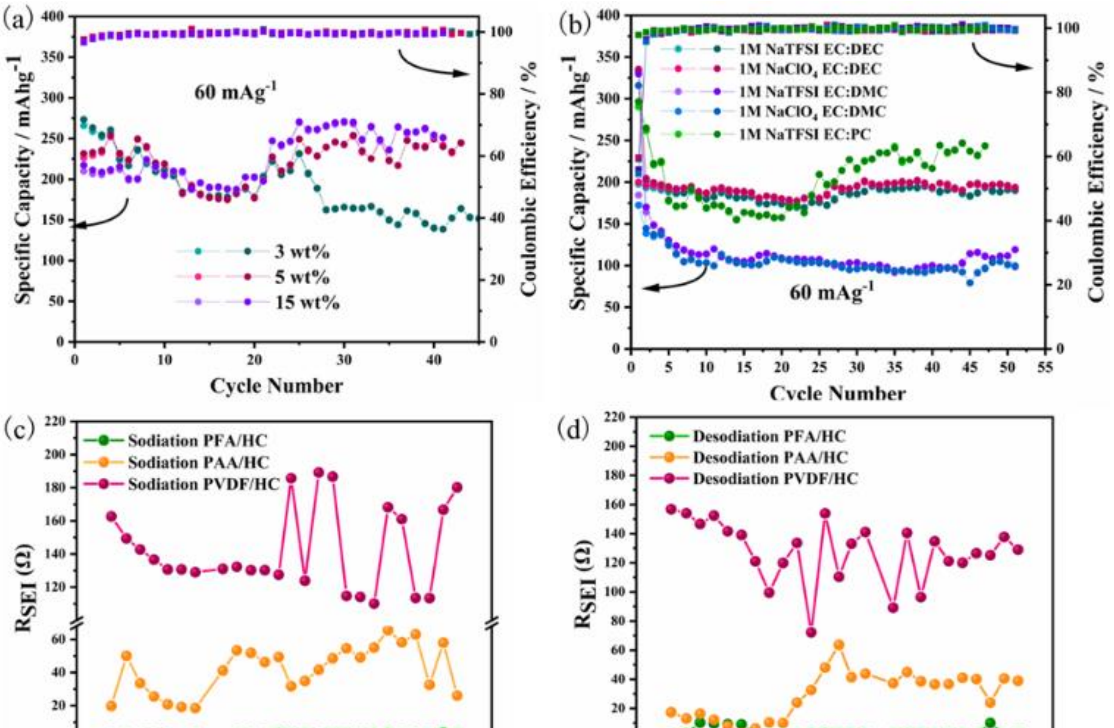

Figure 7: (a) Long cycling of PFA/HC containing varied amount of PFA binder. (b) long cycling of PFA/HC in different electrolyte system. R_{SEI} vs. potential plot of (a) sodiation and (b) desodiation of cycled anodic half cells.

The properties of SEI and its effects on Na^+ diffusion into electrodes were determined by DEIS and R_{SEI} vs. potential during sodiation and desodiation as shown in Figure 7 (c) and (d). Nyquist impedance plots at different potentials within the range 0.01-2.5 V are plotted as shown in Figure 8. The different EIS curves of different anodic half cells at varied potentials are due to dynamic interphase performance. Fitting of impedance data to an equivalent circuit using RL(QR)(QR)(Q/CR)W was conducted. The R_{SEI} vs. potential during sodiation and desodiation are plotted as shown in Figure 7 (c) and (d). It was observed that PFA/HC has lower R_{SEI} compared to PAA/HC and PVDF/HC. This recommends that high Na^+ ion transference SEI is formed on the HC electrode surface leading to better reversible capacity and rate performance in PFA/HC. The dense polar carboxylic group influences the R_{SEI} by lowering the activation energy and resistance due to more interaction with Na^+. R_{SEI} vs. potential plots showed stable R_{SEI} values of PFA/HC compared to PAA/HC and PVDF/HC owing to presence of uniform layer of SEI on the surface of PFA/HC electrode, which is non-uniform in PAA/HC and PVDF/HC electrodes. Elevated R_{SEI} values for PFA/HC (Figure 7 (d)) were noted within the desodiation voltage range of 0.01-0.5 V. This observation can likely be attributed to the numerous interactions between Na^+ ions and the densely packed polar functional groups of PFA. As a result, this interaction may impede the desodiation process from the SEI within that specific potential range.

PFA enhances cell performance due to various factors: (a) the dense carboxylic groups in PFA serve as poly anions that cover the surface of HC and act as part of SEI. (b) The solvated positively charged Na^+ interacts with unpaired electrons found in the negatively polarised oxygen atom of the -COOH group, accelerating the Na^+ desolvation and intercalation into HC. These factors induce a thin and stable SEI formation from the electrolyte decomposition and enhance charge transfer of Na^+ across the electrode-electrolyte interface[274]. The continuous presence of carboxylic acid groups on the polymer chain enhances Na^+ diffusion within electrode, which increases specific capacity, lowers polarization and enhances SIB performance. In addition, the dense carboxylic acid forms many inter/intra polymer complexes through hydrogen bonding, increasing structural integrity and capacity retention[213].

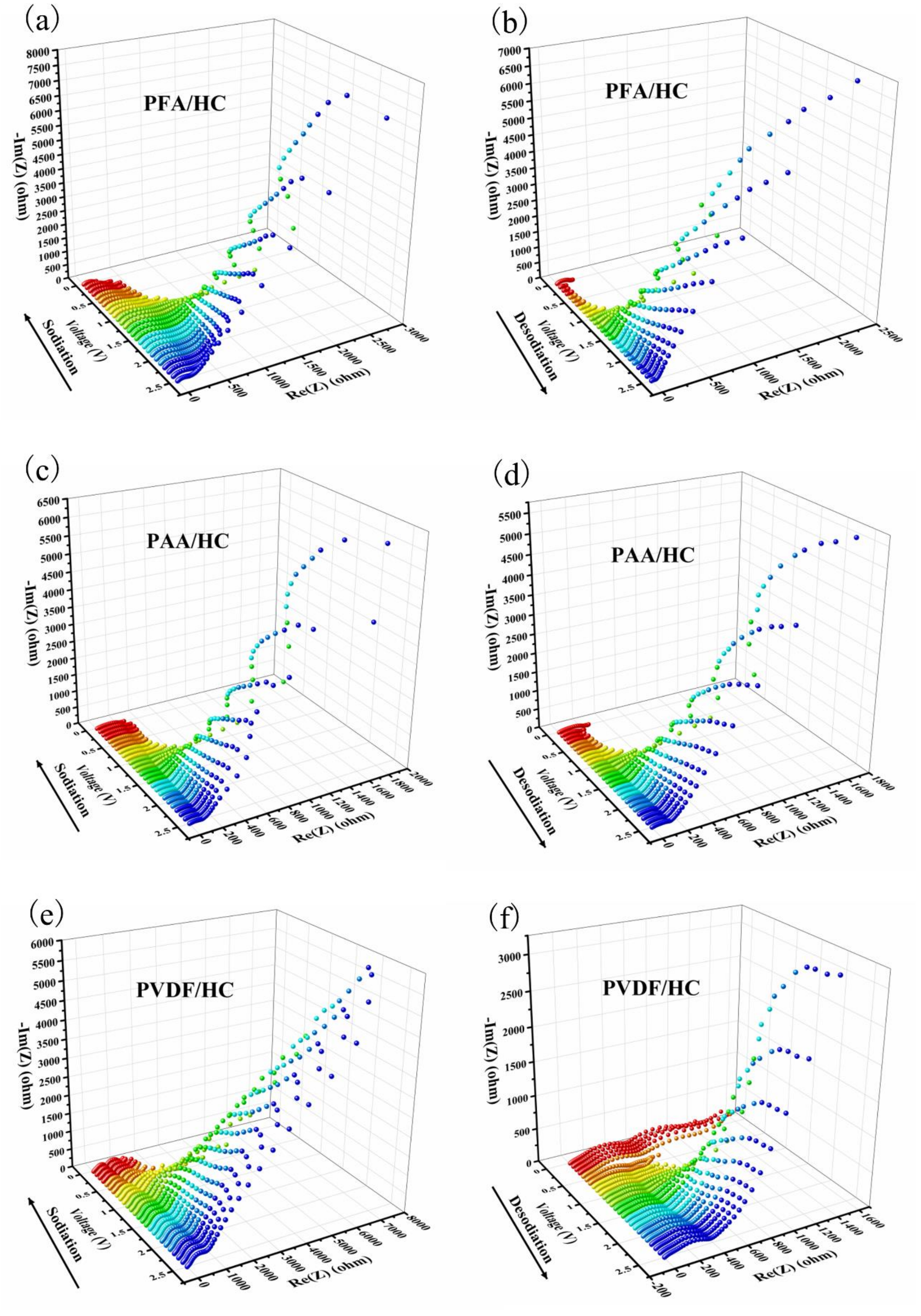

Figure 8: DEIS plot at different potential range of PFA/HC, PAA/HC and PVDF/HC during sodiation and desodiation.

The interphase analysis of HC electrodes will provide details on the dissimilarity of surface chemistry that has occurred due to the presence of various binders. There might be an influence of binders on the electrolyte decomposition mechanism. Thus, interfacial properties such as SEI composition and electrode surface morphology after cycling might have changed and need analysis. To investigate the interfacial composition chemistry, XPS analysis was performed on cycled HC electrodes with PFA, PAA and PVDF binders. High-resolution spectra and binding energies of deconvoluted peaks are presented. The C 1s spectra (Figure 9 (a), (b) and (c)) in all the cycled HC electrodes with various binders showed typical species such as sp^3 C-C, C-O, C=O and Na_2CO_3. Wherein, the presence of C-O and C=O is believed to result from electrolyte decomposition on the electrode surface, as supported by the evidence provided by the O 1s spectra (Figure 9 (d), (e) and (f))[275,276]. The detection of a C=C peak from HC found only in the C 1s spectrum of PFA/HC, indicates that the X-rays can scan beneath the thin SEI formed in PFA/HC electrode. A higher concentration of C-O and C=O observed in the cycled electrode with PFA binder could be from the dense carboxylic groups present in the PFA binder and from carbonate species present in the SEI. C-F peak is only observed from the cycled electrode containing PVDF binder, indicating the peak might be from the PVDF binder functional group. In addition, PFA/HC has a thick layer of inorganic species (Na_2CO_3, Na_2O and NaCl) confirmed by the composition percentage (Table 2 and 3) of the C 1s, O 1s and Cl 2p (Figure 9 (g), (h) and (i)) spectra. The presence of rich inorganic species in the inner of the double layer of SEI facilitates rapid transport of Na^+ and inhibits continuous electrolyte decomposition[277,278]. The composition percentage of ROCONa, C-O and C=O in O 1s spectra of PAA/HC and PVDF/HC are higher, suggesting that SEI contains large organic carbonate derived component due to constant degradation of organic solvent (Table 3)[279,280]. Na KLL auger peak also appears in the O 1s spectra for all the electrodes[249]. The thick inorganic beneath and thin outer organic species SEI of PFA/HC contribute towards robust SEI during long-term cycling stability of the HC electrode. The dynamic nature of SEI, wherein the outer organic layer gets dissolved or stripped during discharge, leaving the inner inorganic layer exposed directly to the electrolyte. Hence, a rich thick inorganic layer with high modulus strength is needed to prevent continuous electrolyte decomposition and enhance rate capability and Na^+ transport into the HC[281].

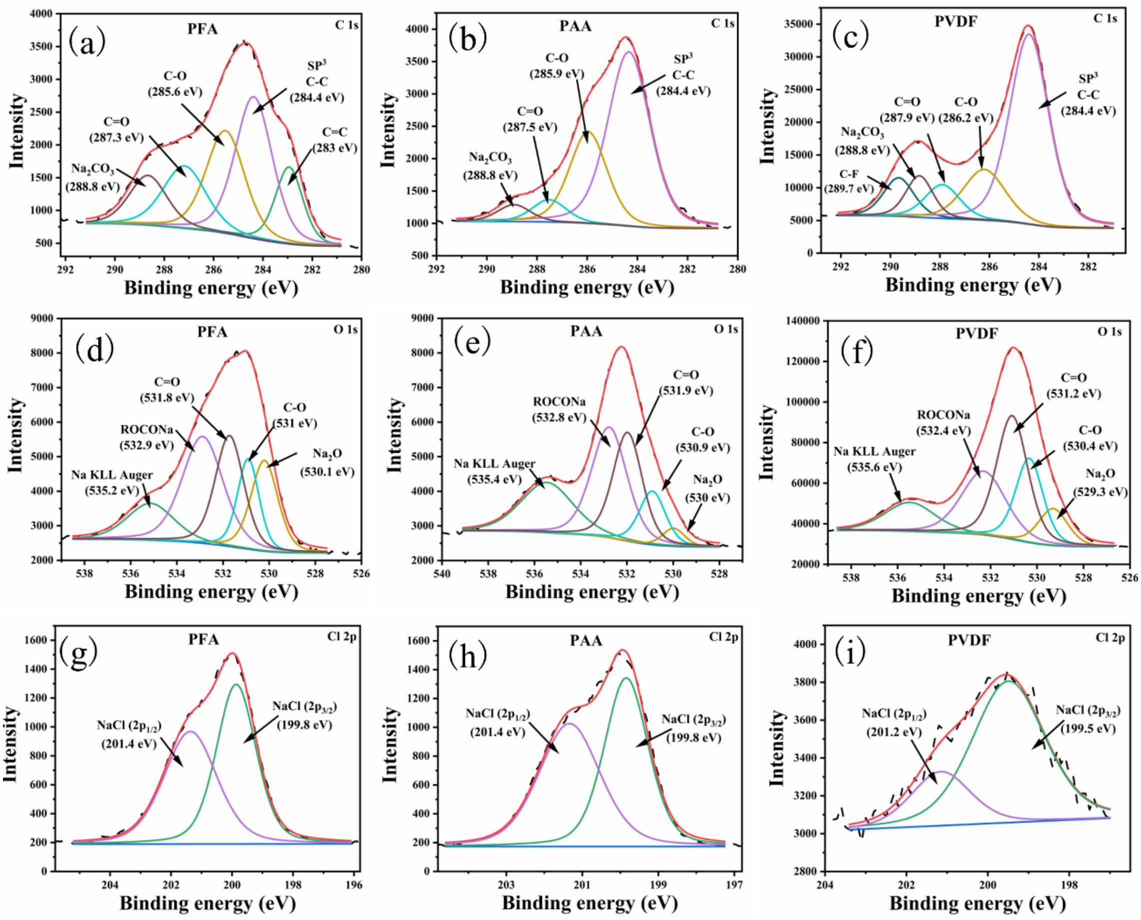

Figure 9: XPS analysis of C 1s, O 1s and Cl 2p of cycled HC electrode containing different binders.

Table 2: Elemental composition percentage obtained from area under the curve of the C 1s XPS spectra.

Elemental species	PFA	PAA	PVDF
C=C	13.3%		
C-C	33.1%	60.5%	56.8%
C-O	24.8%	28.5%	16.5%
C=O	16.8%	6.3%	9%
Na_2CO_3	11.7%	4.5%	8.5%
C-F			8.9%

Table 3: Elemental composition percentage obtained from area under the curve of the O 1s XPS spectra.

Elemental species	PFA	PAA	PVDF
Na_2O	20.9%	3.4%	9.3%
C-O	18.6%	12.2%	20%
C=O	22.9%	27.5%	33.3%
ROCONa	24.4%	34%	24.5%
Na KLL Auger	13%	22.7%	12.6%

The morphology study of the cycled HC electrodes with PFA, PAA and PVDF binders can shed light on the electrochemical performances of the respective coin cells. After 300 cycles the coin cells were disassembled, and the electrode surface morphologies were observed under SEM. The freshly prepared HC electrodes with varied binders showed to have a uniform, porous structure with good adherence to current collector (Figure 10 (a_1), (b_1) and (c_1)). The SEM images of cycled PFA/HC (Figure 10 (a_2) and (a_3)) electrode indicate uniform SEI formation due to electrolyte reduction and a crack-free electrode surface. While the PAA/HC (Figure 10 (b_2) and (b_3)) and PVDF/HC (Figure 10 (c_2) and (c_3)) electrodes showed cracks from the top view. Note that the thread-like particles observed in SEM images on top of the cycled electrode surface are of the separator's glass fibre. The cross-sectional view of the post-cycled PAA/HC (Figure 11 (e)) and PVDF/HC (Figure 11 (f)) electrodes showed massive cracks and detachment/peeling off from the current collector compared to pristine electrodes (Figure 11(b), 11(c)). Whereas cycled PFA/HC (Figure 11 (d)) electrode maintains crack-free and structural integrity of the electrode with intact electrical contact to the current collector compared to pristine electrode (Figure 11(a)), which helps enhance the cycling performance. PFA binder firmly holds the electrode materials to the current collector surface and maintains the integrity of the HC electrode. It might be due to many chemical bonds formed between binder polar groups and current collector, while only intermolecular forces form between PVDF and current collector. The interface between the electrode material and SEI film can't be identified because the thickness of SEI is ~8 nm, making interphase impossible to be observed in SEM[166]. Besides, the cross-link formation by the inter and intra-molecular hydrogen bonding PFA binder has greater modulus and hardness, helping alleviate volume change stress during sodiation/desodiation of HC electrode.

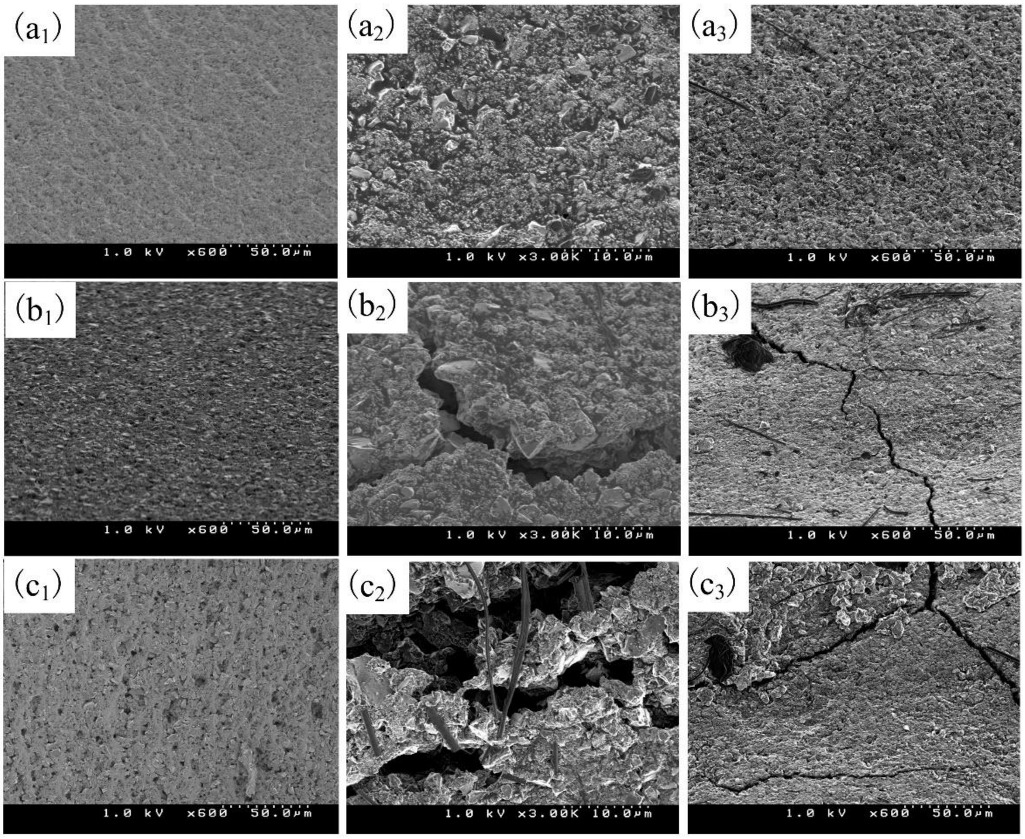

Figure 10: Top view SEM images of pristine HC electrodes with (a_1) PFA, (b_1) PAA and (c_1) PVDF binders. Top view SEM images of cycled HC electrodes with $(a_2)(a_3)$ PFA, $(b_2)(b_3)$ PAA and $(c_2)(c_3)$ PVDF binders at two different magnifications (10 μm and 50 μm).

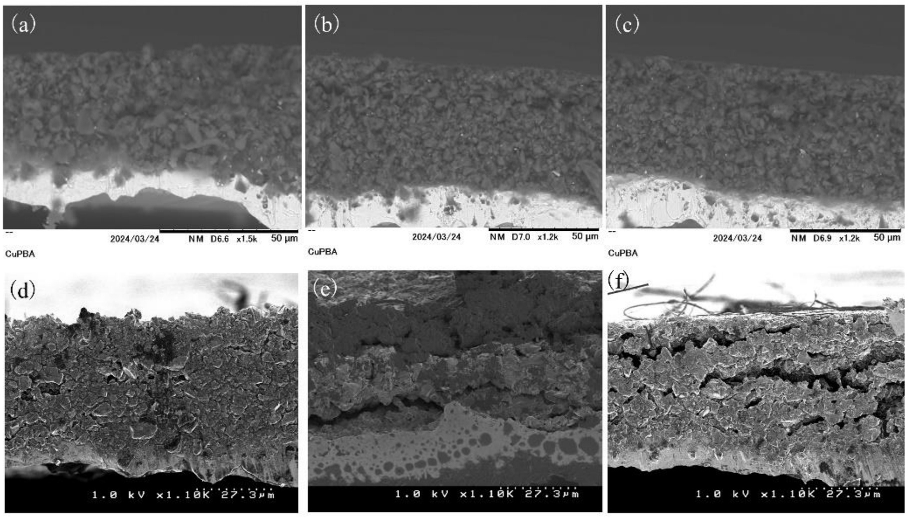

Figure 11: Cross-section view of pristine HC electrodes containing (a) PFA, (b) PAA and (c) PVDF binder. Cross-sectional SEM of cycled HC electrode with (d) PFA, (e) PAA and (f) PVDF binders.

Changes in electrode morphology and SEI after charging and discharging were observed. The formation of SEI film on the surface of the electrodes containing different binders can be confirmed by the slight disappearance of the electrode surface roughness compared to the pristine electrodes. Additionally, crack formation on electrode material after long cycling is observed in PAA/HC and PVDF/HC which is mitigated in the PFA/HC. Therefore, dense hydrogen bonding and strong interaction with the current collector preserve the integrity of the electrode material.

Conclusions:

In summary, we utilise dense polar carboxylic acid functional groups polymer poly(fumaric acid) as a promising, cost-effective and environmentally friendly binder for HC anodes in sodium-ion batteries. The less flexible polymer backbone and high concentration of functional groups exhibited better rheology and electrochemical study owing to carboxylic acid interaction with the electrode component and more importantly with Na^+. PFA/HC exhibits, higher ICE of 80.8 % and delivers higher reversible rate capacities of 332, 313, 303, 251, 132 and 119 $mAhg^{-1}$ at current densities of 10, 20, 30, 60, 150 and 200 mAg^{-1} compared to PAA/HC and PVDF/HC. Moreover, PFA/HC retains 85.4% of its reversible specific capacity for more than 250 cycles of sodiation/desodiation at a higher current density of 60 mAg^{-1} with the highest specific capacity achieved of up to 288 $mAhg^{-1}$. The enhanced specific capacity is closely related to the continuous carboxylic acid group present in the backbone of the polymer which forms an ion path for augmenting the Na^+ migration and transporting ions to every edge of the disordered graphite. PFA binder modifies the SEI, leading to enhanced Na^+ kinetics at the interface such as lower activation energy of 50.7 $kJmol^{-1}$, higher Na^+ ion diffusion coefficient of 4.64E-11 cm^2s^{-1} and lower R_{SEI} compared to PAA/HC and PVDF/HC. Due to the passivation of HC defects by dense formation of hydrogen bonding with the oxygen functional groups at the surface, continuous electrolyte decomposition was suppressed by reducing the contact between the electrode and electrolyte. The cycling stability was improved owing to inorganic-rich SEI and no loss of electrode integrity by dense hydrogen bonding within the electrode was confirmed by XPS and SEM respectively. Hence, the present study on water-soluble PFA binder opens an area of design development of dense functional polar groups polymer for better electrochemical performance in sodium-ion batteries such as enhancing the rate capability and specific capacity, thereby showing great potential for sodium-ion batteries' practical application.

Chapter 5

Enhanced Performance of High-Density Functional Groups Based Poly(ionic liquid) Binder for Graphitic Anode in Li-ion Batteries

Abstract

In quest for better performance and extended cycle life in Li-ion battery electrodes, the binder's choice holds immense significance. Conventional binders like PVDF are passive polymers lacking the ability to transport Li^+. This limitation poses constraints in fast charging and long cycle life. Thus, the imperative lives in the development of novel binders designed to facilitate Li^+ transport within electrodes. Poly(ionic liquid) (PIL) is shown to inherit high ionic conductivity, electrochemical stability and better interaction with electrolytes. Herein, we synthesized a novel water-soluble high-density imidazolium-based functional group PIL (PMAI) and evaluated it as binder in LIBs. PMAI-based electrode (PMAI/Gr) exhibits excellent electro-chemical performance, achieving 80% capacity retention at 750 cycles with specific capacity of 298 mAh g^{-1} at 1C compared to PVDF binder. In fast charging at 5C rate, PMAI/Gr delivers a higher discharge capacity of 85 mAh g^{-1} than PVDF/Gr (47 mAh g^{-1}). Postmortem analysis reveals noticeable electrode degradation containing PVDF binder, characterized by high charge transfer resistance and thick organic species at SEI. In contrast, when PMAI serve as binders, high content of inorganic species in SEI and crack-less electrode is observed, resulting in reduced overpotential, lower activation energy and enhanced Li^+ diffusion. The novel design and thorough examination of densely functionalized groups of PMAI binder have the potential to attract interest, not only for graphite electrodes but also for various high-energy-density electrode materials.

Introduction:

Lithium-ion batteries (LIBs) provide an effective solution for storing energy from intermittent sources. As global demand for lithium is set to rise, the importance of LIBs, which are currently the most competitive battery technology, becomes increasingly evident. The pursuit of higher energy density storage is driven by the increasing need for electric vehicles, mobile electronic devices and renewable energy systems. Traditionally, much effort goes into improving electrode materials and electrolytes, with less focus on enhancing electrically passive elements like binders in battery electrodes.

Binders play a crucial role in influencing the composition of the solid electrolyte interphase (SEI), stability and irreversible capacity loss of LIBs[282,283]. SEI layer improves free Li^+ ion movement and insulates electron transfer, further enhancing the cycle life and inhibiting electrolyte decomposition[284]. The tunability of SEI is mainly carried out using additives (vinylene carbonate, fluoroethylene carbonate, lithium bis(oxalate) borate) and electrolyte solvent composition[285]. However, novel binders can limit the use of additives, surface coating[286] and structural modification[287] which requires additional steps in battery fabrication.

Convention polymer binders such as poly(vinylidene fluoride) (PVDF) and styrene-butadiene rubber (SBR) are non-ionic conducting polymer binders. These binders encounter greater challenges when employed in high-capacity electrodes that undergo substantial volume changes during cycling, resulting in electrode fractures and delamination[288]. In addition, PVDF needs environmentally hazardous organic solvent N-methyl-2-pyrrolidone (NMP) for making electrode slurry[164,173,289]. Brandell et al. reported that PVDF infiltrates pores of various dimensions, significantly diminishing the surface area and pore volume accessible to electrolytes after cell fabrication[290]. Considering ionic conductivity in electrodes, which occurs by absorption of the electrolytes onto the electrode surface, the transport of ions from the electrolyte into the electrode surface facilitates lithiation/delithiation[291]. Developing novel binders with better mechanical adhesion, enhanced surface compatibilities, self-healing and Li^+ transport/conducting abilities will enhance rate capability and long cycling stability in LIBs. Hence, a novel binder that aligns with the pragmatic requirements of industrial manufacturing is highly desired.

Ionic liquids (IL) are molten salts comprised of organic cations and organic/inorganic anions that have lower melting points than 100 ^{O}C. Some promising properties are high ionic conductivity, better electrochemical stability and low volatility, leading to their use in many dye-sensitized solar cells[292], capacitors[293], light emitting devices[294] and electrolytes in lithium-ion batteries[295]. Polymers containing IL moieties have been used as polymer electrolytes for various applications[296]. Poly(ionic liquid) (PILs) is an ionic polymer consisting of a polymer backbone with cationic or anionic side chains bonded to an opposite ionic species of ionic liquids. PILs are an emerging class of functional group polymers. These polymers are gaining increasing interest due to their distinct chemical and physical characteristics, derived from their ability to retain the properties of IL while incorporating the inherent attributes of polymers. The advantages of such polymer are better ionic conductivity, flexibility and wide electrochemical window[297]. Few works based on the PILs have been reported in the field of binders for LIBs such as thiazolium-type PILs[298], polyvinylimidazolium nanoparticle PILs[299] and imidazolium-based PILs[300] for $LiFePO_4$-based cathode. The results suggest that PIL binders enhances both the specific capacity and cycle stability by establishing pathways for both ions and electrons within the electrode domain while facilitating the desolvation of Li^+. Poly(diallyldimethylammonium) based binders with fluorinated and non-fluorinated counter anions showed better capacity retention and cycling stability when employed in cathode electrodes. The results are due to the better ionic conductivity of binder and electrolyte uptake which enhances the Li^+ transport in electrode[301,302]. PIL nanoparticles obtained from polymerization of 1-vinyl-3-alkyl imidazolium showed better capacities and cyclability when combined with graphite and $Li_4Ti_7O_{12}$ electrodes[303]. Our lab reported that poly[vinylbenzylallylimidazolium bis(trifluoromethane)sulfonylimide] as a binder in graphite electrodes for LIBs. The binder showed better capacity retention and cycle life due to ion-conducting pathways, limiting electrolyte degradation and enhanced wettability facilitated by the binder[164]. In brief, integrating IL moiety into polymer creates many advantages such as ionic conductivity, flexibility, good binding and compatibility with electrode materials.

Looking into the benefits of PILs in the LIBs and the limited amount of work carried out in the area of PILs as a binder for LIBs, has encouraged the authors to synthesise a PIL-based novel binder for graphite anode. Otsu et al. reported many polymethylene-based polymers and indicated that their stiff polymer backbone might show different properties than the polyethylene-based binders[136,137]. Herein, we synthesized a novel high-density functional group PILs binder based on polymethylene, poly(oxycarbonylmethylene 1-allyl-3-methyimidazolium) (PMAI). This polymer consists of consecutive carboxylate functional groups at every carbon unit of the polymer chain which is ionically interacted to 1-Allyl-3-methyimidazolium cation species. The dense IL functional groups will enhance the ionic conductivity by forming ion channels and transporting Li^+ across the edges of the graphite layers, thereby increasing the specific capacity of the LIBs. 1-Allyl-3-methyimidazolium is used due to its high thermal stability[304], low viscosities, better ionic conductivity, and large potential windows[305]. Imidazolium-based binders are shown to create a beneficial polarizing environment for the desolvation of Li^+. This desolvation process might lower the activation energy when Li^+ is inserted into a solid material of electrode[299]. Hence, considering the positive impact the dense functional group will pose for enhancing the LIB's electrochemical performances, PMAI was used as a binder for graphite anode. In the direction of commercialization of better LIB technology, rheology and various electrochemical studies were carried out to study the PMAI’s effect on SEI, electrode morphology after cycling and galvanostatic charge-discharge and the results were compared with commercial counterpart PVDF binder.

Experimental:

Poly(ionic liquid) synthesis:

PMAI was synthesized from ion exchange with the polymer poly(hydroxycarbonylmethylene) (PHCM) which was derived from poly(ethoxycarbonylmethylene) (PECM). PECM was prepared from radical bulk polymerization of diethyl fumarate (Sigma Aldrich, 98%) utilized 2,2’-azobis(isobutyronitrile) (AIBN, Sigma-Aldrich, >98%) as radical initiator within a vacuum Schlaker reaction tube at 70 ºC for duration of 24 hours. Subsequently, the polymer was purified by washing with hexane and dried in a vacuum environment overnight. Further to obtain PHCM, PECM was base hydrolyzed in a solvent mixture of $EtOH:H_2O$ (2:1) using an excess of KOH (Wako) under reflux conditions. The reaction mixture was slightly acidified by adding 1N HCl (Sigma-Aldrich, 12N) and then dialyzed using a cellulose acetate tube provided by Fisherbrand. Finally, water from the aqueous solution was evaporated post-dialysis to yield PHCM. 1-allyl-3-methylimidazolium hydroxide was synthesized via anion exchange of 2 gm of 1-allyl-3-methylimidazolium chloride (AmImCl) dissolved in 100 ml water using amberlite IRN78 OH hydroxide form

(Supelco) column. Water was evaporated from the aqueous 1-Allyl-3-methylimidazolium hydroxide (AmImOH) and dried overnight under a vacuum at 60 ºC. PHCM (200 mg) and AmImOH (482 mg) were dissolved in water and stirred overnight at room temperature. Finally, the product was washed with acetone after evaporating water from the aqueous PMAI and then dried under a vacuum. The yield of PMAI polymer is 78%.

Synthetic characterization:

The chemical structure of PMAI was confirmed by ^{1}H NMR and ^{13}C NMR (Bruker Advance II-400 MHz spectrometer) and FT-IR spectroscopy (PerkinElmer 100 FTIR spectrometer). The thermal property was evaluated by TGA using Hitachi STA7200 thermal analysis system under nitrogen atmosphere at a heating rate of 10 ºC min^{-1}.

Electrode preparation and cell assembling:

Graphite slurries were obtained by mixing 80% battery grade graphite (Sigma-Aldrich), 10% super P conductive carbon (Alfa Aesar) and 10% PMAI binder in water for 2 h using mechanical mixing to obtain a homogenous slurry. The resulting slurry was coated on a copper sheet using doctor blade of 100 μm and dried under vacuum at 80 ºC for 24 h. The electrodes were calendared using a hot roll press machine and then punched in 13 mm diameter circular discs. PVDF (Sigma-Aldrich) binder-based electrodes are obtained using the above procedure. Coin cells of CR2025 were assembled with lithium as counter and reference electrodes, while graphite electrode as working electrodes. Polypropylene separator was wetted with 70 μl 1 M $LiPF_6$ in EC/DEC (1:1 v/v) (Sigma-Aldrich) electrolyte. The cells were assembled in an argon-filled glovebox with 0.5 ppm< H_2O and 0.5 ppm< O_2 atmosphere content. The PMAI binder-based anodic half cells are named PMAI/Gr, while PVDF binder-based anodic half cells are named PVDF/Gr.

Electrochemical characterization:

Cyclic voltammetry (CV) was conducted at sweep rates of 0.1, 0.2, 0.4, 0.6, 0.8 and 1 mV s^{-1} under a voltage range of 0.01-2.1 V using Biologic Science Instruments. Electrochemical impedance spectroscopy (EIS) measurement was performed on cycled electrode using Biologic Science Instruments at a voltage amplitude of 10 mV and frequency range of 1.0 MHz to 0.1 Hz. From the ESI result, SEI resistance (R_{SEI}) after SEI formation and diffusion coefficient were determined. The galvanostatic charge-discharge cycling was carried out with Electrofield ABE 1024 in a 0.01-2.1 V voltage range. The electrochemical performance was tested at varied C-rates of 0.1C, 0.25C, 0.5C, 0.75C, 1C and 2C and long-term cycling of 800 cycles at 1C and 5C. Using Biologic Science Instruments, dynamic electrochemical impedance spectroscopy was measured with the cycled electrodes at varied voltage perturbations at a frequency range of 1.0 MHz to 0.1 Hz. The activation energy was calculated from the Arrhenius plot obtained from the EIS data performed at different temperatures using cycled anodic half-cells.

Peel test and Postmortem characterization:

Peel tests were conducted on a 40 mm long graphite electrode using an Instron 3342 apparatus. During the peel test, adhesive tape was affixed to the roll-pressed coated electrode and peeled at a 180° angle at a consistent displacement rate of 2 mm min^{-1}. After galvanostatic charge-discharge cycling, the coin cells were decrimped inside the glove box and the anodes were washed with diethyl carbonate to remove $LiPF_6$ salts from the surface. SEM images were obtained using Hitachi S-4500 at an accelerating voltage of 1.0 kV and compared with pristine electrodes. SEI composition of the electrodes was determined using X-ray photoelectron spectroscopy (Fisons instruments S-probe TM 2803)

Results and discussions:

We reported the novel synthesis of high-density functional groups polymer based on imidazolium type PIL PMAI via a three-step process: radical polymerization, ester hydrolysis and neutralization. Figure 1 (a) shows the synthetic route of the PMAI synthesis from the monomer diethyl fumarate. We confirmed the PMAI synthesis using ^{1}H NMR, ^{13}C NMR and FT-IR. ^{1}H NMR spectrum (Figure 1(b)) revealed the presence of PHCM methine hydrogen peak at 2.98 ppm and imidazolium cation unit hydrogen peaks are assigned in the spectrum. ^{13}C NMR peaks are assigned with respect to each carbon of the PMAI as shown in Figure 1 (c). The characteristic ^{13}C NMR peaks are methine carbon of PHCM at 62.4 ppm and methyl peak of 1-allyl-3-methylimidazolium at 30 ppm. To confirm that all the carboxylate group of the PHCM is interacting with the cation imidazolium unit, ^{1}H NMR integration was performed for the methine peak of PHCM and methylene peak of imidazolium (Figure 1(d) and 1(e)). The integration confirmed the presence of 1:2 hydrogen value of methine to methylene peak.

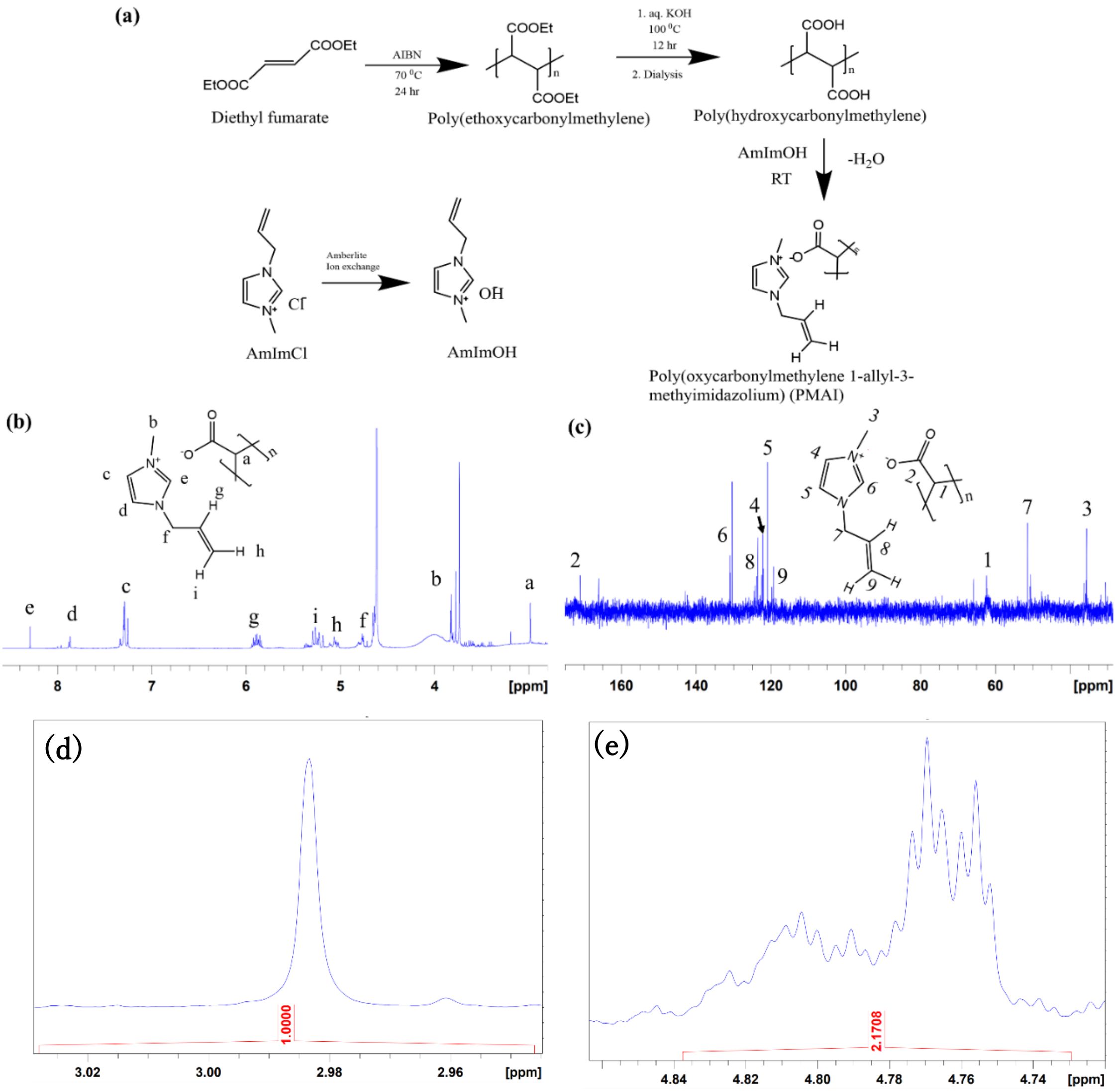

Figure 1: (a) Synthetic route to PMAI. (b) ^{1}H NMR spectrum (D_2O). (C) ^{13}C NMR spectrum (D_2O). ^{1}H NMR peak and integration value of (d) methine peak of PHCM and (e) methylene peak of imidazolium.

In addition, the pH of PMAI showed 8.0 which indicates that neither free carboxylic acid nor hydroxide is present (Figure 2(a)). To further support the formation of PILs, FT-IR spectroscopy was conducted. The IR spectrum of PIL in Figure 2(b) shows a board peak at 3500 cm^{-1} corresponds to C-O^{-} AmIm^{+} stretching and a carbonyl peak at 1725 cm^{-1}. Characteristics of imidazole ring peaks are indicated by the presence of a peak at 1582 cm^{-1} to C-N stretching vibration, 1157 cm^{-1} to C-H unsymmetrical bending vibration and 3151 cm^{-1} to C=C-H[306]. The average molecular weight of PHCM was determined to be 3000 m/z from the MALDI-TOF and showed peaks at intervals of 58 m/z (CHCOOH) as shown in Figure 2(c). The thermal stability of PMAI binder was determined using TGA analysis (Figure 2(d)). The value of 10 wt. % loss temperature is above 150 ºC. Hence the binder is stable at extreme operating temperatures of LIBs. The results from the characterization of PMAI confirm the formation of the PIL.

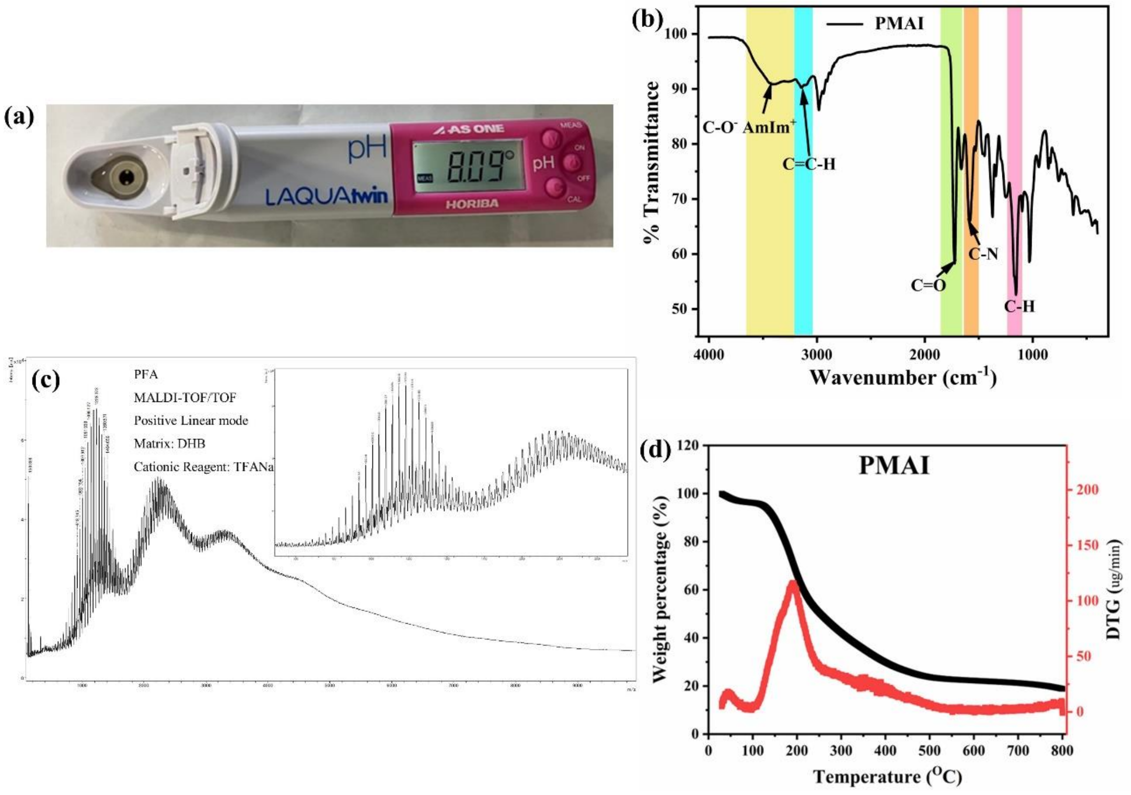

Figure 2: (a) pH measurement of PMAI using pH meter. (b) FT-IR profile of PMAI. (c) MALDI-TOF data of PFA. (d) TGA profile of PMAI.

A stable structure of the electrode can be maintained during long cycling by strong adhesion between the current collector and active material using a binder. The binding capacity of binders was evaluated using a 180º peel test at a tensile speed of 2 mm/min. The force vs. displacement profile of the peel test is shown in Figure 3. The average peel force of the PMAI binder-based electrode is found to be 10.9 N which is higher than the PVDF binder-based electrode with 9.8 N. This clearly shows that PMAI binder adhesion capacity is stronger than PVDF binder systems. The existence of dense functional groups in the PMAI-based PIL promotes chemical bonding within the active materials and also to the current collector resulting in a stronger binding capability.

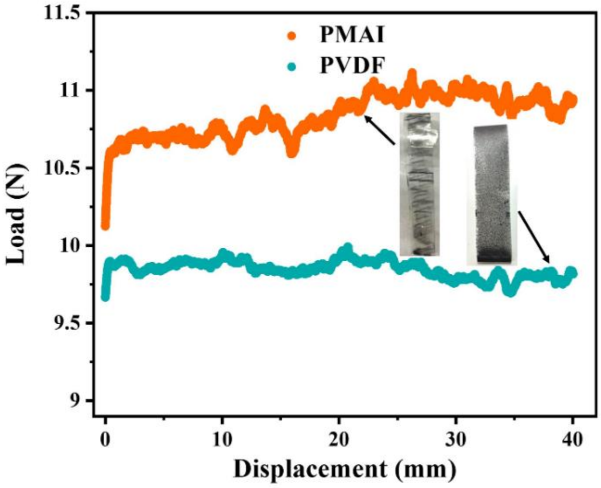

Figure 3: Peeling curves of electrodes with PMAI and PVDF binders. Inset: Image of tape after peel test.

In order to investigate the impact of binders' interactions with the active components and electrolytes on the electrochemical performances, CV measurements were performed for PMAI/Gr and PVDF/Gr. During the first cathodic sweep, the PMAI/Gr (Figure 4(a)) and PVDF/Gr (Figure 4(b)) displayed electrolyte reduction peaks around 0.6 V and a distinctive lithiation peak at a low potential of ~0.01 V. The electrolyte decomposition on the graphite surface leads to the formation of the SEI which facilitates Li^+ transport and prevents continuous electrolyte decomposition. In the consecutive scans, the electrolyte decomposition peaks do not exist indicating the formation of stable SEI film. In the case of PMAI/Gr, the first cycle cathodic curve between 1.7 V to 0.8 V shows a reduction peak, while in PVDF/Gr the first cycle curve overlaps with the subsequent cycles at the range. This indicates that the PIL binder gets reduced before the electrolyte decomposition. This helps in the formation of functionalized SEI which influences the lithiation-delithiation process. On the contrary, the anodic peak located at 0.2 V results from the delithiation process of graphite. The overpotential, calculated as the difference in the anodic peaks between 0.1 mV/sec and 1 mV/sec of CV for PMAI/Gr (Figure 4(c)), was found to be lower (0.150 V) compared to PVDF/Gr (0.196 V) (Figure 4(d)). Indicating that the PIL binders facilitate higher Li^+ transport and lowering internal impedance.

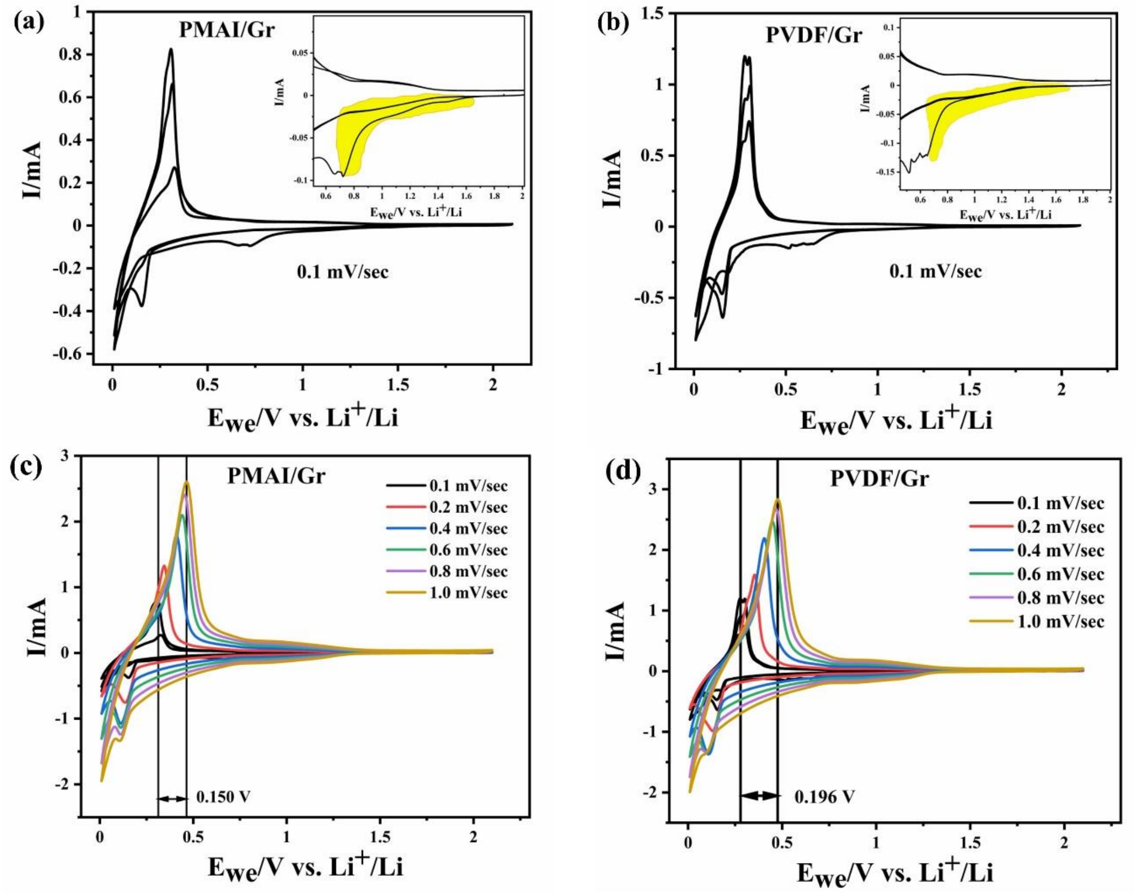

Figure 4: CV curves of (a) PMAI/Gr and (b) PVDF/Gr at 0.1 mV s^{-1}. CV curves at varied potential rates of (c) PMAI/Gr and (d) PVDF/Gr.

To further study interphase impedance and Li^+ diffusion coefficient in graphite anode, EIS was carried out on cycled electrodes. Figure 5(a) shows the Nyquist diagram, which consists of a semicircle sited in a high-medium frequency range corresponding to SEI resistance (R_{SEI}) and charge transfer resistance (R_{CT}). While the slash at low frequency arises from the free diffusion of Li^+ within active material. An equivalent circuit fitting using R(QR)(CR)W was used for obtaining resistance values. The lower R_{CT} (21.9 Ω) observed in PMAI/Gr compared to PVDF/Gr (125.9 Ω) suggests that the dense functional group within the polymeric ionic liquid (PIL) binder could enhance the Li^+ conduction network within the electrode domain. This improvement is attributed to the inherent ionic conductivity of the PIL binder, setting it apart from PVDF. Furthermore, the PMAI/Gr has a lower R_{SEI} of 11.08 Ω than PVDF/Gr with 29.97 Ω, owing to PIL's influence in forming thin and stable SEI. Compared to PVDF, the PMAI binder with dense functional groups could maintain the structural integrity of electrode during a long cycling process.

Thus, PMAI binder could ease graphite's expansion stress and accelerate the formation of stable SEI film.

The ion diffusion coefficient and activation energy were measured to investigate the Li^+ kinetics at the SEI and electrode. From the EIS data at low-frequency domain, the Warburg factor (σ) was obtained from the Randles equation by plotting the real impedance vs. square root of angular frequency ($\omega^{-1/2}$)

$$Z' = R_e + R_{contact} + \sigma\omega^{-1/2} \quad \text{...eq (1)}$$

Using the Warburg factor, the Li^+ diffusion coefficient (D_{Li+}) was calculated using the following equation[158]:

$$D_{Li^+} = \frac{R^2T^2}{2A^2F^4C^2\sigma^2} \quad \text{...eq (2)}$$

Where R-gas constant (8.314 J k^{-1} mol^{-1}), T- temperature, A- electrode surface area (1.76 cm^{-2}), F- Faraday constant (96500 C mol^{-1}), C- Li^+ molar concentration (1 mol cm^{-3}). The PMAI/Gr presents higher D_{Li+} values of 1.03E-10 cm^2 sec^{-1} which is two order magnitude larger than PVDF/Gr (3.08E-12 cm^2 sec^{-1}), boosting Li^+ mobility and better electrochemical performance (Figure 5(b)). Further activation energies of PMAI/GR and PVDF/Gr were calculated from EIS at different temperatures.

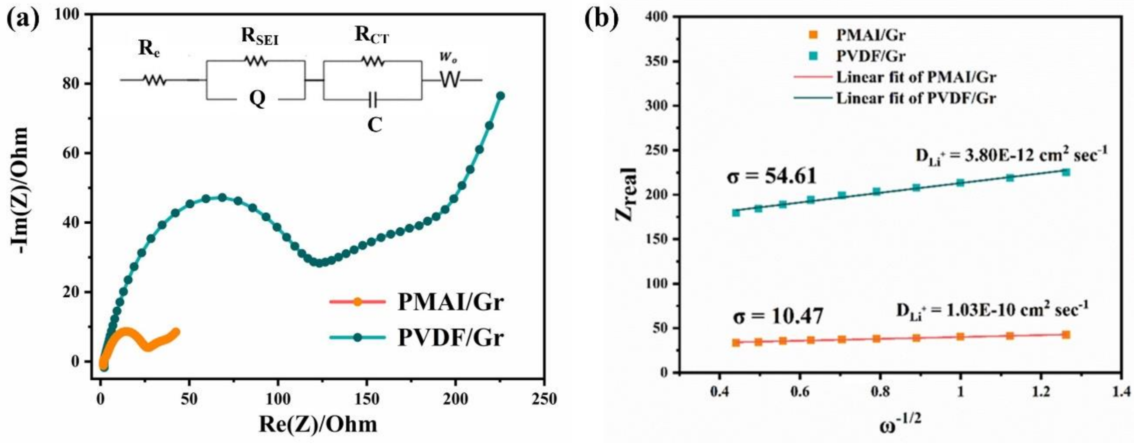

Figure 5. (a) Impedance curves of cycled PMAI/Gr and PVDF/Gr. Inset: Equivalent circuit for EIS fitting. (b) Correlation of Z_{real} and $\omega^{-1/2}$ in the low-frequency region for PMAI/Gr and PVDF/Gr.

The activation energy of ion charge transfer process signifies the barrier Li^+ must overcome when transitioning between electrode and electrolyte interface. E_a can be determined from the slope of plot log(1/R_{CT}) versus reciprocal of temperature (1/T). The Arrhenius equation for obtaining E_a is[194]:

$$\ln\left(\frac{1}{R_{CT}}\right) = \ln(A) - \left(\frac{E_a}{R}\right)\frac{1}{T} \quad \ldots \text{eq(3)}$$

Where R_{CT}- charge transfer resistance, ln(A)-frequency factor, R-gas constant and T-temperature in Kelvin. Figure 6(a) and 6(b) shows the Nyquist plots at lithiation state (~0.1 V) measured after charge-discharge cycles. Equivalent circuit fitting of the impedance spectra was carried out using R(QR)(QR)W to determine the R_{CT}. Xu et al. reported that the activation energy values change with the electrolyte compositions[307,308]. Suggesting that E_a at graphite depends on either Li^+ desolvation or the SEI nature or both. The PMAI/Gr activation energy is calculated to be 36.2 kJ mol^{-1} which is lower than PVDF/Gr with 62.1 kJ mol^{-1} from the Arrhenius plots as shown in Figure 6(c). The Li^+ kinetic studies indicate that the interfaces formed in the PMAI/Gr facilitate diffusion through the system, owing to PIL ionic conductivity and electrolyte absorption, which enhances ion mobility during charge-discharge.

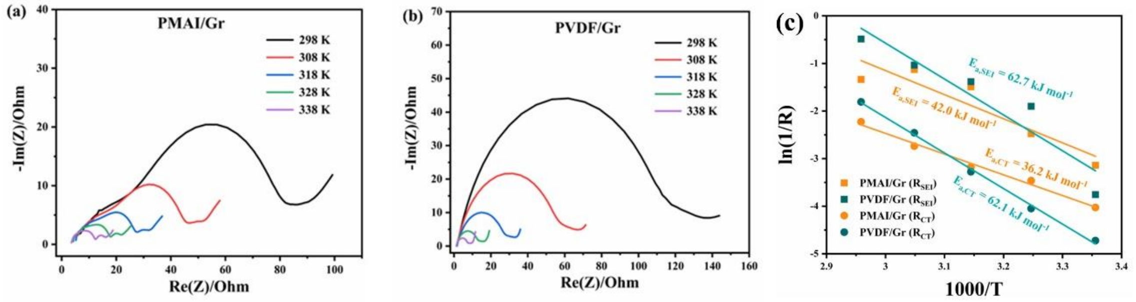

Figure 6: EIS curves at varied temperature of cycled (a) PMAI/Gr and (b) PVDF/Gr. (c) Arrhenius plots of R_{SEI} and R_{CT} at varied temperatures.

The galvanostatic charge-discharge performance was investigated to analyze the binder's ability to perform long cycle life. The formation of the SEI during the initial lithiation process is attributed to an irreversible reduction reaction involving ethylene carbonate, occurring at around 0.6 V. This phenomenon is clearly evident in the specific capacity vs. voltage profile and the dQ/dV plot for both PMAI/Gr and PVDF/Gr, as illustrated in Figure 7. Furthermore, a distinct PMAI reduction peak was observed in the voltage range of 1.8-0.8 V, preceding the reduction of the electrolyte, in both the charge-discharge curves (Figure 7(a)) and the dQ/dV plot (Figure 7(c)) of PMAI/Gr, which aligns with earlier observations recorded in CV curves. The peak is absent in the subsequent cycle due to the formation of a stable film on the surface of electrode. The PMAI binder reduction leads to a lower initial lithiation-specific capacity of PMAI/Gr to 428.9 mAh g^{-1}, than PVDF/Gr with 606.4 mAh g^{-1} and not due to excess electrolyte degradation for film formation. Hence, the initial coulombic efficiency of PMAI/Gr (78%) is higher compared to PVDF/Gr (52%). Reduction of non-soluble PMAI binder at the interface can improve binders' adherence to graphite by forming chemical bonds upon reduction[309].

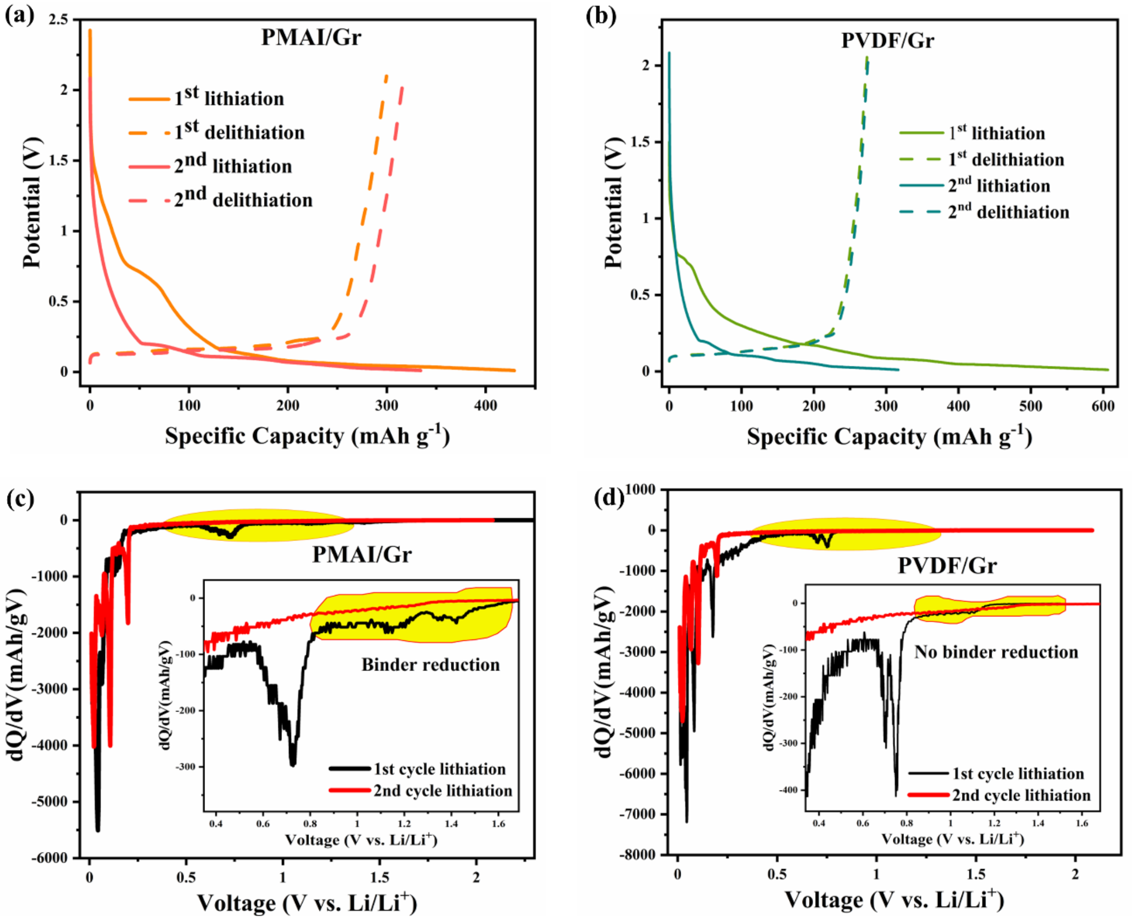

Figure 7. Lithiation-delithiation voltage profiles at 0.1C rate of (a) PMAI/Gr and (b) PVDF/Gr. dQ/dV plots for first and second lithiation cycle at 0.1C rate of (c) PMAI/Gr and (d) PVDF/Gr.

The rate capability of the anodic half cells was measured by galvanostatic charge-discharge at increasing current densities. Figure 8 summarizes the specific capacity of PMAI and PVDF binders from 0.1C to 2C. The specific capacity of PMAI/Gr are 344 mAh g^{-1}, 207 mAh g^{-1}, 112 mAh g^{-1}, 99 mAh g^{-1}, 96 mAh g^{-1} and 71 mAh g^{-1}at 0.1C, 0.2C, 0.5C, 0.75C, 1C and 2C respectively. While PVDF/Gr showed 281 mAh g^{-1}, 156 mAh g^{-1}, 95 mAh g^{-1}, 72 mAh g^{-1} 66 mAh g^{-1} and 44 mAh g^{-1} at 0.1C, 0.2C, 0.5C, 0.75C, 1C and 2C respectively. It can be studied that the water-processed PMAI binder delivers higher specific capacity values at all applied current densities than PVDF binder cells by boosting Li$^+$ transport in the electrode domain.

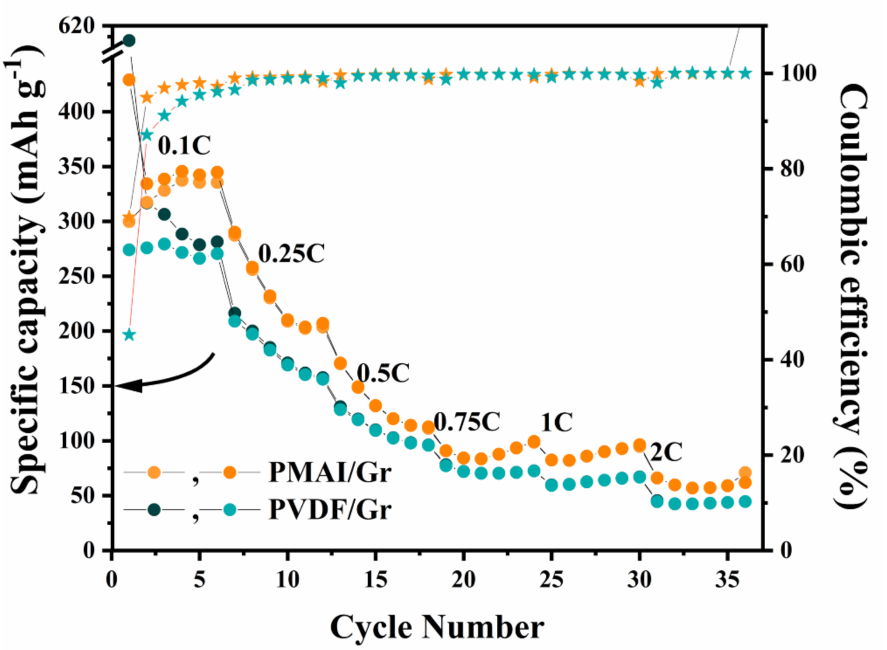

Figure 8. Charge-discharge performance at varied current densities of PMAI/Gr and PVDF/Gr.

Further investigation on long cycling capability was executed at 1C and 5C. Figure 9(a) shows PMAI/Gr and PVDF/Gr cycling performances up to 800 cycles at 1C. PMAI/Gr achieved a maximum specific capacity of 298 mAh g^{-1} with approximately 80% capacity retention of the maximum specific capacity after 750 cycles, while PVDF/Gr demonstrated a specific capacity of 228 mAh g^{-1} with 72% capacity retention. Fast charging capability at high current density of 5C, which provides harsh and accelerated ageing of the electrode materials was assessed (Figure 9(b)). PMAI/Gr exhibits a high specific capacity of 85 mAh g^{-1}, while PVDF presents a low specific capacity 47 mAh g^{-1} for 1000 cycles. The PMAI binder showed remarkable specific capacity at 5 C-rate, due to the formation of nano heterojunction between PIL/electrolyte of the electrode surface which enhances charge carrier mobility. The increase of reduction species formed at the graphite electrode caused a decline in long-cycling performance in PVDF/Gr due to growth in SEI. Whereas the high-capacity retention of PMAI/Gr at a high charging rate is linked to reduced reduction products formed between electrode/electrolyte interface. It is evident that PMAI binder has influenced electrolyte reduction in cells and demonstrated better performance when compared to conventional PVDF binder.

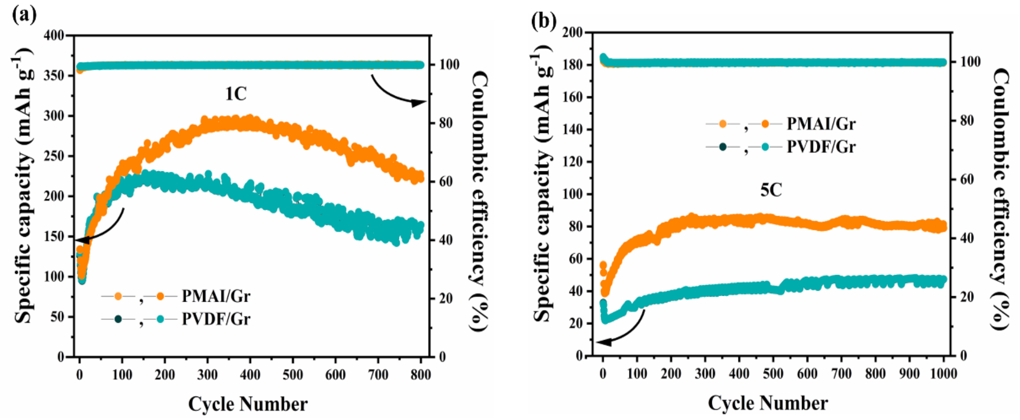

Figure 9: Galvanostatic cycling of PMAI/Gr and PVDF/Gr at (a) 1C and (b) 5C for 800 and 1000 cycles.

Battery ageing was investigated using differential capacity analysis (DCA) for characterization of the State of Health (SOH) through peak identification corresponding to phase transformations of active material. Figure 10 shows the DCA curves of different cycles as dQ/dV vs. V for PMAI/Gr and PVDF/Gr during lithiation and delithiation. The main cause for fast capacity fading of PVDF/Gr is analyzed by dQ/dV curves. A shift in the peaks towards voltages and a decrease in the peak heights as the cycle number increases during both the lithiation and delithiation is observed in Figures 10(b), 10(c). This indicates that the PVDF/Gr undergoes conductivity loss due to loss of active material[310], decomposition of electrolyte/SEI growth and lithium plating[272]. No such difference in dQ/dV peak is observed during cycling of PMAI/Gr, indicating no change in surface composition and loss of electronic pathway[311]. The analysis helped the cell polarization resistance change observed in PVDF/Gr cell upon cycling leading to capacity fade and degradation. Hence DCA analysis confirms that the PMAI binder helps in maintaining the structural integrity of the electrode and prevents parasitic reaction on the surface of the electrode.

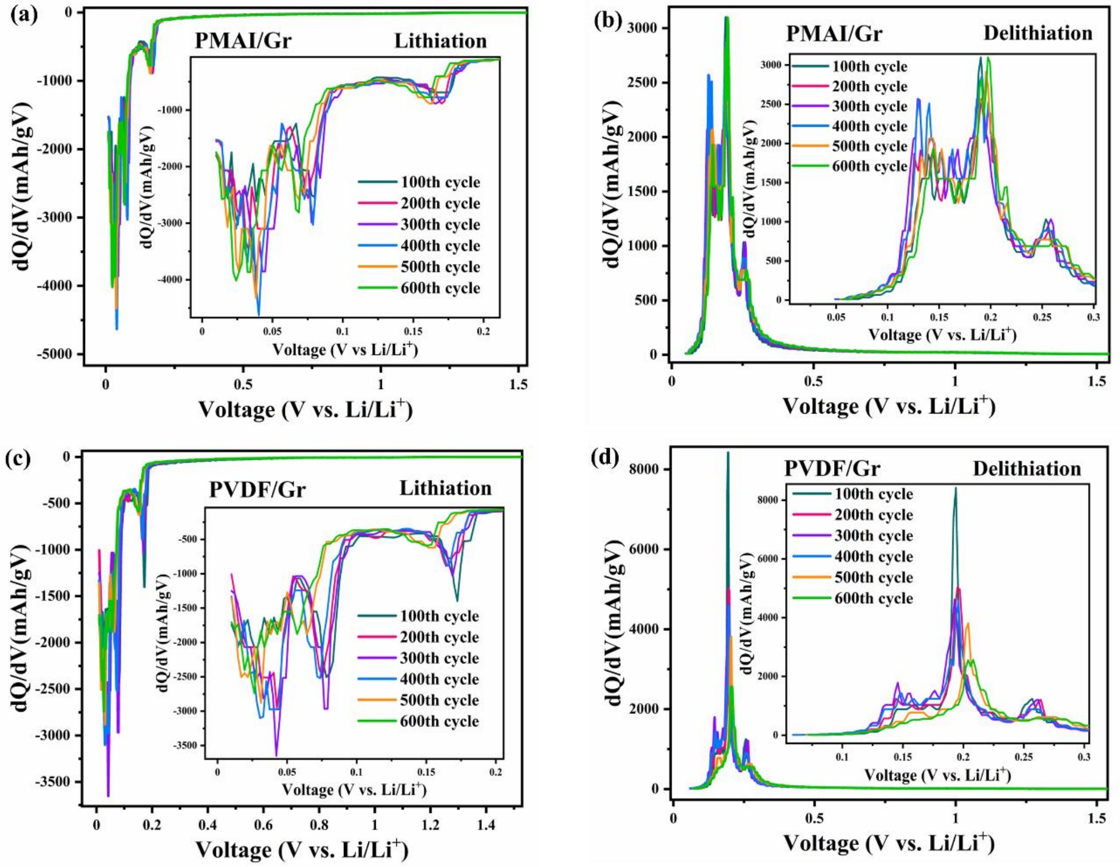

Figure 10: dQ/dV plots at different cycles of PMAI/Gr during (a) lithiation and (b) delithiation. dQ/dV plots at different cycles of PVDF/Gr during (c) lithiation and (d) delithiation.

To gain further insight into the kinetics of Li$^+$ during state of charge, dynamic electrochemical impedance spectroscopy on the cycled electrodes was measured at varied voltages. The Nyquist plots for PMAI and PVDF during lithiation and delithiation are plotted in Figure 11(a), 11(b), 11(c) and 11(d). The experimental impedance data was fitted using an equivalent circuit model RL(QR)(QR)(C/QR)W. The circuit consists of ohmic resistance (R_e), which is resistance from current collector and electrolyte; solid electrolyte interphase resistance (R_{SEI}); charge transfer resistance (R_{CT}); diffusion resistance (R_{diff}), constant phase element (CPE), capacitance (C) and Warburg diffusion element (W). The R_{SEI} and R_{CT} influence the electrochemical performances of a cell. The R_{SEI} values in PMAI/Gr during lithiation and delitiation are lower than PVDF/Gr (Figure 11(e) and 11(f)). Indicating the formation of thin and stable SEI on the surface of PMAI/Gr electrode which protects and accommodates the volume change during cycling.

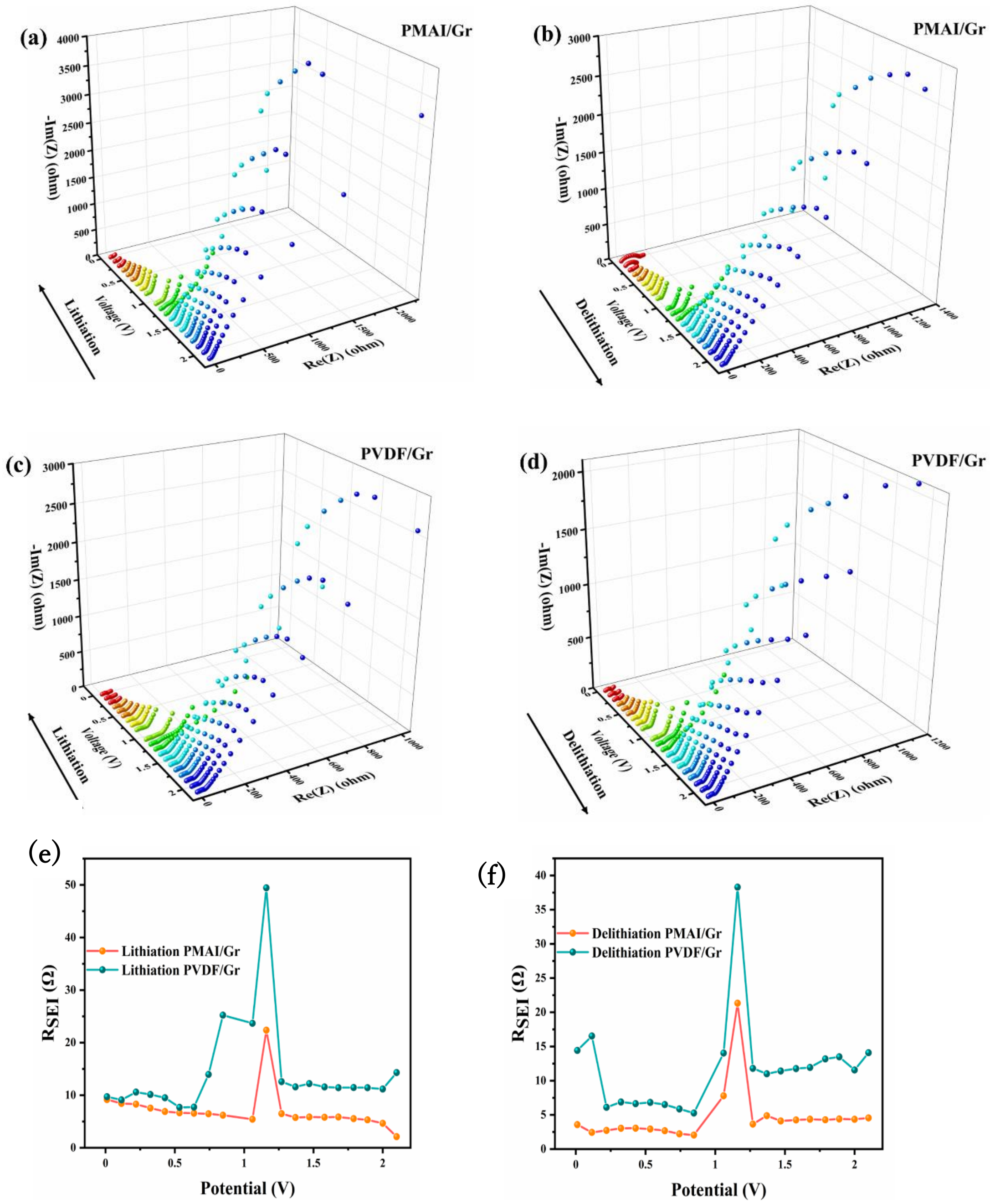

Figure 11: Nyquist plots at different voltages of PMAI/Gr during (a) lithiation and (b) delithiation. Nyquist plots at different voltages of PVDF/Gr during (c) lithiation and (d) delithiation. R_{SEI} vs. voltage plots during (c) lithiation and (d) delithiation of cycled anodic half-cells.

In contrast, high R_{SEI} values of PVDF/gr are ascribed to poor influence of PVDF binder on SEI formation and structural integrity of electrode[112,165]. The higher R_{SEI} values in the lithiation voltage region than the rest of voltage region of PMAI/Gr due to the Li concentration gradient within the electrode is more pronounced. Thereby hindering the lithiation process at the SEI and the electrode. The abrupt increase in R_{SEI} values at ~ 1 V for both PMAI/Gr and PVDF/Gr electrodes may be attributed to the initiation of lithiation and the termination of delithiation processes. These events can result in changes to the concentration gradient on either side of the SEI and alterations in ionic mobility within the SEI, subsequently influencing the overall resistance of the cell.

Surface chemistry of the cycled cells was obtained from XPS analyses to understand the species composition in the SEI. For the electrodes containing PMAI and PVDF binders, the signals of C 1s (ca. 284 eV), O 1s (ca. 535 eV) and F 1s (ca. 686 eV) were recorded and presented in Figure 12. The species concentration calculated from the XPS analyses is tabulated in Tables 1, 2 and 3. In particular, the PMAI/Gr and PVDF/Gr electrodes C 1s spectra contributed significantly to sp3 carbon at 284.6 eV[207,312]. Both the electrodes contain the same species derived from electrolyte decomposition on the surface such as C-O, C=O, and Li_2CO_3 with almost the same concentration for C=O and Li_2CO_3. However, the concentration of C-O species is high due to the contribution of the C-N which overlaps with the C-O peak[313]. This confirms that the reduction of binder before electrolyte degradation leads to the formation of SEI containing nitrogen species which helps in the facile transport of Li^+ through SEI while limiting Li^+ flux localization[314]. The C-O and C=O peaks can contribute from the binder, leading to a higher concentration of the species. The presence of C-O, C=O and Li_2CO_3 species in O 1s spectra and its similar concentration in the PMAI/Gr and PVDF/Gr electrode confirms that the presence of the species at the SEI and the high concentration of C-O peak in C 1s spectra is due to the overlap of C-N species[315]. F 1s spectra showed the presence of Li_xPOF_y and LiF in both electrodes, but the PMAI/Gr electrode has the presence of a high concentration of LiF[316]. Zhang et al. reported that the inorganic species in SEI, such as Li_2CO_3 and LiF, offer mechanical and chemical protection while also regulating Li^+ transport. Despite the moderately low ionic conductivity of Li_2CO_3 and LiF, surprisingly when they come into contact, they promote accumulation of space charges at their interfaces. This phenomenon generates higher concentration of ionic carriers, enhances Li^+ transport and reduces electron leakage. Hence the high concentration of LiF and presence of Li_2CO_3 contributes to increased current efficiency and long-term cycle stability[317].

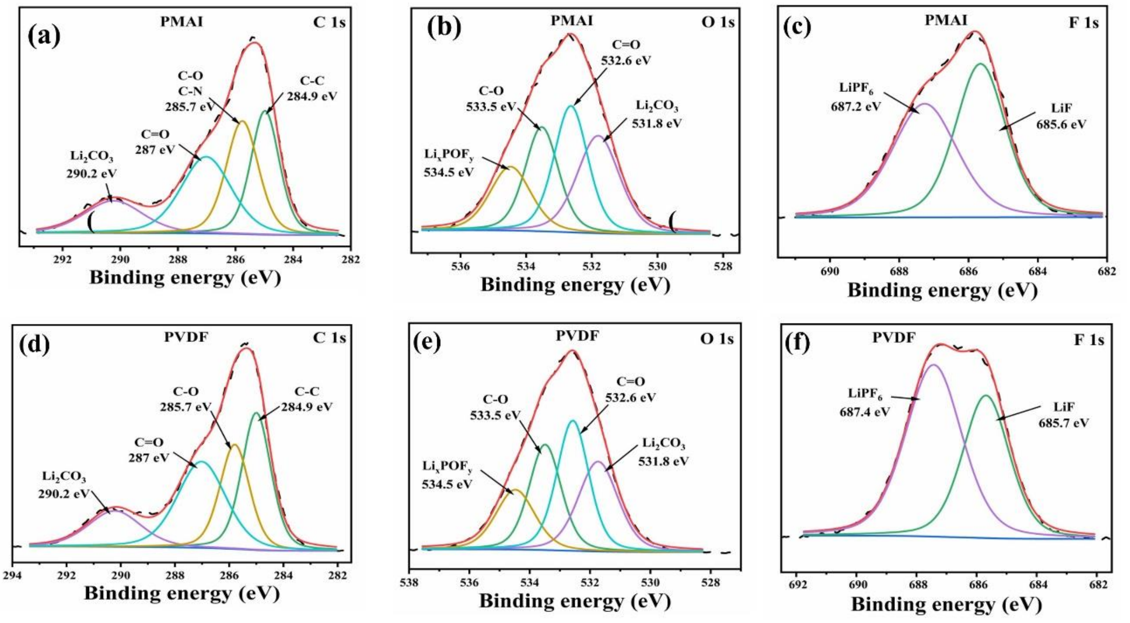

Figure 12: XPS spectra of cycled PMAI/Gr of (a) C 1s, (b) O 1s and (c) F 1s. XPS spectra of cycled PVDF/Gr of (d) C 1s, (e) O 1s and (f) F 1s electrodes.

Table 1: Species composition percentage is determined by analyzing the area under the curve of C 1s XPS spectra.

C 1s	C-C	C-O	C=O	Li_2CO_3
PMAI	27.30%	28.30%	29.80%	14.50%
PVDF	30.10%	23.50%	31.50%	14.40%

Table 2: Species composition percentage is determined by analyzing the area under the curve of O 1s XPS spectra.

O 1s	Li_2CO_3	C=O	C-O	Li_xPOF_y
PMAI	28.40%	29.50%	24%	17.90%
PVDF	26.50%	30%	25.20%	17.20%

Table 3: Species composition percentage is determined by analyzing the area under the curve of F 1s XPS spectra.

F 1s	LiF	$LiPF_6$
PMAI	51.60%	48.90%
PVDF	40.80%	59.40%

The surface morphology and microenvironment of the pristine and aged graphite electrodes were studied using SEM to further investigate the effect of binder on graphite electrode structure and electrochemical stability. The SEM images of the pristine electrode surface are shown in Figure 13(a1), 13(b1). As noted, the graphite particles displayed uniform distribution throughout the surface and interior of electrodes. After cycling, the aged electrodes' surface SEM images shown in Figure 13(a2), 13(a3) showed shining with no cracks in the PMAI-based electrode, indicating the stable electrode structure inhibits particle degradation and enhances lithium mobility during cycling. In the PVDF-based electrodes cracks and voids are formed across the surface which may hinder the Li^+ diffusion and increase the electrolyte decomposition (Figure 13(b2), 13(b3)). This supports the higher R_{SEI} observed after fitting impedance, impacting electrochemical performances and Li^+ diffusion coefficient.

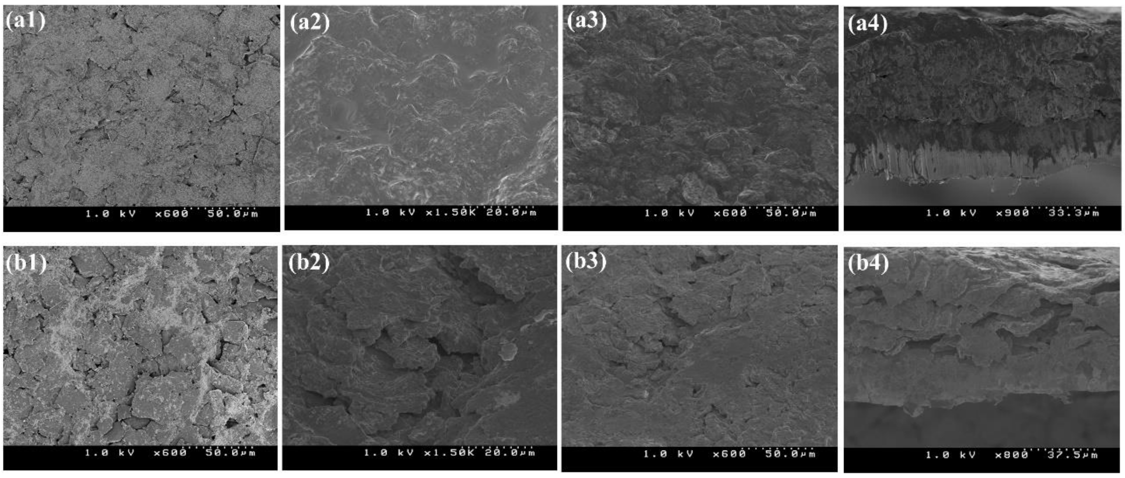

Figure 13: Top view: (a1) SEM image of pristine PMAI/Gr electrode. (a2) and (a3) SEM images of cycled PMAI/Gr electrode. Top view: (b1) SEM image of pristine PVDF/Gr electrode. (b2) and (b3) SEM images of cycled PVDF/Gr electrode. Cross-sectional SEM images of cycled (a4) PMAI/Gr and (b4) PVDF/Gr electrodes.

On the cross-section image of aged electrodes, as shown in Figure 13(a4), the graphite particles are evenly distributed and compact with no contact gap between the current collector and the graphite particles of aged PMAI-based electrodes. Whereas the cross-section image of the aged PVDF-based electrode shows cracks in the electrode depth and also loss of contact between the current collector and graphite particles (Figure 13(b4)). Hence the capacity loss observed in PVDF/Gr was probably induced by electrode structure degradation. The presence of PMAI binder is not solely located on base plains, but also aggregates at the edges, effectively bridging various graphene layers. Thereby contributing to the prevention of exfoliation of graphite by acting as nano-scale stitches[303]. It can be concluded that incorporating PMAI binder with ionic conductive properties, will enhance the Li^+ transport along the electrode and increase the specific capacity, thereby aiding cell performance and preserving electrode's integrity throughout cycling.

Conclusion:

In conclusion, a novel water-soluble poly(oxycarbonylmethylene 1-allyl-3-methyimidazolium (PMAI), containing high-density imidazolium functional groups, was synthesized and characterized using NMR and FT-IR. PMAI was evaluated as a binder using an aqueous processing method for battery electrode fabrication of LIBs, offering a more sustainable and cost-effective alternative to the conventional organic-processed PVDF. The presence of dense polar groups and free anions enhances affinity with electrolyte solvent and increases the Li^+ diffusion coefficient (1.03E-10 cm^2 sec^{-1}). The CV, charge-discharge profile, and dQ/dV analyses have consistently demonstrated that PMAI gets reduced before that of ethylene carbonate in PMAI/Gr. This unique behavior plays a crucial role in the formation of a stable and thin SE that is enriched with inorganic (LiF, Li_2CO_3) and C-N species. The resulting SEI layer not only fosters reduced SEI resistance (11.08 Ω) but also contributes to lower activation energy (36.2 kJ mol^{-1}) and decreased overpotential (0.150 V), collectively enhancing the electrochemical performance and efficiency compared to PVDF/Gr. PMAI/Gr showed enhanced long cycling performances with higher capacity retention of 80% after 750 cycles at 1C with a maximum specific capacity of 298 mAh g^{-1} than PVDF/Gr. In addition, PMAI/Gr demonstrated superior charge-discharge at a 5C fast charging rate with a maximum specific capacity of 85 mAh g^{-1} for 100 cycles. This can be elucidated by the greater ionic conductivity and enhanced electrolyte absorption exhibited by PMAI/Gr binders. These properties further increase lithium mobility within the electrodes. Postmortem analysis on the aged electrode reveals a crackless uniform surface on the PMAI/Gr electrode, in contrast to PVDF/Gr electrode. The difference can be attributed to the exceptional peel strength observed by the PMAI binder in the peel test. The results not only establish PMAI as a better binder for replacing PVDF in LIBs but also act as a catalyst in exploring deeper into the mechanisms of densely functional group polymers that underlie the unique functionality of PIL binders in the enhanced electrochemical performance.

Chapter 6

Novel Densely Imidazolium Functionalized Water Soluble Poly(ionic liquid) Binder for Hard Carbon Anode in Sodium-Ion Batteries

Abstract

Sodium-ion battery (SIB) operation has always been challenging due to sluggish Na^+ kinetics and transport limitations at the electrode interface and along the electrode domain. Enhancing the specific capacity through tuning the desolvation energy, charge transfer resistance and ionic conductance using functionalized binder in hard carbon (HC) is poorly understood. Here, a novel water-soluble concentrated imidazolium functionalized poly(ionic liquid) (PIL) binder, Poly(oxycarbonylmethylene 1-allyl-3-methyimidazolium) (PMAI), was synthesized. The electrochemical performance of HC anode using PMAI binder was studied and compared with conventional PVDF binder. The PMAI binder is shown to be reduced during cyclic voltammetry and charge/discharge at 0.9 V vs. Na+/Na, leading to better adhesion with electrode components and formation of functionalized SEI. The PMAI/HC`s initial coulombic efficiency is 74% and a maximum specific capacity of 254 mAh g^{-1} with a capacity retention of 96.2% after 200 cycles at 60 mA g^{-1}. PMAI-containing electrodes showed better rate capability at different current densities than PVDF binder. PMAI-based HC electrode exhibits an enhanced Na^+ diffusion coefficient, low R_{SEI} and R_{CT} and decreased activation energy of desolvation, which is ascribed to densely polar ionic liquid groups along the binder, enhancing the ionic conductivity in electrode, influencing the Na^+ diffusion kinetics at the surface and formation of functionalized SEI due to binder reduction. This work shows that the battery-specific capacity can be enhanced using densely functionalized PIL, which is considered for further optimization of SIB.

Introduction:

In addressing modern societal demands for electronic devices characterized by enhanced efficiency and performance, a need for high-performance, affordable and safe energy storage technologies has become increasingly pressing[163,318]. Over the past thirty years, lithium-ion batteries (LIBs) have served as attractive power sources, offering applications ranging from small portable devices to transportation systems. However, concerns have emerged regarding the sustainability of lithium as a resource, driven by concerns related to its scarcity, cost and concentrated geographical distribution. Considering the growing demand for rechargeable batteries, these drawbacks limit future large-scale applications. Research hovering over sodium-ion batteries (SIBs) has garnered attention, mainly due to the abundant and readily available sodium in nature, low cost, and high electrochemical potential[11]. However, the larger sodium ionic radius has created challenges related to phase stability, ion kinetics and interphase formation. Consequently, the quest for cost-effective, high-performance electrode materials for SIBs remains a significant hurdle. Recent interests are in exploring various cathodes for SIBs, such as layered transition metal oxides[319–321] and polyanion-type compounds[322–326]. Simultaneously, potential anode materials have been reported encompassing hard carbon[327], soft carbon[328], metal oxide[329], transition metal sulfide[330], transition metal dichalcogenides[331] and nano composite[332]. Among anode materials, sodium alloy anode materials offer significantly higher capacities. However, they exhibit substantial volume expansion during sodiation, leading to structural damage and consequently poor cycle durability[333]. Therefore, hard carbon remains promising, considering the cost implications for potential scaling up, and stands out as the most promising anode material.

Hard carbon emerges as a promising anode for LIBs and SIBs, attributed to its low operating potentials and high specific capacities[334]. The poor specific capacity and capacity retention are caused by the formation of uneven, thick and poor mechanical strength solid electrolyte interphase (SEI) at the defect-rich HC[335,336]. Significant approaches have been directed towards crafting better SEI by optimizing defects[337,338], artificial SEI[237], dopant modification[339], presodiation[340] and additives[279]. Nevertheless, these methods involve intricate synthetic routes, are sensitive to experimental conditions, have high costs and lack desirable scalability. Enhancing battery performance involves using a functional binder, a crucial component of electrodes. An alternative approach to introducing a pre-existing protective layer is to choose a different functional polymer as a binder which creates a thin polymer layer on the HC. Functional polymers are expected to modify the surface chemistry of the electrode, serving as a protective layer between the active material and the electrolyte at the electrode-electrolyte interface[170]. Furthermore, the poor rate capability of HC resulting from sluggish Na^+ diffusion kinetics can be improved by incorporating Na^+ diffusion channels into the electrode domain. This is achieved by employing a Na^+ conducting functional binder, thereby enhancing the stability and rate performance of SIBs. To date, poly(vinylidene fluoride)[247], carboxymethyl cellulose[247], chondroitin sulfate A[250], sodium lignosulfonate[249] and trifunctional sodium alginate/polyethylene oxide[248] are reported as binders for HC. PVDF contains inactive C-F functional groups that do not provide enough strength to hold the electrode components, leading to poor cycle stability. In addition, it uses N-methyl pyrrolidone, a toxic organic solvent in slurry preparation. While the other binders provide electrode stability and somewhat influence SEI formation through the presence of hydroxyl or carboxylic groups or sulfate. Nevertheless, these groups cannot offer improved ion channels into the electrode, enhance the wettability of the electrolyte on the electrode for Na^+ diffusion kinetics, or lower the activation energy of desolvation, respectively. These factors enhance the rate capability and the electrodes' long cycling stability. Therefore, a suitable dense functional group binder is desired to improve the Na^+ kinetics and SEI, impacting the electrochemical performance of SIBs.

This study synthesises a novel poly(ionic liquid) (PIL) binder incorporating high-density oxycarbonyl 1-allyl-3-methylimidazolium functional groups. The PIL, designated poly(oxycarbonylmethylene 1-allyl-3-methyimidazolium) (PMAI), is polymethylene based polymer, featuring a rigid polymer backbone that distinguishes it from polyethylene-based binders, suggesting unique properties[136,137]. The dense arrangement of consecutive functional groups within the PIL is anticipated to enhance ion conduction into the electrode domain through a hopping mechanism along the polymer chain. The superior wettability of PIL with the electrolyte, coupled with polar functional groups, is expected to boost ion mobility by forming a PIL/electrolyte heterojunction at the interface. This phenomenon will likely reduce the activation energy associated with Na^+ desolvation and influence electrolyte decomposition. Notably, the imidazolium group exhibits reduction at a lower potential, facilitating the formation of a more effective SEI and promoting adhesion to graphite upon reduction[303]. Furthermore, the dense functional groups of PIL binder serve a protective role, mitigating excess electrolyte decomposition on the electrode surface. This work introduces, for the first time, the utilization of a PIL binder in an HC anode for SIBs. Various electrochemical and post-mortem studies were conducted to study the impact of dense functional group PIL binder on electrochemical performance and provided a comparative analysis with the conventionally used PVDF.

Experimental:

Preparation of Binder:

Poly(oxycarbonylmethylene 1-allyl-3-methyimidazolium) was prepared by cation exchange with the polymer poly(hydroxycarbonylmethylene) (PFA) that was obtained from poly(ethoxycarbonylmethylene) (PECM) by ester hydrolysis. PECM was synthesized following our previous reports[318]. PHCM was synthesized by base hydrolysis of PECM by refluxing a solution containing EtOH:H_2O (2:1) and excess of KOH for 24 hr. After the completion of the reaction, the reaction mixture was acidified upon adding 1N HCl and dialyzed using Fisherbrand regenerated cellulose dialysis tubing. Following water from the resulting solution was vacuum evaporated to yield PHCM. 2 gm of 1-allyl-3-methylimidazolium chloride (AmImCl) was added to 100 ml water and was anion exchanged using a column containing amberlite IRN78 OH hydroxide form (Supelco) to obtain 1-allyl-3-methylimidazolium hydroxide (AmImOH). AmImOH was concentrated by evaporating water and then vacuum dried overnight under 60 ºC. To obtain PMAI, 200 mg of PHCM and 482 mg of AmImOH were added to 20 ml of water and the resulting mixture was stirred at room temperature overnight. After that, the water was removed, followed by washing with acetone and then the product was dried under a vacuum. PMAI polymer yield was determined to be 78%.

Hard Carbon Anodes preparation:

80 wt% HC (Kuranode Type 2(5µm)), 10 wt% super P conductive carbon (Alfa Aesar) and 10 wt% binders (PMAI or PVDF) were mixed using a solvent (water for PMAI and NMP for PVDF) to form a homogenous slurry, which was coated on copper foil using doctor blade (100µm) and dried under vacuum at 80 ºC for 24 hr. respectively. Subsequently, the dried coated electrodes were cut into 13 mm discs. CR2025 coin cells were fabricated using 1M $NaClO_4$ in ethylene carbonate (EC)/propylene carbonate (PC) electrolyte, glass fiber (Whatman) as separator and sodium disc as a counter electrode. The anodic half-cells are named PMAI/HC and PVDF/HC.

Synthetic and electrochemical characterization:

PMAI chemical structure was analyzed using ^{1}H NMR and ^{13}C NMR (Bruker Advance II-400 MHz spectrometer). Further FT-IR spectroscopy (PerkinElmer 100 FTIR spectrometer) was used to evaluate functional groups of the polymer. The thermal stability of the binder was determined using thermogravimetric analysis (TGA, Hitachi STA7200 thermal analysis system) under N_2 flow at a 10 ºC min^{-1} heating rate. Binder adhesion strength was tested by peel test using Instron 3342 apparatus. A 40 mm length HC electrode was affixed with adhesive tape on the HC side and peeled at a displacement rate of 2 mm min^{-1} at 180 ºC. Moreover, Biologic Science Instruments measured cyclic voltammetry (CV) at different rates from 0.1 to 1 mV s^{-1} between 0.01 and 2.5 V vs. Na^+/Na. The electrochemical impedance spectroscopy (EIS) was performed at frequencies ranging from 1mHz to 1MHz using Biologic Science Instruments at an amplitude of 10 mV. The galvanostatic charge-discharge curves were obtained from Electrofield ABE1024 at different current densities. Microstructure morphology was observed by SEM (using Hitachi S-4500) at an accelerating voltage of 1.0 kV. The elemental analysis and chemical bonding formation were analyzed using X-ray photoelectron spectroscopy (Fisons instruments S-probe TM 2803).

Results and discussions:

We synthesized novel high-density oxycarbonyl 1-allyl-3-methylimidazolium functional groups containing PIL, as represented in Figure 1(a). The three-step process includes bulk radical polymerization followed by base-catalyzed ester hydrolysis and, lastly, neutralization. The use of 1-Allyl-3-methylimidazolium is assigned to its superior thermal stability, diminished viscosities, improved ionic conductivity, and wide potential windows[304,305]. Further, the chemical structure was tested using ^{1}H NMR spectra, as shown in Figure 1(b). The methine proton of the polymer main chain appeared at 2.98 ppm, and the signals of the imidazolium cation unit are assigned in the spectra. The ^{13}C NMR spectrum of PMAI featured all carbon atoms of the polymer, wherein the characteristic methine and methylene carbon peaks appeared at 62.4 ppm and 30 ppm, respectively (Figure 1(c)). Peak integration of methine and methylene peaks was performed to evaluate each carboxylate unit interacting with an imidazolium unit. The integration ratio of the proton was determined to be 1:2 of methine to methylene proton peak, as shown in Figure 1(d) and 1(e), proving the complete reaction.

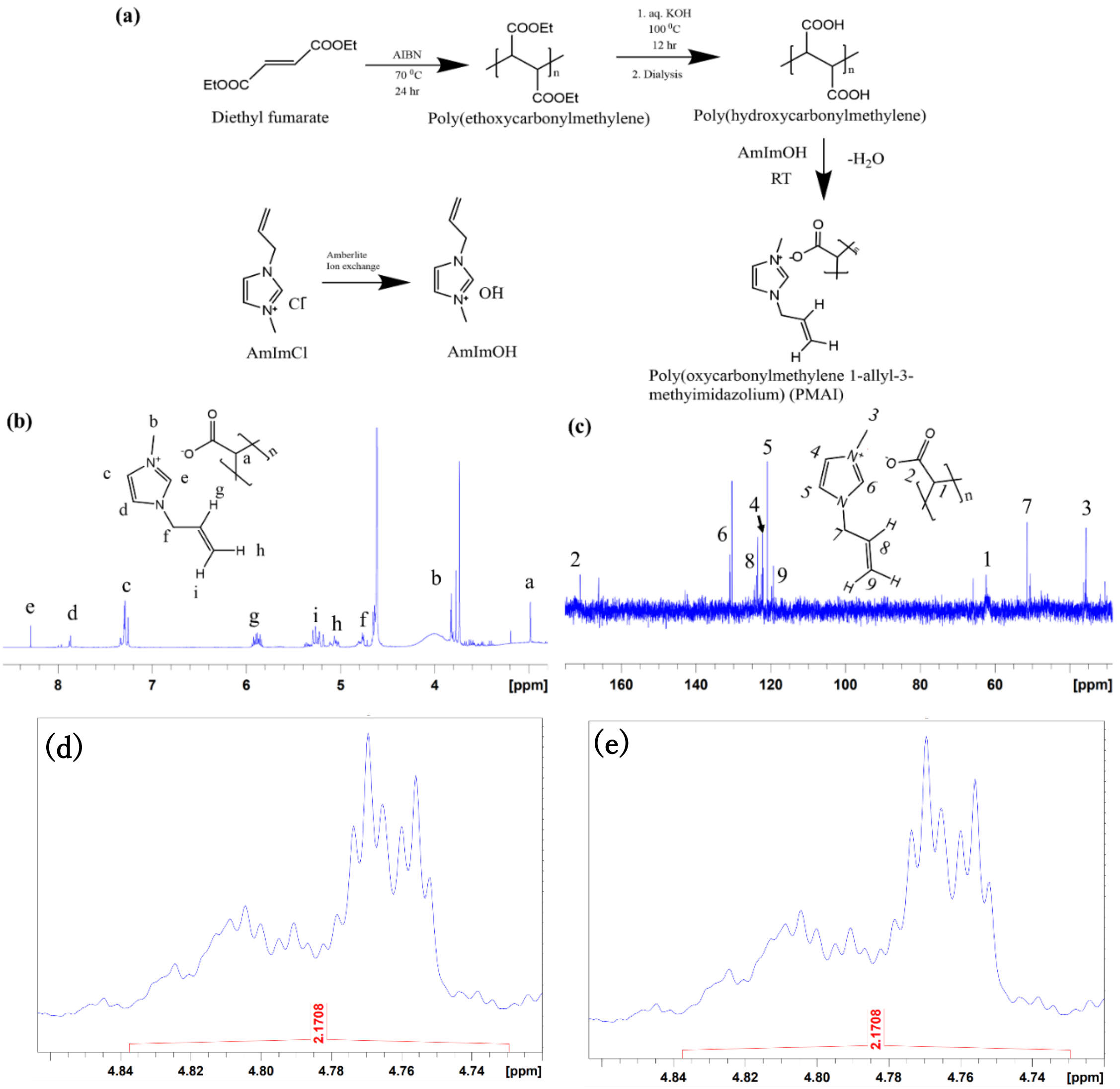

Figure 1: (a) Synthetic route to PMAI. (b) ^{1}H NMR spectrum (D_2O). (C) ^{13}C NMR spectrum (D_2O). ^{1}H NMR peak and integration value of (d) methine peak of PHCM and (e) methylene peak of imidazolium

Initial confirmation of polymer formation was indicated from the pH, which was determined to be 8.0 (Figure 2(a)). FT-IR spectroscopy revealed a board band centered at 3500 cm^{-1} for COO^-AmIm^+ stretching and a carbonyl peak of carboxylate at 1725 cm^{-1} (Figure 2(b))[298,318]. Imidazolium unit is characterized by the presence of C-N stretching vibration at 1582 cm^{-1}, C-H unsymmetrical bending vibration[341,342] at 1157 cm^{-1} and C=C-H at 3151 cm^{-1}. Figure 2(c) presents PFA's MALDI-TOF mass data, revealing that the polymer has continuous carboxylic molecules. For example, the ~44 g mol^{-1} difference in the 1007.61 and 1051.93 m/z values in Figure 2(c) for PFA is equal to the molecular weight of -COOH functional groups of the polymer. TGA of the resulting PMAI polymer was carried out to determine the thermal stability (Figure 2(d)). The initial 10 wt.% decomposition temperature is ~150 ºC. Indicates the binder stability at higher operating temperatures of SIBs. Characterization of PMAI revealed the formation of the polymer through this novel synthetic route, paving the way for subsequent potential applications.

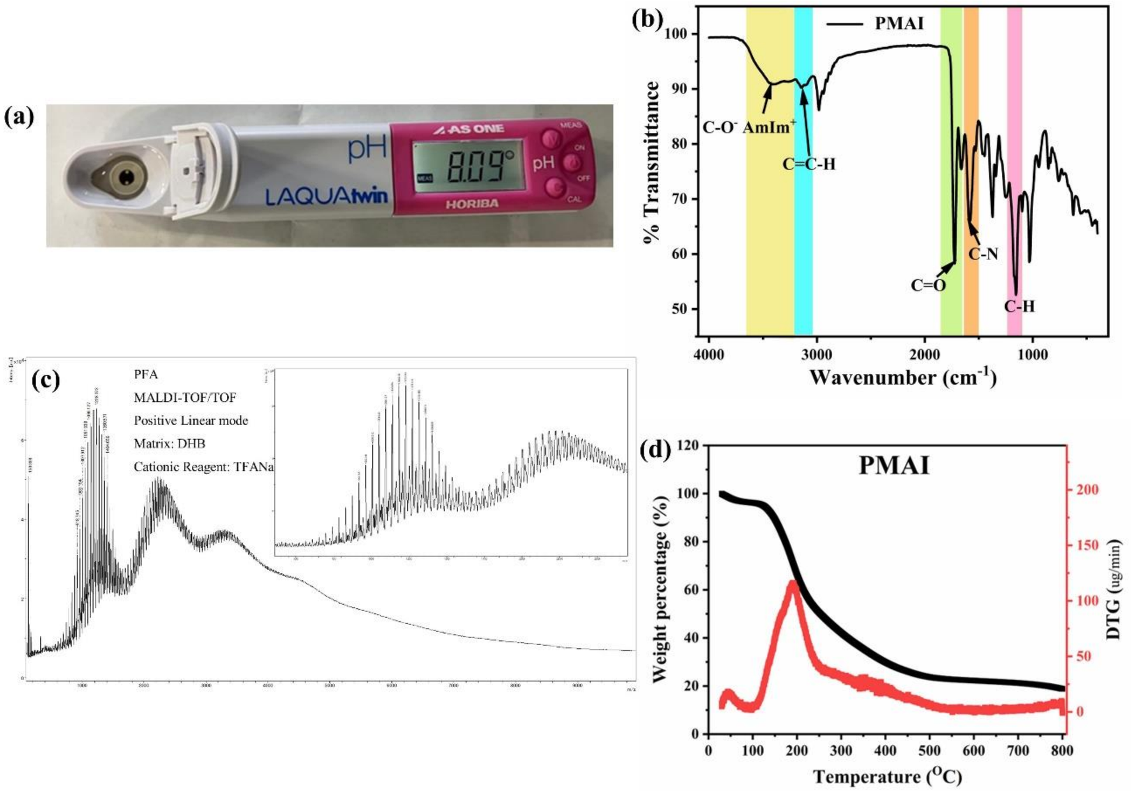

Figure 2: (a) pH measurement of PMAI using pH meter. (b) FT-IR profile of PMAI. (c) MALDI-TOF data of PFA. (d) TGA profile of PMAI.

The ability to maintain a stable structure even after extended cycling is attributed to strong adhesion between the current collector and active material using a functional binder, ensuring structural stability[343]. Consequently, the 180º peel test investigated the strong PMAI adhesion to active material and copper foil, correlating to stable electrochemical performance[344]. Figure 3 illustrates the force vs. displacement profile, revealing that the average force exerted by a PMAI-based electrode is determined to be 11.0 N, whereas that of a PVDF-based electrode is 9.9 N. The strong adhesion of the high-density functional group polymer binder PMAI is due to the strong interaction of the functional polar group of the binder with the HC and copper, which prevents separation of HC particles and ensures retention of the electrode's mechanical and electrical integrity upon cycling forming self-healing capability.

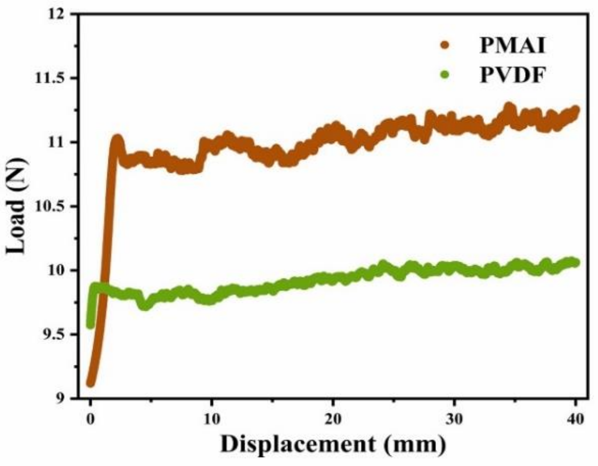

Figure 3: Displacement vs. load of electrode peel test containing different binders.

To compare the impact of the two binders on the HC material's electrochemical properties, we examined the Na^+ intercalation/deintercalation processes within the voltage range of 0.01-2.5 V vs. Na^+/Na. This investigation includes cyclic voltammetry (CV), impedance spectroscopy and galvanostatic charge–discharge. The CV profiles of both PMAI/HC (Figure 4(a)) and PVDF/HC (Figure 4(b)) at 0.1 mV s^{-1} exhibit SEI formation peak at ~0.5 V in the first reduction cycle before Na^+ reduction at ~0.1 V. The Na^+ anodic/cathodic peaks of PMAI/HC and PVDF/HC exhibited at 0.01/0.14 V and 0.01/0.17 V, respectively, suggesting PMAI/HC has lower polarization and faster ion kinetics than PVDF/HC. The second and third CV curves almost overlap, suggesting the absence of continuous electrolyte reduction and a stable SEI layer formation during the first cycle in both PMAI/HC and PVDF/HC. Additionally, only in PMAI/HC a board peak is observed at ~0.7 V, corresponding to reduction of the imidazolium group within the binder[303], which precedes reduction of EC in the electrolyte. Thus, leading to the formation of functionalized SEI which might facilitate ion diffusion and limit excess electrolyte reduction. CV curves of PMAI/HC and PVDF/HC at different scan rates are shown in Figure 4(c) and 4(d).

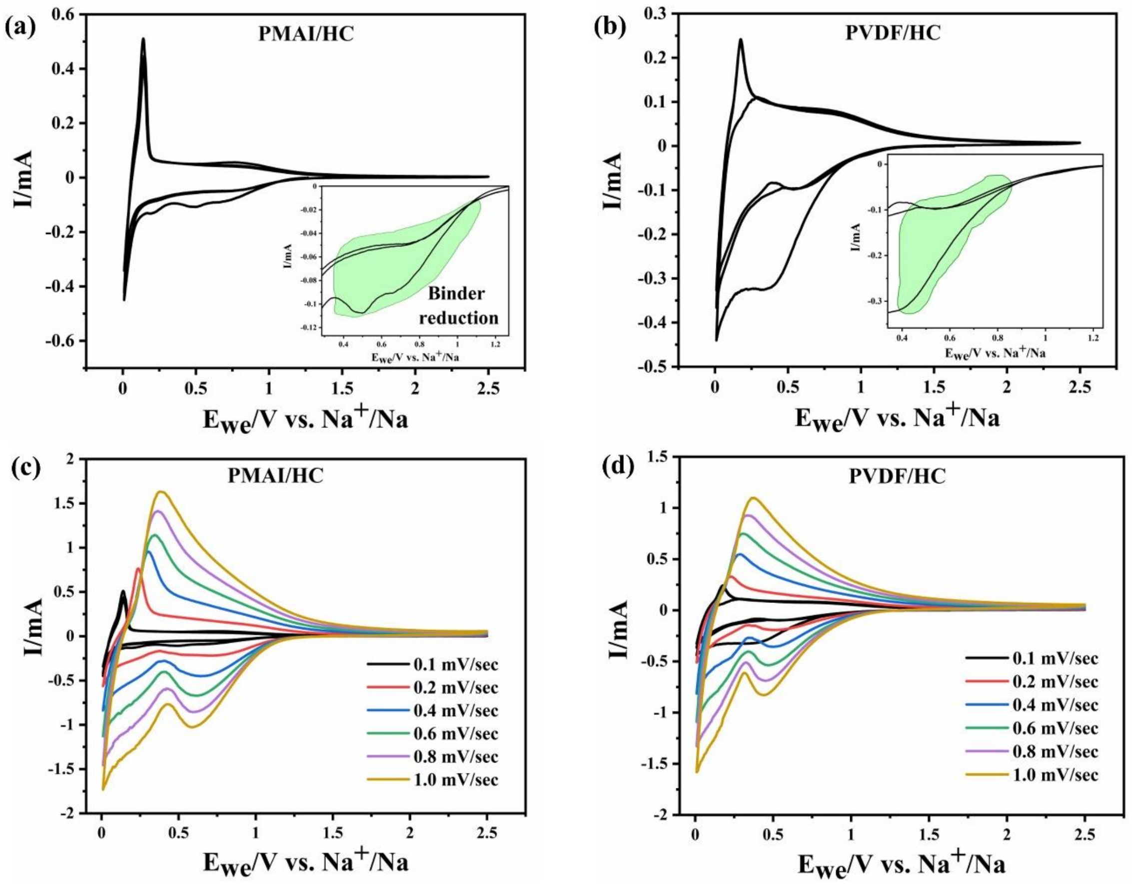

Figure 4: CV profiles of (a) PMAI/HC and (b) PVDF/HC at 0.1 mV s^{-1}, Inset: Zoom in view of CV. CV profile at different voltage rates of (c) PMAI/HC and (d) PVDF/HC.

Further analysis was conducted to elucidate Na^+ diffusion kinetics at the interphase and electrode bulk. Figure 5(a) shows the Nyquist plots of the HC-based anodic half-cell before and after CV studies, exhibiting a semicircle in the high to medium-frequency region and a linear line in the low-frequency range. The semicircle corresponds to internal resistance, charge transfer resistance across electrolyte/electrode interface (R_{CT}) and SEI resistance (R_{SEI})[345,346]. The resistance values are determined by circuit fitting of EIS curves using the circuit $R_s(QR_{SEI})(QR_{CT})W$. Where R_s represents ohmic resistance, Q denotes constant phase element and W is Warburg resistance. Both PMAI/HC and PVDF/HC showed a decrease in the diameter of the semicircle after CV, indicating a decrease in resistance due to the formation of SEI at the surface of the HC electrode. The circuit fitting analysis of after CV EIS data for PMAI/HC reveals relatively smaller resistances for R_{CT} at 3360 Ω and R_{SEI} at 29.44 Ω compared to PVDF/HC, where R_{CT} is 9738 Ω and R_{SEI} is 87.87 Ω. This observation suggests that the PMAI binder contributes to forming a thinner SEI, promoting favorable ion transfer processes and resulting in lower polarization. Moreover, the Warburg impedance (Z_w), represented as an inclined linear line within low-frequency region of Figure 5(a), correlates to Na^+ diffusion coefficient (D_{Na+}) of sodium ions. D_{Na+} is calculated using[158,318]:

$$D_{Na^+} = \frac{R^2T^2}{A^2n^4F^4C^2\sigma^2} \dots . eq(1)$$

Where R stands the gas constant, T represents temperature, A denotes surface area of electrode, n is the no. of electrons per sodium during oxidation, F signifies Faraday constant, C is Na^+ concentration, and σ represents Warburg factor which is linked to Z`:

$$Z' = R_e + R_{contact} + \sigma\omega^{-1/2} \dots . eq(2)$$

Figure 5(b) shows the correlation between Z_{real} (Z`) and $\omega^{-1/2}$ of PMAI/HC and PVDF/HC in the low-frequency region. With respect to eq (1) the slope of the linear fit is inversely related to D_{Na+}. The D_{Na+} calculated value of PMAI/HC is 3.35E-13 cm^2 s^{-1}, three times the value of PVDF/HC with 1.01E-13 cm^2 s^{-1}. Here, the interfacial behavior influence diffusion coefficient, attributed to the coupling of reduced charge transfer resistance, decrease in SEI layer resistance and ionic conductivity promoted by PMAI in electrode domain.

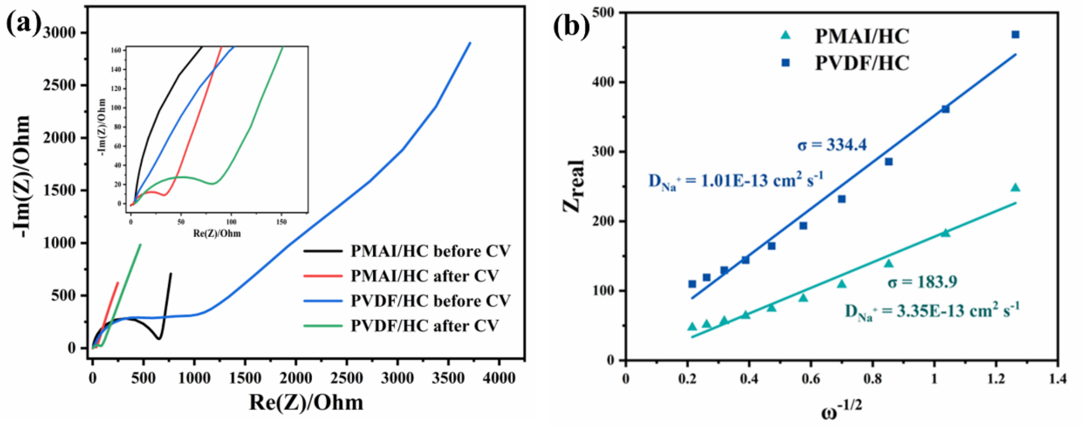

Figure 5: (c) EIS spectra of anodic half-cells. (d) The Z` vs. $\omega^{-1/2}$ curves in the low-frequency range.

To investigate, the binder influence on SEI layer and interfacial kinetics. Temperature-dependent EIS experiment was conducted to reveal ion diffusion kinetics. By employing temperature dependance R_{CT} and R_{SEI} values, activation energy (E_a) can be determined for Na^+ intercalation at potential 0.1 V using the Arrhenius equation[194,347]:

$$\text{Ln}(1/R_{CT}) = \ln(\text{A}) - \frac{E_a}{R}\left(\frac{1}{T}\right) \ldots eq(3)$$

Where, A, R and T represent temperature (K), gas constant (8.314 $JK^{-1}mol^{-1}$) and frequency factor, respectively. The R_{CT} and R_{SEI} values are obtained by fitting the Nyquist curves (Figure 6(a) and 6(b)) using the circuit $R_s(QR_{SEI})(QR_{CT})W$. R_{CT} values are usually larger than R_{SEI}, and the resistance decreases as temperature increases. PMAI/HC showed lower R_{SEI} and R_{CT} than PVDF/HC at different temperatures. The activation energy for Na^+ transport through SEI and electrolyte/electrode interface (charge transfer step) were calculated using the Arrhenius equation, illustrated in Figure 6(c). In PMAI/HC, E_a due to SEI (E_{SEI}) and charge transfer (E_{CT}) are 47.43 kJ mol^{-1} and 50.21 kJ mol^{-1}, respectively, which is lower than PVDF/HC with 47.43 kJ mol^{-1} and 50.21 kJ mol^{-1} for E_{SEI} and E_{CT} respectively. The result indicated that Na^+ transport faces lower impedance at the interface of the PMAI containing electrode, which enhances faster Na^+ diffusion by better decoordination of solvent from Na-ion solvation complexes[348,349]. Here, we propose that PMAI binder helps in formation of thin functional SEI, better ion conduction along edges of HC particles and facilitating desolvation of Na^+ at the interface by forming heterojunction between PIL and electrolyte[298].

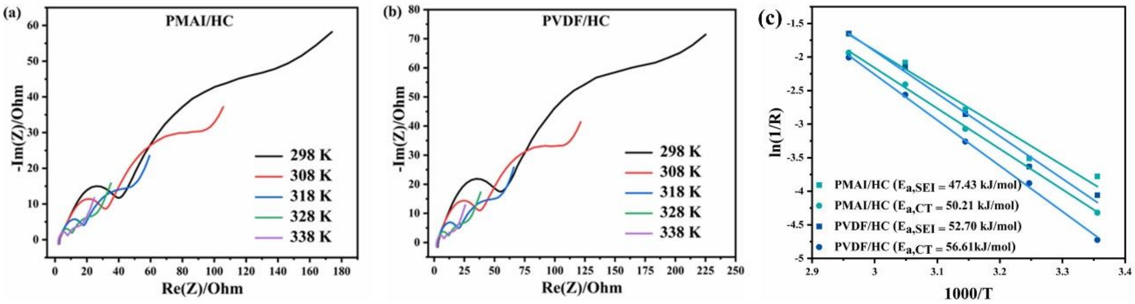

Figure 6: Nyquist plots at different temperatures of cycled (a) PMAI/HC and (b) PVDF/HC electrodes. (c) Arrhenius plot of SEI resistance and charge transfer resistance.

In order to investigate the effect of binder on extended sodiation/desodiation of HC electrode, galvanostatic charge/discharge (GCD) was carried out. Figure 6(a) shows long cycling charge/discharge specific capacities of the PMAI/HC and PVDF/HC at 60 mA g^{-1} after two cycles of precycling at 30 mA g^{-1}. The maximum specific capacity attended by PMAI/HC is 254 mAh g^{-1} with an initial coulombic efficiency (ICE) of 74 %, which is higher than PVDF/HC with 178 mAh g^{-1} and ICE of 47 %. The capacity retention with respect to initial specific capacity at 60 mA g^{-1} of PMAI/HC electrode after 200 cycles is calculated to be 96.2 %, which is much higher than that of PVDF/HC at 88.3 %. The rate capability of the anodic half cells containing different binders were tested at different current densities from 10 mA g^{-1} to 200 mA g^{-1}, as shown in Figure 6(b). PMAI/HC shows better rate capability and delivers a specific capacity of 224 mAh g^{-1} at 10 mA g^{-1} than PVDF/HC with 193 mAh g^{-1}. In addition, PMAI/HC delivers a specific capacity of about 74 mAh g^{-1} at 200 mA g^{-1}; the current density is 20 times higher than the initial current densities and shows a higher capacity than PVDF/HC with 60 mAh g^{-1}.

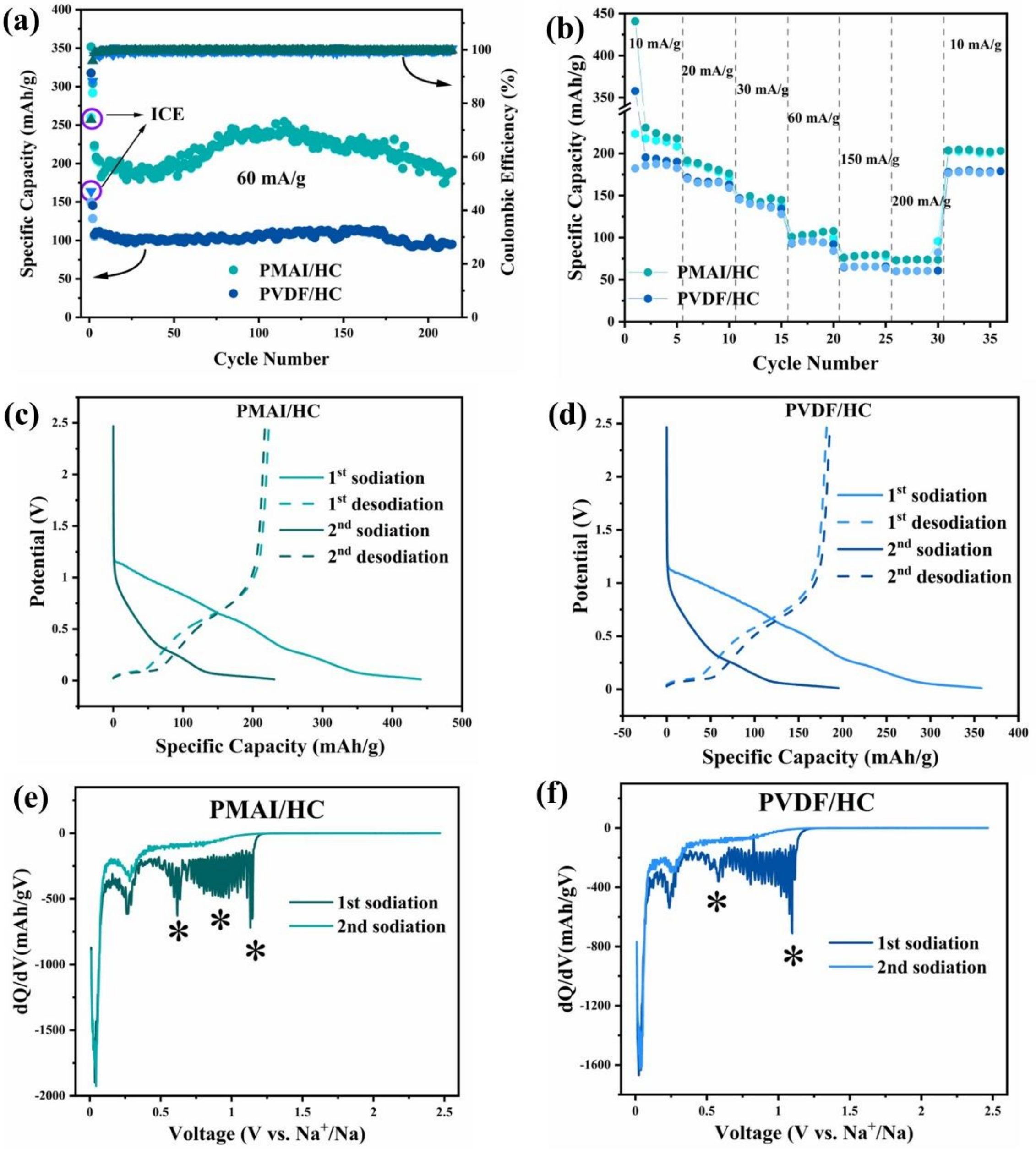

Figure 7: (a) Long cycling stability performance at 60 mA g^{-1} of PMAI/HC and PVDF/HC. (b) Rate performance at varied current densities. Capacity vs. potential curves at 10 mA g^{-1} of (c) PMAI/HC and (d) PVDF/HC. dQ/dV plots obtained from galvanostatic profiles at 10 mA g^{-1} of (e) PMAI/HC and (f) PVDF/HC.

GCD profiles of the first and second cycles of HC-based electrodes, as shown in Figure 6(c) and 6(d), showed two clear regions of sodium storage processes and SEI formation in the first sodiation cycle. The two storage regions are sloping at high potential and plateau at low potential <0.1 V. Dahn et al. proposed an insertion-filling mechanism for sodium storage[350]. Wherein the slope region from ~1 V to 0.1 V is due to Na^+ insertion between parallel or nearly parallel layers, and the plateau corresponds to metal insertion into nanovoids. This was experimentally proved by Dhabi et al. using X-ray diffraction and pore size distribution[351]. The first sodiation curve does not overlap with second sodiation, indicating electrolyte reduction reaction at the surface of HC electrode leading to formation of SEI. Further, dQ/dV plots at 10 mA g^{-1} are obtained to gain insight into the reduction, as shown in Figure 6(e), 6(f). In the first sodiation processes, PVDF/HC displays two apparent reduction peaks at 1.09 V and 0.58 V, which are ascribed to PC and EC decomposition, respectively and vanish in the following cycles[352]. In contrast, PMAI/HC showed three peaks at 1.13 V, 0.92 V and 0.61 V in the first sodiation cycle. Where 1.13 V and 0.61 V are solvent reduction peaks, while 0.92 V corresponds to binder reduction as initially indicated from the CV studies. Zamory et al. mentioned that imidazolium-based IL undergoes reduction when combined with low operating potential electrode, which can be taken advantage of when employing non-soluble PIL; the reduction reaction occurs between PIL binder and other components of electrode helping in binder adhesion to HC by chemical bonding[303]. Hence, PMAI binder helps form functional SEI containing reduced binder product which facilitates Na^+ intercalation/deintercalation and stability of the electrode during extended cycling.

Differential capacity analysis was performed to investigate battery ageing and characterise the State of Health (SOH) by peak change identification. The dQ/dV curves at different cycles of PMAI/HC and PVDF/HC are shown in Figure 8. The peak intensity steadily diminishes in PVDF/HC electrode, whereas the peak intensity remains somewhat unchanged for PMAI/HC electrode. This indicates that PVDF binder-containing electrode undergoes loss of conductivity due to active material loss, which is consistent with cycling stability difference compared to little effect in the presence of PMAI binder[272,310,311].

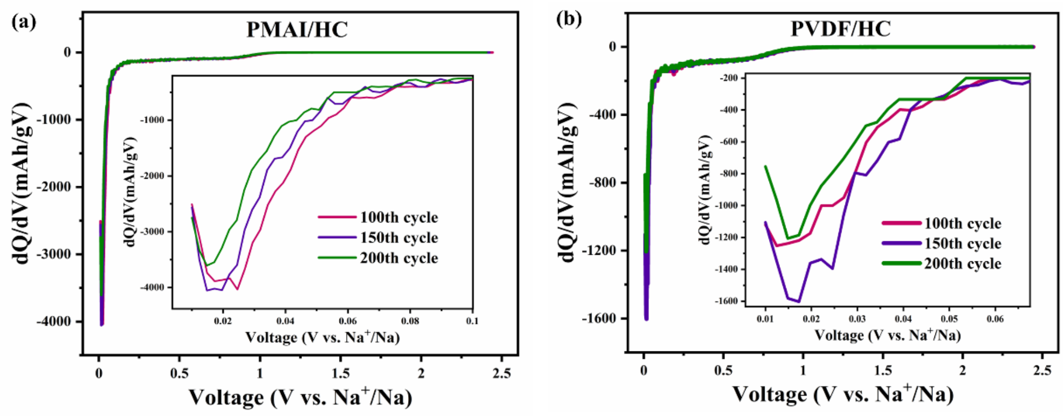

Figure 8: dQ/dV curves at different cycles of (a) PMAI/HC and (b) PVDF/HC.

The impedance to Na^+ kinetics at different potentials in the 0.01 V-2.5 V range was determined using dynamic electrochemical impedance spectroscopy on cycled electrode. The PMAI/HC and PVDF/HC Nyquist plots during sodiation and desodiation are plotted in Figure 9(a), 9(b), 9(c) and 9(d). An equivalent circuit $R_sL(QR_{SEI})(QR_{CT})(XR_{diff})W$ which fits with a high chi-square value, was used on impedance profile. In the circuit, R_s denotes ohmic resistance, R_{SEI} corresponds to SEI resistance, R_{CT} represents charge transfer resistance, R_{diff} is diffusion resistance, Q is constant phase element, X = Q or capacitance (C) and W is Warburg impedance. The PMAI/HC exhibits lower R_{SEI} (Figure 9(e)) and R_{CT} (Figure 9(f)) than PVDF/HC at corresponding sodiation and desodiation potential. Further confirming the formation of thin SEI by the influence and reduction of PMAI binder, and the presence of polar groups in PMAI facilitates Na^+ transport at the electrolyte/electrode interface. The stable R_{SEI} values along the potential range indicate that PMAI/HC contains stable SEI at the HC electrode surface at different potentials[112,165,173]. Moreover, R_{CT} values during sodiation are higher than desodiation in both PMAI/HC and PVDF/HC. This might be due to increased resistance of Na^+ in deeper penetration into electrode structure, while during desodiation, the structure becomes more relaxed, leading to lower R_{CT}. In addition, the Na^+ diffusion during sodiation into the electrode might be a limiting factor, which is facile during desodiation[164,286].

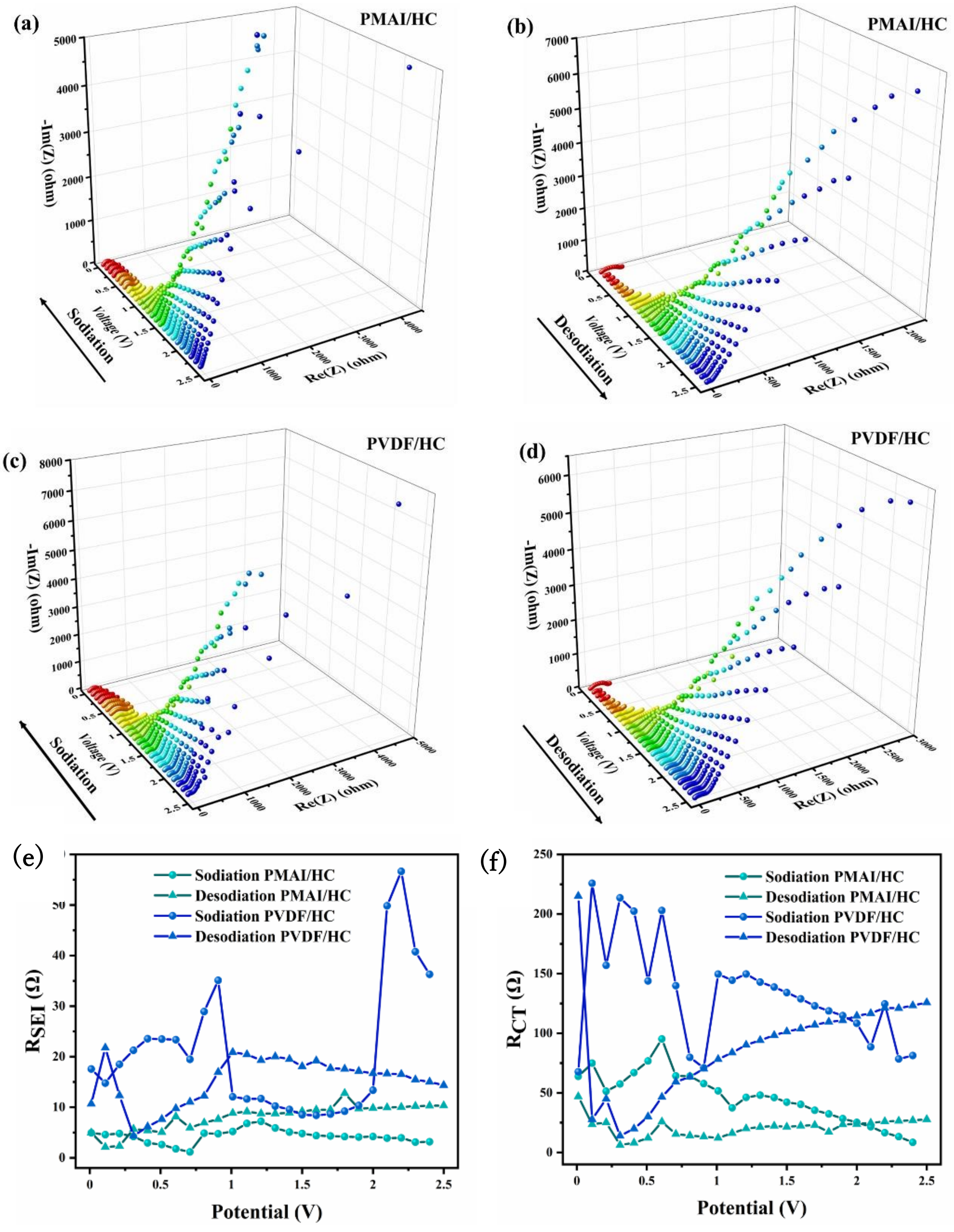

Figure 9: Nyquist profiles at varied voltage during (a) sodiation and (b) desodiation of PMAI/HC and (c) sodiation and (d) desodiation PVDF/HC. (a) R_{SEI} and (b) R_{CT} values during sodiation and desodiation of PMAI/HC and PVDF/HC.

Chemical analysis of HC surface was examined using XPS to understand the SEI film's chemical structure after long cycling of electrodes. Both PMAI/HC and PVDF/HC were analyzed to understand binders' influence on SEI composition. The concentration percentage of each species composition is tabulated in Tables 1, 2. The C 1s XPS results of PMAI/HC and PVDF/HC are shown in Figure 10(a) and 10(d), respectively. Both the anodic half cells contain SP^3 C-C, C=O, C-O and Na_2CO_3 species at the SEI[248–250]. But the PVDF/HC electrode showed a C-F peak which is due to binder containing C-F bond, whereas PMAI/HC electrode showed the presence of C=C and C-N peaks. The presence of a C=C peak originates from the binder reduction product containing imidazolium units at SEI, which helps in ionic conduction along SEI during high Na^+ flux at sodiation potential range. The overlap C-N peak with C-O peak is confirmed by the O 1s spectra concentration analysis[313,315]. The C-N/C-O peak is of higher concentration in C 1s spectra, while in O 1s spectra (Figure 10(b)), the C-O and C=O peak concentrations are the same, confirming the two peaks' overlap[248,250]. This also confirmed the reduction of binder and presence of C-N species at the SEI, enhancing Na^+ transport along the SEI. The higher concentration of C-O and C=O species from the O 1s spectra of PMAI/HC electrode might be from the contribution of the binder. An inorganic-rich phase at the inner layer of SEI is confirmed from Na_2O and NaCl peaks observed from the O 1s (Figure 10(b), 10(e)) and Cl 2p spectra (Figure 10(c), 10(f)), respectively, in both the PMAI/HC and PVDF/HC[353]. The low ICE value in PVDF/HC, might be due to Na trapping at SEI during the reduction of electrolytes, as confirmed by the high concentration of the inorganic species containing sodium elements.

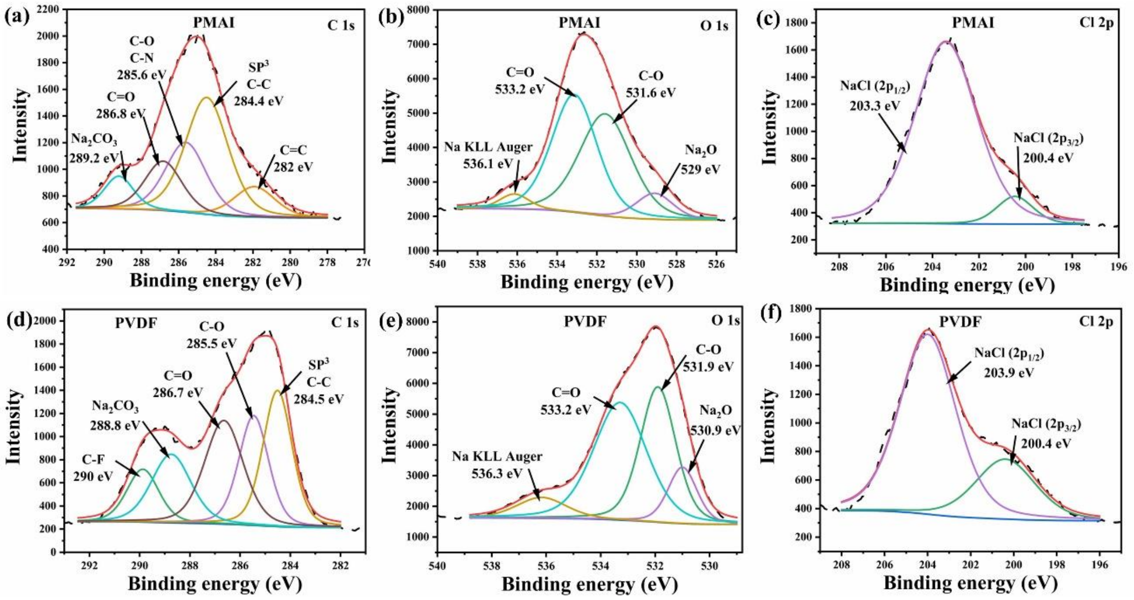

Figure 10: O 1s XPS spectra of the cycled electrode containing (a) PMAI and (d) PVDF binders. Cl 2p XPS spectra of cycled electrode containing (b) PMAI and (c) PVDF binders.

Table 1: The concentration percentage of each species in C 1s spectra is determined using the area under the curve.

C 1s	C=C	C-C	C-O	C=O	Li_2CO_3	C-F
PMAI	10.5 %	42 %	23.9 %	15.4 %	8 %	
PVDF		25.3 %	20.9 %	25.5 %	17.3 %	10.7 %

Table 2: The concentration percentage of each species in O 1s spectra is determined using the area under the curve.

O 1s	Na_2O	C-O	C=O	Na KLL Auger
PMAI	7.9 %	43.4 %	44.4 %	3.6 %
PVDF	11.8 %	35.6 %	45.4 %	7.5 %

The morphology of HC electrodes with different binders after charge/discharge studies was investigated using SEM. Pristine electrodes containing different binders showed a uniform distribution of HC on the current collector, as shown in Figure 11(a), 11(d). A significant change in morphology was observed in PMAI/HC (Figure 11(b)) and PVDF/HC (Figure 11(e)) electrodes after cycling in terms of visible film formation. PVDF/HC showed cracks on the surface, facilitating thick SEI formation, and leading to continuous decomposition of electrolyte and sodium consumption. Moreover, the thick closed membranous film will significantly affect Na-ion migration along the SEI film, thus hindering cycling performance. The cracks on the surface also signify that the PVDF binder provides weak adhesion between HC particles, leading to poor capacity and stability of electrode. Nevertheless, the PMAI/HC electrode maintains a better structural integrity after cycling, confirming the effect of dense polar functional groups in facilitating adhesion with and between the particles. Besides, Figure 11(c), 11(f) present cross-section images of PMAI/HC and PVDF/HC electrodes. When PMAI serves as binder, no gap or cracks are observed within the electrode and between the electrode and current collector, as seen in PVDF/HC electrode. This gap eventually leads to ion and electron conductivity loss and will be widen during extended cycling. Hence, reducing PMAI binder improves adhesion with copper foil and electrode stability.

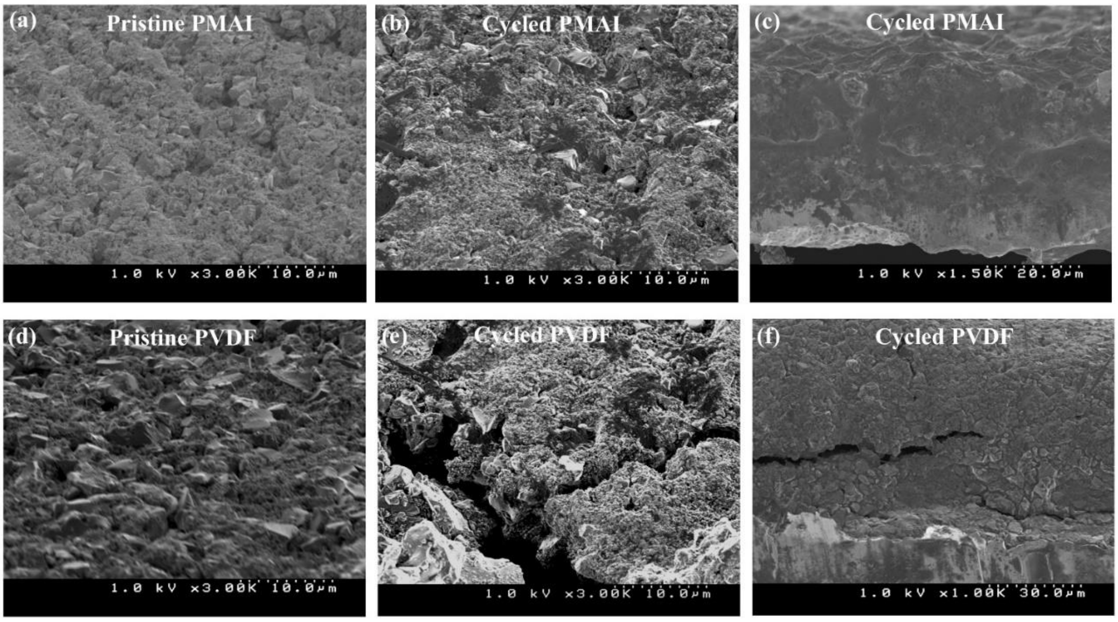

Figure 11: (a) and (d) pristine electrode containing PMAI and PVDF binder respectively. Top view of cycled (b) PMAI and (e) PVDF binder containing electrodes. Cross-section view of cycled (c) PMAI and (f) PVDF binder containing electrodes.

Conclusion:

In this work, we synthesised a water-soluble novel high-density 1-allyl-3-methyimidazolium functional groups PIL binder, poly(oxycarbonylmethylene 1-allyl-3-methyimidazolium (PMAI), which was characterised using ^{1}H and ^{13}C NMR and FT-IR. PIL (PMAI) was utilized as a binder for the first time to fabricate low-cost, environmentally friendly HC anode for SIBs. The concentrated functional groups in PMAI play a key role in facilitating thin, stable, and functional species containing SEI and enhancing the Na^+ kinetics compared to PVDF. In addition, PMAI enhances ICE, rate capability and extended charge /discharge stability. HC electrode containing PMAI binder demonstrates a high specific capacity of 254 mAh g^{-1}, boasting capacity retention of 96.2 % with respect to initial specific capacity at 60 mA g^{-1} current density after 200 cycles. These robust performances are attributed to better diffusion coefficient (3.35E-13 cm^2 s^{-1}), lower R_{SEI} and R_{CT}, and reduced activation energy (E_{SEI} = 47.43 kJ mol^{-1} and E_{CT} = 50.21 kJ mol^{-1}) than PVDF electrode. The densely functionalized polymer provided superior advantages such as inhibiting continuous electrolyte decomposition, binder reduction for better adhesion, low polarization and good stability of electrode morphology. Our work establishes that high-density functional group PIL binders for HC anodes are an effective approach for making SIB commercialization and also open up an avenue for enhancing SIB`s electrochemical performances.

Chapter 7

Conclusion:

As global energy demands increase alongside rapid technological advancements, the need for sustainable energy solutions becomes necessary. Traditional non-renewable resources are reducing, prompting the exploration of alternative energy sources. Renewable energy technologies, while addressing long-term energy needs, must also meet criteria such as high energy density, economic feasibility, safety, and environmental sustainability. Metal-ion batteries are at the forefront of this transition, lauded for their portability and high energy density. However, several challenges remain, particularly regarding electrolytes, water soluble bio-based binders, which are crucial for maintaining conductivity, diffusivity of lithium ions, stability and enhanced specific capacity without compromising electrode compatibility.

Chapter 1 presents an exhaustive review of materials relevant to secondary ion batteries, detailing the roles of the anode, cathode, binder and electrolyte. The author provides a comprehensive analysis of various components, discussing their classifications, material properties, and production values. The focus then shifts to the challenges associated with non-aqueous solvent electrolyte and polymethylene-based binders, emphasizing the potential benefits of high-density functional group polymer chemistry. This foundation sets the stage for the research objectives and scope.

Chapter 2 explores the usage poly(ethoxycarbonylmethylene) (PECM), a high-density functional group polymer as polymer electrolyte. we identified three key traits: (i) the use of a high-density functional group polymer as a polymer electrolyte, (ii) the impact of polymer polarity on electrolyte performance, and (iii) high ionic conductivity and transference number without additives. PECM, characterized by its polar aprotic nature and ethoxy carbonyl ester groups, demonstrated an ionic conductivity of 3.08×10^{-4} S cm^{-1} at 51 °C and a high transference number of 0.98 with PECM/LiTFSI (1:1). These side chain groups facilitate weak interactions and solvation spheres around lithium ions, promoting their movement while hindering bulky anions. The Li/LiNCAO cathodic half-cell with PECM showed superior cycling performance, maintaining 167 mAh g^{-1} capacity with 80% retention over 100 cycles at 0.2 C, and performed well at various current densities. This study highlights that incorporating polar aprotic polymers in lithium-ion battery electrolytes enhances lithium ion solvation, stabilizes the SEI, reduces dendrite risk, offers thermal stability, and expands the electrochemical stability window. Our findings suggest that this approach could lead to affordable, environmentally friendly polymer electrolytes, significantly contributing to the development of commercial lithium-ion batteries based on organic polymer electrolytes.

In Chapter 3, the author investigates the application of poly(fumaric acid) (PFA) using novel synthesis route aimed at reducing costs and minimizing hazardous chemicals while maintaining polymer functionality. PFA offers enhanced rheological properties, such as high viscosity and peel strength, improving graphite anode lamination and electrochemical performance. Compared to polyethylene-based polymers, polymethylene-based PFA, with its decreased flexibility and higher carboxylic acid concentration, demonstrates superior lithium-ion diffusion kinetics, supported by impedance spectroscopy (R_{CT}), activation energy, and diffusion coefficient studies. PFA-based anodic half-cells exhibited better rate capabilities at various current densities. At a 1C long cycling rate, the PFA-based cells achieved a reversible specific capacity of 325 mAh g^{-1} with 79% retention after 700 cycles. PFA/Gr cells showed excellent fast charging at 5C, with reduced polarization and stable coulombic efficiency, reaching 54 mAh g^{-1} in 1.5 minutes. DEIS studies indicated a low R_{SEI} value in the lithiation and delithiation voltage regions, facilitating Li^+ passage into the electrode. Postmortem analyses confirmed a thin SEI layer on the PFA/Gr electrode surface, without exfoliation or cracks. This work demonstrates that high-density functional group polymer binders are environmentally friendly and exhibit superior long cycling, fast charging, and high-loading performance in lithium-ion batteries. Continued research on polymethylene-based high-density functional group polymer binders promises advancements in high-energy rechargeable batteries.

Chapter 4 introduces poly(fumaric acid) as environmentally friendly binder for hard carbon anodes in SIB. The polymer's less flexible backbone and high concentration of functional groups enhance rheology and electrochemical performance due to interactions with both the electrode components and sodium ions. The PFA/HC combination achieved a higher ICE of 80.8% and superior reversible rate capacities at varied current densities, outperforming PAA/HC and PVDF/HC. Additionally, PFA/HC retained 85.4% of its specific capacity after over 250 cycles at 60 mA g^{-1}, reaching a maximum specific capacity of 254 mAh g^{-1}. The high specific capacity is attributed to the continuous carboxylic acid groups in the polymer backbone, which create pathways for Na^+ migration, enhancing ion transport throughout the disordered graphite. The PFA binder also modified the SEI, improving Na^+ kinetics at the interface with a lower activation energy, a higher Na^+ ion diffusion coefficient, and lower R_{SEI} compared to PAA/HC and PVDF/HC. The formation of dense hydrogen bonds between the polymer and oxygen functional groups on the electrode surface reduced continuous electrolyte decomposition by minimizing contact between the electrode and electrolyte. This resulted in improved cycling stability due to an inorganic-rich SEI and maintained electrode integrity, as confirmed by XPS and SEM analyses. This study suggests that the water-soluble PFA binder, with its dense functional polar groups, can significantly enhance electrochemical performance in sodium-ion batteries, offering great potential for practical applications.

Chapter 5 we developed a novel, water-soluble poly(oxycarbonylmethylene 1-allyl-3-methylimidazolium) (PMAI), containing high-density imidazolium functional groups, and characterized using NMR and FT-IR. Evaluated as a binder for LIBs through an aqueous processing method, PMAI offers a sustainable and cost-effective alternative to conventional PVDF. The dense polar groups and free anions in PMAI enhance its affinity with electrolyte solvents, increasing the Li^+ diffusion coefficient. Electrochemical analyses, including CV, charge-discharge profiles, and dQ/dV analyses, showed that PMAI reduces before ethylene carbonate in PMAI/Gr, aiding in the formation of a stable, thin SEI layer enriched with inorganic (LiF, Li_2CO_3) and C-N species. This SEI layer reduces SEI resistance, lowers activation energy, and decreases overpotential, enhancing electrochemical performance compared to PVDF/Gr. PMAI/Gr demonstrated superior long cycling performance at 1C and 5C with enhanced specific capacity of 298 mAh g^{-1} and 85 mAh g^{-1} respectively. These improvements are due to the greater ionic conductivity and enhanced electrolyte absorption provided by PMAI/Gr binders, increasing lithium mobility within the electrodes. Postmortem analysis revealed a crackless, uniform surface on the aged PMAI/Gr electrode, contrasting with the PVDF/Gr electrode, attributed to the superior peel strength of the PMAI binder. These results establish PMAI as a superior binder for LIBs, encouraging further exploration of densely functional group polymers and their role in enhancing electrochemical performance.

Chapter 6 deals with synthesizing a novel, water-soluble, high-density polymer binder, poly(oxycarbonylmethylene 1-allyl-3-methylimidazolium) (PMAI), characterized using NMR and FT-IR. For the first time, PMAI was used as a binder for fabricating low-cost, environmentally friendly hard carbon HC anodes for SIBs. The functional groups in PMAI play a crucial role in forming a thin, stable SEI and enhancing Na^+ kinetics compared to PVDF. PMAI improved the ICE, rate capability, and charge/discharge stability. The HC electrode with PMAI binder exhibited a high specific capacity of 254 mAh g^{-1}, retaining 96.2% of its initial capacity at a current density of 60 mA g^{-1} after 200 cycles. This performance is attributed to a better diffusion coefficient (3.35×10^{-13} cm^2 s^{-1}), lower R_{SEI} and R_{CT}, and reduced activation energy (E_{SEI} = 47.43 kJ mol^{-1} and E_{CT} =

50.21 kJ mol^{-1}) compared to PVDF electrodes. The densely functionalized polymer provided benefits such as inhibiting continuous electrolyte decomposition, enhancing adhesion, reducing polarization, and maintaining electrode morphology stability. Our work demonstrates that high-density functional group PIL binders for HC anodes are an effective strategy for advancing SIB commercialization and improving their electrochemical performance.

Publications and Conferences

Publications

1. Charge–Discharge Behavior of Lithium-Ion Batteries Using a Polymer Electrolyte Bearing High-Density Functional Groups

Amarshi Patra and Noriyoshi Matsumi
ACS Applied Energy Materials 2023 6 (23), 11973-11982
DOI: 10.1021/acsaem.3c02137

2. Water-Soluble Densely Functionalized Poly(Hydroxycarbonylmethylene) Binder for Higher-Performance Hard Carbon Anode-Based Sodium-Ion Batteries

Amarshi Patra and Noriyoshi Matsumi
Journal of Materials Chemistry A 2024, Inpress.
https://doi.org/10.1039/D4TA00285G.

Conferences

1. 72nd The Society of Polymer Science, Japan (SPSJ)

May 2023
Poster Presentation on the title:
“Charge-Discharge Study of Li-ion Secondary Batteries using Poly(substituted methylene) as Electrolyte. ”

2. 6th International Conference on Clean Energy and Technology 2023

Jun 2023
Oral Presentation on the title:
“Charge-discharge Study of Li-ion Secondary Batteries Using Poly(ethoxycarbonyl methylene) as Electrolyte. ”

3. 72rd The Society of Polymer Science, Japan (SPSJ)

September 2023
Poster Presentation on the title:
“Charge-discharge Behavior of LIB Using Polymer Electrolyte Bearing High Density Functional Groups.”

4. ECSJ The 64th Battery Symposium in Japan

Nov 2023
Oral Presentation on the title:
“Polymethylene-based High-Density Functional Groups Polymer Binder in Metal-Ion Batteries.”

References

1 G. Zhou, F. Li and H. M. Cheng, in *Energy and Environmental Science*, Royal Society of Chemistry, 2014, vol. 7, pp. 1307–1338.

2 F. Cheng, J. Liang, Z. Tao and J. Chen, *Advanced Materials*, 2011, **23**, 1695–1715.

3 M. Li, J. Lu, Z. Chen and K. Amine, *Advanced Materials*, 2018, 30.

4 J.-M. Tarascon and M. Armand, *Issues and challenges facing rechargeable lithium batteries*, 2001.

5 David. Linden and T. B. Reddy, *Handbook of batteries*, McGraw-Hill, 2002.

6 M. Armand and J.-M. Tarascon, *Building better batteries*, 2008.

7 P. Kurzweil, *J Power Sources*, 2010, **195**, 4424–4434.

8 B. Liu, J. G. Zhang and W. Xu, *Joule*, 2018, 2, 833–845.

9 S. K. Das, S. Mahapatra and H. Lahan, *J Mater Chem A Mater*, 2017, 5, 6347–6367.

10 C. You, X. Wu, X. Yuan, Y. Chen, L. Liu, Y. Zhu, L. Fu, Y. Wu, Y. G. Guo and T. Van Ree, *J Mater Chem A Mater*, 2020, 8, 25601–25625.

11 L. Chen, M. Fiore, J. E. Wang, R. Ruffo, D. K. Kim and G. Longoni, *Adv Sustain Syst*, 2018, 2.

12 Y. Li, Y. Lu, C. Zhao, Y. S. Hu, M. M. Titirici, H. Li, X. Huang and L. Chen, *Energy Storage Mater*, 2017, **7**, 130–151.

13 S. Hemavathi, S. Srirama and A. S. Prakash, *ChemBioEng Reviews*, 2023, 10, 1123–1145.

14 R. Holze, *Journal of Solid State Electrochemistry*, 2012, **16**, 2845–2846.

15 T. Kim, W. Song, D. Y. Son, L. K. Ono and Y. Qi, *J Mater Chem A Mater*, 2019, 7, 2942–2964.

16 G. E. Blomgren, *J Electrochem Soc*, 2017, **164**, A5019–A5025.

17 D. Deng, *Energy Sci Eng*, 2015, 3, 385–418.

18 E. Peled, *The Electrochemical Behavior of Alkali and Alkaline Earth Metals in Nonaqueous Battery Systems-The Solid Electrolyte Interphase Model*, .

19 N. Nitta and G. Yushin, *Particle and Particle Systems Characterization*, 2014, 31, 317–336.

20 M. H. Hossain, M. A. Chowdhury, N. Hossain, M. A. Islam and M. H. Mobarak, *Chemical Engineering Journal Advances*, 2023, **16**, 100569.

21 D. Aurbach, B. Markovsky, G. Salitra, E. Markevich, Y. Talyossef, M. Koltypin, L. Nazar, B. Ellis and D. Kovacheva, *J Power Sources*, 2007, **165**, 491–499.

22 N. A. Kaskhedikar and J. Maier, *Advanced Materials*, 2009, 21, 2664–2680.

23 M. Winter, J. O. Besenhard, M. E. Spahr and P. Novák, *Advanced Materials*, 1998, **10**, 725–763.

24 D. Aurbach, B. Markovsky, I. Weissman, E. Levi and Y. Ein-Eli, *Electrochim Acta*, 1999, **45**, 67–86.

25 J. Cho, *J Mater Chem*, 2010, **20**, 4009–4014.

26 M. N. Obrovac and L. J. Krause, *J Electrochem Soc*, 2007, **154**, A103.

27 M. N. Obrovac and L. Christensen, *Electrochemical and Solid-State Letters*, , DOI:10.1149/1.1652421.

28 T. D. Hatchard and J. R. Dahn, *J Electrochem Soc*, 2004, **151**, A838.

29 S. Woo Lee, M. T. McDowell, J. Wook Choi and Y. Cui, *Nano Lett*, 2011, **11**, 3034–3039.

30 X. Hua Liu, F. Fan, H. Yang, S. Zhang, J. Yu Huang and T. Zhu, *ACS Nano*, 2013, **7**, 1495–1503.

31 M. Park, Y. Cho, K. Kim, J. Kim, M. Liu and J. Cho, *Angewandte Chemie*, 2011, **123**, 9821–9824.

32 M. Haro, T. Song, A. Guerrero, L. Bertoluzzi, J. Bisquert, U. Paik and G. Garcia-Belmonte, *Physical Chemistry Chemical Physics*, 2014, **16**, 17930–17935.

33 X. Hua Liu, S. Huang, S. Tom Picraux, J. Li, T. Zhu and J. Yu Huang, *Nano Lett*, 2011, **11**, 3991–3997.

34 L. Liu, F. Xie, J. Lyu, T. Zhao, T. Li and B. G. Choi, *J Power Sources*, 2016, **321**, 11–35.

35 C. Kim, H. Kim, M. K. Sadan, M. Jeon, G. B. Cho, T. H. Nam, K. K. Cho, J. H. Ahn and H. J. Ahn, *J Alloys Compd*, 2021, **886**, 161240.

36 R. Chen, T. Zhao, X. Zhang, L. Li and F. Wu, *Nanoscale Horiz*, 2016, 1, 423–444.

37 C. Tian, F. Lin and M. M. Doeff, *Acc Chem Res*, 2017, **51**, 89–96.

38 K. Nishimura, T. Douzono, M. Kasai, H. Andou, Y. Muranaka and Y. Kozono, *J Power Sources*, 1999, **81–82**, 420–424.

39 J. Ling, C. Karuppiah, S. G. Krishnan, M. V. Reddy, I. Izwan Misnon, M. Hasbi Ab Rahim, C.-C. Yang and R. Jose, *Energy & Fuels*, 2021, **35**, 10428–10450.

40 M. Kotal, S. Jakhar, S. Roy and H. K. Sharma, *J Energy Storage*, 2022, **47**, 103534.

41 R. Chen, T. Zhao, X. Zhang, L. Li and F. Wu, *Nanoscale Horiz*, 2016, 1, 423–444.

42 J. Xing, S. Bliznakov, L. Bonville, M. Oljaca and R. Maric, *Electrochemical Energy Reviews*, 2022, 5.

43 K. Xu, *Chem Rev*, 2014, 114, 11503–11618.

44 Kazunori Ozawa, *Lithium Ion Rechargeable Batteries*, Wiley-VCH Verlag GmbH & Co., Weinheim, 2009.

45 K. Gao, L. Sun, K. Wang and Y. Zhang, *Mater Today Energy*, 2023, **37**, 101413.

46 X. Zhao, C. Wang, H. Liu, Y. Liang and L. Z. Fan, *Batter Supercaps*, 2023, 6.

47 Z. Song, F. Chen, M. Martinez-Ibañez, W. Feng, M. Forsyth, Z. Zhou, M. Armand and H. Zhang, *Nat Commun*, , DOI:10.1038/s41467-023-40609-y.

48 J. C. Barbosa, R. Gonçalves, C. M. Costa and S. Lanceros-Méndez, *ACS Omega*, 2022, **7**, 14457–14464.

49 K. Sashmitha and M. U. Rani, *Polymer Bulletin*, 2023, 80, 89–135.

50 S. Liang, W. Yan, X. Wu, Y. Zhang, Y. Zhu, H. Wang and Y. Wu, *Solid State Ion*, 2018, **318**, 2–18.

51 W. Ren, C. Ding, X. Fu and Y. Huang, *Energy Storage Mater*, 2021, **34**, 515–535.

52 Z. H. Li, H. P. Zhang, P. Zhang, Y. P. Wu and X. D. Zhou, *J Power Sources*, 2008, **184**, 562–565.

53 P. Raghavan, J. W. Choi, J. H. Ahn, G. Cheruvally, G. S. Chauhan, H. J. Ahn and C. Nah, *J Power Sources*, 2008, **184**, 437–443.

54 J. R. Kim, S. W. Choi, S. M. Jo, W. S. Lee and B. C. Kim, *Electrochim Acta*, 2004, **50**, 69–75.

55 Q. Shi, M. Yu, X. Zhou, Y. Yan and C. Wan, *J Power Sources*, 2002, **103**, 286–292.

56 B. Ameduri, *Chem Rev*, 2009, **109**, 6632–6686.

57 H. S. Choe, J. Giaccai, M. Alamgir and K. M. Abraham, *Electrochim Acta*, 1995, **40**, 2289–2293.

58 M. Egashira, H. Todo, N. Yoshimoto and M. Morita, *J Power Sources*, 2008, **178**, 729–735.

59 C. Wu and W. Zeng, *Chem Asian J*, 2022, 17.

60 A. J. Bhattacharyya, M. Patel and S. K. Das, *Monatsh Chem*, 2009, 140, 1001–1010.

61 K. S. Perera, M. A. K. L. Dissanayake, S. Skaarup and K. West, in *Journal of Solid State Electrochemistry*, Springer Science and Business Media, LLC, 2008, vol. 12, pp. 873–877.

62 S. Ramesh and K. C. Wong, *Ionics (Kiel)*, 2009, **15**, 249–254.

63 W. Pu, X. He, L. Wang, Z. Tian, C. Jiang and C. Wan, *Ionics (Kiel)*, 2008, **14**,

27–31.

64 M. Patel, K. G. Chandrappa and A. J. Bhattacharyya, *Electrochim Acta*, 2008, **54**, 209–215.

65 Y. V Baskakova, O. V Yarmolenko and O. N. Efimov, *Russian Chemical Reviews*, 2012, **81**, 367–380.

66 Y. Shi, X. Zhou and G. Yu, *Acc Chem Res*, 2017, **50**, 2642–2652.

67 L. Rao, X. Jiao, C.-Y. Yu, A. Schmidt, C. O'Meara, J. Seidt, J. R. Sayre, Y. M. Khalifa and J.-H. Kim, *ACS Applied Materials & Interfaces*, 2022, **14**, 861–872.

68 J. Yoon, G. Han, S. Cho, C. Lee, E. Lee, K. Yoon and H.-J. Jin, *ACS Appl Polym Mater*, 2023, **5**, 1199–1207.

69 N. Yuca, H. Zhao, X. Song, M. Ferhat Dogdu, W. Yuan, Y. Fu, V. S. Battaglia, X. Xiao and G. Liu, *ACS Applied Materials & Interfaces*, 2014, **6**, 17111–17118.

70 M. Wu, X. Xiao, N. Vukmirovic, S. Xun, P. K. Das, X. Song, P. Olalde-Velasco, D. Wang, A. Z. Weber, L.-W. Wang, V. S. Battaglia, W. Yang and G. Liu, *J Am Chem Soc*, 2013, **135**, 12048–12056.

71 IGOR KOVALENKO, BOGDAN ZDYRKO, ALEXANDRE MAGASINSKI, BENJAMIN HERTZBERG, ZORAN MILICEV, RUSLAN BURTOVYY, IGOR LUZINOV and GLEB YUSHIN, *Science (1979)*, 2011, **334**, 75–79.

72 D. Mazouzi, B. Lestriez, L. Roué and D. Guyomard, *Electrochemical and Solid-State Letters*, , DOI:10.1149/1.3212894.

73 J. Shim, R. Kostecki, T. Richardson, X. Song and K. A. Striebel, *J Power Sources*, 2002, **112**, 222–230.

74 W. Zhu, J. Zhou, S. Xiang, X. Bian, J. Yin, J. Jiang and L. Yang, *Front Chem*, 2021, 9.

75 Z. B. P. Designed Research; L, -K T P Performed Research; L, P. | ; H. Sentan Kagaku and G. Daigakuin Daigaku, , DOI:10.1073/pnas.1202636109/-/DCSupplemental.

76 Y. Zhao, B. Liu, L. Pan and G. Yu, *Energy Environ Sci*, 2013, 6, 2856–2870.

77 H. Wu, G. Yu, L. Pan, N. Liu, M. T. McDowell, Z. Bao and Y. Cui, *Nat Commun*, , DOI:10.1038/ncomms2941.

78 Y. Shi and G. Yu, *Chemistry of Materials*, 2016, **28**, 2466–2477.

79 H. Zhao, Z. Wang, P. Lu, M. Jiang, F. Shi, X. Song, Z. Zheng, X. Zhou, Y. Fu, G. Abdelbast, X. Xiao, Z. Liu, V. S. Battaglia, K. Zaghib and G. Liu, *Nano Lett*, 2014, **14**, 6704–6710.

80 H. Pan, Y. S. Hu and L. Chen, *Energy Environ Sci*, 2013, 6, 2338–2360.

81 B. Dunn, H. Kamath and J.-M. Tarascon, *Electrical Energy Storage for the Grid: A Battery of Choices System power ratings, module size*, .

82 C. X. Zu and H. Li, *Energy Environ Sci*, 2011, **4**, 2614–2624.

83 J. M. Tarascon, *Nat Chem*, 2010, 2, 510.

84 Y. Nishi, *J Power Sources*, 2001, **100**, 101–106.

85 J. Y. Hwang, S. T. Myung and Y. K. Sun, *Chem Soc Rev*, 2017, 46, 3529–3614.

86 P. Adelhelm, P. Hartmann, C. L. Bender, M. Busche, C. Eufinger and J. Janek, *Beilstein Journal of Nanotechnology*, 2015, **6**, 1016–1055.

87 M. D. Slater, D. Kim, E. Lee and C. S. Johnson, *Adv Funct Mater*, 2013, **23**, 947–958.

88 J. P. Parant, R. Olazcuaga, M. Devalette, C. Fouassier and P. Hagenmuller, *J Solid State Chem*, 1971, **3**, 1–11.

89 A. S. Nagelberg and W. L. Worrell, *J Solid State Chem*, 1979, **29**, 345–354.

90 E. de la Llave, V. Borgel, K.-J. Park, J.-Y. Hwang, Y.-K. Sun, P. Hartmann, F.-Francois Chesneau and D. Aurbach, *ACS Applied Materials & Interfaces*, 2016, **8**, 1867–1875.

91 K. Kubota and S. Komaba, *J Electrochem Soc*, 2015, **162**, A2538–A2550.

92 P. Thomas, J. Ghanbaja and D. Billaud, *Electrochim Acta*, 1999, **45**, 423–430.

93 R. Alcántara, J. M. Jiménez-Mateos, P. Lavela and J. L. Tirado, *Electrochem commun*, 2001, **3**, 639–642.

94 V. Palomares, P. Serras, I. Villaluenga, K. B. Hueso, J. Carretero-González and T. Rojo, *Energy Environ Sci*, 2012, 5, 5884–5901.

95 S. Komaba, W. Murata, T. Ishikawa, N. Yabuuchi, T. Ozeki, T. Nakayama, A. Ogata, K. Gotoh and K. Fujiwara, *Adv Funct Mater*, 2011, **21**, 3859–3867.

96 X. Xia and J. R. Dahn, *J Electrochem Soc*, 2012, **159**, A515–A519.

97 D. A. Stevens and J. R. Dahn, *J Electrochem Soc*, 2001, **148**, A803.

98 L. Joncourt, M. Mermoux, P. Touzain, L. Bonnetain, D. Dumas and B. Allard, *Journal of Physics and Chemistry of Solids*, 1996, **57**, 877–882.

99 A. Ponrouch, E. Marchante, M. Courty, J. M. Tarascon and M. R. Palacín, *Energy Environ Sci*, 2012, **5**, 8572–8583.

100 J. Y. Luo, W. J. Cui, P. He and Y. Y. Xia, *Nat Chem*, 2010, **2**, 760–765.

101 Y. Wang, J. Yi and Y. Xia, *Adv Energy Mater*, 2012, 2, 830–840.

102 X. Wu, Y. Cao, X. Ai, J. Qian and H. Yang, *Electrochem commun*, 2013, **31**, 145–148.

103 D. Guironnet, L. Caporaso, B. Neuwald, I. Göttker-Schnetmann, L. Cavallo and S. Mecking, *J Am Chem Soc*, 2010, **132**, 4418–4426.

104 C. Chen, S. Luo and R. F. Jordan, *J Am Chem Soc*, 2008, **130**, 12892–12893.

105 W. Weng, Z. Shen and R. F. Jordan, *J Am Chem Soc*, 2007, **129**, 15450–15451.

106 T. Kochi, S. Noda, K. Yoshimura and K. Nozaki, *J Am Chem Soc*, 2007, **129**, 8948–8949.

107 S. Luo, J. Vela, G. R. Lief and R. F. Jordan, *J Am Chem Soc*, 2007, **129**, 8946–8947.

108 G. W. Cowell and A. Ledwith, *Quarterly Reviews, Chemical Society*, 1970, **24**, 119–167.

109 M. Imoto and T. Nakaya, *Journal of Macromolecular Science, Part C*, 1972, **7**,

1–48.

110 K. J. Shea, *Chemistry – A European Journal*, 2000, **6**, 1113–1119.

111 E. Drent, R. Van Dijk, R. Van Ginkel, B. Van Oort and R. I. Pugh, *Chemical Communications*, 2002, **2**, 744–745.

112 B. Srimitra Mantripragada, R. Badam and N. Matsumi, *ACS Appl Energy Mater*, 2022, **5**, 6903–6912.

113 K. S. Patnaik, R. Badam, Y. Peng, K. Higashimine, T. Kaneko and N. Matsumi, *Chemical Communications*, 2021, **57**, 13704–13707.

114 K. M. Diederichsen, E. J. McShane and B. D. McCloskey, *ACS Energy Lett*, 2017, **2**, 2563–2575.

115 K. Xu, *Chem Rev*, 2004, **104**, 4303–4418.

116 K. Xu, *Chem Rev*, 2014, 114, 11503–11618.

117 S. Han, *Sci Rep*, , DOI:10.1038/s41598-019-42050-y.

118 S. Han, *Sci Rep*, , DOI:10.1038/srep46718.

119 D. E. Fenton, J. M. Parker and P. V. Wright, *Polymer (Guildf)*, 1973, **14**, 589.

120 S. Ramesh and S. C. Lu, *J Appl Polym Sci*, , DOI:10.1002/app.36790.

121 K. S. Ngai, S. Ramesh, K. Ramesh and J. C. Juan, *Ionics (Kiel)*, 2016, 22, 1259–1279.

122 H.-J. Rhoo, H.-T. Kim, J.-K. Park and T.-S. Hwangb, *Ionic conduction in plasticized PVC/PMMA blend polymer electrolytes*, Ekevier Science Ltd, 1997, vol. 42.

123 C. Berthier, W. Gorecki, M. Minier, M. B. Armand, J. M. Chabagno and P. Rigaud, *Solid State Ion*, 1983, **11**, 91–95.

124 M. Watanabe, K. Nagaoka and I. Shinohara, *Ionic Conductivity of Hybrid Films Based on Polyacrylonitrile and Their Battery Application*, .

125 E. Tsuchida, H. Ohno and K. Tsunemi, *CONDUCTION OF LITHIUM IONS IN POLYVINYLIDENE FLUORIDE AND ITS DERIVATIVES-I*, .

126 K. Tsunemi, H. Ohno and E. Tsuchida, *A MECHANISM OF IONIC CONDUCTION OF POLY (VINYLIDENE FLUORIDEtLITHIUM PERCHLORATE HYBRID FILMS*, .

127 G. Frand, M. Rezrazi, C. Rousselot and C. Truche, *SOLID STATE IOWICS Fast ion transport in new lithium electrolytes gelled with PMMA. 1. Influence of polymer concentration*, 1993, vol. 66.

128 Y. Liu, Q. Zeng, Z. Li, A. Chen, J. Guan, H. Wang, S. Wang and L. Zhang, *Advanced Science*, 2023.

129 J. Mindemark, M. J. Lacey, T. Bowden and D. Brandell, *Prog Polym Sci*, 2018, **81**, 114–143.

130 H. Xu, J. Xie, Z. Liu, J. Wang and Y. Deng, *MRS Energy & Sustainability*, , DOI:10.1557/mre.2020.3.

131 A. Buchheit, M. Grünebaum, B. Teßmer, M. Winter and H.-D. Wiemhöfer, *The Journal of Physical Chemistry C*, 2021, **125**, 4371–4378.

132 B. Commarieu, A. Paolella, S. Collin-Martin, C. Gagnon, A. Vijh, A. Guerfi and K. Zaghib, *J Power Sources*, 2019, **436**, 226852.

133 D. Rosenbach, A. Krimalowski, H. Erabhoina and M. Thelakkat, *J Mater Chem A Mater*, , DOI:10.1039/d2ta00800a.

134 E. Ihara, 2010, pp. 191–231.

135 A. Matsumoto, K. Fukushima and T. Otsu, *Synthesis of Substituted Polymethylenes by Radical Polymerization of N,N,N>N'-Tetraalkylfumaramides and Their Characterization*, .

136 T. Otsu, T. Yasuhara, K. Shiraishi and S. Mori, *Radical High Polymerization of Di-tert-Butyl Fumarate and Novel Synthesis of High Molecular Weight Poly(Fumaric Acid) from Its Polymer**, 1984, vol. 12.

137 T. Otsu, T. Yasuhara and A. Matsumoto, *Journal of Macromolecular Science: Part A - Chemistry*, 1988, **25**, 537–554.

138 J. Evans, C. A. Vincent and P. G. Bruce, *Electrochemical measurement of transference numbers in polymer electrolytes*, .

139 E. Ihara, Y. Ishiguro, N. Yoshida, T. Hiraren, T. Itoh and K. Inoue, *Macromolecules*, 2009, **42**, 8608–8610.

140 C. Reichardt, *Solvatochromic Dyes as Solvent Polarity Indicators*, .

141 C. Hubert, D. Fichou, P. Valat, F. Garnier and B. Villeret, *A solvatochromic dye-doped polymer for detection of polar additives in hydrocarbon blends*, 1995, vol. 36.

142 K. Xu, *Chem Rev*, 2004, **104**, 4303–4418.

143 M. Fan, Y. Liang, F. Zhou and W. Liu, *RSC Adv*, 2012, **2**, 6824–6830.

144 Z. Liu, K. Shikinaka, Y. Otsuka and Y. Tominaga, *Chemical Communications*, 2022, **58**, 4504–4507.

145 I. Der Wu and F. C. Chang, *Polymer (Guildf)*, 2007, **48**, 989–996.

146 F. B. Dias, L. Plomp and J. B. J. Veldhuis, *Trends in polymer electrolytes for secondary lithium batteries*, 2000, vol. 88.

147 K. H. Choi, S. H. Kim, H. J. Ha, E. H. Kil, C. K. Lee, S. B. Lee, J. K. Shim and S. Y. Lee, *J Mater Chem A Mater*, 2013, **1**, 5224–5231.

148 M. Ebadi, T. Eriksson, P. Mandal, L. T. Costa, C. Moyses Araujo, J. Mindemark and D. Brandell, *Macromolecules*, 2020, **53**, 764–774.

149 C. A. Angell, *MOBILE IONS IN AMORPHOUS SOLIDS*, 1992, vol. 43.

150 S. Seki, M. A. B. H. Susan, T. Kaneko, H. Tokuda, A. Noda and M. Watanabe, *Journal of Physical Chemistry B*, 2005, **109**, 3886–3892.

151 V. Sharova, A. Moretti, T. Diemant, A. Varzi, R. J. Behm and S. Passerini, *J Power Sources*, 2018, **375**, 43–52.

152 M. Doyle, T. F. Fuller and J. Newman, ~ *Pergamon THE IMPORTANCE OF THE LITHIUM ION TRANSFERENCE NUMBER IN LITHIUM/POLYMER CELLS*, 1994, vol. 39.

153 L. Meabe, S. R. Peña, M. Martinez-Ibañez, Y. Zhang, E. Lobato, H. Manzano, M. Armand, J. Carrasco and H. Zhang, *Journal of Physical Chemistry C*, 2020, **124**, 17981–17991.

154 M. Hofmann, F. Nagler, M. Kapuschinski, U. Guntow and G. A. Giffin, *ChemSusChem*, 2020, **13**, 5962–5971.

155 I. A. Shkrob, J. A. Gilbert, P. J. Phillips, R. Klie, R. T. Haasch, J. Bareño and D. P. Abraham, *J Electrochem Soc*, 2017, **164**, A1489–A1498.

156 R. Jung, R. Morasch, P. Karayaylali, K. Phillips, F. Maglia, C. Stinner, Y. Shao-Horn and H. A. Gasteiger, *J Electrochem Soc*, 2018, **165**, A132–A141.

157 H. S. Liu, Z. R. Zhang, Z. L. Gong and Y. Yang, *Electrochemical and Solid-State Letters*, , DOI:10.1149/1.1738471.

158 R. Nandan, N. Takamori, K. Higashimine, R. Badam and N. Matsumi, *J Mater Chem A Mater*, 2022, **10**, 5230–5243.

159 B. Roy, P. Cherepanov, C. Nguyen, C. Forsyth, U. Pal, T. C. Mendes, P. Howlett, M. Forsyth, D. MacFarlane and M. Kar, *Adv Energy Mater*, , DOI:10.1002/aenm.202101422.

160 J. Alvarado, M. A. Schroeder, T. P. Pollard, X. Wang, J. Z. Lee, M. Zhang, T. Wynn, M. Ding, O. Borodin, Y. S. Meng and K. Xu, *Bisalt Ether Electrolytes: A Pathway Towards Lithium Metal Batteries with Ni-rich Cathodes*, .

161 W. Xue, M. Huang, Y. Li, Y. G. Zhu, R. Gao, X. Xiao, W. Zhang, S. Li, G. Xu, Y. Yu, P. Li, J. Lopez, D. Yu, Y. Dong, W. Fan, Z. Shi, R. Xiong, C. J. Sun, I. Hwang, W. K. Lee, Y. Shao-Horn, J. A. Johnson and J. Li, *Nat Energy*, 2021, **6**, 495–505.

162 A. Patra and N. Matsumi, *ACS Appl Energy Mater*, 2023, **6**, 11973–11982.

163 S. N. Mishra, S. Punyasloka, B. S. Mantripragada, A. Pradhan and N. Matsumi, *ACS Appl Energy Mater*, , DOI:10.1021/acsaem.3c02129.

164 T. Pindi Jayakumar, R. Badam and N. Matsumi, *ACS Appl Energy Mater*, 2020, **3**, 3337–3346.

165 A. Gupta, R. Badam and N. Matsumi, *ACS Appl Energy Mater*, 2022, **5**, 7977–7987.

166 H. Adenusi, G. A. Chass, S. Passerini, K. V. Tian and G. Chen, *Adv Energy Mater*, 2023, 13.

167 P. Verma, T. Sasaki and P. Novák, *Electrochim Acta*, 2012, **82**, 233–242.

168 S. Menkin, D. Golodnitsky and E. Peled, *Electrochem commun*, 2009, **11**, 1789–1791.

169 S. S. Zhang, *J Power Sources*, 2006, **162**, 1379–1394.

170 F. Jeschull, M. J. Lacey and D. Brandell, *Electrochim Acta*, 2015, **175**, 141–150.

171 M. Winter, *Z. Phys. Chem*, 2009, **223**, 1395–1406.

172 G. Xu, Q. bo Yan, A. Kushima, X. Zhang, J. Pan and J. Li, *Nano Energy*, 2017, **31**, 568–574.

173 A. Gupta, R. Badam, A. Nag, T. Kaneko and N. Matsumi, *ACS Appl Energy Mater*, 2021, **4**, 2231–2240.

174 W. J. Song, S. H. Joo, D. H. Kim, C. Hwang, G. Y. Jung, S. Bae, Y. Son, J. Cho, H. K. Song, S. K. Kwak, S. Park and S. J. Kang, *Nano Energy*, 2017, **32**, 255–262.

175 L. Zhang, L. Chai, Q. Qu, L. Zhang, M. Shen and H. Zheng, *Electrochim Acta*, 2013, **105**, 378–383.

176 K. Soeda, Y. Matsui, M. Yamagata and M. Ishikawa, *ECS Trans*, 2013, **53**, 93–102.

177 F. Jeschull, D. Brandell, M. Wohlfahrt-Mehrens and M. Memm, *Energy Technology*, 2017, **5**, 2108–2118.

178 Z. Zhang, T. Zeng, C. Qu, H. Lu, M. Jia, Y. Lai and J. Li, *Electrochim Acta*, 2012, **80**, 440–444.

179 J. H. Lee, U. Paik, V. A. Hackley and Y. M. Choi, *J Power Sources*, 2006, **161**, 612–616.

180 S. Komaba, N. Yabuuchi, T. Ozeki, K. Okushi, H. Yui, K. Konno, Y. Katayama and T. Miura, *J Power Sources*, 2010, **195**, 6069–6074.

181 S. Komaba, K. Okushi and H. Groult, *ECS Trans*, 2008, **11**, 63–70.

182 F. Jeschull, J. Maibach, R. Félix, M. Wohlfahrt-Mehrens, K. Edström, M. Memm

and D. Brandell, *ACS Appl Energy Mater*, 2018, **1**, 5176–5188.

183 J. H. Lee, U. Paik, V. A. Hackley and Y. M. Choi, *J Power Sources*, 2006, **161**, 612–616.

184 N. S. Hochgatterer, M. R. Schweiger, S. Koller, P. R. Raimann, T. Wöhrle, C. Wurm and M. Winter, *Electrochemical and Solid-State Letters*, , DOI:10.1149/1.2888173.

185 *Preparation of Poly(fumric acid) from Poly(di-t-butyl fumarate) and Poly(di-trimethylsilyl fumarate)*, .

186 N. Raimundo, B. E. Baysal and G. S. Shadel, *Trends Mol Med*, 2011, 17, 641–649.

187 P. Yadav, A. K. Chauhan, R. B. Singh, S. Khan and G. Halabi, *Functional Foods and Nutraceuticals in Metabolic and Non-Communicable Diseases*, 2022, 325–337.

188 S. T. Yang, K. Zhang, B. Zhang and H. Huang, *Comprehensive Biotechnology, Second Edition*, 2011, **3**, 163–177.

189 T. G. M. Dhar and A. J. Dyckman, *Comprehensive Medicinal Chemistry III*, 2017, **5–8**, 395–419.

190 J. Nam, E. Kim, R. K.K, Y. Kim and T. H. Kim, *Sci Rep*, , DOI:10.1038/s41598-020-71625-3.

191 K. M. Kim, W. S. Jeon, I. J. Chung and S. H. Chang, *J Power Sources*, 1999, **83**, 108–113.

192 A. N. Preman, H. Lee, J. Yoo, I. T. Kim, T. Saito and S. K. Ahn, *J Mater Chem A Mater*, 2020, 8, 25548–25570.

193 J. Padarti, S. Hirai, H. Sakagami, T. Matsuda, H. Suzuki and T. Ohno, *Journal of the Ceramic Society of Japan*, 2022, **130**, 832–836.

194 A. Pradhan, R. Badam, R. Miyairi, N. Takamori and N. Matsumi, *ACS Mater Lett*, 2023, **5**, 413–420.

195 T. Zhu, Q. Hu, G. Yan, J. Wang, Z. Wang, H. Guo, X. Li and W. Peng, *Energy*

Technology, , DOI:10.1002/ente.201900273.

196 T. R. L. C. Paixão, *ChemElectroChem*, 2020, **7**, 3414–3415.

197 X. Wan, T. Mu, B. Shen, Q. Meng, G. Lu, S. Lou, P. Zuo, Y. Ma, C. Du and G. Yin, *Nano Energy*, 2022, **99**, 107334.

198 T. Doi, Y. Iriyama, T. Abe and Z. Ogumi, *Anal Chem*, 2005, **77**, 1696–1700.

199 H. Sano, M. Kitta and H. Matsumoto, *J Electrochem Soc*, 2016, **163**, D3076–D3079.

200 A. Celik-Kucuk and T. Abe, *J Power Sources*, 2023, **581**, 233478.

201 M. Gao, N. Liu, Y. Chen, Y. Guan, W. Wang, H. Zhang, F. Wang and Y. Huang, *Chemical Communications*, 2015, **51**, 12118–12121.

202 X. Rao, Y. Lou, J. Chen, H. Lu, B. Cheng, W. Wang, H. Fang, H. Li and S. Zhong, *Front Energy Res*, , DOI:10.3389/fenrg.2020.00003.

203 J. H. Chang, M. W. Pin, J. Choi, J. Park, G. M. Choi, J. Yun, K. Y. Cho, Z. A. Chandio, I. Kim, Y. Kim, V. V. T. Padil and J. Y. Cheong, *Sustainable Chemistry for the Environment*, 2023, **2**, 100012.

204 J. Sun, X. Ren, Z. Li, W. Tian, Y. Zheng, L. Wang and G. Liang, *J Alloys Compd*, 2019, **783**, 379–386.

205 J. H. Lee, S. Lee, U. Paik and Y. M. Choi, *J Power Sources*, 2005, **147**, 249–255.

206 M. Yang, P. Chen, J. Li, R. Qi, Y. Huang, P. Müller-Buschbaum, Y. J. Cheng, K. Guo and Y. Xia, *J Mater Chem A Mater*, 2023, **11**, 6205–6216.

207 R. I. R. Blyth, H. Buqa, F. P. Netzer, M. G. Ramsey, J. O. Besenhard, P. Golob and M. Winter, *Appl Surf Sci*, 2000, **167**, 99–106.

208 S. Li, Q. Meng, M. Fan, K. Yang and G. Tian, , DOI:10.1007/s11581-020-03590-w/Published.

209 D. Versaci, R. Nasi, U. Zubair, J. Amici, M. Sgroi, M. A. Dumitrescu, C. Francia, S. Bodoardo and N. Penazzi, *Journal of Solid State Electrochemistry*, 2017, **21**, 3429–3435.

210 K.-F. Chiu, H.-J. Leu, S.-H. Su and R.-Z. Wu, *ECS Trans*, 2016, **73**, 289–304.

211 E. Pohjalainen, O. Sorsa, J. Juurikivi and T. Kallio, *Energy Technology*, 2016, **4**, 470–472.

212 S. S. Zhang, K. Xu and T. R. Jow, *J Power Sources*, 2004, **138**, 226–231.

213 D. Shin, H. Park and U. Paik, *Electrochem commun*, 2017, **77**, 103–106.

214 D. V. Carvalho, N. Loeffler, M. Hekmatfar, A. Moretti, G. T. Kim and S. Passerini, *Electrochim Acta*, 2018, **265**, 89–97.

215 F. Jeschull, M. J. Lacey and D. Brandell, *Electrochim Acta*, 2015, **175**, 141–150.

216 G. Suo, S. Musab Ahmed, Y. Cheng, J. Zhang, Z. Li, X. Hou, Y. Yang, X. Ye, L. Feng, L. Zhang and Q. Yu, *J Colloid Interface Sci*, 2022, **608**, 275–283.

217 G. Suo, Y. Cheng, R. Mu, X. Hou, Y. Yang, X. Ye and L. Zhang, *J Colloid Interface Sci*, 2023, **641**, 981–989.

218 A. Rudola, C. J. Wright and J. Barker, *Energy Material Advances*, 2021, 2021.

219 K. Bhawana, M. Gautam, G. K. Mishra, N. Chakrabarty, S. Wajhal, D. Kumar, D. P. Dutta and S. Mitra, *Carbon N Y*, 2023, **214**, 118319.

220 A. Kanwade, S. Gupta, A. Kankane, M. K. Tiwari, A. Srivastava, J. A. Kumar Satrughna, S. Chand Yadav and P. M. Shirage, *RSC Adv*, 2022, 12, 23284–23310.

221 Y. F. Zhu, Y. Xiao, S. X. Dou, Y. M. Kang and S. L. Chou, *eScience*, 2021, **1**, 13–27.

222 D. Pahari, A. Kumar, D. Das and S. Puravankara, *Int J Energy Res*, 2022, 46, 21894–21927.

223 Q. Wang, J. Li, H. Jin, S. Xin and H. Gao, *InfoMat*, 2022, 4.

224 K. Bhawana, A. Roy, N. Chakrabarty, M. Gautam, D. P. Dutta and S. Mitra, *Electrochim Acta*, 2022, **425**, 140744.

225 M. A. Muñoz-Márquez, M. Zarrabeitia, E. Castillo-Martínez, A. Eguía-Barrio, T. Rojo and M. Casas-Cabanas, *ACS Applied Materials & Interfaces*, 2015, **7**, 7801–7808.

226 M. Dahbi, N. Yabuuchi, K. Kubota, K. Tokiwa and S. Komaba, *Physical Chemistry Chemical Physics*, 2014, 16, 15007–15028.

227 R. Dong, L. Zheng, Y. Bai, Q. Ni, Y. Li, F. Wu, H. Ren and C. Wu, *Advanced Materials*, , DOI:10.1002/adma.202008810.

228 E. Olsson, J. Cottom, H. Au, Z. Guo, A. C. S. Jensen, H. Alptekin, A. J. Drew, M. M. Titirici and Q. Cai, *Adv Funct Mater*, , DOI:10.1002/adfm.201908209.

229 F. Xie, Z. Xu, A. C. S. Jensen, F. Ding, H. Au, J. Feng, H. Luo, M. Qiao, Z. Guo, Y. Lu, A. J. Drew, Y. S. Hu and M. M. Titirici, *J Mater Chem A Mater*, 2019, **7**, 27567–27575.

230 X. X. He, W. H. Lai, Y. Liang, J. H. Zhao, Z. Yang, J. Peng, X. H. Liu, Y. X. Wang, Y. Qiao, L. Li, X. Wu and S. L. Chou, *Advanced Materials*, , DOI:10.1002/adma.202302613.

231 K. Y. Zhang, Y. Q. Fu, H. H. Liu, J. L. Yang, M. Y. Su, Y. Wang and X. L. Wu, *Phys Scr*, , DOI:10.1088/1402-4896/ad0d6d.

232 J. M. Cao, K. Y. Zhang, J. L. Yang, Z. Y. Gu and X. L. Wu, *Chinese Chemical Letters*, 2024, **35**, 109304.

233 Z. Y. Gu, X. T. Wang, Y. L. Heng, K. Y. Zhang, H. J. Liang, J. L. Yang, E. H. Ang, P. F. Wang, Y. You, F. Du and X. L. Wu, *Sci Bull (Beijing)*, 2023, **68**, 2302–2306.

234 H. S. Hirsh, B. Sayahpour, A. Shen, W. Li, B. Lu, E. Zhao, M. Zhang and Y. S. Meng, *Energy Storage Mater*, 2021, **42**, 78–87.

235 L. Xiao, H. Lu, Y. Fang, M. L. Sushko, Y. Cao, X. Ai, H. Yang and J. Liu, *Adv Energy Mater*, , DOI:10.1002/aenm.201703238.

236 H. Lohani, A. Kumar, P. Kumari, A. Ahuja, M. Gautam, A. Sengupta and S. Mitra, *ACS Applied Materials & Interfaces*, 2022, **14**, 37793–37803.

237 H. Lu, X. Chen, Y. Jia, H. Chen, Y. Wang, X. Ai, H. Yang and Y. Cao, *Nano Energy*, 2019, **64**, 103903.

238 H. Fang, S. Gao, M. Ren, Y. Huang, F. Cheng, J. Chen and F. Li, *Angewandte Chemie - International Edition*, , DOI:10.1002/anie.202214717.

239 G. Suo, B. Zhao, R. Mu, C. Lin, S. Javed, X. Hou, X. Ye, Y. Yang and L. Zhang, *J Energy Storage*, 2024, **77**, 109801.

240 Y. Huang, L. Zhao, L. Li, M. Xie, F. Wu and R. Chen, *Advanced Materials*, 2019, 31.

241 A. Ponrouch, E. Marchante, M. Courty, J. M. Tarascon and M. R. Palacín, *Energy Environ Sci*, 2012, **5**, 8572–8583.

242 S. Trivedi, V. Pamidi, S. P. Bautista, F. N. A. Shamsudin, M. Weil, P. Barpanda, D. Bresser and M. Fichtner, *Adv Energy Mater*, 2023.

243 B. T. Young, C. C. Nguyen, A. Lobach, D. R. Heskett, J. C. Woicik and B. L. Lucht, *J Mater Res*, 2019, **34**, 97–106.

244 C. Cuong Nguyen, T. Yoon, D. M. Seo, P. Guduru and B. L. Lucht, *ACS Applied Materials & Interfaces*, 2016, **8**, 12211–12220.

245 Y. Kondo, T. Fukutsuka, Y. Yokoyama, Y. Miyahara, K. Miyazaki and T. Abe, *J Appl Electrochem*, 2021, **51**, 629–638.

246 J. Pati, H. Raj, S. K. Sapra, A. Dhaka, A. K. Bera, S. M. Yusuf and R. S. Dhaka, *J Mater Chem A Mater*, 2022, **10**, 15460–15473.

247 M. Dahbi, T. Nakano, N. Yabuuchi, T. Ishikawa, K. Kubota, M. Fukunishi, S. Shibahara, J. Y. Son, Y. T. Cui, H. Oji and S. Komaba, *Electrochem commun*, 2014, **44**, 66–69.

248 J. L. Xia, A. H. Lu, X. F. Yu and W. C. Li, *Adv Funct Mater*, , DOI:10.1002/adfm.202104137.

249 R. Gond, H. D. Asfaw, O. Hosseinaei, K. Edström, R. Younesi and A. J. Naylor, *ACS Sustain Chem Eng*, , DOI:10.1021/acssuschemeng.1c05263.

250 W. Li, X. Guo, K. Song, J. Chen, J. Zhang, G. Tang, C. Liu, W. Chen and C. Shen, *Adv Energy Mater*, , DOI:10.1002/aenm.202300648.

251 R. R. Li, Z. Yang, X. X. He, X. H. Liu, H. Zhang, Y. Gao, Y. Qiao, L. Li and S. L. Chou, *Chemical Communications*, 2021, **57**, 12406–12416.

252 M. Azeem, A. K. Borg-Karlson and G. K. Rajarao, *Bioresour Technol*, 2013, **144**,

684–688.

253 I. Goldberg and J. S. Rokem, *Encyclopedia of Microbiology, Third Edition*, 2009, 421–442.

254 B. Ameduri, *Chem Rev*, 2009, **109**, 6632–6686.

255 Z.-Y. Gu, J.-M. Cao, J.-Z. Guo, X.-T. Wang, X.-X. Zhao, S.-H. Zheng, Z.-H. Sun, J.-L. Yang, K.-Y. Zhang, H.-J. Liang, K. Li and X.-L. Wu, *J Am Chem Soc*, 2024, **146**, 4652–4664.

256 S. Komaba, T. Ozeki and K. Okushi, *J Power Sources*, 2009, **189**, 197–203.

257 S. Komaba, N. Yabuuchi, T. Ozeki, K. Okushi, H. Yui, K. Konno, Y. Katayama and T. Miura, *J Power Sources*, 2010, **195**, 6069–6074.

258 D. Bresser, D. Buchholz, A. Moretti, A. Varzi and S. Passerini, *Energy Environ Sci*, 2018, **11**, 3096–3127.

259 N. Lingappan, L. Kong and M. Pecht, *Renewable and Sustainable Energy Reviews*, 2021, **147**, 111227.

260 K. Gotoh, T. Ishikawa, S. Shimadzu, N. Yabuuchi, S. Komaba, K. Takeda, A. Goto, K. Deguchi, S. Ohki, K. Hashi, T. Shimizu and H. Ishida, *J Power Sources*, 2013, **225**, 137–140.

261 H. Chen, M. Ling, L. Hencz, H. Y. Ling, G. Li, Z. Lin, G. Liu and S. Zhang, *Chem Rev*, 2018, 118, 8936–8982.

262 *Preparation of Poly(fumric acid) from Poly(di-t-butyl fumarate) and Poly(di-trimethylsilyl fumarate)*, .

263 S. Komaba, W. Murata, T. Ishikawa, N. Yabuuchi, T. Ozeki, T. Nakayama, A. Ogata, K. Gotoh and K. Fujiwara, *Adv Funct Mater*, 2011, **21**, 3859–3867.

264 J. Pan, Y. Sun, Y. Yan, L. Feng, Y. Zhang, A. Lin, F. Huang and J. Yang, *JACS Au*, 2021, **1**, 1208–1216.

265 P. Oh, H. Lee, S. Park, H. Cha, J. Kim and J. Cho, *Adv Energy Mater*, , DOI:10.1002/aenm.202000904.

266 U. Westerhoff, K. Kurbach, F. Lienesch and M. Kurrat, *Energy Technology*, 2016,

4, 1620–1630.

267 Z. Zhang, YingHuang, G. Zhang and L. Chao, *Energy Storage Mater*, 2021, **41**, 631–641.

268 S. Kim, D. Y. Han, G. Song, J. Lee, T. Park and S. Park, *Chemical Engineering Journal*, 2023, **473**, 145441.

269 R. Morita, K. Gotoh, M. Fukunishi, K. Kubota, S. Komaba, N. Nishimura, T. Yumura, K. Deguchi, S. Ohki, T. Shimizu and H. Ishida, *J Mater Chem A Mater*, 2016, **4**, 13183–13193.

270 H. Au, H. Alptekin, A. C. S. Jensen, E. Olsson, C. A. O'Keefe, T. Smith, M. Crespo-Ribadeneyra, T. F. Headen, C. P. Grey, Q. Cai, A. J. Drew and M. M. Titirici, *Energy Environ Sci*, 2020, **13**, 3469–3479.

271 M. Dubarry, V. Svoboda, R. Hwu and B. Y. Liaw, *Electrochemical and Solid-State Letters*, , DOI:10.1149/1.2221767.

272 A. J. Smith and J. R. Dahn, *J Electrochem Soc*, 2012, **159**, A290–A293.

273 M. Wang, Q. Wang, X. Ding, Y. Wang, Y. Xin, P. Singh, F. Wu and H. Gao, *Interdisciplinary Materials*, 2022, **1**, 373–395.

274 S. Komaba, N. Yabuuchi, T. Ozeki, K. Okushi, H. Yui, K. Konno, Y. Katayama and T. Miura, *J Power Sources*, 2010, **195**, 6069–6074.

275 L. El Ouatani, R. Dedryvère, J. B. Ledeuil, C. Siret, P. Biensan, J. Desbrières and D. Gonbeau, *J Power Sources*, 2009, **189**, 72–80.

276 M. Vadivazhagan, R. Jayan and K. Nallathamby, *Energy & Fuels*, 2022, **36**, 1081–1090.

277 I. Moeez, H.-D. Lim, J.-H. Park, H.-G. Jung and K. Yoon Chung, *ACS Energy Lett*, 2019, **4**, 2060–2068.

278 K. Edström, M. Herstedt and D. P. Abraham, *J Power Sources*, 2006, **153**, 380–384.

279 M. Carboni, J. Manzi, A. R. Armstrong, J. Billaud, S. Brutti and R. Younesi, *ChemElectroChem*, , DOI:10.1002/celc.201801621.

280 G. N. Suresh babu, S. D and N. Kalaiselvi, *J Alloys Compd*, 2021, **851**, 156894.

281 A. Wang, S. Kadam, H. Li, S. Shi and Y. Qi, *NPJ Comput Mater*, 2018, 4.

282 J.-S. Bridel, T. Azaïs, M. Morcrette, J.-M. Tarascon and D. Larcher, *Chemistry of Materials*, 2009, **22**, 1229–1241.

283 L. Fransson, T. Eriksson, K. Edström, T. Gustafsson and J. O. Thomas, *J Power Sources*, 2001, **101**, 1–9.

284 V. A. Agubra and J. W. Fergus, *J Power Sources*, 2014, **268**, 153–162.

285 T. Kennedy, M. Brandon, F. Laffir and K. M. Ryan, *J Power Sources*, 2017, **359**, 601–610.

286 S. Gourang Patnaik, T. Pindi Jayakumar, Y. Sawamura and N. Matsumi, *ACS Appl Energy Mater*, 2021, **4**, 2241–2247.

287 H. Zhao, J. Ren, X. He, J. Li, C. Jiang and C. Wan, *Solid State Sci*, 2008, **10**, 612–617.

288 Y. Shi, X. Zhou and G. Yu, *Acc Chem Res*, 2017, **50**, 2642–2652.

289 L. Man, Y. Yang, H. Wang, Y. Wang, Y. An, J. Bao, C. Wang and Z. Yang, *ACS Appl Energy Mater*, 2021, **4**, 3803–3811.

290 M. J. Lacey, F. Jeschull, K. Edström and D. Brandell, *The Journal of Physical Chemistry C*, 2014, **118**, 25890–25898.

291 S. Vauthier, M. Alvarez-Tirado, G. Guzmán-González, L. C. Tomé, S. Cotte, L. Castro, A. Guéguen, D. Mecerreyes and N. Casado, *Mater Today Chem*, 2023, **27**, 101293.

292 Y. Bai, Y. Cao, J. Zhang, M. Wang, R. Li, P. Wang, S. M. Zakeeruddin and M. Grätzel, *Nat Mater*, 2008, **7**, 626–630.

293 A. Balducci, W. A. Henderson, M. Mastragostino, S. Passerini, P. Simon and F. Soavi, *Electrochim Acta*, 2005, **50**, 2233–2237.

294 R. D. Costa, E. Ortí, H. J. Bolink, S. Graber, C. E. Housecroft and E. C. Constable, *Adv Funct Mater*, 2010, **20**, 1511–1520.

295 E. Paillard, Q. Zhou, W. A. Henderson, G. B. Appetecchi, M. Montanino and S. Passerini, *J Electrochem Soc*, 2009, **156**, A891.

296 H. Ohno, *Electrochim Acta*, 2001, **46**, 1407–1411.

297 G. B. Appetecchi, G. T. Kim, M. Montanino, M. Carewska, R. Marcilla, D. Mecerreyes and I. De Meatza, *J Power Sources*, 2010, **195**, 3668–3675.

298 K. Grygiel, J.-S. Lee, K. Sakaushi, M. Antonietti and J. Yuan, *ACS Macro Lett*, 2015, **4**, 1312–1316.

299 J. Yuan, S. Prescher, K. Sakaushi and M. Antonietti, *J Mater Chem A Mater*, 2015, **3**, 7229–7234.

300 J. S. Lee, K. Sakaushi, M. Antonietti and J. Yuan, *RSC Adv*, 2015, **5**, 85517–85522.

301 A. C. Rolandi, C. Pozo-Gonzalo, I. de Meatza, N. Casado, D. Mecerreyes and M. Forsyth, *Advanced Energy and Sustainability Research*, , DOI:10.1002/aesr.202300149.

302 S. Vauthier, M. Alvarez-Tirado, G. Guzmán-González, L. C. Tomé, S. Cotte, L. Castro, A. Guéguen, D. Mecerreyes and N. Casado, *Mater Today Chem*, 2023, **27**, 101293.

303 J. Von Zamory, M. Bedu, S. Fantini, S. Passerini and E. Paillard, *J Power Sources*, 2013, **240**, 745–752.

304 H. Zhang, J. Wu, J. Zhang and J. He, *Macromolecules*, 2005, **38**, 8272–8277.

305 R. Zarrougui, R. Hachicha, R. Rjab and O. Ghodbane, *J Mol Liq*, 2018, **249**, 795–804.

306 Y. Pei, S. Chu, Y. Zheng, J. Zhang, H. Liu, X. Zheng and K. Tang, *ACS Sustainable Chemistry & Engineering*, 2018, **7**, 2530–2537.

307 K. Xu and A. Von Wald Cresce, *J Mater Res*, 2012, **27**, 2327–2341.

308 S. S. Zhang, K. Xu and T. R. Jow, *Electrochim Acta*, 2006, **51**, 1636–1640.

309 P. Bonhôte, A.-P. Dias, N. Papageorgiou, K. Kalyanasundaram and M. Grätzel, *Inorg Chem*, 1996, **35**, 1168–1178.

310 M. Dubarry, V. Svoboda, R. Hwu and B. Y. Liaw, *Electrochemical and Solid-State Letters*, , DOI:10.1149/1.2221767.

311 M. Dubarry, V. Svoboda, R. Hwu and B. Y. Liaw, *J Power Sources*, 2007, **165**, 566–572.

312 R. Dedryvère, S. Leroy, H. Martinez, F. Blanchard, D. Lemordant and D. Gonbeau, *J Phys Chem B*, 2006, **110**, 12986–12992.

313 S. Aldroubi, B. Larhrib, L. Larbi, I. B. Malham, C. M. Ghimbeu, L. Monconduit, A. Mehdi and N. Brun, *J Mater Chem A Mater*, 2023, **11**, 16755–16766.

314 S. Park, S. Kim, J. A. Lee, M. Ue and N. S. Choi, *Chem Sci*, 2023.

315 R. Grissa, V. Fernandez, N. Fairley, J. Hamon, N. Stephant, J. Rolland, R. Bouchet, M. Lecuyer, M. Deschamps, D. Guyomard and P. Moreau, *ACS Appl Energy Mater*, 2018, **1**, 5694–5702.

316 M. Xu, Y. Liu, B. Li, W. Li, X. Li and S. Hu, *Electrochem commun*, 2012, **18**, 123–126.

317 Q. Zhang, J. Pan, P. Lu, Z. Liu, M. W. Verbrugge, B. W. Sheldon, Y.-T. Cheng, Y. Qi and X. Xiao, *Nano Lett*, 2016, **16**, 2011–2016.

318 A. Patra and N. Matsumi, *ACS Appl Energy Mater*, , DOI:10.1021/acsaem.3c02137.

319 A. Kanwade, S. Gupta, A. Kankane, M. K. Tiwari, A. Srivastava, J. A. Kumar Satrughna, S. Chand Yadav and P. M. Shirage, *RSC Adv*, 2022, 12, 23284–23310.

320 B. V. Rami Reddy, R. Ravikumar, C. Nithya and S. Gopukumar, *J Mater Chem A Mater*, 2015, **3**, 18059–18063.

321 V. R. Reddy Boddu, M. Palanisamy, L. Sinha, S. C. Yadav, V. G. Pol and P. M. Shirage, *Sustain Energy Fuels*, 2021, **5**, 3219–3228.

322 A. Sarkar, S. Sarkar and S. Mitra, *J Mater Chem A Mater*, 2017, **5**, 24929–24941.

323 P. Barpanda, L. Lander, S. I. Nishimura and A. Yamada, *Adv Energy Mater*, 2018, 8.

324 M. Casas-Cabanas, V. V. Roddatis, D. Saurel, P. Kubiak, J. Carretero-González,

V. Palomares, P. Serras and T. Rojo, *J Mater Chem*, 2012, **22**, 17421–17423.

325 S. P. Vanam and P. Barpanda, *Electrochim Acta*, 2022, **431**, 141122.

326 H. Kabbour, D. Coillot, M. Colmont, C. Masquelier and O. Mentré, *J Am Chem Soc*, 2011, **133**, 11900–11903.

327 N. Sun, H. Liu and B. Xu, *J Mater Chem A Mater*, 2015, **3**, 20560–20566.

328 R. Alcántara, J. M. Jiménez-Mateos, P. Lavela and J. L. Tirado, *Electrochem commun*, 2001, **3**, 639–642.

329 M. M. Rahman, A. M. Glushenkov, T. Ramireddy and Y. Chen, *Chemical Communications*, 2014, **50**, 5057–5060.

330 P. Song, J. Yang, C. Wang, T. Wang, H. Gao, G. Wang and J. Li, *Nanomicro Lett*, , DOI:10.1007/s40820-023-01082-w.

331 M. R. Panda, A. Raj K, A. Ghosh, A. Kumar, D. Muthuraj, S. Sau, W. Yu, Y. Zhang, A. K. Sinha, M. Weyland, Q. Bao and S. Mitra, *Nano Energy*, 2019, **64**, 103951.

332 D. Su, H. J. Ahn and G. Wang, *Chemical Communications*, 2013, **49**, 3131–3133.

333 W. Luo, C. Bommier, Z. Jian, X. Li, R. Carter, S. Vail, Y. Lu, J.-J. Lee and X. Ji, *ACS Applied Materials & Interfaces*, 2015, **7**, 2626–2631.

334 D. A. Stevens and J. R. Dahn, *J Electrochem Soc*, 2001, **148**, A803.

335 S. Wenzel, T. Hara, J. Janek and P. Adelhelm, *Energy Environ Sci*, 2011, **4**, 3342–3345.

336 C. Bommier, W. Luo, W. Y. Gao, A. Greaney, S. Ma and X. Ji, *Carbon N Y*, 2014, **76**, 165–174.

337 Nagmani, A. Kumar and S. Puravankara, *Battery Energy*, , DOI:10.1002/bte2.20220007.

338 A. Beda, C. Vaulot, F. Rabuel, M. Morcrette and C. M. Ghimbeu, *Energy Advances*, 2022, 185–190.

339 M. Dar, K. Majid and M. Wahid, *Journal of Electroanalytical Chemistry*, 2021,

899, 115669.

340 M. Liu, J. Zhang, S. Guo, B. Wang, Y. Shen, X. Ai, H. Yang and J. Qian, *ACS Applied Materials & Interfaces*, 2020, **12**, 17620–17627.

341 T. Rajkumar and G. Ranga Rao, *Mater Chem Phys*, 2008, **112**, 853–857.

342 T. Yamada and M. Mizuno, *ACS Omega*, 2022, **7**, 29804–29812.

343 A. V. Kubarkov, A. A. Asharchuk, O. A. Drozhzhin, E. A. Karpushkin, K. J. Stevenson, E. V. Antipov and V. G. Sergeyev, *ACS Appl Energy Mater*, 2021, **4**, 12310–12318.

344 A. Clara Rolandi, C. Pozo-Gonzalo, I. de Meatza, N. Casado, M. Forsyth and D. Mecerreyes, *ACS Appl Energy Mater*, 2023, **6**, 8616–8625.

345 L. Ling, Y. Bai, Z. Wang, Q. Ni, G. Chen, Z. Zhou and C. Wu, *ACS Applied Materials & Interfaces*, 2018, **10**, 5560–5568.

346 Z.-Y. Gu, Z.-H. Sun, J.-Z. Guo, X.-X. Zhao, C.-D. Zhao, S.-F. Li, X.-T. Wang, W.-H. Li, Y.-L. Heng and X.-L. Wu, *ACS Applied Materials & Interfaces*, 2020, **12**, 47580–47589.

347 A. Funabiki, M. Inaba and Z. Ogumi, *J Power Sources*, 1997, **68**, 227–231.

348 W. Zhang, X. Sun, Y. Tang, H. Xia, Y. Zeng, L. Qiao, Z. Zhu, Z. Lv, Y. Zhang, X. Ge, S. Xi, Z. Wang, Y. Du and X. Chen, *J Am Chem Soc*, 2019, **141**, 14038–14042.

349 S. Sawayama, R. Ochi, T. Kawaguchi, Y. Katayama, M. Morita and K. Fujii, *ACS Appl Energy Mater*, 2023, **6**, 989–996.

350 D. A. Stevens and J. R. Dahn, *High Capacity Anode Materials for Rechargeable Sodium-Ion Batteries*, 2000, vol. 147.

351 M. Dahbi, M. Kiso, K. Kubota, T. Horiba, T. Chafik, K. Hida, T. Matsuyama and S. Komaba, *J Mater Chem A Mater*, 2017, **5**, 9917–9928.

352 L. Ling, Y. Bai, Z. Wang, Q. Ni, G. Chen, Z. Zhou and C. Wu, *ACS Applied Materials & Interfaces*, 2018, **10**, 5560–5568.

353 I. Moeez, D. Susanto, J. H. Park, J. Y. Kim, H. D. Lim and K. Y. Chung, *Adv*

Funct Mater, , DOI:10.1002/adfm.202210370.